

DIPARTIMENTO DI FISICA E ASTRONOMIA
Corso di Dottorato di Ricerca in Astronomia
CICLO XXVI

HOMOGENEOUS ANALYSIS OF A SAMPLE OF OPEN CLUSTERS
IN THE CONTEXT OF THE BOCCE PROJECT
AND THE GAIA-ESO SURVEY

Dottorando
Paolo Donati

Relatori
Chiar.mo Prof. F. R. Ferraro
Dott.ssa A. Bragaglia

Coordinatore
Chiar.mo Prof. L. Moscardini

Esame finale anno 2014

Settore Concorsuale: 02/C1 – Astronomia, Astrofisica, Fisica della Terra e dei Pianeti
Settore Scientifico-Disciplinare: FIS/05 – Astronomia e Astrofisica

Acknowledgements

I am grateful to Angela Bragaglia, Monica Tosi, Michele Cignoni, Giacomo Beccari, Elena Pancino, Donatella Romano, Alessio Mucciarelli, Gabriele Cocozza, and all the people of the EPInArBo node. This research project would not have been possible without their help.

A special thank goes to Alessandra, for her patience.

Paolo

Abstract

The open clusters are commonly thought of as sparsely populated, loosely concentrated, barely gravitationally bound systems of a few tens or hundreds of stars. They can be described as simple stellar populations, which makes them useful templates for stellar evolution models. In our Galaxy, the Milky Way, we know about 3000 open clusters, of very different ages. The youngest formed a few million years ago while the oldest system known, Berkeley 17, is about 9 Gyr old. Open clusters are mainly located in the Galactic thin disc, with distances from the Galactic centre in the range 4–22 kpc and a height scale on the disc of about 200 pc. Their chemical properties trace those of the environment in which they formed, the disc, and in general with metallicity in the range $-0.5 < [\text{Fe}/\text{H}] < +0.5$ dex. Through photometry and spectroscopy it is possible to study relatively easily the properties of the open clusters and estimate their age, distance, and chemical abundances. For these reasons they are considered primary tracers of the chemical properties and chemical evolution of the Milky Way disc.

The main subject of this thesis is the comprehensive study of several open clusters. The research embraces two different projects: the Bologna Open Cluster Chemical Evolution project (BOCCE) and the Gaia-ESO Survey. The first is a long-term program, aiming at studying the chemical evolution of the Milky Way disc by means of a homogeneous sample of open clusters. The latter is a large public spectroscopic survey, conducted with the high-resolution spectrograph FLAMES@VLT and targeting about 10^5 stars in different part of the Galaxy and $\sim 10^4$ stars in about 100 open clusters. The common ground between the two projects is, indeed, the study of the properties of the open clusters, to be used as tracers of the disc's characteristics.

The method of BOCCE consists in using both accurate photometry, to derive age, distance, reddening and approximate metallicity, and high-resolution spectroscopy for accurate chemical characterisation. The key aspect of the programme is homogeneity. For this reason all the analyses of the clusters are carried out using the same methodology to avoid spurious systematics in the parameters' estimates. To our knowledge, this project is one of the very few that combine homogeneous analysis in both the photometric and spectroscopic domain for the study of open clusters. The sample of clusters with complete photometric analysis is now composed by 34 objects. Eight of them (Berkeley 27, Berkeley 34, Berkeley 36, Berkeley 81, NGC 1817, NGC 2141, NGC 2849, and NGC 6134) are part of my thesis research and the main subjects of three different publications (Donati et al. 2012; Ahumada et al. 2013; Donati et al. 2014a). The other two clusters I worked on (NGC 2158 and Trumpler 5) are still under analysis and will be part of a different publication, in preparation. They are all old objects (from about 1 to 7 Gyr), mainly located in the third quadrant ($180^\circ < l < 270^\circ$) of the Galactic disc. Only Be 81 and NGC 6134 are located toward the Galactic centre. The clusters with high-resolution spectroscopic analysis are only 11 objects out of the 34. Though still far from the final goal of collecting about 50 clusters fully char-

acterised, it is possible to draw a first picture of the BOCCE database and contextualise it within the Galactic chemical evolution models. We presently cannot discriminate between the two main suggestions about the true shape of the radial metallicity distribution of the Galactic disc. We do find indications that open clusters could match either a step-like distribution with the inner disc (within 9 kpc) more metal rich ($\langle[\text{Fe}/\text{H}]\rangle = +0.1$ dex) than the outer one ($\langle[\text{Fe}/\text{H}]\rangle = -0.3$ dex) or a steep negative gradient within 12 kpc (slope of about -0.11 dex kpc $^{-1}$) and an outer plateau. The comparison with a Galactic chemical evolution model seems to favour the interpretation of the negative gradient but the agreement with data is still far from optimal. The BOCCE database needs to reach a larger number of objects as well as to extend the spectroscopic analysis to all of them in order to have a more accurate statistic. On the other hand, other factors, such as the cluster's dynamics within the disc and the radial migration, deserve further investigations both at the observational and theoretical level because they can have a significant impact on the predictions of the Galactic chemical evolution.

Within the Gaia-ESO Survey I collaborated to the preparation of the observations and to the spectroscopic analysis of both intermediate and high-resolution spectra. In particular, I worked on the implementation of two different codes used for the analyses: DOOp and FAMA. They are fully described in two different papers which I co-authored (Cantat-Gaudin et al. 2013 and Magrini et al. 2013a). Using the data of the first eighteen months of observations I worked on the kinematical and chemical information that was obtained for one of the targeted open clusters, Trumpler 20. The combination of photometric information (reanalysed from literature) and the one from the Survey led to an unprecedented and accurate analysis of the cluster's parameters. These results are part of one of the first publications of the Survey, Donati et al. (2014b). Two more old open clusters, NGC 4815 and NGC 6705, have been studied in a similar way; one paper is already submitted, one is in preparation. From accurate chemical abundances (Magrini et al., 2013b) it was possible to assess the chemical pattern of each object and compare it with field stars and chemical models. Even though these three clusters are located at similar Galactocentric distances, the spectroscopic analysis suggests that they formed in different environments.

The impressive scientific outcome of the Gaia-ESO Survey and the unique framework of homogeneity of the BOCCE project can propose, especially once combined together, a much more accurate description of the properties of the open clusters. In turn, this will give fundamental constraints for the interpretation of the properties of the Galactic disc. Further improvements will be obtained with the Gaia mission. The precise and accurate determinations of distances and proper motions will greatly improve our understanding of the Milky Way.

Contents

List of Acronyms	i
1 Open Clusters as tracers of the Galactic disc	1
1.1 Open Clusters	1
1.1.1 Definition	2
1.1.2 Properties of OCs	4
1.2 Chemical Evolution of the Galactic disc	13
1.2.1 Abundance gradient in the disc	14
1.2.2 Other metallicity tracers	17
1.2.3 Theoretical models	19
1.3 Where do we stand	21
2 Bologna Open Cluster Chemical Evolution Project	23
2.1 Photometry	25
2.2 Spectroscopy	29
3 The Gaia-ESO Survey	33
3.1 Scientific Rationale	33
3.1.1 Gaia in a nutshell	33
3.1.2 Spectroscopic survey	34
3.2 Technical aspects	36
3.3 Observational strategy	37
3.4 Survey consortium & organisation	39
3.4.1 WG4: Cluster’s targets selection	41
3.4.2 WG10 & WG11: spectral analysis	42
3.5 Other Surveys	43
4 Photometric study	47
4.1 Photometric analysis - DAOPHOT	47
4.2 The synthetic CMD technique	48
4.3 The artificial star experiment	51
5 Five Open Clusters on a small FoV	55
5.1 Be 27, Be 34, Be 36	55
5.1.1 The Data	55
5.1.2 Clusters’ centre	61
5.1.3 Clusters parameters using synthetic colour-magnitude diagrams	63
5.2 NGC 2849, NGC 6134	77
5.2.1 Observations and data reduction	77

5.2.2	Colour-Magnitude Diagrams	79
5.2.3	Clusters Parameters	82
6	The advantage of wide-fields for Open Clusters	89
6.1	Berkeley 81, NGC 1817, NGC 2141	89
6.1.1	The Data	91
6.1.2	Centre of gravity and density profile	99
6.1.3	Differential reddening	102
6.1.4	Synthetic CMD	106
6.2	Ongoing work	115
6.2.1	NGC 2158	115
6.2.2	Trumpler 5	117
7	First Gaia-ESO Survey data	121
7.1	DOOp	122
7.1.1	DAOSPEC: a brief description	122
7.1.2	DOO pipeline	122
7.2	FAMA and the traditional EW analysis	126
7.2.1	FAMA in a nutshell	127
7.3	Trumpler 20, NGC 4815, M 11	130
7.3.1	Tr 20	130
7.3.2	Observational data	130
7.3.3	Photometric analysis	132
7.3.4	Spectroscopic analysis	138
7.3.5	Cluster parameters	144
7.3.6	NGC 4815 and M 11	148
7.3.7	Chemical patterns	150
8	BOCCE update	151
8.1	The general properties of the BOCCE OCs	151
8.2	BOCCE OCs as tracers of the disc properties	159
8.2.1	Do we really see a radial metallicity gradient in the Galactic disc? . .	163
8.2.2	Galactic chemical evolution model	165
9	Summary and Conclusions	171
	Bibliography	175

List of Acronyms

- BBC** Stellar evolutionary models of Bressan et al. (1993); Fagotto et al. (1994)
- BOCCE** Bologna Open Cluster Chemical Evolution Project
- BRGB** Base of the Red Giant Branch
- CCD** Charge-Coupled Device
- CDS** The Strasbourg Astronomical Data Center, see <http://cds.u-strasbg.fr/>
- CFHT** Canadian–France–Hawaii telescope
- CMD** Colour-Magnitude Diagram
- DAML02** Catalogue of open clusters (Dias et al., 2002)
- DOOp** DAOSPEC Option Optimiser pipeline
- DR** Differential Reddening
- ESO** European Southern Observatory
- EW** Equivalent Width
- FAMA** Fast Automatic Moog Analysis
- FIES** Fibre-fed Echelle Spectrograph
- FoV** Field of View
- FRA** Stellar evolutionary models of Dominguez et al. (1999)
- FST** Stellar evolutionary models of Ventura et al. (1998)
- FWHM** Full Width Half Maximum
- GC** Globular Cluster
- GCE** Galactic Chemical Evolution
- GSC** Guide Star Catalogue (Lasker et al., 2008)
- HRS** High-Resolution Spectroscopy
- ISM** Interstellar Medium
- IMF** Initial Mass Function
- IR** Infrared
- LBC** Large Binocular Camera
- LBT** Large Binocular Telescope
- LF** Luminosity Function
- LTE** Local Thermodynamic Equilibrium
- MAI** Morphological Age Index
- MAR** Morphological Age Ratio
- MS** Main Sequence

MSTO Main Sequence Turn-Off
MSTP Main Sequence Termination Point
MW Milky Way
MWSC Milky Way Star Cluster catalogue (Kharchenko et al., 2013)
NOT North Optical Telescope
NTT New Technology Telescope
OC Open Cluster
OIG Optical Imager Galileo
PI Principal Investigator
PMS Pre-Main Sequence
RC Red Clump
RGB Red Giant Branch
r.m.s. root mean square
RH Red Hook
RV Radial Velocity
sCMD Synthetic Colour-Magnitude Diagram
SF Star Formation
SFR Star Formation Rate
SGB Sub Giant Branch
SNR Signal to Noise Ratio
SSC Super Star Cluster
SSP Simple Stellar Population
TNG Telescopio Nazionale Galileo
TO Turn-Off
UVES Ultraviolet and Visual Echelle Spectrograph
VLT Very Large Telescope
WEBDA Web version of the Base Données Amas (BDA) database, see <http://webda.physics.muni.cz>
WFI Wide Field Imager
WOCS WIYN Open Clusters Survey (von Hippel & Sarajedini, 1998)

Chapter 1

Open Clusters as tracers of the Galactic disc

Star clusters are often thought as the main, if not unique, environment in which stars form, implying that all the stars in a galaxy have originated in clusters or associations. In this context, star clusters are fundamental to describe all the properties of their parent galaxy. Actually, the idea that most, if not all, stars form in star clusters (see Baumgardt & Kroupa, 2007) is no longer an exhaustive explanation of what results from observations. A comparison of the observed number of clusters embedded in their original gas with older, gas-free open clusters (OCs) suggests that 90 per cent of clusters must either start in an unbound state or become unbound during the gas removal phase (Carpenter 2000; Lada & Lada 2003). The heating and subsequent expulsion of gas by ionising radiation, winds or supernovae in clusters containing high mass stars, but with relatively low star forming efficiency is likely to unbind a significant fraction of their stars and possibly disrupt the whole cluster (Hills 1980; Bastian 2011). Alternatively, it is possible that the importance of clustered star formation has been overestimated and that stars are formed hierarchically in environments with a wide range of initial densities: bound clusters formed from the densest regions whilst associations formed at low densities (Bastian, 2011).

Nevertheless, star clusters represent valuable information on the properties of galaxies. For example, they are very important test beds to study the galactic disc velocity. They are fundamental to understand star formation processes, they are laboratories for stellar evolution, and they can be used to study the chemical properties of the galaxies and their evolution with time, as they inherited the chemical properties of their forming situ.

In this chapter I focus on the importance of the OCs as tools to study the properties of the Milky Way (hereafter MW) disc, starting from the description of their properties and then comparing them with other Galactic constituents generally used to study the properties of the MW (individual stars such as red giants or Cepheids, H II regions, and planetary nebulae).

1.1 Open Clusters

OCs have long been recognised as important tools in the study of the Galactic disc (see e.g. Friel 1995 for a review of the old OCs and Lada & Lada 2003 for young clusters). They are a unique sample of star clusters spanning a wide range of ages and positions, each one with different chemical composition that is a valuable trace of the characteristics of the cloud

where they formed. Young clusters and associations are studied for many purposes, such as determining the spiral arm structure of the MW, investigating the mechanisms of star formation and its recent history, and constraining the initial luminosity and mass functions in aggregates of stars. The old OCs, though a minority component, are excellent probes of early disc evolution. They can be dated relatively easily and can be seen at large distances; their brightest stellar components of giants can be well exploited for precise measurements of radial velocity (hereafter RV) and composition.

1.1.1 Definition

A clear-cut definition of OCs still does not exist. The distinction between different type of star clusters is not yet based on quantitative arguments but rather on a general qualitative description. In our Galaxy star clusters are groups of stars, associations of stars, OCs, and globular clusters (GCs). In external galaxies very massive star clusters, called super star clusters (SSCs), are also found. In the MW only Westerlund 1, a young massive cluster, can be considered an SSC (see Portegies Zwart et al., 2010). The order of this list reflects the increasing number of stars, with GCs the most massive and concentrated star clusters (if we exclude SSCs). For example, OCs are “*commonly thought of as sparsely populated, loosely concentrated, barely gravitationally bound systems of a few tens or hundreds of stars*” (Friel, 1995). This intuitive concept matches with the average appearance of OCs but we face also extreme cases (e.g., very poorly populated or very highly concentrated OCs, like in Fig. 1.1).

In their review on embedded clusters, Lada & Lada (2003) proposed a definition of an OC. Stars in a cluster are physically related when they have a sufficiently large stellar mass volume density, if in a state of virial equilibrium, to render the group stable against tidal disruption by the galaxy (i.e., $\rho_* \geq 0.1M_\odot\text{pc}^{-3}$) and by passing interstellar clouds (i.e., $\rho_* \geq 1.0M_\odot\text{pc}^{-3}$). Adopting the criterion of Adams & Myers (2001)¹, they suggested a minimum number of 35 stars. Therefore a star cluster is a group of 35 or more physically related stars whose stellar mass density exceeds $1.0M_\odot\text{pc}^{-3}$. This definition helps discriminating an OC from star associations and star groups.

Considering the opposite limit, how can we distinguish an OC from a GC? Carretta et al. (2010), by studying the chemical abundances of a sample of 19 GCs and adding literature data, proposed to identify GCs with those clusters where there is a Na-O anticorrelation. This is because the presence of (anticorrelated) large spreads in light elements abundances implies that there are at least two stellar populations, i.e. that the cluster was massive enough to keep gas polluted from the first generation and form a second generation. This operative definition tries to separate clusters on the basis of quite well defined physical properties. In Fig. 1.2 (their figure 3) the absolute luminosity M_V and age of many OCs and GCs are shown, together with lines of constant mass. Carretta et al. (2010) identified the region in which the GC sample is separated from the OC sample, implicitly giving a definition of GC based on cluster mass. Accordingly, they suggested that OCs should be not more massive than about $4 \times 10^4 M_\odot$ and should not show any Na-O anticorrelation. However, the situation is not completely clear. The case of NGC 6791 is emblematic. Geisler et al. (2012) found that it shows a Na-O anticorrelation, so it should be considered a GC notwithstanding its small mass (similar, by the way, to that of Be 39, where Bragaglia et al. 2012 did not find any indication of Na-O anticorrelation). Whether this evidence is real or

¹This criterion makes the hypothesis that the cluster consists of enough members to insure that its evaporation time (i.e., the time it takes for internal stellar encounters to eject all its members) be greater than 10^8 years (the typical lifetime of OCs in the field, see Sec. 1.1.2).



(a) Antares' association.

(b) OC M67.



(c) GC M92.

Figure 1.1: Different types of star clusters are shown: (a) a star association, (b) the OC M67, (c) the GC M92. M92 is the most massive and concentrated but also the oldest (about 11 Gyr). M67 is less concentrated and as old as ~ 4 Gyr. The star association is formed by OB types stars. The pictures, here used only for descriptive purposes, are available on www.wikipedia.org.

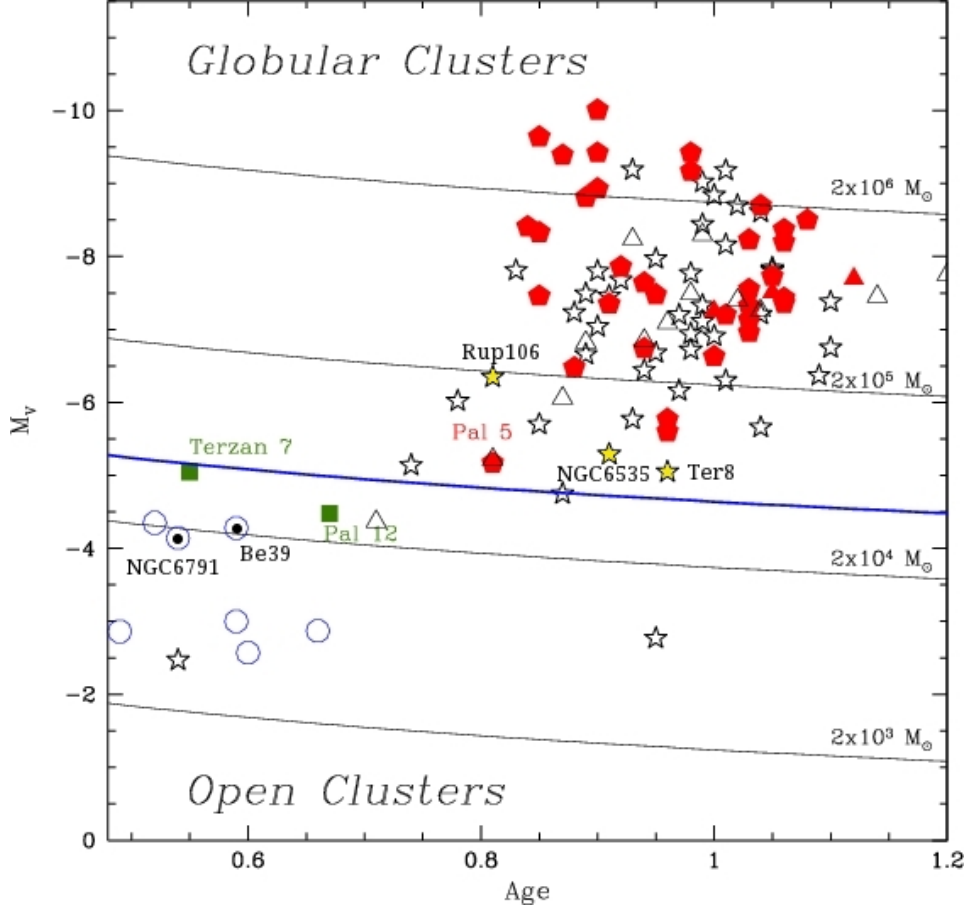


Figure 1.2: Relative age parameter vs. absolute magnitude M_V for GCs and OCs. Red filled pentagons and triangles are GCs where Na-O anticorrelation has been observed, in the MW or the Large Magellanic Cloud, respectively; green squares are clusters that do not show evidence of Na-O anticorrelation. Open stars and triangles mark clusters for which not enough data is available. Finally, open circles are old open clusters. Superimposed are lines of constant mass. The heavy blue solid line (at a mass of $4 \times 10^4 M_\odot$) is the proposed separation between globular and open clusters. Reproduced from Carretta et al. (2010).

not (see Bragaglia et al., submitted Jan. 2014) further analyses are needed to constrain the clusters' classification. Even though such distinctions might not be neat, investigations of peculiar cases should be encouraged especially concentrating on all the known clusters at the mass boundary between OCs and GCs.

1.1.2 Properties of OCs

OCs have been studied by many authors at different levels of detail. For this reason there is a large data collection on them but, unfortunately, it is highly inhomogeneous.

In literature there are several publicly available catalogues/databases collecting in a unique framework all the information on known OCs. The most famous and historically important one is the catalogue of Lynga & Palous (1987), the first list of all the known OCs at that time with estimated properties. Nowadays, the main ones are the WEBDA², which

²WEBDA is the Web version of the Base Données Amas (BDA) database, originally developed by

collects and merge the information from different catalogues and publications, the DAML02 catalogue (see Dias et al., 2002), the catalogue described in Chen et al. (2003) (with the recent update reported in Chen & Hou 2009), and the most recent Milky Way Star Cluster project (MWSC) catalogue (see Kharchenko et al., 2013).

In this chapter I will use the information from DAML02 (version 3.3) to describe the main properties of the OCs. In DAML02 all the basic parameters are stored, as well as other results, that are available in literature (the main reference is the WEBDA), and the values are not homogenised. For easiness of use, all the relevant information is accessible in a single file which is constantly updated. There are 2174 OCs, visible in the optical and/or infrared³ (IR) wavelength ranges. Out of these, 1658 (76.3%) have a determination of distance, age, and reddening, but only 202 (9.3%) have chemical abundances estimates. If we classify the OCs on the basis of the presence, or lack thereof, of their red clump (hereafter RC), the major post-main sequence evolutionary phase whose onset occurs at an age of about 300 Myr, we count 815 OCs younger than this limit and 814 older ($\sim 50\%$ of the OCs with age determination). The old population is especially interesting for the study of the disc history and is the main subject of this work.

Sizes and masses

In DAML02 almost all the objects have an estimate of the diameter (2168 OCs, 99.7%). This is mostly based on visual inspections and only a few systems have been studied in details for their structural properties (see e.g. Seleznev et al. 2010; Cignoni et al. 2011, and Donati et al. 2014a) as this requires accurate photometry on relatively large fields of view (FoVs). The magnitude limit can be a strong bias for the size determination (from simple dynamical evolution assumptions the more massive, brighter stars are more concentrated) while a small FoV can be insufficient to fully cover the extension of the clusters (the advent of photometric surveys such as SDSS and 2MASS is changing the scene) resulting in a less precise determination of the structural parameters. From the DAML02 catalogue it appears that 75% of the OCs have a diameter in the range 0.6–12 arcmin with a median value of 5 arcmin. Exploring the statistics for the young and old OCs it turns out that the 75% of young OCs encompass a larger range of diameters (0.6–20 arcmin) with a median of 7 arcmin, while the old OCs have diameters within 0.6–11 arcmin with a median of 5 arcmin. The data available in DAML02 are not homogeneous and some of these estimates are derived from visual inspection which can accommodate large errors. However, they are useful to describe the general properties of OCs. Kharchenko et al. (2013), using 2MASS photometry and proper motions, derived the core radius and tidal radius of 2961 clusters, almost all the objects in the MWSC catalogue (it contains 3006 clusters of all type), with a homogeneous analysis. They found two distributions for the two King’s model parameters, and for 75% of old OCs they obtained a median core radius of ~ 1.2 pc and a median tidal radius of ~ 8.8 pc, larger values than for young OCs (1.1 pc and 7.6 pc respectively). In terms of angular sizes, a tidal radius of about 8 pc corresponds to a FoV of 5 arcmin only for very distant clusters (distance from the Sun $d_{\odot} > 10$ kpc). This implies that the extension of the nearby clusters is much larger than suggested in DAML02.

Unfortunately the information on masses is not recorded in the databases and, moreover,

J. C. Mermilliod and maintained by Ernst Paunzen, Christian Stütz, and Jan Janik at the Department of Theoretical Physics and Astrophysics of the Masaryk University, Brno (Czech Republic). The website is <http://webda.physics.muni.cz>

³In DAML02 several clusters recently discovered using the 2MASS survey (Skrutskie et al., 2006) have been considered (see Dutra & Bica, 2001). Ninety-two additional clusters have been discovered in the infrared thanks to the VISTA survey (see Borissova et al., 2011) but not yet considered in this catalogue.

it is available only for few objects. According to the OC definition given in Sec. 1.1.1, the OCs' mass should range between about $500M_{\odot}$ and $4 \times 10^4 M_{\odot}$. However, mass cannot be determined easily, the errors are large and different methods can give very different results. Mass estimates rely on star counts and can be very uncertain if data are limited in magnitude or available for relatively small FoV. Dynamical models predict that stars will linger around the very much larger tidal radii for old clusters, so one expects to see cluster members well outside the apparent diameter (most closely associated to a half-mass diameter). Most star counts do not reach to these distances and omit many potential cluster members. Furthermore, OCs host substantial binary populations (see Bragaglia & Tosi, 2006), 30% on average. Star counts need to be corrected for this large and often uncertain factor. Moreover observed luminosity functions cover a limited range in mass and call for significant extrapolation of the mass function to low masses, where potentially most of the cluster mass resides. Lastly, dynamical evolution in old clusters is expected to be very effective at causing mass segregation and the evaporation of low mass stars. Compensations for all these effects worsen the precision on the mass determinations which are likely underestimated. From available data in literature, Friel (1995) suggested that old OCs were stellar systems with initial masses in excess of $10^4 M_{\odot}$.

OC dynamical evolution

Observational work on defining the structural and internal dynamical properties of OCs has not advanced as far as similar studies on GCs. The high precision and accuracy required are not easily achieved for OCs. The contamination of field stars and the effects of the Galaxy's gravitational potential within the disc are dramatically higher than for GCs, generally residing far from the Galactic plane. This means that the dynamical footprint of GCs stars with respect to contaminants is more evident and more precisely determined (both in RV and proper motion) than in OCs.

The available evidence, both observational and theoretical, indicates that OCs that have survived to ages of at least a billion years have undergone significant dynamical evolution. As suggested by Lada & Lada (2003) and following works on clusters formation (e.g. Bastian, 2011), star clusters suffered important dynamical evolution since their birth. In the early works published by King (1962, 1966), it is stressed that OCs follow the surface density profiles expected for isothermal spheres modified by tidal forces and are best fit by models with small ratios of tidal to core radii, or concentration parameter, of 6 to 8. The typical core radii and tidal radii of OCs are of about 1–2 pc and 10–25 pc respectively, as found in Kharchenko et al. (2013).

Segregation and evaporation are two different dynamical mechanisms predicted by models. They set after a time scale defined by the relaxation time⁴. After relaxation, the more massive members sink into lower orbits becoming more concentrated in the inner part of the cluster (segregation), while, on the contrary, low mass members can have speed greater than the escape velocity of the system and “evaporate” from the cluster. Many evidence of segregation has been found for different old OCs by looking at the luminosity function in the inner region (a flat profile is an indication of segregation). Radially flat or decreasing luminosity functions at the low mass regime are a strong suggestion of the evaporation mechanism.

⁴The typical relaxation time in star clusters is $\tau_{relax} \approx \frac{0.1N}{\ln N} \tau_{cross}$, where τ_{cross} is the dynamical crossing time of the system while N is the number of stars it contains (Binney & Tremaine, 2008). The typical crossing time in OCs is of order 10^6 years and the evaporation time for a stellar system in virial equilibrium is $\tau_{ev} \approx 10^2 \tau_{relax}$ (Lada & Lada, 2003).

The dynamical evolution of the OCs is affected by the Galactic tidal field and by the interaction with very massive structures, such as interstellar clouds, through disruptive forces if encounters occur. Such encounters could in principle be able to completely disrupt star clusters in time scales of 10^8 to 10^9 years, strongly depending on the cluster's mass and concentration. It seems that the old OCs we see today were able to survive because of their structural characteristics and orbits that allowed them to limit or avoid encounters with disruptive giant molecular clouds. On the other hand, the ghostly objects survived to dynamical disruption and known as OC remnants, may play a fundamental role in our understanding of the subject of OC evolution and dissolution. OC remnants are what remains of old OCs and can be studied to improve the statistics of old open clusters in the Galactic disc, as well as understanding its formation and early evolution (see Carraro et al., 1999).

Galactic position

It has long been known, since van den Bergh first noticed it in 1958, that young and old OCs have different positions in the Galaxy. The oldest OCs reach the farthest distances from the Galactic centre and the Galactic plane. Whether this characteristic is a consequence of the older dynamical age, which results, for instance, on important variations in the orbits due to interaction with spiral arms (see Roškar et al., 2012), or it is an “evolutionary selection” (in the sense that the farthest orbits let OCs avoid disruptive encounters within the disc) or a combination of both, is still under discussion. It might even be more complex than this. In fact it has been proposed by Yong et al. (2005) that outer disc OCs might originate from past mergers events. By using peculiar chemical signatures as derived from high-resolution spectroscopy (HRS) of giants and RC stars they suggested that the outer OCs (in their sample 5 OCs with Galactocentric distance R_{GC} greater than 12 kpc) have experienced a star formation and nucleosynthetic history unlike any known Galactic population. There seems to be evidence that a significant merger event is currently taking place in the outer disc. The Galactic anti-centre stellar structure, GASS, is possibly the result of tidal accretion of a dwarf satellite galaxy as suggested in Frinchaboy et al. (2004). So it is possible that outer OCs may be associated with one or more merger events. On the other hand, Carraro et al. (2007) did not find any stringent evidence of extra-galactic origin of the outer OCs from chemical abundances arguments. At the same time, they suggested that more precise proper motion studies of these clusters would greatly help to understand their kinematical properties, and would constitute an important step ahead for the knowledge of the outer Galactic disc.

By using the DAML02 catalogue, it appears that old OCs span the largest range in Galactocentric distances, reaching $R_{GC} \simeq 22$ kpc (Berkeley 29) as shown in Fig. 1.3a. The younger population is more concentrated. The general appearance of the OCs distribution on the MW disc is highly biased by the incompleteness of the available OCs samples. There is a lack of objects in the inner region of the Galaxy, in particular of old ones. This is partly due to the high extinction in the optical that is present toward this region of the MW that conceals old star clusters. Young clusters are more luminous and blue with respect to the average population of the thin disc and bulge of the MW, and can be spotted relatively more easily with respect to the older ones. However, there could also be a physical selection effect since cluster survival for long times is more difficult in the denser and hostile central regions. Further studies, especially in the IR, like those with the VISTA surveys (see Borissova et al., 2011) will help.

Old OCs have a larger dispersion in the the height above the Galactic plane (z) than

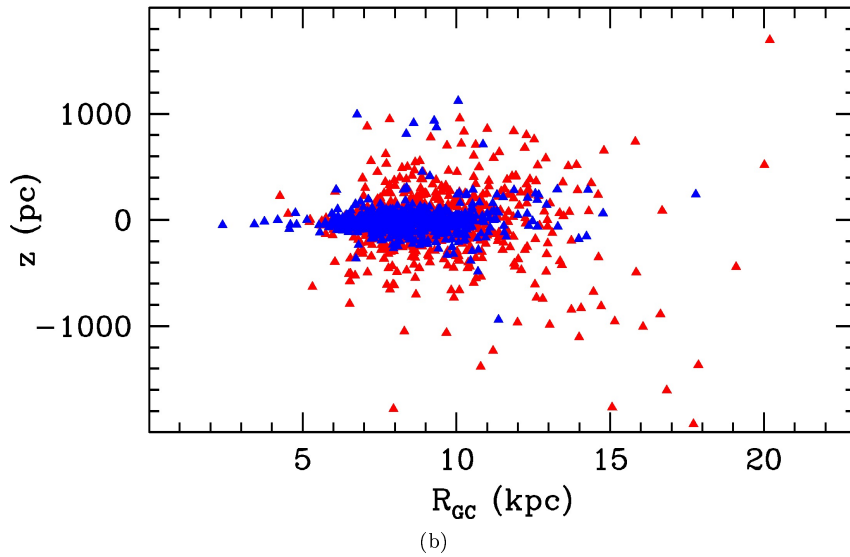
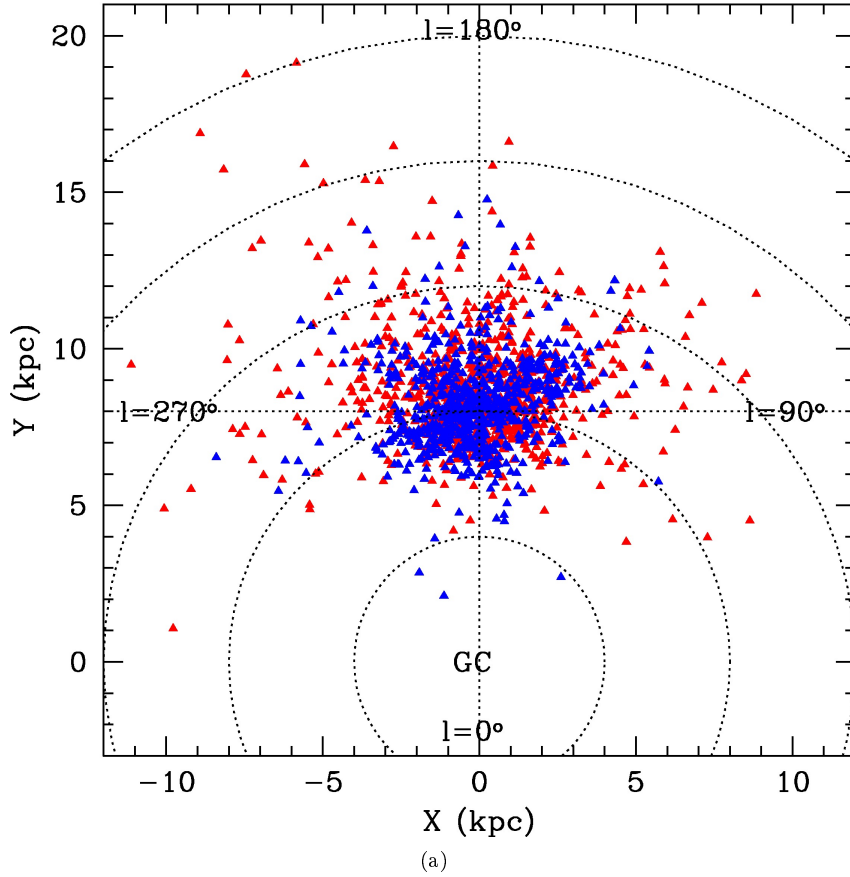


Figure 1.3: (a) Distribution of OCs projected onto the Galactic plane. Red points are old OCs while blue points are the young ones. It is clearly visible that old OCs reach the farthest distances from the Galactic centre (GC in figure), while the young ones are more concentrated. (b) Distribution of OCs on the plane R_{GC}, z (height above the Galactic plane). Red points are old OCs (age > 300 Myr) while blue points are the young ones (age < 300 Myr). The old OCs have a more dispersed distribution, though there are some young OCs reaching large heights above the plane. The data are taken from DAML02 v3.3.

young OCs (dispersion of ~ 300 pc and 130 pc, respectively, with respect to the Galactic plane, see Fig. 1.3b). Old OCs have a much more evolved dynamical history and could have suffered dramatic variations of their orbits during their lifetime. On the other hand, lying at higher Z enhanced their survivability, shielding them from the disruptive effects of encounters with interstellar clouds. Young OCs, instead, have a smaller scale-height. As they have a shorter dynamical history they trace their birth place. In fact, it is known that star forming regions in galaxies appear to occur by gravitational instability in galactic disc (Elmegreen, 2011). In particular, the gas is generally compressed more than the stars in a spiral density wave. Within spiral arms both gravitational instabilities and cloud collisions trigger molecular cloud formation and conglomeration more efficiently than in inter-arm regions. The star formation rate per unit area is high in the arms as a result (Elmegreen, 2011). As discussed for example in Lada & Lada (2003), Elmegreen (2011), and Bastian (2011) the young clusters trace the interstellar clouds in which they form and this is evidently explained in figure 3.6 of Bastian (2011) (taken from Gutermuth et al. 2008), here re-proposed in Fig. 1.4. For this reason young OCs are interesting to understand the spiral structure of the MW. Fig. 1.5 is taken from Dias & Lépine (2005); they consider OCs of different ages in the solar neighbourhood. From left to right one can readily appreciate how very young OCs trace a seemingly regular spiral structure, while at increasing clusters' age, the spatial distribution gets more scattered so that no structure can be detected anymore, since these clusters had time to move away from their birth place. Carraro (2013) and

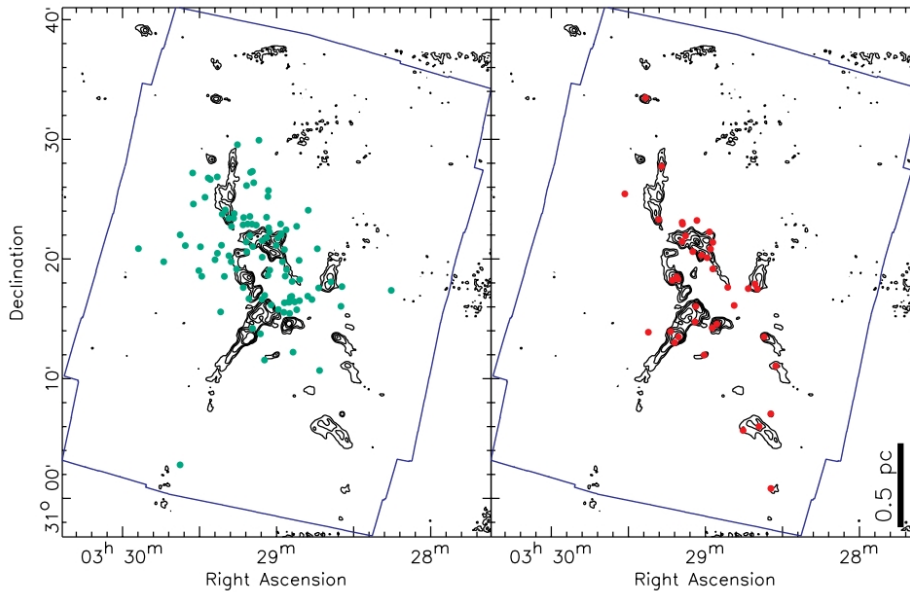


Figure 1.4: The spatial distribution of young stellar objects in the young embedded star-forming region NGC 1333. The contours show dense gas and the points represent young objects (red points, right panel) and older ones (green points, left panel). The spatial distribution of points in the right panel matches the gas distribution quite well, showing a very filamentary structure. In the left panel the points also generally follow the gas, however, due to their older age they have dynamically evolved to some degree. This shows that stellar clusters do not form as a centrally concentrated system with the gas/star in equilibrium, but rather as a filamentary/hierarchical structure where individual components may (or may not) merge from the final stellar system. Reproduced from Bastian (2011).

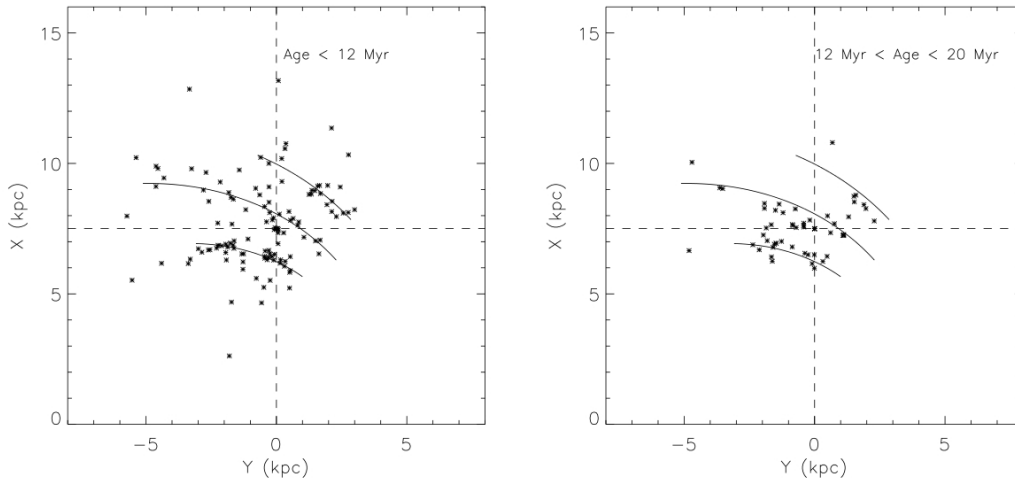


Figure 1.5: Spatial distribution of OCs in the solar neighbourhood as a function of their age. The Sun is at coordinates (0, 7.5); the Galactic center is at (0,0). Distances are in kpc. The usual Y-and X-axis centred on the Sun are shown as dashed lines. Reproduced from Dias & Lépine (2005).

Carraro et al. (2013) summarised the present day knowledge of the spiral structure of the Galactic thin disc and the outer disc as revealed by stars and young OCs. They concluded that the main disagreements among various tracers are still to be settled in order to obtain a better knowledge of the MW spiral structure.

Kinematics

In the DAML02 catalogue 1190 (54.7%) OCs have proper motions, and 543 (25.0%) have radial velocities (RVs). The more recent MWSC contains proper motion determination for 3006 star clusters (the majority, 2808 objects, are OCs but associations and GCs are included too) and RVs for about 700 clusters. Most proper motions in MWSC lie within $\pm 10 \text{ mas yr}^{-1}$ (Kharchenko et al. 2013 quoted an error of $\sim 2 \text{ mas yr}^{-1}$) and the RVs within $\pm 100 \text{ km s}^{-1}$ (error of $\pm 1.0 \text{ km s}^{-1}$). This large sample can be used to look at the details of the velocity distributions and investigate correlations with other cluster properties.

Such information is necessary to determine the space motions of clusters. For instance, past studies of the kinematics of old OCs (e.g. Carraro & Chiosi, 1994a) indicated that they follow orbits that keep them far from the plane and in the outer disc (see Friel 1995 for a summary on these studies). In a few cases the observed velocities indicate significantly non circular orbits. In a recent study, Wu et al. (2009), using as main reference catalogue the DAML02, calculated the orbit of 488 OCs (most of them younger than 500 Myr) and discussed their kinematical properties. The velocity dispersions of OCs in the three velocity components increase with the age of the cluster sample and they have a mean eccentricity of about 0.1 (similar to thin-disc giants, F and G dwarfs but smaller than that of GCs and thick-disc giants).

Studying the systemic properties of old OCs gives insight on the processes that create or destroy clusters and on those that enable the clusters to survive to old ages. In particular, by using the OCs that lie out of the plane it should be possible to distinguish between the alternative pictures of cluster formation: either the clusters are formed in special events with orbits that allow them to survive, or we are simply seeing the tail of a distribution from

which the lower velocity (lower scale height) members have been destroyed (see Friel 1995 for a general discussion and Bastian 2011 for investigations on cluster disruption mechanisms).

Kinematical data of OCs are also particularly important to study the dynamical properties of our Galaxy and to investigate their effect on the time evolution of the abundance gradient in the Galactic disc. Dias & Lépine (2005), for example, used the kinematics information of 212 OCs (from DAML02) to trace back their orbits and locate their birthplace. Their aim was to trace the motion of the spiral arms comparing the position of the young OCs (which trace present-day spirals) and old OCs birthplace (which they suggest trace earlier positions of the spiral arms). Their results strongly favour the idea that the spiral pattern rotates like a rigid body.

Wu et al. (2009) used kinematical information to compare the metallicity gradient of the MW for OCs within $R_{GC} < 13.5$ kpc using their current position and their apogalactic position. They showed that apogalacticon is the place where a cluster spends the largest fraction of its life and find that the observed current metallicity gradient is similar to that derived from the most probable observed positions of the clusters.

Accurate kinematical information for the whole population of OCs will be available thanks to Gaia (see Ch. 3 for a description of the mission). Coupled with orbit computations, it will be possible to study with unprecedented precision the motion of about a billion of stars and thousands of OCs, finally obtaining a more definite delineation of dynamics in the disc and its impact on the present-day and past disc properties.

Age determination

OCs can be easily dated and for this reason provide an important advantage in studies of the evolution of the Galaxy. OCs, in fact, can be thought as simple stellar populations (SSP) and their evolutionary status can be derived by analysing the morphology of their observational colour-magnitude diagrams (hereafter CMDs). The SSP paradigm is supported by the fact that cluster's stars formed in a relatively short time. Lada & Lada (2003) described the age spread found in very young clusters. It could reach about 10 Myr in some cases but it is usually lower than 3 Myr. Even though these measurements are affected by limited accuracy, there is no evidence of molecular emission from around clusters with ages in excess of 5 Myr, suggesting that the lifetimes of molecular clouds typically do not exceed 5-10 Myr. Moreover, there are no known OCs that show peculiar star formation history (prolonged or with multiple bursts). In spite of the intrinsic uncertainties, OCs provide a fairly accurate, at least in a relative sense, age relationship with which to study changes in the structure and chemistry of the MW.

The main methods used to provide cluster ages for old OCs are the isochrone fitting and the morphological age index, MAI (or $\delta(V)$ parameter, that is the magnitude difference between the main sequence turn-off and the RC), defined by Janes & Phelps (1994) as a variant of the morphological age ratio, or MAR, developed by Anthony-Twarog & Twarog (1985).

The MAI, and so the age, is related to the change in CMD turn-off (TO) and evolved star luminosity and colour. It is well suited for the old OCs, typically characterised by the presence of stars in the later stages of stellar evolution, both along the red giant branch (RGB) and in the RC, i.e. the population of stars in the He-core burning phase of stellar evolution, analogous to the red Horizontal Branch of older/lower-mass stars. For these old populations the absolute magnitude and colour of the RC stars are roughly constant (for stars more massive than $1.4M_{\odot}$, hence for OCs older than about 4 Gyr, see Salaris & Cassisi 2005), while the luminosity of the TO becomes fainter and the colour redder, as the

cluster ages. The age calibration is based on representative ages from isochrone fitting for well studied OCs and GCs, resulting in an approximately linear relation between MAI and cluster age (see, for instance, Salaris et al. 2004 for a new and homogeneous calibration of the $\delta(V)$ -age-[Fe/H] relationship from a sub sample of 10 clusters with accurate and deep photometry). The MAI is a robust relative age indicator while caution should be used to estimate true cluster age. For instance, it produces an age > 10 Gyr for Be 17 (Friel, 1995) while the age of the cluster is about 8 Gyr when using the evolutionary models (Bragaglia et al., 2006a).

The isochrone fitting method relies in finding the best match of the predicted evolutionary sequences of stellar evolution models overlying them to the observational CMDs. It is the main method adopted for old OCs, allowing stringent constraints on the clusters' age. However, even more precise ages can be obtained by using the synthetic CMD technique. This technique is an evolution of the isochrone fitting method and models with more accuracy the transformations from the theoretical to the observational plane of the stellar evolutionary models, taking into account the observational errors and the completeness level of the data (see details in Sec. 4.2).

Young OCs are dated using several different techniques as explained, for instance, in Soderblom et al. (2013), the most accurate one being the Lithium Depletion Boundary technique, performing in the age range 20-200 Myr.

To study the OC system of the MW it would be ideal to have ages consistently determined using a uniform set of theoretical evolutionary models for all the OCs. Unfortunately, such precise, homogeneous, and detailed age determinations do not exist for most OCs. Often the photometric data do not reach faint enough magnitudes and/or the cluster sequences are complicated by important field contamination hindering a proper age determination. Furthermore, different methodologies and the wide variety of theoretical models used in literature make it difficult to reach a consistent age ranking by simply collecting cluster ages as quoted in literature (as done, for instance, in the WEBDA and DAML02 catalogues). Several groups have attempted to build homogeneous age determinations, but they are still limited by small sample sizes, the lack of excellent quality photometry, and the lack of accurate OCs auxiliary parameters (such as average Galactic reddening and metallicity). The largest catalogue implementing homogeneous ages determinations is the one described in Kharchenko et al. (2013). They use the recent Padova stellar models and the isochrone fitting method for all the clusters (pre-main sequence isochrones are based on different models). However they used solar metallicity isochrones ($Z = 0.019$) to determine OCs parameters. They did not fine tune Z because they claimed that at the high metallicity regime typical of OCs (of the order of the solar value) it has a mild influence on ages determinations, especially using IR data, as in their case⁵. The internal error on the age estimates is of 10% for old OCs but the external one (based on comparison with literature results of clusters in common) is of the order of 40%. They suggest that this discrepancy may be due to the differences among the adopted theoretical models or to poor membership determinations that might lead to ambiguous interpretations. Looking at the age distribution of the catalogue the median value is 0.4 Gyr, and 75% of the OCs is within 1 Gyr. The old OCs have a median age of 0.9 Gyr, and 75% of them is within 1.5 Gyr.

The age distribution recovered by the DAML02 catalogue is not so different. The whole sample of OCs has a median value of 0.3 Gyr, and 75% of it is within 0.8 Gyr. Restricting to the old OCs (age > 300 Myr), the median value is 0.8 Gyr and 75% of them is younger than 1.4 Gyr. In Fig. 1.6 the age distribution based on DAML02 is shown (in red the distribution

⁵Oddly, they do not seem to find OCs older than 6.5 Gyr. This, coupled with the assumption on metallicity and the non ideal photometric set, indicates that more work is required.

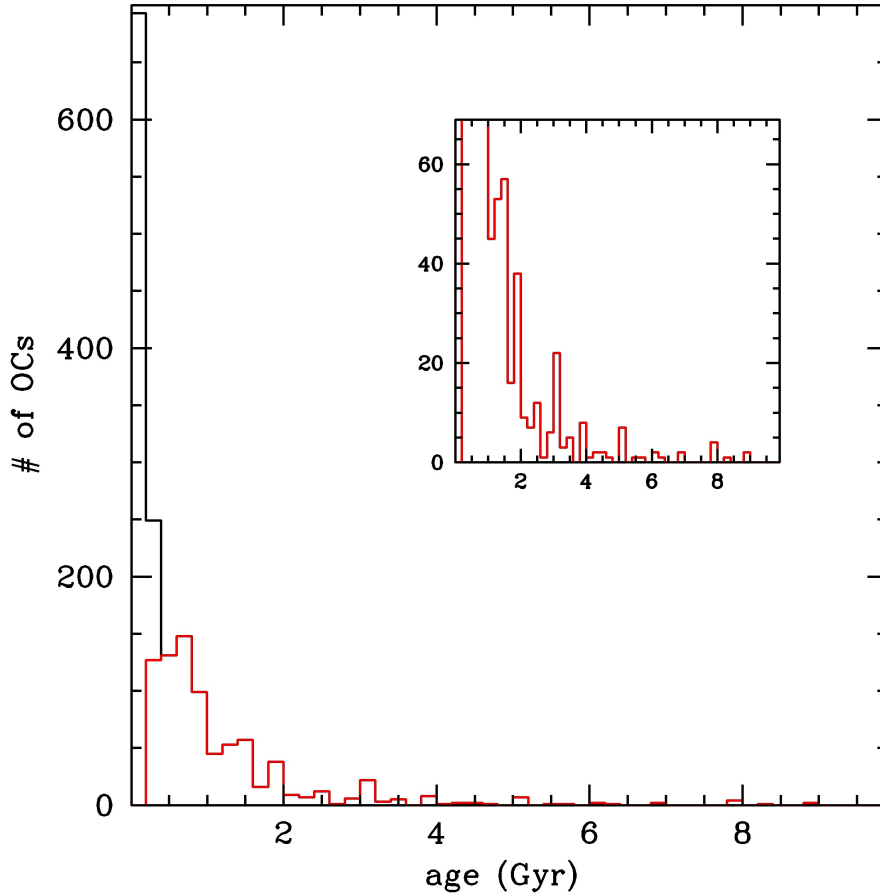


Figure 1.6: Age distribution of the OCs listed in the DAML02 catalogue. The black histogram is obtained considering all the OCs, while the red one is for the old counterpart only. The inset panel is a zoom to highlight the distribution of the old OCs.

of the old OCs). The remaining 25% of the long-lived tail of OCs, older than 1.4 Gyr, is formed by 211 objects (13% of the DAML02 catalogue). However, those with very large ages, above 4 Gyr, are only 27 (about 2%).

1.2 Chemical Evolution of the Galactic disc

OCs have long been used to trace the chemical structure and evolution of the disc. They form an excellent time line along which to study the progress of overall enrichment in the disc (Friel, 1995). Moreover, they span different positions and cover the typical metallicity range of the thin disc. For these reasons, OCs are potentially very useful to describe the disc properties. Their distance estimates have a precision of about 10% (e.g. Kharchenko et al., 2013) or better. In Fig. 1.7 the metallicity distribution of OCs in the DAML02 catalogue is shown. The $[\text{Fe}/\text{H}]$ values span the range $-1.0 < [\text{Fe}/\text{H}] < 0.5$ dex. 75% of the objects considered are in the metallicity range $-0.4 < [\text{Fe}/\text{H}] < 0.08$ dex. OCs do not show notable correlation with age and metallicity (see Fig. 1.7) but rather a large dispersion (r.m.s. ~ 0.3 – 0.4 dex) at nearly all ages. This evidence is confirmed by several studies

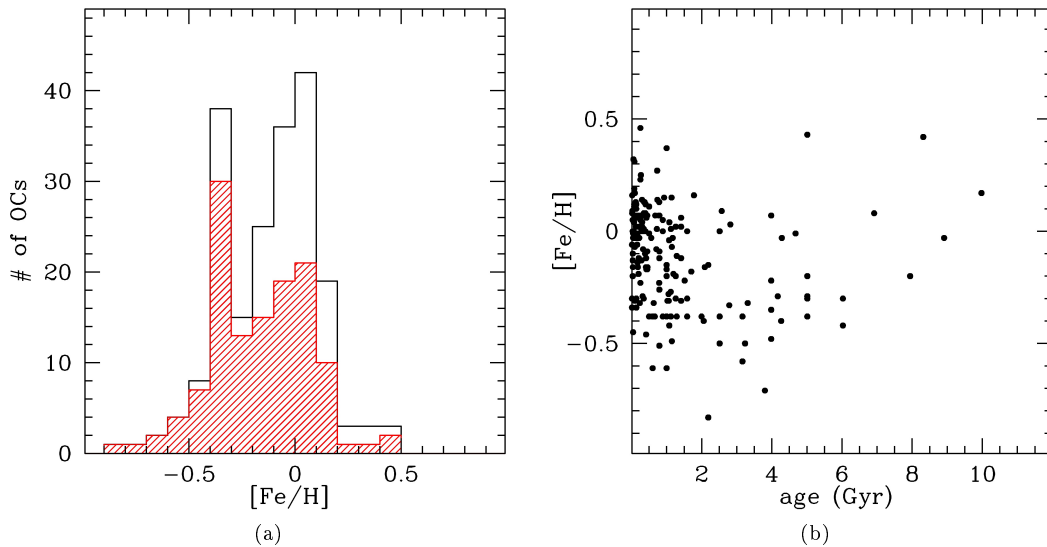


Figure 1.7: Metallicity distribution of the OCs listed in the DAML02 catalogue. (a) The black histogram is obtained considering all the OCs, while the red one is for the old counterpart only. (b) Metallicity versus age. There is a large metallicity dispersion for each age bin and no significant age-metallicity relation.

(see e.g. Friel et al., 2002; Bragaglia & Tosi, 2006; Carraro et al., 2007; Magrini et al., 2009; Pancino et al., 2010; Jacobson et al., 2011b). Clusters’ metallicities have been derived with a wide variety of methods. Photometric abundance indicators, such as those based on *UBV*, *DDO*, *Washington*, and *Strömgren* photometric systems, provide about half of the metallicity estimates cited in DAML02 (99 objects). Spectroscopic estimates are available for the remaining half (105 objects) but only a small sample of 48 OCs have abundances determined from HRS⁶. Most of these methods yield overall metallicities that are formally accurate to 0.1 to 0.15 dex in [Fe/H] (but do heavily depend on the accuracy of the calibrators used), while HRS is virtually more accurate. The advent of excellent astronomical facilities (large telescopes and multi-object spectrographs, for instance) and the joined efforts for large international astronomical surveys are going to change this picture (see discussions in next chapters), making metallicities based on HRS much more numerous.

In the next paragraphs I will consider some of the many studies that over the years have used the OC population to trace abundance gradients and to investigate the relation between the age and metallicity. OCs are not the only tracers of the disc properties and various studies concentrate on Cepheids, planetary nebulae (PNe), and H II regions. I will briefly present the main results obtained from these objects.

1.2.1 Abundance gradient in the disc

The sample of OCs has increased with time, permitting a better coverage of the parameter space of distance-age-metallicity needed to understand the disc properties and their evolution with time. Nevertheless, the first analyses of Janes (1979), Panagia & Tosi (1981), Lynga

⁶It is worth to note that only a fraction of the available HRS-based metallicities are considered in DAML02. As discussed, e.g., in Heiter et al. (2014), in literature there are HRS analyses for about 80 OCs.

& Palous (1987), and Janes et al. (1988) on small samples (tens of OCs) already pointed out that there is a significant decrease of overall metallicity with increasing Galactocentric radius. This was confirmed by all the following works until the early 2000's. The common features of the observational studies are the negative radial gradient of [Fe/H] abundance, the absence of an age-metallicity relation in OCs, and the absence of abundance patterns with disc height (see e.g. Carraro & Chiosi 1994b; Friel 1995). Friel et al. (1995) and Carraro et al. (1998) found a gradient of about $-0.09 \text{ dex kpc}^{-1}$ in the distance range $7 < R_{GC} < 17$ kpc and no variation of it with age or position, at odds with Cameron (1985) and Panagia & Tosi (1981) who suggested a time variation of the gradient. Twarog et al. (1997) described a sharp discontinuity between the inner part of the disc ($6 < R_{GC} < 10$ kpc) and the outer part. No significant trend was visible in their data but rather a step distribution, with the inner disc of about solar metallicity and the outer disc metal poorer (about 0.3 dex of difference). Friel et al. (2002) confirmed an abundance gradient of $-0.06 \pm 0.01 \text{ dex kpc}^{-1}$ over a range in Galactocentric radius of 7 to 16 kpc and suggested the evidence of a steepening of the gradient with increasing cluster age. Salaris et al. (2004) found an overall slope relationship between [Fe/H] and R_{GC} consistent with Friel et al. (2002), but a decrease of this slope with cluster age.

It is from the beginning of 2000 –when the appearance of new improved instruments for observations (such as, for instance, HIRES at the Keck telescope or UVES at the Very Large Telescope, VLT) made it feasible to study an increasing number of clusters, even the distant ones, with HRS– that almost all the studies seem to converge toward a common point of view on the radial metallicity gradient derived by OCs: the inner disc shows an overall negative gradient, the outer disc shows a flattening⁷ (see, e.g. Yong et al. 2005, 2012; Carraro et al. 2007; Sestito et al. 2008; Pancino et al. 2010; Jacobson et al. 2011b that used HRS observations in combination with available HRS data in literature). In Fig. 1.8 the radial metallicity distribution of the OCs is shown, together with the interpretation of a single or double gradient, as an example. The steepening of the gradient with increasing age is found in several recent studies (see, e.g., Magrini et al., 2009; Andreuzzi et al., 2011; Jacobson et al., 2011b) but further investigations are needed to confirm whether this variation is significant (Yong et al., 2012). Lépine et al. (2011) confirmed, at variance, a step distribution similarly to the earlier work of Twarog et al. (1997) and a flat distribution in the outer disc ($R_{GC} > 8.5$ kpc).

All these works agree on the conclusion that more accurate and homogeneous data are needed. The sample of OCs with chemical abundance analyses obtained with HRS is still small (< 100). Moreover, the differences in the analyses methods have stronger effect on metallicity than the differences in the quality of the observations (Heiter et al., 2014). In any case, HRS is the only technique to distinguish the subtleties of the chemical evolution within the Galactic disc. The analyses of chemical elements such as α -elements and neutron capture elements has proven to be fundamental to reveal peculiar chemical patterns (e.g. Yong et al. 2012 for OCs, Gratton et al. 2004 for GCs, Mitschang et al. 2013 for field stars, and Freeman & Bland-Hawthorn 2002 for a review on the chemical tagging). The ongoing/planned large spectroscopic surveys, such as the Gaia-ESO Survey (see Ch. 3 for details), APOGEE (e.g. Frinchaboy & SDSS-III Collaboration, 2010), and GALAH (Zucker et al., 2013) are pushing forward such studies, providing homogeneous determinations of chemical abundances for a large sample of OCs and field stars of all ages.

However, homogeneity is a key requirement also for the determinations of the other OCs' properties besides metallicity. In this sense, the Bologna Open Cluster Chemical Evolution

⁷Inner and outer disc extensions are defined by the discontinuity in the gradient, whose precise location is still debated, but roughly positioned at $R_{GC} \sim 12$ kpc.

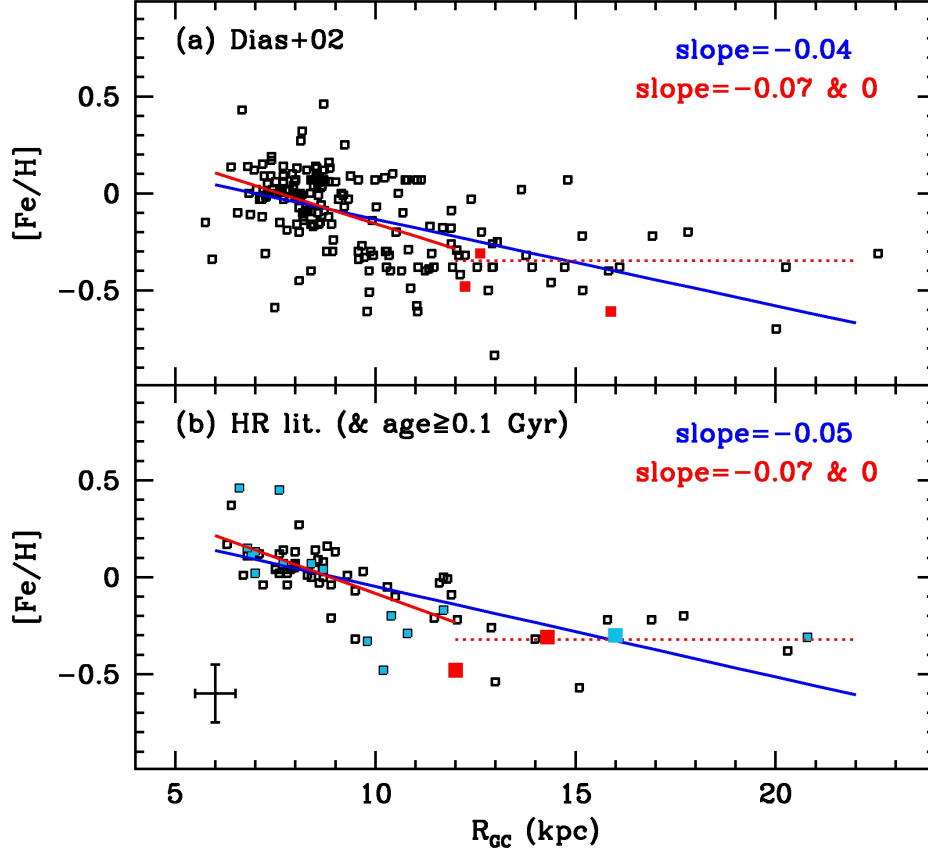


Figure 1.8: The metallicity gradient as defined by OCs. (a) R_{GC} and $[Fe/H]$ are taken from DAML02. The two lines represent the fit to the data using a single slope (in blue) or two, within 12 kpc from the Galactic centre and farther than this limit (in red). The three clusters indicated by filled (red) squares are the one analysed in Andreuzzi et al. (2011). (b) The same, but using only 72 OCs older than 0.1 Gyr and for which the metallicity has been derived with high-resolution spectroscopy; filled, light-blue squares indicate OCs for which $[Fe/H]$ has been determined within the Bologna Open Clusters Chemical Evolution project (see Ch. 2). Reproduced from Andreuzzi et al. (2011).

project (BOCCE project, see Ch. 2 for details) is one of the few projects that aim at deriving homogeneous OCs' parameters from both accurate photometry and HRS. Ages, distances, metallicities, and additional clusters' properties of a selected sample of old OCs are derived with the same methodology using photometric and spectroscopic data. The golden sample of the BOCCE project will be completely self-consistent in the main parameters used for the study of the chemical evolution of the disc, avoiding spurious interpretations that can be attained with an inhomogeneous data set.

Further improvements in studying the chemical evolution of the disc can be obtained using not only iron as tracer, but other elements, like oxygen. Oxygen is a better tracer,

compared to iron, for studying galactic chemical evolution (Maderak et al., 2013) because it has the advantage of coming primarily from one dominant source, namely, Type II SNe. Since O is produced by hydrostatic burning prior to the explosion, its yield is well described by nucleosynthesis models alone, the results of which depend primarily on the progenitor properties rather than the hydrodynamical details of the explosion. In addition to having a single production source the 10^6 – 10^7 yr timescale of Type II SNe in principle allows stellar O abundances in the Galaxy to respond quickly to enrichment, and thus O has the potential to exhibit a robust correlation with stellar age. On the other hand the reliability of O measurements is still debated as they are hindered by technical difficulties and theoretical subtleties.

1.2.2 Other metallicity tracers

Due to their short lifetimes, Cepheids, OB stars, H II regions are tracers of the present-day properties of the disc for their relatively short life. PNe, instead, describe earlier epochs.

Classical Cepheids are robust distance indicators (Leavitt & Pickering, 1912) and have been widely adopted in stellar astrophysics and in cosmology as primary standard candles, as fundamental physics laboratories to constrain evolutionary and pulsation properties of intermediate-mass stars, and as stellar tracers of young stars in the thin disc and in the Magellanic Clouds. In this context they are fundamental observables to constrain the chemical enrichment of disc stellar populations and play a key role in constraining the physical assumptions adopted in galactic chemical evolution (hereafter GCE) models. As discussed e.g. in Genovali et al. (2013), metallicity gradients based on Cepheids provide slopes of the order of -0.05 / -0.06 dex kpc^{-1} (see e.g. Pedicelli et al. 2009; Luck & Lambert 2011), but controversial results due to inhomogeneous data and analysis methods need review. With this aim they built a sample of 420 Cepheids combining their data with the literature ones. They found a steady increase in metallicity when approaching the innermost disc regions and did not find evidence of an azimuthal variation in the metallicity distribution (see Fig. 1.9, their figure 2). At variance, Lépine et al. (2011) suggested that a step function, with a step of 0.3 dex at 9.5 kpc, produces a fit of the same quality of a linear fit in the interval 6–13 kpc. Moreover, they suggested that a local ($7 < R_{GC} < 11$ kpc) azimuthal gradient is evident (0.05 dex kpc^{-1}), probably due to the spiral structure.

Galactic H II regions are the formation sites of massive OB stars and they reveal the locations of current Galactic star formation. Their chemical abundances indicate the present state of the inter-stellar medium (ISM) and reveal the elemental enrichment caused by the nuclear processing of many stellar generations. Early studies of H II regions revealed positive Galactic radial gradients of the derived electron temperatures (see e.g. Shaver et al., 1983). The electron temperature radial gradient was interpreted as a metallicity gradient since the balance of heating and cooling within H II regions is sensitive to the abundance of metal coolants, such as carbon and oxygen. For instance, the increase of electron temperature implies a decrease in O. The bulk of the data do indicate that the MW disc has a negative radial metallicity gradient, but not much else is really certain. Recent works, such as e.g. Rood et al. (2007) and Balser et al. (2011), confirmed a negative gradient. In the first case a slope of -0.043 dex kpc^{-1} is found; in the latter study a slope in the range -0.03 to -0.07 dex kpc^{-1} is determined. H II regions are particularly important because they are one of the few if not the only means to study the radial metallicity gradient in external galaxies (see e.g. Moustakas et al., 2010).

OB-type stars are young (<10 Myr) and their abundances trace the metallicity near their current location. Daflon & Cunha (2004) studied the distribution of metallicity with

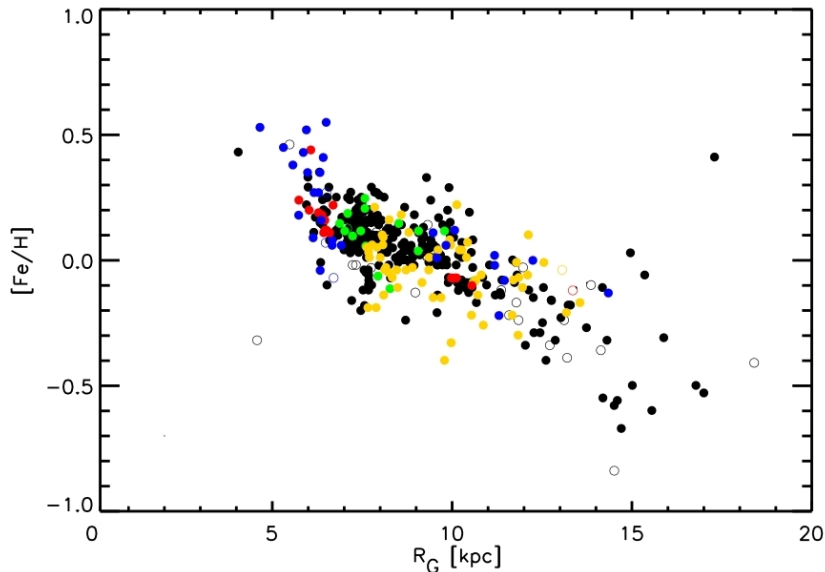


Figure 1.9: Iron abundance of Galactic classical Cepheids versus Galactocentric distance. Spectroscopic measurements based on different data sets are plotted with different colours (see Genovali et al. 2013 for details).

Galactocentric distance for a large sample of main-sequence OB stellar members of clusters and associations in the Galactic disc. The slope averaged from all elements within the Galactocentric distances 4.7–13 kpc is found to be -0.042 ± 0.007 dex kpc^{-1} , and the O gradient, in particular, is -0.031 dex kpc^{-1} .

PNe represent the Galactic stellar population with progenitors of turnoff mass M_{TO} between ~ 1 and $8M_{\odot}$, probing Galactic ages between $3 \cdot 10^7$ yr and ≥ 10 Gyr. PNe are distributed in the Galactic disc, bulge, and halo and hence probe different Galactic components. The recent studies of Stanghellini & Haywood (2010) and Henry et al. (2010) found radial negative $[\text{O}/\text{H}]$ gradient of -0.023 ± 0.006 dex kpc^{-1} in the first case and -0.058 ± 0.006 dex kpc^{-1} in the latter one (they explored a large disc sample, up to $R_{GC} \sim 20$ kpc). However, they suggested different time evolution of the gradient, that could steepen or remain unchanged. Gradients of O and Fe abundance from young and intermediate-age populations (OB stars/H II regions and OCs respectively) are in agreement with those of PNe.

Nevertheless, all this objects have some drawbacks. Cepheids and H II regions can be used to constrain only the present-day disc properties and the latter suffer large uncertainties in distance determinations. PNe can describe the earlier epochs of disc evolution but the huge uncertainties on their distances restrict their use as reliable tracers. On the contrary, OCs do not suffer these drawbacks and represent, in fact, a unique opportunity to probe the disc properties and their time evolution. Moreover, they can be used to study the abundances of a large number of elements in stars. The fact that it is possible to obtain precise age and distance determination relatively easily and that OCs are located at a wide range of Galactocentric distances, are decisive properties. Thus, they can fully address the issue of the time evolution of the metallicity gradient, provided that a homogeneous analysis is performed.

1.2.3 Theoretical models

The radial metallicity gradient and its evolution with time provide strong constraints on our understanding of the formation and evolution of galaxies. Depending on the relative importance of the different mechanisms involved in the formation of the Galactic thin disc, a gradient can settle and flatten or steepen with time, as we will see in the following. GCE models for the disc have been continuously improved over the last decades. However, the issue of the time evolution of the radial abundance gradients is far from being settled unequivocally both from the theoretical and observational points of view (e.g. Magrini et al., 2009). The four basic observational facts evident from OCs – the existence of either a negative radial abundance gradient within the inner disc or a step distribution, the flattening of the gradient in the outer disc, the lack of any correlation between cluster age and metallicity, and the appreciable dispersion in metallicity at any age and position in the disc – present a challenge to theories of GCE. GCE models are able to reproduce the present-day radial distribution of several chemical elements, as derived from observations of astrophysical objects representative of the current chemical composition of the disc (for instance H II regions), but in general disagree on the predicted behaviour of its time evolution. As described in Magrini et al. (2009) (but see also Tosi 1996 for a thoughtful direct comparison of several different models), GCE models can be divided in two groups: models which predict a steepening of the metallicity gradient with time (e.g., Tosi 1988; Chiappini et al. 1997, 2001) and those which predict a flattening with time (e.g., Mollá et al. 1997; Portinari & Chiosi 1999; Hou et al. 2000). The main differences between the two groups of models are the efficiency of the enrichment processes in the inner and outer regions of the Galactic disc, namely the star formation rate (SFR), and the nature of the material (primordial or pre-enriched) falling from the halo onto the disc (the infall). In models of the former type the outer disc is pre-enriched by the previous evolution of the halo, and during the first Gyr its metallicity is affected very little by the relatively lower SFR in the disc. Since the infall decreases rapidly with increasing Galactocentric radius, reflecting the strongly concentrated mass distribution in the halo, a larger amount of metal poor material falls in the central regions than in the outer Galactic disc. Thus, a positive metallicity gradient is initially established. When the halo collapse phase is over, the metallicity increases more rapidly in the inner disc than in the outer Galaxy, because of a combination of higher SFR at small radii and continuous dilution by infall at large radii, reversing the sign of the gradient. In contrast, in models of the second type, the initially vigorous star formation activity in the inner disc and the metal-poor composition of the infalling gas produce a rapid increase of the metallicity near the Galactic center. In the inner regions the metallicity increases rapidly, reaching its final value in the first 2–3 Gyr of disc evolution, whereas the enrichment of the outer disc is slower, resulting in a progressive flattening of the radial gradient. In this group of models, various infall rates have been assumed: a very rapid one simulating the formation of the disc from a monolithic collapse of the halo, or one much diluted with time, simulating a hierarchical formation of the disc by continuous infall of gas from the intergalactic medium. These rates produce different time evolution of the metallicity gradient: a rapid flattening or a uniform increase of the metallicity with essentially no change of slope, respectively. Determinations of abundance gradients in the disc at different ages are thus crucial to disentangle among different evolutive scenarios.

Magrini et al. (2009) used a sample of OCs with metallicity based on HRS to address the issue of the Galactic metallicity gradient. They found the best-fit for a GCE model characterised by an inside-out formation of the disc. The infall of gas is represented by an exponential law which, combined with the distribution of gas in the halo, produces a rapid

collapse in the regions with $R_{GC} < 12$ kpc and a uniform accretion in the outer regions. The inner regions are rapidly evolving due to the higher infall and SFR, while the outer parts evolve more slowly. The metallicity in the outer disc increases uniformly at all radii without a marked change of slope of the gradient. Peculiar episodes of mergers in the past history of the Galaxy would explain the outer metallicity plateau indicated by the older clusters (but see Chiappini et al. 2001). In Fig. 1.10 (their figure 1) the radial metallicity gradient

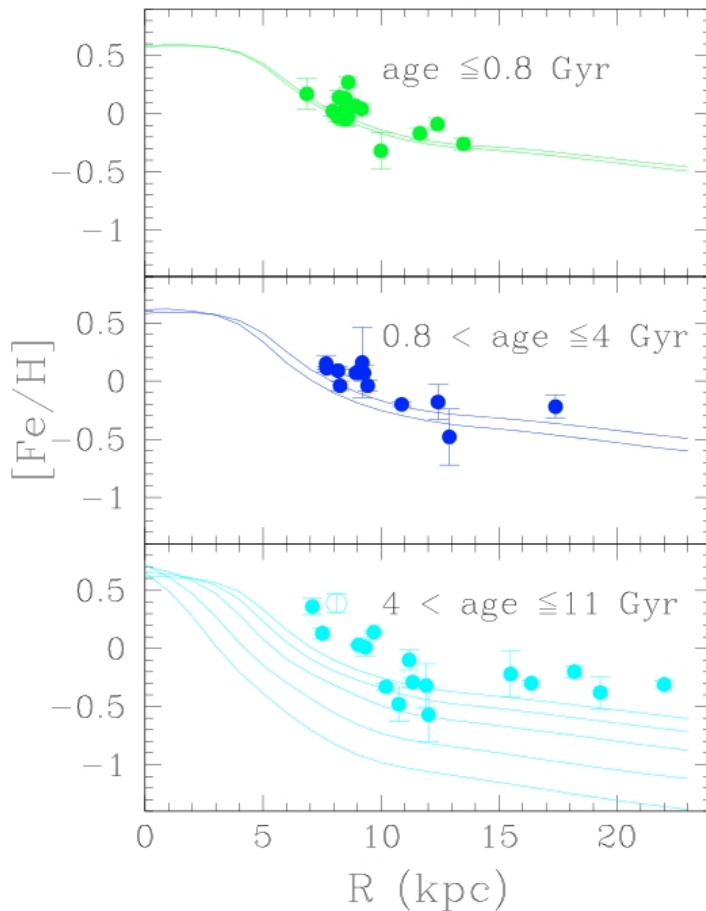


Figure 1.10: Gradient of $[\text{Fe}/\text{H}]$: comparison between high-resolution data of OCs with the model described in Magrini et al. (2009). Different panels show abundances for different age bins. The models adopted to compare with observations are for 0 and 1 Gyr ago (panel 1), 1 and 4 Gyr ago (panel 2), and 4, 6, 8, 10, 11 Gyr ago (panel 3). Reproduced from Magrini et al. (2009).

of their OCs sample for different age bins is shown and compared with the GCE models. While the younger clusters are reproduced, the models seem to have more difficulties with the old clusters, representative of the early epochs of the disc formation.

This outer plateau is studied in details by Yong et al. (2005). They suggested that even though the model of Chiappini et al. (2001) (like that of Magrini et al. 2009) accurately predicts the plateau beyond $R_{GC} = 12$ kpc, as well as enhanced $[\alpha/\text{Fe}]$ and $[\text{Eu}/\text{Fe}]$, the hypothesis of outer disc formation from gas leftover from the halo should be discarded. Both angular momentum arguments and abundance pattern require a different nucleosynthetic history for the formation of the outer disc. Yong et al. (2005) proposed that a significant merger event is currently taking place beyond 12 kpc from the Galactic centre and that outer OCs were created from such event, even though this is not confirmed by Carraro et al. (2007).

Alternatively, Lépine et al. (2011) using a selection of literature data suggested a different metallicity distribution and explanation. They proposed that the gap that appears clearly in their data at $R_{GC} = 8.5$ kpc (they adopted $R_{GC,\odot} = 7.5$ kpc), which separate the inner

and the outer flat metallicity distribution, can be explained with dynamical arguments. The radius of the gap coincides with corotation and with the Cassini-like ring-shaped region of a void of gas discovered by Amôres et al. (2009). The gap in the distribution of clusters would then tell us that the star formation is inhibited in the region of gas void, while the step in the metallicity distribution indicates that the void forms a barrier that prevents the transportation of gas from one side to the other, favouring the evolution of metallicity independently on the two sides. The corotation barrier only acts on the gas, not on the stars; many stars have orbits with strong deviations from circularity, and there is no impediment for them to cross the resonance; what is more, stars on circular orbits are scattered across the corotation radius (Sellwood & Binney, 2002; Lépine et al., 2003), and thus naturally cross the chemical barrier. Stars with different origins but suffering radial migration might have a strong impact on ‘blurring’ and ‘churning’ metallicity radial gradient.

As just mentioned, another complication, that only recently began to be considered in models, is radial migration. Roškar et al. (2008) described the influence of radial migration on the properties of the Galactic disc. From their dynamical simulations they suggested that stars migrate across significant distances due to resonant scattering with transient spiral arms, while preserving their circular orbits. According to Roškar et al. (2008), up to 50% of solar neighbourhood stars were actually born at inner/outer radii. Thus, the effect of radial motions of stars could not be a second order one. The slope of the metallicity gradient decreases with increasing age of stellar population because radial migration causes more mixing in older populations, creating the appearance of flatter gradients at early times (at odds with the real initial condition of the simulation). Schönrich & Binney (2009) proposed a GCE model in which both the angular momentum exchange across corotation of minor transient spiral features and the range of radii swept by stars on non-circular orbits are taken into account. However, such recent models are still axisymmetric in essence, and do not take into account some of the basic features of our non-axisymmetric Galaxy and cannot at present reproduce observed features (as outlined in Lépine et al. 2011).

Whether the mechanism of radial migration can be extended to OCs as well and which is the effect of dynamics on their radial distribution is still under investigation. Wu et al. (2009) claimed that OCs do not move much from their original distance from the Galactic centre and Magrini et al. (2010) suggested that the final slope of the radial metallicity gradient using the cluster birthplaces instead of their present R_{GC} distances does not yield significantly different values. Jilková et al. (2012) did not find strong arguments in favour of radial migration to explain the dynamical properties of NGC 6791. At the moment, no clear predictions on clusters’ dynamics exist, thus also recent studies of the disc’s GCE are based on simple models. For instance, Heiter et al. (2014) used different GCE models to compare with their OCs sample (a tentative homogenisation of literature abundances). Although their list of discussed models is not exhaustive, they concluded that none of them succeeds in predicting the radial metallicity gradient of OCs.

More elaborate chemodynamical models taking into account the main effects of the grand-design spiral pattern of the MW are thus now required to reproduce observations.

1.3 Where do we stand

OCs are reliable tracers of the properties of the disc. They span different ages, positions, and metallicities, all of which can be derived relatively easily. They offer a unique laboratory to study the time-line of the chemical evolution within the disc, revealing the picture of the disc properties at early epochs and at present-day. However, firm conclusions have

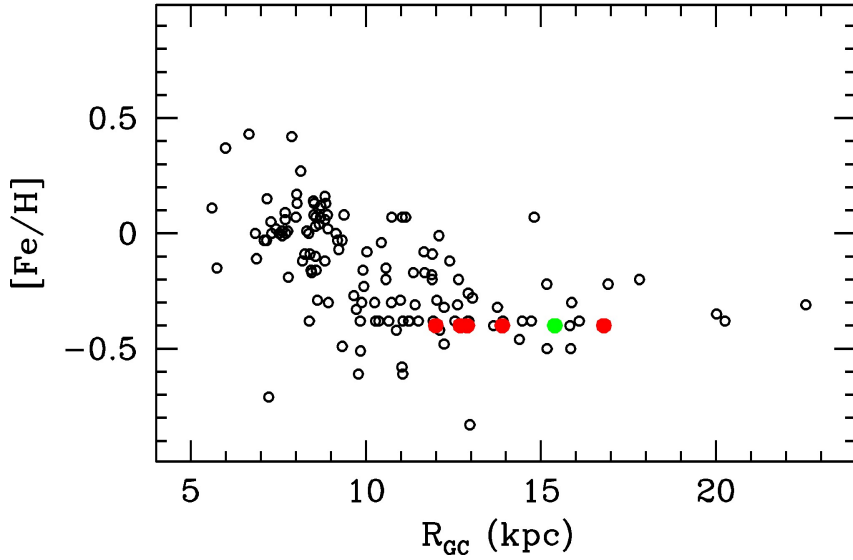
still not been reached. Most of the literature works of the last decades seem to agree on a steep inner metallicity gradient (within $R_{GC} \sim 12\text{--}13$ kpc) and a flatter outer one, but there is no concordance on whether the inner gradient steepens or flattens with time, or on whether we can speak of a gradient at all, since some studies suggest instead a step distribution. Theoretical models of GCE are not yet able to give an unequivocal answer. Furthermore, the impact of stars migration in studying the radial gradient of the disc has to be considered. Whether migration applies to OCs as well or not is still under study but certainly GCE theorists should consider dynamics in their models.

All observational works on OCs point out the need of larger and homogeneous sample of OCs, in order to limit systematic errors which seriously jeopardise the correct interpretation of the data. HRS is strongly suggested to understand the details of the abundances of the disc, as other elements in addition to Fe can better describe the spatial distribution and its evolution with time or probe different nucleosynthetic regimes. A consistent and homogeneous database of OCs is fundamental also in the photometric observations. Only photometric analyses can provide age, distance, and reddening estimates. The BOCCE project stands out with respect to other similar studies, aiming at accurate photometry and HRS for a large sample of old OCs (see Ch. 2), significantly filling the parameter space needed to understand the GCE using a completely homogeneous analysis. Finally, the large surveys of our Galaxy, both photometric and spectroscopic ones, will play an unprecedented role for our knowledge of the MW. Among them, the Gaia astrometric satellite and the Gaia-ESO Survey, described in Ch. 3, will dramatically expand the actual database of information on OCs.

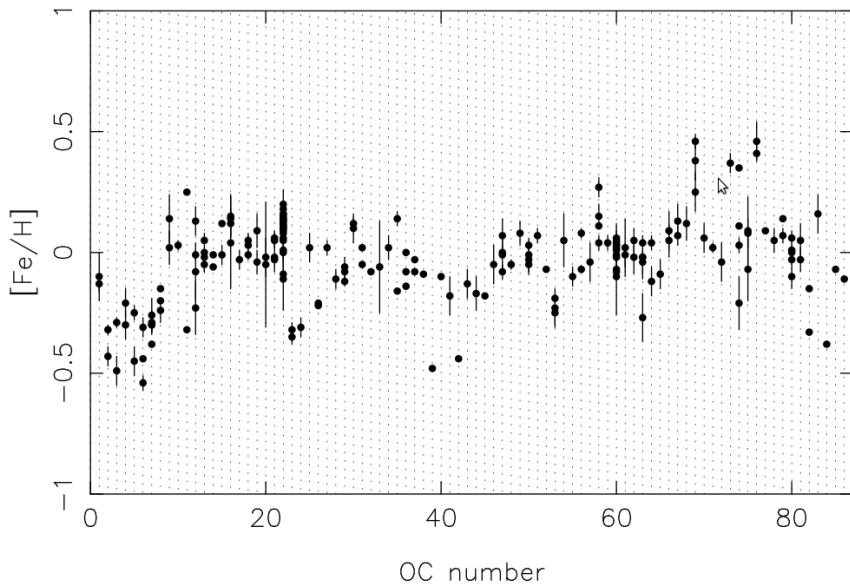
Chapter 2

Bologna Open Cluster Chemical Evolution Project

The Bologna Open Cluster Chemical Evolution Project (BOCCE hereafter) is a long term project aiming at studying the chemical evolution of the disc of the MW Bragaglia & Tosi see 2006. It is devoted to OCs because, as amply explained in Ch. 1, they are reliable tracers of the properties of the Galactic disc. They can be considered as records of its history and evolution. OCs are the perfect tools to study the chemical evolution of the disc because they span different ages, metallicities, and positions and can reveal how the chemical abundances vary spatially and with time within the Galactic disc. The basic information we need for our study are time (clusters' age), position (clusters' distances), and metallicity (clusters' chemical abundances) i.e. a three dimensional parameter space. However, for a proper statistical sampling of this 3D space, we need a consistent database of objects. For example, if we want to distinguish at least between young OCs (age <0.3 Gyr) and old OCs (those with age in the range $0.3 < \text{age} < 1.4$ and those older than 1.4 Gyr), and similarly, between OCs with sub-solar, solar, and super-solar abundances, we need to divide in three bins each axis of the 3D space considered, that is 27 bins at minimum. An estimate of the density of objects in this space will have Poisson noise of order unity unless we have at least 54 OCs. As said, this is the basic parameters space useful for our investigation. If we want to consider also the azimuthal position and height above the disc for a more comprehensive and accurate analysis of the disc's properties, the number of objects required increases accordingly. Even though in literature there are numerous evaluations of OCs' parameters (at least age, distance, and metallicity), accurate estimations of the clusters' abundances, i.e. those based on HRS, are available only for a small fraction. Moreover, the old OCs and the outer ones are still poorly investigated (see discussion in Ch. 1). Furthermore, the main problem with literature data is that they are highly inhomogeneous. Systematic differences are present between authors that can arise from various combined factors, from the quality of the data (especially for older data) to the differences in the adopted methods. It is not surprising to find inconsistent results for the same cluster when disparate analysis methods are used or to see systematic differences in photometric catalogues of the same object. For example, in Fig. 2.1 we show the representative case of Berkeley 31 and a figure taken from Heiter et al. (2014) which strikingly explain the problem of using parameters coming from non-homogeneous data sets. The OC Berkeley 31 has been analysed by several authors and an age spanning from 2 Gyr up to 8 Gyr, and R_{GC} in the range 11–17 kpc have been derived. Such differences are most probably due to contrasting quality in the photometric catalogues



(a)



(b)

Figure 2.1: (a) The radial metallicity distribution obtained for the old OCs using the DAML02 catalogue. The red points are the different parameter estimates of Berkeley 31. In green the value derived within BOCCE. (b) The plot is taken from Heiter et al. 2014 (their figure 1) and shows the mean metallicity of the OCs considered in their work; note the existence of even large differences for the same cluster.

that, in some cases, can hamper an accurate evaluation of the evolutionary status of the clusters. 2.9 Gyr and $R_{GC} \sim 15$ kpc are the results obtained within BOCCE (see Cignoni et al., 2011). Heiter et al. (2014) selected HRS analyses of OCs' red giant stars and showed how large can be the lack of homogeneity for the clusters studied by several authors. For example, the Hyades (OC number 22) are located very close to the Sun hence they should have about solar metallicity. However, the mean metallicity estimates available in literature

can range from sub-solar to super-solar values, in contrast with the expectations.

For this reason several authors have started to build their own homogeneous OCs collections like, for example, those described in Twarog et al. (1997); Friel et al. (2002); Carraro & Costa (2007) and Jacobson et al. (2011b). However, they had to accept some compromises, either they adopted literature values for ages and distances or combined metallicities estimates coming from distinct sources.

An interesting project is the WIYN¹ Open Cluster Study (WOCS, von Hippel & Sarajedini 1998), a long and useful series of coordinated papers on OCs relying on WIYN 3.5 m telescope data. It aims at obtaining comprehensive photometric, astrometric, and spectroscopic data for a small number (~ 10) of nearby key clusters spanning the widest possible range of age and metallicity, measuring Fe, C, O, Li, and hopefully N abundances, precise radial velocities, proper motions, and broadband colours.

The method adopted in BOCCE consists in using both photometry and spectroscopy to derive accurate cluster parameters. Through photometry age, position, Galactic reddening, and approximate metallicity can be recovered, while HRS is used for accurate metallicity determination and detailed chemical abundances. The key aspect of the project is specifically homogeneity with the unquestionable advantage of using a fully homogeneous and accurate data-set in both spectroscopy and photometry with respect to similar OCs surveys.

2.1 Photometry

All the BOCCE OCs have accurate photometry in at least two colours of the optical B , V , and I Johnson-Cousins magnitude system. Observations in two colours (i.e. at least three bands) are preferred for a more robust constraint on photometric metallicity (see discussion in the following paragraphs). Photometric accuracy is an important requirement in order to have a good description of all the evolutionary phases of the stellar populations under study, well covering both the faint main sequence (MS) and the bright RGB with the smallest photometric error. For this reason, a large FoV is preferred, as it can be used to recover the spatial information that can be extracted with photometric imaging (determination of the cluster centre or density profile, for instance) and to observe as many cluster's stars as possible (more massive stars, as TO and giant stars, are expected to be more concentrated, while the less massive ones, lower MS stars, are more spatially spread). Numerous photometric catalogues are available in the literature for a large number of OCs, but they cannot be used for the BOCCE project because they are not homogeneous. In some cases they are of poor quality and/or based on small FoV. For OCs that are poorly populated and/or with large angular diameter, the small FoV limits a good description of all the evolutionary phases. As discussed in Sec. 1.1.2, the median diameter of the old OCs in DAML02 is 5 arcmin and the optimal FoV dimension able to embrace the bulk of the clusters should be of the same order of magnitude. Moreover, external fields, i.e. photometric imaging of FoV pointed at a sufficient distance from the cluster centre, are important to estimate the field stars pollution. Such blank fields are not always available in literature. For loosely populated clusters and/or set in heavily contaminated environment (see for instance the case of Berkeley 81 discussed in Sec. 6.1.1), the comparison of the observational CMDs of the central part of the cluster and the ones obtained for an outer part helps defining the evolutionary sequences of the OC, otherwise one could be led astray by the field contamination.

¹The WIYN Observatory is a joint facility of the University of Wisconsin–Madison, Indiana University, Yale University, and the National Optical Astronomy Observatories.

The cluster parameters estimation (mainly age, distance, and metallicity) is obtained comparing the observational plane, i.e. the empirical CMD, and the theoretical one (the luminosity and temperature relation predicted by the stellar evolutionary models). Within the BOCCE project this comparison is achieved by using the synthetic CMD technique, described in detail in Sec. 4.2. Very briefly, this technique relies on a Monte-Carlo extraction of a simple stellar population based on the adopted evolutionary models. Observational features (such as photometric errors, photometric completeness, and field contamination derived from the observations) are taken into account. This is a fundamental step of the synthetic CMD technique and is needed for a robust study. The external field is used to reproduce with better accuracy the effect of foreground and background stars within the synthetic CMD, so to better discriminate the genuine cluster sequences from the field contamination. The comparison of the synthetic CMD and the observational one is considered satisfying when the observational CMD morphology is well reproduced by the synthetic one. Several indicators are used to find the best solution: the observed magnitude level and colour of the age sensitive indicators of a stellar population (the main sequence TO and RC, for instance) must be well reproduced as well as the observed luminosity function.

The advantage of this technique with respect, for example, to isochrone fitting, is its accuracy. With the synthetic CMD the prediction of the theoretical models in terms of number of stars for each evolutionary phase (particularly important for OCs which are poorly populated and heavily contaminated) and the observational effects of the quality of the photometry (the main effect being the spread of the evolutionary sequences) are taken into account. This clearly provides a larger number of constraints and leads to a better selection of the solution.

The metallicity derived from photometry, however, is approximate. This is essentially due to two factors. The first one is the uncertainty in the transformation from the theoretical plane to the observational one. For example one assumption of this transformations is *gray* atmosphere. This simplification is valid for hot and massive stars where very few absorption lines are present but not in the case of lower MS or giant stars, where the absorption features become more relevant. For instance, we found in our project several cases in which we could not obtain a good description of the observed colour for all the cluster phases, obtaining a synthetic CMD too red or too blue for the RC, RGB or lower MS phases (see e.g. Cignoni et al., 2011). The second factor is the combination of observational photometric errors, sensitivity to metallicity of a given set of theoretical models, and adopted chemical abundances representative of the solar composition, which places a limit to the precision of the metallicity estimates. If photometry is available in at least three different filters the sensitivity to metallicity is largely improved, as described in Tosi et al. (2007). Finding the best solution that can reproduce at the same time the observational CMD in two different colours is a stronger constraint on the metallicity. In Fig. 2.2 we show a figure taken from Tosi et al. (2007) for the case of King 11. Nonetheless, as found by Ahumada et al. (2013) and described in Sec. 5.2.3, the main uncertainty for the metallicity derived from photometry still remains the photometric conversion. As outlined in that paper, sometimes when isochrones match well in $B - V$, they fail in $V - I$. The reason for this is not straightforward: it cannot simply be metallicity or age and a difference in the metal mixture is suggested as a complementary explanation.

Finally, the accuracy of the photometric catalogue plays an important role. Hidden systematic errors, for example in the calibration to a photometric system, can jeopardise the correct interpretation. In Donati et al. (2014b) (see Sec. 7.3.2) we showed that important differences between two different catalogues available in literature for the OC Trumpler 20, both apparently of very good precision but evidently of different accuracy, hinder the metal-

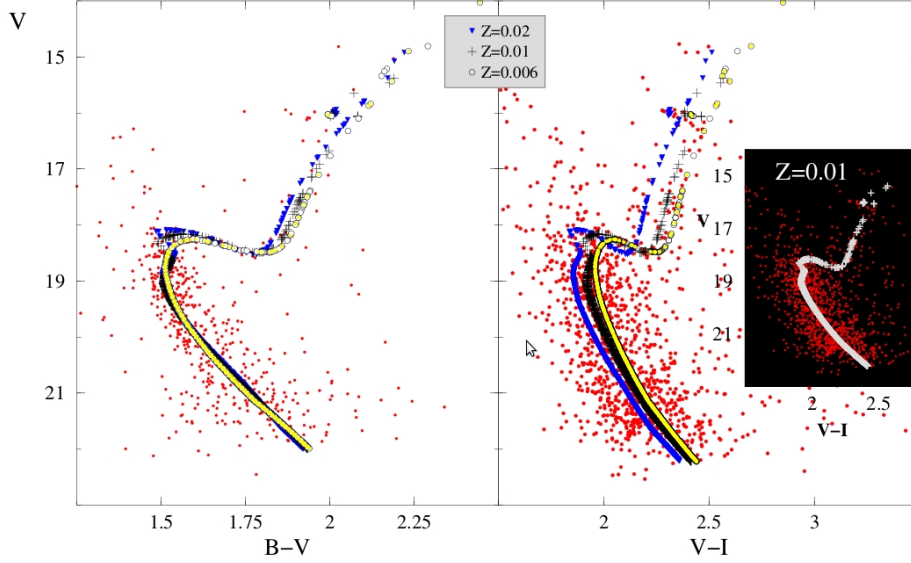


Figure 2.2: The left panel shows the $V, B - V$ data and the three best solutions (at $Z=0.006, 0.01, 0.02$) that all reproduce the observed CMD of the central zone of King 11, while the right panel shows the same models overlaid on the $V, V - I$ data (in this case stars from the whole field are shown). Only the solution at $Z=0.01$ (for an easier understanding it is isolated in the small panel on the right) can well fit at the same time the two different CMDs. Reproduced from Tosi et al. (2007).

licity estimate from photometric data.

The BOCCE OCs with complete photometric analysis are 34. I analysed 8 of them which are described in this thesis in Ch. 5 and 6 together with the provisional analyses of two more. I adopted the synthetic CMD method to define their evolutionary status and derive distance and approximate metallicity. Five out of eight (Berkeley 27, Berkeley 34, Berkeley 36, NGC 2849, and NGC 6134) were observed on a relatively small FoV, but of comparable angular dimension to the median value of OCs' diameter found in DAML02. However, by considering the typical King tidal radius of OCs (about 9 pc, see Ch. 1), they can be much more extended than 5 arcmin. In Fig. 2.3 the apparent angular dimension of objects with a radius of 9 pc is plotted versus the distance from the Sun. In the same figure also the apparent angular dimension of objects with a radius of 1.2 pc (the typical King core radius) is considered. It is worth noticing that the estimates of the OCs' tidal radius quoted in the MWSC catalogue have a dispersion of 6 pc and an internal error of the order of 25%. However, from a qualitative point of view, only OCs further than 10 kpc from us are fully observable within 5 arcmin and only Be 29 has been observed at such distance. On the other hand, we were able to observe all the BOCCE OCs within the King core radius. For the other three OCs (Berkeley 81, NGC 1817, and NGC 2141) I could exploit photometric data on a larger FoV and for two of them (NGC 1817, the closest of the three, revealed to be much more extended than our FoV) I was able to derive their radial density profile and accurately evaluate their structure parameters. For 11 OCs out of 34 we have metallicity derived from HRS (see next section). In Fig. 2.4 we show the radial metallicity distribution obtained from the BOCCE database, the main result of the project. The circles are OCs with metallicity estimated with HRS. Filled points and open ones refer to two different methods adopted for stellar atmosphere parameters estimation (see next paragraph).

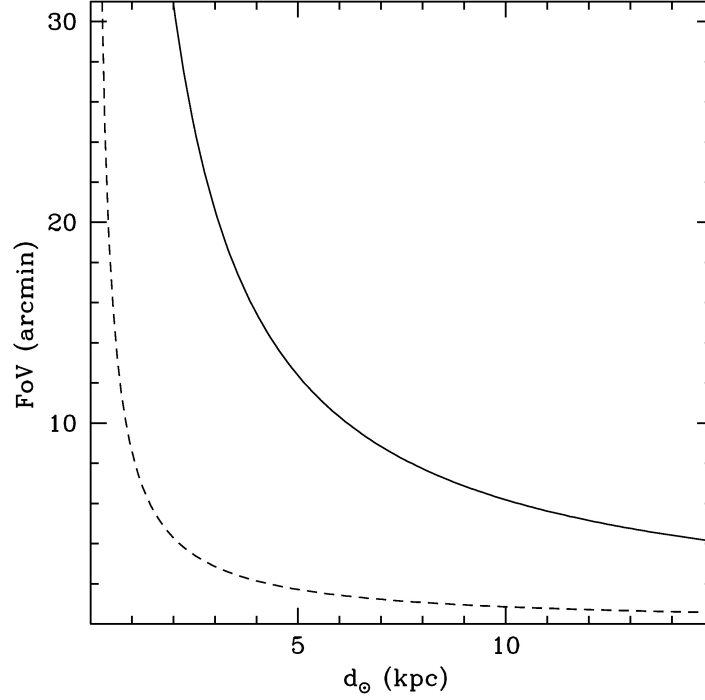


Figure 2.3: Angular dimension of the FoV needed to observe OCs within the typical tidal radius (~ 9 pc) and within the typical core radius (~ 1.2 pc) with respect to the distance from us. The continuous and dashed lines refer to the tidal and core radii respectively.

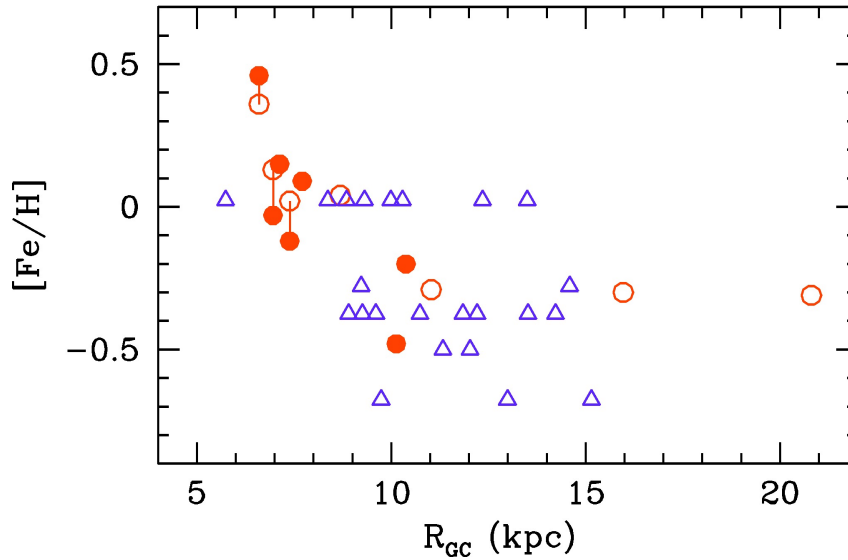


Figure 2.4: Radial metallicity distribution of the OCs within the BOCCE database. The circles are clusters with HRS abundance analysis. Open and filled circles highlight the two different type of HRS analysis (see Sec. 2.2). The typical error on $[\text{Fe}/\text{H}]$ is about 0.1 dex. Triangles are OCs with metallicity estimated from photometry.

2.2 Spectroscopy

Inside the BOCCE database we have a complete spectroscopic analysis for 11 OCs. They are about one third of the total sample but the aim is to analyse spectroscopically all the other clusters in order to obtain a homogeneous sample in photometry and spectroscopy. To maintain the highest homogeneity possible we limit the spectroscopic sample to stars in the same evolutionary phase and we use high-resolution spectra only ($R \gtrsim 30000$, necessary for high-metallicity spectra where the line crowding is large). RC and RGB cluster stars are preferentially chosen because they are the most reliable for abundance analysis. In particular, RC stars are the main targets because they are bright and stand clearly in the observational CMDs with respect to field objects, improving the chance to select clusters' members. Furthermore, they have very similar parameters (within each cluster and among clusters) thus enhancing the homogeneity of the results.

For all clusters, we adopt the same analysis method which consists on the classical approach of the equivalent widths (EWs) method. The same linelist and atomic and damping parameters are adopted throughout the analysis. Abundance analysis is performed using the model atmospheres by Kurucz (1993). The atmosphere parameters T_{eff} and surface gravity g are derived spectroscopically, using excitation and ionisation equilibria, respectively, while microturbulence ξ is optimised by minimising the slope of the relationship between $\log n(FeI)$ and the observed EWs. The detailed descriptions of the analyses can be found in Bragaglia et al. (2001) for the method used for measuring EWs, in Carretta et al. (2004) and Sestito et al. (2008) for the two methods used to derive the stellar atmosphere parameters. In Carretta et al. (2004, 2005) and Sestito et al. (2006, 2008) the linelists for all the elements considered in the spectra analysis is described while Gratton et al. (2006), Sestito et al. (2007), and Carretta et al. (2007) describe the analysis of the very metal-rich clusters (NGC 6253 and NGC 6791) using spectrum synthesis.

We stress that homogeneity in the spectroscopic measurements is as important as in the photometric analysis. Fig. 2.1 outlines this aspect, showing that HRS analyses available in literature for the same OC can be largely discrepant from each other. In some cases differences up to 0.4 dex can be found. These inconsistencies can be ascribed to several aspects that contribute to the analysis process: the number and the spectral type of stars used (statistics), the quality of the spectra (e.g. signal-to-noise ratio, SNR), the continuum tracing, the adopted atomic parameters, the EWs measurement, the model atmosphere, the spectral code, and the atmospheric parameters. Moreover, because of different analyses and physical assumptions, the chemical abundances derived are referred to different temperature and metallicity scales, making rather difficult and arbitrary any attempt of homogenisation of literature data. Although the number of spectroscopic studies of OCs is increasing, at present day there is not a significant sample with homogeneous analysis that can reliably used to trace the chemical properties of the Galactic disc. The BOCCE spectroscopic sample is limited, at this stage, to the age range of 0.9–6 Gyr, while the whole sample of the BOCCE database includes OCs as young as 0.1 Gyr (NGC 7790) and as old as 8.5 Gyr (Berkeley 17). About half of the objects with HRS analysis is concentrated in the inner region of the Galactic disc ($5 < R_{GC} < 10$ kpc) while the outer disc ($10 < R_{GC} < 20$ kpc) is poorly sampled.

In Fig. 2.5 we show the comparison of the iron abundance of our spectroscopic sample with the HRS analyses available in literature. In most cases we have a nice agreement (like, for example, clusters 10 and 14, Pismis 2 and NGC 6819 respectively). In some other cases, there are differences of the order of 0.3 dex like for OC number 7 (Berkeley 29). However, considering that the errors on individual [Fe/H] determinations are typically of the order of

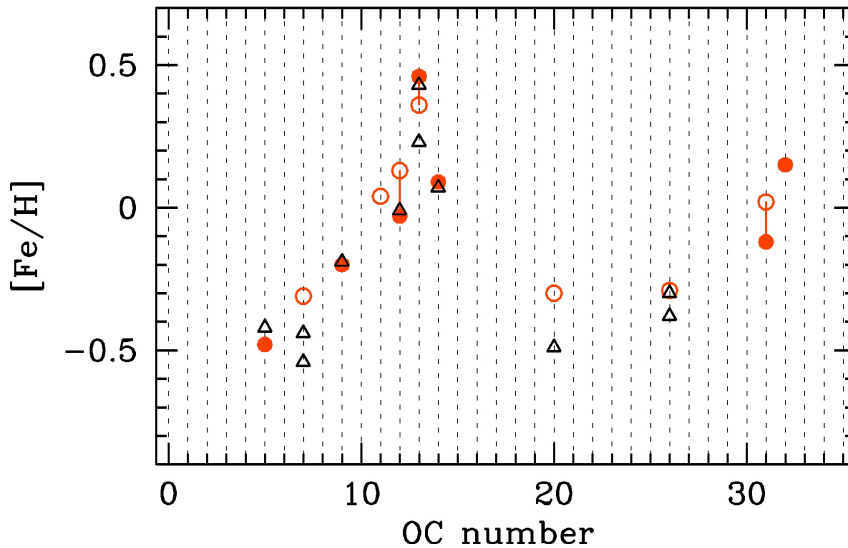


Figure 2.5: Metallicity estimates obtained with HRS for OCs in common between the BOCCE project (red points) and the literature (black points). The correspondence between number and cluster is given in Tab. 2.1.

0.1–0.15 dex, all the measures shown in figure are consistent within the uncertainties.

The BOCCE project is in progress. The spectroscopic analysis, even if at the moment available for only one third of the OCs analysed so far, will be completed for all the clusters. Moreover, the BOCCE database should be enlarged: from rough considerations, at least ~ 50 objects are needed to have a statistically significant sample useful to trace the Galactic chemical evolution of the disc. In Ch. 4 I detail the methods used for the photometric analysis, while in Ch. 5 and 6 I describe the analyses performed as part of the thesis project on 8 OCs out of 34 and the ongoing analysis on two more clusters. Even if we are far from the goal of about 50 clusters, with the 34 OCs already analysed it is possible to draw preliminary considerations on the potentiality of the project. In Ch. 8 I summarise the properties of the clusters analysed so far and discuss the Galactic disc properties as derived from our homogeneous sample. The BOCCE project is not an isolated programme and its goals are shared by several photometric and spectroscopic surveys, some of which led by international collaborations. The BOCCE project could benefit from collaborations with these surveys. For example, if there is a sufficient number of objects in common it will be possible to homogenise the results in a single and larger sample. This would efficiently improve the statistical power needed to describe the properties of the MW disc. One of these surveys is the Gaia-ESO Survey in which I am involved. It will observe tens of thousands of stars in about 100 OCs to obtain a comprehensive HRS chemical abundance analyses. In the next chapter I will describe the Gaia-ESO Survey and briefly sketch other similar ground-based surveys. The unprecedented scientific legacy they will leave is of paramount importance to understand the evolution of our Galaxy.

In Tab. 2.1 all the 34 OCs with complete photometric analysis in the BOCCE database with the corresponding parameters are recorded.

Table 2.1: Information on the BOCCE clusters for which a complete photometric analysis has been published. The metallicity Z is from the photometry, while $[\text{Fe}/\text{H}]$ is from HRS (BOCCE or literature) and can have multiple values. For $[\text{Fe}/\text{H}]$, the flag A means BOCCE, B means the FLAMES sample (similar technique), C means literature.

Nr	Cluster	l	b	$(m - M)_0$	E(B-V)	Z	age Gyr	R_{GC} (kpc)	$[\text{Fe}/\text{H}]$	Ref phot	Ref Spec
1	Berkeley 21	186.84	-2.51	13.50	0.78	0.004	2.20	12.99	-0.53	1	C, 10
									-0.31		C, 11
2	NGC 2099	177.64	+3.09	10.50	0.36	0.008	0.43	9.26	+0.01	1	C, 12
3	Berkeley 22	199.90	-8.08	13.80	0.64	0.020	2.40	13.50	-0.32	1	C, 13
									-0.45		C, 11
4	NGC 2168	186.59	+2.22	9.80	0.20	0.008	0.18	8.91	-0.21	1	C, 14
5	NGC 2243	239.48	-18.01	12.74	0.08	0.004	4.80	10.13	-0.48	1	A, 15
									-0.42		C, 16
6	Collinder 110	209.65	-1.98	11.45	0.57	0.004	1.70	9.74	+0.03	1	C, 12
7	Berkeley 29	197.98	+8.03	15.60	0.12	0.004	3.70	20.81	-0.44	1	C, 17
									-0.54		C, 18
									-0.31		B, 19
8	NGC 2323	221.67	-1.33	10.20	0.22	0.020	0.12	8.85	-	1	
9	NGC 2506	230.56	+9.94	12.60	0.00	0.020	1.70	10.38	-0.20	1	A, 23
									-0.19		C, 22
10	Pismis 2	258.85	-3.34	12.70	1.29	0.020	1.10	9.31	-	1	
11	NGC 2660	265.93	-3.01	12.30	0.40	0.020	0.95	8.69	+0.04	1	B, 24
12	Collinder 261	301.68	-5.53	12.20	0.30	0.020	6.00	6.96	-0.03	1	A, 30
									+0.13		B, 19
									-0.22		C, 31
									-0.01		C, 32
13	NGC 6253	335.46	-6.25	11.00	0.23	0.050	3.00	6.60	+0.46	1	A, 33
									+0.36		B, 34
									+0.43		C, 35
									+0.23		C, 36
14	NGC 6819	73.98	+8.48	12.20	0.12	0.020	2.00	7.71	+0.09	1	A, 37
									+0.07		C, 38
15	NGC 6939	95.90	+12.30	11.30	0.34	0.020	1.30	8.37	+0.00	1	C, 39
16	NGC 7790	116.59	-1.01	12.65	0.54	0.020	0.10	9.99	-	1	
17	Berkeley 66	139.43	+0.22	13.30	1.22	0.008	3.80	11.85	-0.48	2	C, 13
18	NGC 1817	186.18	-12.99	11.10	0.23	0.008	1.10	9.61	-0.07	3	C, 20
									-0.16		C, 21
									-0.11		C, 22
19	Berkeley 17	175.65	-3.65	12.20	0.62	0.008	8.50	10.74	-0.10	4	C, 40
20	Berkeley 20	203.48	-17.37	14.70	0.13	0.008	5.80	15.97	-0.49	2	C, 18
									-0.30		B, 19
21	King 8	176.39	+3.12	13.20	0.52	0.020	1.30	12.35	-	5	
22	NGC 2141	198.04	-5.80	13.20	0.36	0.008	1.90	12.21	-0.14	3	C, 18
									+0.00		C, 20
23	Berkeley 23	192.61	+5.45	13.75	0.33	0.008	1.30	13.52	-	5	
24	Berkeley 27 ^a	207.78	+2.60	13.20	0.50	0.006	1.50	12.03	-	6	
25	Berkeley 31	206.25	+5.12	14.40	0.19	0.004	2.90	15.15	-0.53	5	C, 18
26	Berkeley 32	207.95	+4.40	12.60	0.12	0.008	5.20	11.03	-0.29	7	B, 24
									-0.30		C, 26
									-0.30		C, 27
									-0.38		C, 11

Table 2.1 – continued from previous page

Nr	Cluster	l	b	$(m - M)_0$	E(B-V)	Z	age Gyr	R_{GC} (kpc)	[Fe/H]	Ref phot	Ref Spec
27	Berkeley 34 ^a	213.73	+2.11	14.30	0.57	0.010	2.10	14.59	–	6	
28	Tombaugh 2	232.83	-6.88	14.50	0.34	0.008	1.60	14.23	-0.40	2	C, 28
									-0.31		C, 29
29	Berkeley 36	227.38	-0.59	13.15	0.53	0.006	7.00	11.33	–	6	
30	NGC 2849	265.27	+6.36	13.85	0.30	0.020	0.90	10.29	–	8	
31	NGC 3960	294.37	+6.18	11.60	0.29	0.020	0.90	7.39	-0.12	9	A, 25
									+0.02		B, 24
32	NGC 6134	334.92	-0.20	9.95	0.50	0.021	0.90	7.13	+0.15	8	A, 23
33	Berkeley 81	33.70	-2.49	12.40	0.91	0.020	0.90	5.74	–	3	
34	King11	117.16	+6.48	11.75	1.04	0.010	4.25	9.23	–	7	

^aBerkeley 27 and Berkeley 34 are also known as Biurakan 11 and Biurakan 13 respectively

Ref. Phot.: 1 Bragaglia & Tosi (2006); 2 Andreuzzi et al. (2011); 3 Donati et al. (2014b); 4 Bragaglia et al. (2006a); 5 Cignoni et al. (2011); 6 Donati et al. (2012); 7 Tosi et al. (2007); 8 Ahumada et al. (2013); 9 Bragaglia et al. (2006b).

Ref. Spec.: 10 Hill & Pasquini (1999); 11 Yong et al. (2012); 12 Pancino et al. (2010); 13 Villanova et al. (2005); 14 Barrado y Navascués et al. (2001); 15 Gratton & Contarini (1994); 16 Jacobson et al. (2011a); 17 Carraro et al. (2004); 18 Yong et al. (2005); 19 Sestito et al. (2008); 20 Jacobson et al. (2009); 21: Jacobson et al. (2011b); 22 Reddy et al. (2012); 23 Carretta et al. (2004); 24 Bragaglia et al. (2008); 25 Bragaglia et al. (2006a); 26 Friel et al. (2010); 27 Carrera & Pancino (2011); 28 Brown et al. (1996); 29 Villanova et al. (2010); 30 Carretta et al. (2005); 31 Friel et al. (2003); 32 De Silva et al. (2007); 33 Carretta et al. (2007); 34 Sestito et al. (2007); 35 Anthony-Twarog et al. (2010); 36 Montalto et al. (2012); 37 Bragaglia et al. (2001); 38 Frinchaboy et al. (2013); 39 Jacobson et al. (2007); 40 Friel et al. (2005);

Chapter 3

The Gaia-ESO Survey

It is now becoming feasible to survey our Galaxy in the spectroscopic domain by directly observing a large, significant fraction of its stars. For this reason several large astrophysical surveys, supported by large international collaborations, have been designed to observe systematically the major components of our Galaxy.

In this chapter we describe the Gaia-ESO spectroscopic survey, of which we are members, and only briefly expand the discussion on other ongoing or planned spectroscopic surveys. The Gaia-ESO Survey¹, coordinated by the two Co-PIs Gerry Gilmore² and Sofia Randich³, is a public spectroscopic survey designed to target more than 10^5 stars belonging to the Milky Way, systematically covering its major components (from the halo to star forming regions), and stars in about 100 different OCs. It will provide the first homogeneous overview of the distributions of kinematics and detailed elemental abundances leaving an unprecedented legacy knowledge of the Galactic and stellar evolution. The project will complement the information from the Gaia satellite (Perryman et al., 2001), and the combination with the Gaia astrometry will quantify the formation history and evolution of young, mature and ancient Galactic populations.

3.1 Scientific Rationale

3.1.1 Gaia in a nutshell

Gaia (see the ESA website <http://sci.esa.int/gaia/>) is an ambitious ESA space mission that will produce a three dimensional map of the MW. Its core science is to measure the astrometric distances and proper motions of about 1 billion stars to $V \sim 20$ mag, mapping with unprecedented precision the 6 dimensional parameter space of position and velocity of astrophysical objects in our Galaxy and in the Local Group. Its data products will be μ as accuracy astrometry, optical spectrophotometry and medium resolution spectroscopy.

Distance, proper motion, and photometry will be obtained for stars brighter than magnitude $V \simeq 20$, medium-resolution spectra (used for RV determination and chemical abundances analysis, but the latter limited to the brightest objects) for most stars brighter than magnitude $V \simeq 17$. Gaia has been launched on December 19, 2013 toward the L2 Lagrange point of the Sun-Earth system, located 1.5 million km from the Earth in the anti-Sun direc-

¹Detailed description is available at www.gaia-eso.eu and in different papers (Gilmore et al. 2012, Randich & Gilmore 2013, and the related documents Gaia-ESO Survey proposal and management plan

²Institute of Astronomy, University of Cambridge, Madingley Road, Cambridge CB3 0HA, UK

³INAF-Osservatorio Astrofisico di Arcetri, Largo E. Fermi, 5, 50125 Firenze, Italy

Table 3.1: From Hipparcos to Gaia.

	Hipparcos	Gaia ^a
Magnitude limit	$V_{lim} = 12$	$V_{lim} = 20 - 22$ (blue-red sources, respectively)
N. of objects	1.2×10^5	$\geq 10^9$ (2.5×10^7 to $V = 15$, 2.5×10^8 to $V = 18$)
Quasars	none	$\sim 5 \times 10^5$
Galaxies	none	$\sim 10^6 - 10^7$
Astrom. accuracy	~ 1 mas	$\sim 7 - 10 \mu\text{as}$ at $V \leq 12$ $10 - 25 \mu\text{as}$ at $V = 15$, $100 - 300 \mu\text{as}$ at $V = 20$
Broad-band phot.	$2(B, V)$	3 (to V_{lim}) + 1 (to $V = 17$)
Spectrophotometry	none	2 bands (blue/red) to V_{lim}
Spectroscopy (CaT)	none	1-15 km s^{-1} to $V = 16 - 17$
Obs. programme	pre-selected targets	all-sky complete and unbiased

^aExpected Final Catalogue: 2020-22.

tion. The mission is planned for a 5-year long operational phase, which may be extended by one year. The first results are expected in 2016 and their precision, strongly depending on spectral type and magnitude, will be much better than the available determinations. For example, Gaia will reach a factor of ~ 100 better in astrometric accuracy with respect to the Hipparcos mission (see Tab. 3.1). The final full catalogue of the mission is planned for publication in 2021. Though revolutionary in determining distances, proper motions, and RV, Gaia cannot compete in the spectroscopic domain with ground-based instruments. For RV, its sensitiveness will be limited to 3 magnitudes brighter than for astrometric measurements, with a precision poorer than the proper motions determinations. For sources brighter than $V \sim 14$ mag the RV spectrometer will provide information also on rotation and chemistry, and combined with the prism spectra of the blue and red photometer will allow to obtain more detailed and accurate astrophysical parameters.

The Gaia-ESO Survey will be crucial to complement the information of Gaia, much improving the internal precision and robustness in determining the stellar parameters both in the phase-space (the Gaia-ESO Survey will provide RV measurements for stars fainter than $V \sim 17$, in this sense complementing the Gaia observations to its limit), atmospheric parameters, and elemental abundances domains. Even if the Gaia-ESO Survey sample is limited to 10^5 stars, much less than the 10^9 stars that Gaia will observe, for the objects in common it will be possible to have a complete and accurate study. For example, the combined Gaia and spectroscopic data set for the clusters will allow calibration of stellar evolutionary models, which will permit determination of ages and masses and will impact upon a number of fundamental issues like, for instance, the shape of the initial mass function and its universality, the timescale of star formation and star formation histories and largely improving the information on the chemical gradient in the disc of our Galaxy.

3.1.2 Spectroscopic survey

The fundamental questions of contemporary astrophysics that the Gaia-ESO Survey wants to investigate concern how disc galaxies form and evolve, and how their component stars and stellar populations form and evolve. Theoretical models of galaxy formation, which necessarily involve modelling star formation and stellar evolution, face challenging issues and require calibration to well-studied cases. Observations are indeed crucial for a comprehensive understanding of how stars and galaxies were formed and for investigating their actual

structure (Kormendy et al., 2010). Detailed examination of our Galaxy offers a unique privileged point of view on key processes otherwise poorly studied in extragalactic astronomy, while complementing the information from objects at high redshifts.

The Gaia-ESO survey will concentrate on the stars of the MW, and use them to understand the properties of different Galactic components and their evolution with time. Stars can be studied individually or as the smallest elements of more complex systems such as star clusters or galaxies. The information they carry has the potentiality to investigate different astrophysical aspects, fundamental to obtain a comprehensive panorama of the environment in which they live as well as their formation and evolution mechanisms. For example, dynamical interactions of stellar clusters, such as mergers events or cluster dissolution, can be inferred by detecting stellar streams from accurate phase-space positions. Correlations between the dynamical and chemical properties of field stars record the history of star formation and even the past dynamics of the disc. The kinematical structure of the Bulge as deduced from star kinematics would reveal information on its formation mechanism. Star clusters are fundamental astrophysical laboratories to better understand issues in stellar evolution models and in star formation processes. Moreover, they are reliable tracers of the properties and evolution of the Milky Way thin disc (see Ch. 1).

Outflows of various types disperse most of the gas of a cloud in which star formation occurs and the great majority of groups of young stars then quickly dissolve. The more populous groups survive the dispersal, as OCs and GCs, and a fraction of them (the less concentrated one, see Sec. 1.1.1) subsequently disperse through a combination of two-body scattering of other members of the group and tidal disturbance by the gravitational fields of external objects such as giant molecular clouds and spiral arms. Star clusters are a significant source of field stars, maybe the predominant source (even if this had been questioned, see Ch. 1). Among star clusters, the OCs are important to trace different thin disc components covering broad age and metallicity intervals, from a few Myr up to several Gyr, from $\sim 1/3$ to twice solar (see Ch. 1). Each cluster provides a snapshot of stellar evolution. Thus, observations of many clusters at different ages and chemical compositions quantifies stellar evolution, allowing increasingly detailed theoretical models to be tested.

New progresses in understanding the formation and evolution of the Galaxy and its component stars and populations require a statistically adequate sample of stars and OCs. Age, chemical abundances, and kinematics define the dimensions of the parameters space to be investigated. The number of objects required to determine the underlying probability density of objects grows rapidly with the dimensionality of the space. About 10^5 stars and $\sim 10^4$ stars in 100 OCs is the goal of the Gaia-ESO Survey in order to have a sufficient statistical power.

The Gaia-ESO Survey will support a wide variety of studies of stellar populations, the evolution of dynamical systems, and stellar evolution, along with detailed investigation of peculiar objects. In addition, by using as many as 10^4 lines of sight it is possible to aim at providing a full 3D tomography of the local ISM, based on analysis of line of sight extinction. Mass accretion from the circumstellar disc onto young pre-main sequence stars, triggered star formation scenarios, binary fraction as a function of mass and cluster environment, use of lithium both as an age tracer and for a detailed investigation of internal mixing processes in stars, tracing of the local velocity field and the Galactic rotation curve are all outstanding topics that can be investigated with the Gaia-ESO legacy. The large dataset of clusters star spectra will be of interest to the extragalactic community, allowing population studies in complex systems.

3.2 Technical aspects

The Gaia-ESO Survey is carried out on the Fibre Large Array Multi Element Spectrograph (FLAMES, Pasquini et al. 2002) at the Nasmyth focus of the Very Large Telescope (VLT) UT2. FLAMES is the multi-object, intermediate and high resolution fibre facility of the VLT. It offers a large corrected FoV (25 arcmin diameter) and consists of several components. In the following I will focus on the UVES and GIRAFFE spectrographs, the two instruments used within the Survey for spectroscopic observations.

UVES is the high-resolution spectrograph ($R = \frac{\lambda}{\Delta\lambda} \simeq 47000$). Eight single-object fibres are connected to the spectrograph, with an aperture on the sky of 1 arcsec. Only three standard UVES setups are offered, with central wavelengths of 520, 580, and 860 nm and about 200 nm of wavelength coverage.

GIRAFFE is a medium-high resolution spectrograph ($R \sim 6000 - 30000$) for the entire visible range (370–950 nm). It is equipped with two echelles for low and high resolution and uses interference order sorting filters to select the required spectral range within an order. The typical spectral coverage in one exposure is 60–100 nm in low resolution and 20–40 nm in high resolution. The fibre system feeding GIRAFFE consists of different components (see Pasquini et al. 2002 for details) and the one used within the Survey is the MEDUSA one. With MEDUSA is possible to observe 132 separate objects, including sky fibres, and each fibre has an aperture of 1.2 arcsec on the sky.

The Gaia-ESO Survey observations are obtained with both the GIRAFFE spectrograph and the UVES one. The FLAMES spectra are used to quantify individual elemental abundances in each star, to yield precise radial velocity, and map kinematic gradients and phase-space structure throughout the Galaxy. Tab. 3.2, taken from Bragaglia & collaborators (in preparation), gives a summary of the gratings used within the Gaia-ESO Survey for OCs, their characteristics, the kind of clusters (and stars within clusters) that will be observed with them, and the most important lines and elements visible in each. We recall that the field MW stars are instead observed with GIRAFFE setups HR10 and HR21 and UVES 580nm.

Table 3.2: Setups used for GIRAFFE and UVES observation of open clusters.

Setup	$\lambda\lambda$ (nm)	R	No fibres	Stars and clusters on which the setup is mainly used	Prominent lines and elements
UVES					
520	414-621	47000	6	early type stars	H γ , β , and see below the case of blue gratings
580	476-684	47000	8	late type stars	H α , Fe I and II, Fe-peak, α -elements, Na, [O I], Al, n-capture, Li
GIRAFFE					
HR03	403.3-420.1	24800	130	early-type st., young/massive cl.	H δ , He I, Si II and IV, O II, [Si II]
HR05A	434.0-458.7	18470	130	early-type st., young/massive cl.	He I and II, Si III, Mg II, N II and N III, O II
HR06	453.8-475.9	20350	130	early-type st., young/massive cl.	He I and II, Si IV, C III, N II and N III, O II
HR09B	514.3-535.6	25900	130	early-type st., all cl.	Mg b, Fe I and II, Ti II, Cr I and II S II, Mn II
HR14A	630.8-670.1	17740	130	early-type st., young/massive cl.	H α , He I and II, Si II, C II, Ti I, Ba II, TiO
HR15N	647.0-679.0	17000	130	late-type st., all cl.	H α , He I and II, Li, Fe I, Ca, Si, Mg, Ti I, Ba II, [S II], [N II], TiO, CaH

3.3 Observational strategy

The observational strategy is designed to survey the Galactic inner and outer bulge, inner and outer thin and thick discs, the halo and known halo streams. A considerable part of Gaia-ESO Survey observations is devoted to the study of a very large sample of OCs (about 40% of the time).

The VISTA⁴ catalogue and SkyMapper⁵ are the primary source catalogue for field stars. Main reference sources for OCs and their characteristics are WEBDA and DAML02. The 2MASS database and literature and private photometric catalogues are the reference sources for clusters targets selection⁶. These are precise, proven catalogues, ensuring that astrometric and photometric input data are of uniform and optimal quality. All the targets of the Survey are selected always on the basis of their photometric properties. For example, cuts in colour and magnitude are adopted to choose RC and TO stars and OCs' stars (in particular, OCs' stars are selected along the evolutionary sequences, see Sec. 3.4.1).

In order to survey the bulge, primary targets are K giants, including the RC. Iron-peak elements (Fe, Cr, Mn, Co, Ni), alpha elements (Mg, Si, Ca, Ti) and proton capture elements (Sc, V) will be measured with two different GIRAFFE setups (HR10, HR21).

For Halo/thick disc survey F+G stars are the main targets. The spectra will allow the measurements of both iron-peak and alpha elements. The fields are distributed in the whole sky, but predominately in the Galactic cap (SGC, NGC) regions, in order to minimise scheduling clashes with cluster targets and ensure southern and northern fields for scheduling, and photometric overlap with SDSS, PS1, and ESO/VST.

To study the thin disc dynamics several fields will be observed with candidate RC stars to $V \leq 19$ in the Galactic Plane to test spiral/bar dynamics.

About 5000 F,G-stars in the solar neighbourhood (extending beyond 1 kpc from the Sun) will be observed with UVES fibres, to quantify the local detailed elemental abundance distribution functions. The sample is photometrically selected to ensure all possible ages and metallicities for unevolved stars and subgiants samples.

In the case of OCs, the selection of clusters is meant to fine-sample the age-metallicity-distance-mass parameters space. Young clusters (age ≤ 100 Myr) and associations located in the solar vicinity (up to about 1.5 kpc, to enhance the Gaia connection and to be able to reach low mass cluster members) are crucial systems to understand the ongoing star formation (SF) processes and the recent SF history. The main effort, in young clusters and associations, is to obtain a complete and unbiased sample of cluster stars, for which accurate RVs -and possibly abundances- are measured; the strategy is then driven by the GIRAFFE observations. Massive-star clusters ($M \geq 8M_{\odot}$) are studied to understand young, massive, hot MS stars and their influence on the clusters. Knowledge of the kinematics of the massive stars is highly relevant to the cluster dynamics. They are also interesting objects in themselves as they put important constraints on stellar evolution models. Massive stars are furthermore important in determining Galactic abundance gradients: they are young and bright and can describe the recent chemical history of the disc covering large distances in the Galaxy. Intermediate-age and old clusters are valuable tools for the study of the for-

⁴The Visible and Infrared Survey Telescope for Astronomy is a 4-m class wide-field survey telescope equipped with an IR camera and located at ESO's Cerro Paranal Observatory in Chile (see Emerson et al., 2004; McMahon, 2012).

⁵SkyMapper (Keller et al., 2007) is a state-of-the-art automated wide field survey. SkyMapper's mission is to robotically create the first comprehensive digital survey of the entire southern sky. It is located at Siding Spring Observatory in northern New South Wales, Australia.

⁶For instance, we make use of the IPHAS/UVEX (Drew et al., 2005) and VPHAS+ (Drew, 2012) surveys of the Galactic plane.

mation and evolution of the Galactic disc and rare fossils of its past star formation history (see Ch. 1). The main effort for these OCs is the determination of precise chemical abundances, so emphasis is on the spectra of the relatively few stars observed with the UVES fibres. The UVES targets are chosen preferentially on the RC when it is present, to ensure the best homogeneity among different clusters. A secondary goal is to define cluster membership using the RVs obtained with the more numerous GIRAFFE fibres. A clean definition of the evolutionary sequences and especially of key features, is fundamental to derive distance and age through fit to stellar models. This unprecedented sample of stars of all evolutionary phases in clusters of different ages and chemical compositions will give important and stringent constraints to stellar evolutionary models. UVES observes bright stars selected among the most secure members (down to $V = 16.5$, i.e. the limit to obtain $\text{SNR} \sim 50$ in six hours), to be used for accurate abundance determination or for which better precision in RV is required. In the case of old clusters the main targets for UVES are RC stars, while red giant branch (RGB) stars are the second choice. In intermediate-age clusters also MS stars may be targeted. For young clusters, UVES targets are PMS stars and MS stars. In addition to the main targets, for nearby clusters we always try to observe some MS stars, for completeness and inter comparison. The selection of GIRAFFE targets is aimed at observing inclusive and unbiased samples of cluster star candidates rather than only high probability members. Targets are pre-main sequence (PMS) or MS stars (and some evolved stars in old open clusters), with $V \leq 19$, a good match to the Gaia satellite faint limit.

Considerable effort is dedicated to define calibration stars, clusters, special fields, CoRoT fields, stars which are Gaia calibrators, and more to ensure Gaia-ESO is optimally calibrated, and that other major surveys can be calibrated onto consistent parameter scales.

All relevant data in the ESO archive will be re-analysed within the Survey for abundance calibrations and as complementary data. For this reason the target selection is designed to have the maximum scientific outcome, in order not to re-observe objects for which spectra with the required set-up and SNR are already available.

In Fig. 3.1 the map of the fields observed so far is shown.

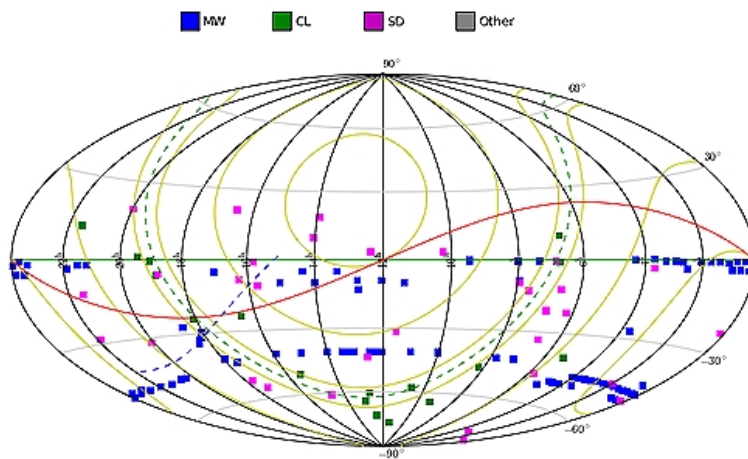


Figure 3.1: The map shows the observed targets of the Gaia-ESO Survey (situation on November 2013, provided by Cambridge Astronomy Survey Unit, CASU). Key: MW = Milky Way, CL = Cluster, SD = Standard. Reproduced from <http://www.gaia-eso.eu/>.

3.4 Survey consortium & organisation

The Gaia-ESO Survey is led by two Co-Principal Investigators, Gerry Gilmore (IoA, Cambridge) and Sofia Randich (INAF, Arcetri). They are the contact point with ESO and are assisted by a steering committee of 12 people. A set of 19 work packages is defined to match tasks requirements inside the Survey. Each working group (WG) has the responsibility of one specific assignment, to guarantee an efficient organisation of efforts and human resources. The tasks range on different technical aspects from the management of the on-site observations (WG0), to target selection and observing blocks (OB) preparation (WG1-4-6, see Bragaglia & collaborators in preparation for a description for the cluster part, and WG3-6 for the field star selection, see Gilmore & collaborators in preparation), data reduction and radial velocities (WG7 for UVES and GIRAFFE, see Sacco & collaborators in preparation), and finally spectral analysis (WG11, Smiljanic & collaborators in preparation and WG10 Recio-Blanco & collaborators in preparation, UVES and GIRAFFE analysis of F-G-K stars, respectively). Other WGs are devoted to more specific stars, such as the analysis of pre-main sequence (WG12) and hot stars (WG13), or of non-standard objects or to Information Technology such as the handling and storage of the data products of the survey. In Table 3.3 the WGs are listed with a brief description of their duties. Italy, and in particular the INAF-Osservatorio Astronomico di Bologna, is highly involved and leads two WGs: WG4 (A. Bragaglia) and WG5 (E. Pancino).

A schematic view of the Gaia-ESO Survey data flow process is shown in Fig. 3.2, where the vertical and transverse interplay of the tasks within the Survey are shown. I am part of WG4, WG10, and WG11, a detailed descriptions of which follows in the next paragraphs.

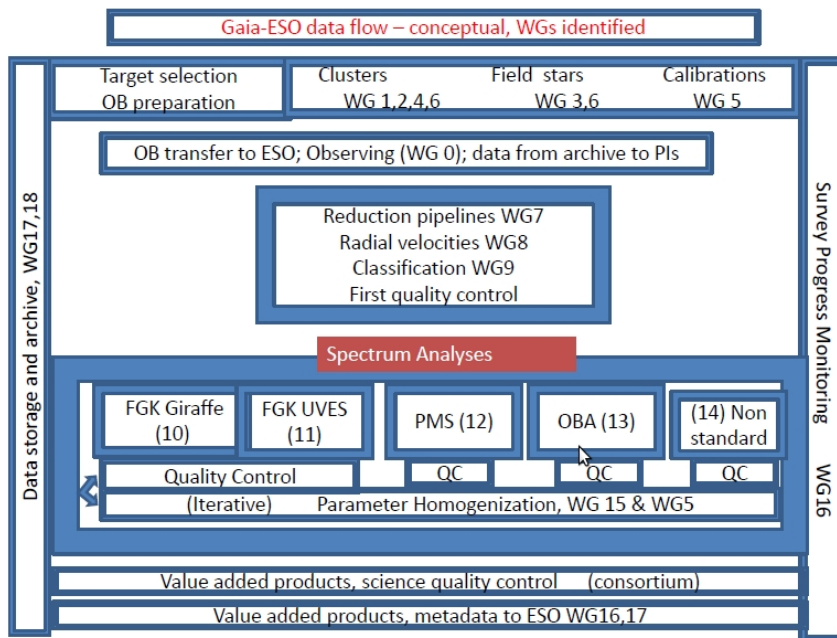


Figure 3.2: Data flow of the Gaia-ESO Survey. Reproduced from <http://www.gaia-eso.eu/>.

Table 3.3: List of the 19 WGs defined in the Gaia-ESO Survey with the main institutes involved and the WG coordinators.

Function	Contributing Groups	Coordinators
Survey Overview	Co-PIs	Gilmore, Randich
Management Overview	Steering Committee	12 members
Paranal Observations	WG0: ESO, Lund, MPiA, Padova	T. Bensby (Se)
Target selection, Calibrators, observing blocks		
Open Clusters: membership analysis auxiliary data target selection	WG1, 4: Alicante, Armagh, Torino, ETH, MSSL, Vienna, MPIA, Palermo, Barcelona, Granada, ZAH Bologna, Madrid (CAB), ESO, ESA, Geneva, Nice, AIP Herts, Arcetri, Uppsala, RO Belg, Leicester, Indiana, Graz, Lisbon, Grenoble, Keele, Catania, IAC, Athens, Exeter, Birmingham, Padova, Porto	E. Alfaro (Sp) E. Paunzen (At) A. Bragaglia (I)
Galactic Plane & Field Selection	WG3: Cambridge, ZAH, ANU, MPIA, Paris, RUG, AIP, MSSL, Strasbourg, Oxford	C. Babusiaux (Fr)
Calibrators & Standards	WG5: AAO, AIP, Uppsala, Cambridge, Bordeaux, Antwerp, Bologna, Madrid, Paris, MPA, ANU	E. Pancino (I)
OB/FPOSS generation: Field Survey Cluster Survey	WG6: Paris, ESO, Cambridge, Lund, AIP, ZAH, Arcetri, Bologna, Catania, Padova, Palermo, IAC, Exeter, Alicante, CAUP, ESO	T. Bensby (Se) E. Flaccomio (I)
Spectrum Extraction Pipelines		
Pipeline Raw Data: GIRAFFE Reduction UVES Reduction	WG7: CASU, Keele Arcetri	M. Irwin (UK) L. Morbidelli (I)
Radial Velocities	WG8: Cambridge, Keele, Arcetri, Antwerp, ZAH	Cambridge/Keele/ Arcetri
Discrete Classification	WG9: Cambridge, MPIA, IAC, Madrid, MSSL, Porto, ZAH	S. Koposov (UK)
Spectrum analyses		
FGK Stars: GIRAFFE	WG10: Paris, MPA, Lund, Uppsala, Nice, Bordeaux, Arcetri, Bologna, Liège, Geneva, Alicante, Nice, ESO, Porto, ZAH, Arcetri, Naples, Catania, Padova, Kaypten, IAC, ANU	A. Recio-Blanco (Fr) C. Allende Prieto (Sp)
FGK Stars: UVES	WG11: Paris, MPA, Lund, Uppsala, Nice, ZAH, Vilnius, Arcetri, ANU, Bologna, AIP, Bordeaux, Indiana, UCM, Herts, Groningen, ESO, Liège, Chile, Naples, Porto, Catania, Alicante, Padova, IAC	A. Korn (Se) R. Smiljanic (ESO)
WG10/11 Interface	Recio-Blanco, Allende Prieto, Pasquini, Smiljanic, Korn, Hill	
Pre-Main-Sequence stars	WG12: Arcetri, Catania, IAA, Naples, Palermo, ETH, CAUP, Keele, Exeter, Madrid (UCM, CAB)	A. Lanzafame (I)
OBA Stars	WG13: Liège, RO Belg, AIP, IAC, OMA, IAA, Madrid, Paris, Alicante, Uppsala, MPIA, Nice, ZAH, Leuven, Herts, Calar Alto, Armagh	R. Blomme (Be)
Unusual Objects	WG14: SRON, Nijmegen, Warwick, IAC, Leuven MPIA, Herts, IAC, ZAH	S. van Eck (Be)
Quality Control, Parameter Homogenization		
Survey Parameter Homogenisation	WG15 & WG5: all spectrum analysis groups	P. Francois (Fr)
Survey monitoring, database, archive		
Survey Progress	WG16: CASU	Co-PIs
Operational database & Phase 3	WG17: CASU/Cambridge	CASU
Survey Archive	WG18: AIP, RUG, Madrid, Vienna, ZAH, Edin	N. Hambly (UK)
Outreach	WG19: Cambridge	N. Walton (UK)

3.4.1 WG4: Cluster’s targets selection

WG4 selects the clusters targets. The selection of OCs follows the requirements described in Sec. 3.3, i.e. careful sampling of the parameter space defined by age, mass, distance, and metallicity. Only clusters with available photometry and stars position (to be brought to a common astrometric system) are retained. The target stars are selected following different criteria for UVES or GIRAFFE: for the former, the most secure members are chosen; for the latter, inclusive and unbiased samples of cluster star candidates rather than only high probability members. To optimise this condition all the available photometric catalogues are used (both in optical and infrared) together with additional information on kinematic whenever possible. For this reason a tight collaboration with WG1 (with the assignment of cluster membership analysis) is of primary value for the best selection. Once membership probability is assigned (the preliminary adopted rule is to give higher priority to stars closer to the cluster centre in the spatial plane and closer to the evolutionary sequences in the theoretical and observational planes) stars in all evolutionary phases are considered from late type stars (dwarfs in the lower MS) to giants in the RC and RGB phases. Among giants the highest priority is given to RC stars, which are usually clearly identified in the observational CMDs and are a strong signature of the stellar population⁷. In old clusters, UVES targets are observed with the 580nm setup and are preferentially RC stars. In clusters with bright early type stars, the 520nm setup is used. The GIRAFFE spectrograph is mainly used for MS (and PMS) stars. The choice of the setup depends on the spectral type. Late-type stars (late F, G, K, and M) are observed with the HR15N setup, to measure H α and Lithium abundance; early type stars, which are likely fast rotators, are observed with HR09B in old clusters and with several blue setups in young clusters (see Tab. 3.2 for details). In Fig. 3.3 we show an example of target selection for three representative cases: a very young cluster (γ Vel) with PMS, a young cluster with dominant hot, high mass stars (NGC 3293), and an old cluster with a well developed RC and RGB (Trumpler 20).

The case of Berkeley 81

In this section I describe the target selection I have performed for the old OC Berkeley 81 (about 1 Gyr) as an example of the tasks of WG4. Berkeley 81 is located toward the Galactic centre, hence it was chosen as descriptive of the inner disc (its Galactocentric distance is ~ 5.7 kpc, see Tab. 6.6). By using the photometric observations reported in Ch. 6, candidate targets were selected only inside a region twice as large as the cluster radius (the value of $2'.7$ taken from Sagar & Griffiths 1998 was adopted) and cuts in magnitude and colour along the RC and the MS phases were imposed. These phases were constrained from the match of theoretical isochrones that best characterise the evolutionary status of the cluster. UVES targets were chosen only among stars in the RC phase. In Fig. 3.4 the selection of candidate targets is shown.

While preparing the observing blocks for this cluster, in order to maximise the chance to observe cluster members with the UVES setup, available RV estimates of giant stars were exploited. The work done by Warren & Cole (2009) and observations taken with the WIYN telescope by E. Friel (private communication) were used for this purpose. The adopted UVES setup was the 580nm while for the GIRAFFE two different configurations were used: MS stars belonging to the upper MS (spectral type A) were observed with HR09B, while fainter stars (spectral type F) were observed with HR15N.

⁷Their selection has proven to be effective. So far, in almost all cases, the selection of RC stars showed very few outliers in chemical abundances or kinematic, reaching high efficiency in selecting cluster members at this stage.

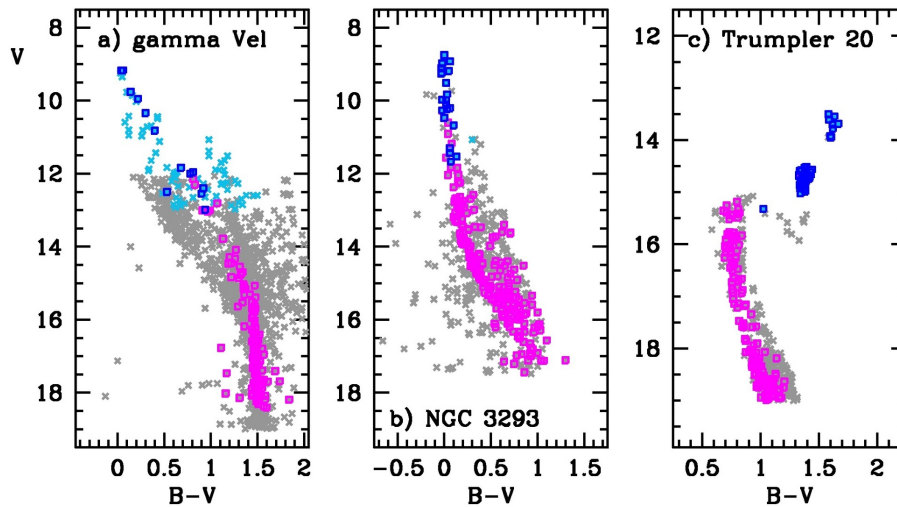


Figure 3.3: The target selections for three reference clusters are shown, as example. From left to right γ Vel, NGC 3293, and Trumpler 20 clusters. The grey and cyan crosses are respectively GIRAFFE and UVES targets. The blue and magenta squares are respectively UVES and GIRAFFE candidate clusters’ members. Reproduced from Bragaglia & collaborators (in preparation).

3.4.2 WG10 & WG11: spectral analysis

WG10 and WG11 are in charge of the abundance analysis of “normal”⁸ FGK stars observed respectively with GIRAFFE and UVES. The main tasks are to process observed spectra, refine astrophysical parameters, deliver elemental abundances to a level appropriate for the relevant stellar type and available SNR, and provide quality control. WG10 focuses on the more numerous intermediate resolution spectra obtained with GIRAFFE while WG11 focuses on high-resolution UVES spectra. The strength of the Survey strategy is that these analyses include a large collaboration among the majority of Europe’s spectra analysis groups. Each one of them has expertise on several standard and special-purpose analysis methodologies. The stellar atmosphere parameters and chemical abundances of the different groups (nodes) involved in the analysis in each WG are combined and homogenised to give a final set of recommended values (see, e.g. for WG11 Smiljanic & collaborators, in preparation).

The spectral analysis has a common ground. The same linelists, model atmospheres (1D MARCS models, Gustafsson et al. 2008), synthetic spectral grids, non-LTE and 3D abundance corrections are adopted. The linelists (containing atomic and molecular data, e.g. *gf*-values and broadening constants) are defined to be adequate for the different categories of targets and spectral intervals, taking into account the resolution of the spectra. They are compiled and distributed among WGs prior the analysis to ensure homogeneity in the derived quantities.

The final products of both WGs are EWs, atmospheric parameters, and elemental abundances for several elements. Final atmospheric parameters and elemental abundances are calculated using EWs and via fits to synthetic spectra. Realistic typical errors for stellar pa-

⁸Cool pre-main sequence stars, O, B, A stars, and non-standard objects are analysed respectively by WG12,13, and 14.

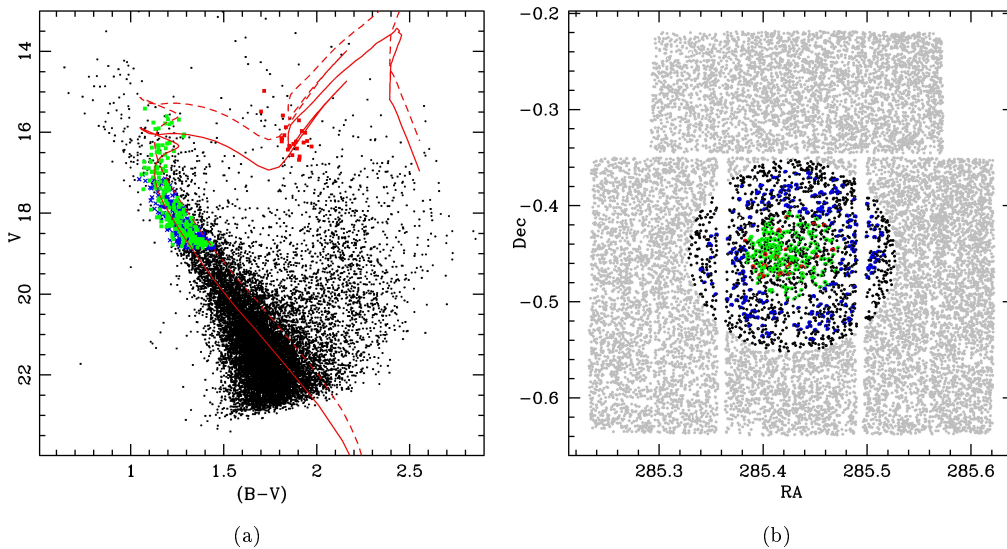


Figure 3.4: Candidate targets selection for the old OC Be 81. (a) CMD obtained using data (black) inside $6'.0$ radius. In red the selected RC stars; in green and blue the selected MS stars. The best-fit isochrone and the sequence of binaries are overlaid to the CMD. (b) LBC@LBT observed region (approximately $23' \times 25'$). In red the RC stars selected inside one cluster’s radius; in green and blue the MS stars selected inside one and two times the cluster’s radius respectively. In black: stars inside 6.0 arcmin.

parameters and abundances derived for the UVES spectra are $\Delta(T_{eff}) \sim 100K$, $\Delta(\log g) \sim 0.2$, $\Delta([Fe/H]) \sim 0.1$ and $\Delta([X/Fe]) \sim 0.1$. However, uncertainties may vary quite significantly from star to star and from element to element. The GIRAFFE errors will typically be ~ 0.15 for $[Fe/H]$ and $[X/Fe]$, and $\sim 0.1 - 0.3$ for Li. Cluster mean values are in principle much smaller.

In this context, WG15 & WG5 are in charge of ensuring that the data products generated by the spectrum analyses are coherent, the resulting stellar atmospheric parameters and abundances homogeneous, the parameters are calibrated onto an identified (set of) external calibrator objects. This homogenisation process is a key aspect of analysis quality control.

I am part of the EPInArBo node, dedicated to the spectral analyses of UVES and GIRAFFE targets within the WG10 and WG11. The EPInArBo node is a collaboration of several people from different institutes (the European Southern Observatory, the INAF Observatories of Padova, Bologna, and Arcetri, Italy, and the University of Indiana, USA).

3.5 Other Surveys

The Gaia-ESO Survey is at the moment the only ongoing survey measuring precise kinematics and stellar elemental abundances for a large sample of stars using high-resolution optical spectra. There are several ongoing surveys with similar scientific goals though different in technical characteristics and approaches. Some use low-resolution, or narrow wavelength ranges, for kinematics and approximate “metallicity”. Others use HRS but in completely different spectral domains (IR, as APOGEE) or with a very different constraint on magnitude limits (as GALAH). Several photometric surveys are also underway or planned (like

those at the VISTA and VST telescopes⁹ and SkyMapper) and will deliver valuable data complementary to spectroscopy.

For the future, the coordination of all these efforts will allow to obtain a comprehensive information, forming an unprecedented legacy for the study of our Galaxy. Since all surveys cover partially different sources with different methods, it is important to understand how well the surveys can be combined, to enhance their effectiveness. This can be obtained by selecting common targets in order to effectively exploit scientific results on the same reference frame. First steps toward this inter-surveys collaboration have already been made, but the process is delicate. A list of the main spectroscopic surveys with a brief description of their aims and technical aspects follows.

- **SDSS I, II, & III:** carried out on a telescope of 2.5 m of diameter, located in the northern hemisphere (New Mexico, USA). SDSS (Sloan Digital Sky Survey) has published some 250 thousand spectra ($R \sim 2000$) providing RV with accuracy to $\sim 10\text{-}20$ km s⁻¹, and [Fe/H] abundances good to ~ 0.25 dex for stars with $14 \leq r \leq 19$. These studies complement the SDSS photometric analyses. SDSS spectra have provided only very limited information on the substructures prominent in the SDSS photometry, due to low precision and sparse spatial sampling. SDSS3 stellar spectroscopy continues, at ~ 5 stars/deg². www.sdss3.org/
- **SDSS-APOGEE:** carried out on the same SDSS telescope facilities in the IR wavelength range. APOGEE, Apache Point Observatory Galactic Evolution Experiment, is a survey of Galactic stellar populations, started in 2012, aimed at obtaining high resolution ($R = 30000$), high SNR (~ 100) spectra in the H band (1.5-1.7 microns) for 10^5 stars, primarily G-M giants, with $11 \leq H \leq 14$. APOGEE will study 50 high latitude Galactic halo fields, 65 bulge fields, and 110 low latitude disc fields, including 30 ‘key calibrator’ and some 200 other star clusters. www.sdss3.org/apogee.php
- **UKST-RAVE:** it used 1.2 m UK Schmidt Telescope of Anglo-Australian Observatory. RAVE, RAdial Velocity Experiment, is a multi-fibre spectroscopic astronomical survey of stars in the MW and its primary aim is to derive the RV of stars from the observed spectra. RAVE has obtained accurate RVs (≤ 5 km/s) by using the same CaT window used by Gaia, but additional information, such as effective temperature, surface gravity, metallicity, photometric parallax and elemental abundance data for the stars, are provided too. It targets $\sim 5 \cdot 10^5$ stars in the magnitude limit range $9 \leq I \leq 13$. www.rave-survey.aip.de/rave/
- **LAMOST:** carried out on a 4 m class telescope in the North hemisphere (China). LEAGUE, LAMOST Experiment for Galactic Understanding and Exploration, and LEGAS, LAMOST ExtraGalactic Surveys, are two surveys both carried out at LAMOST (Large sky Area Multi-Object Spectroscopic Telescope) started in September 2012. LAMOST operates at SDSS resolution ($R \sim 2000$) and is designed to take 4000 spectra in a single exposure. It will be able to observe very large numbers of northern targets, including clusters, at intermediate magnitudes to estimate RVs. www.lamost.org
- **GALAH:** will be shortly carried out at the Anglo-Australian Telescope, a 4 m class telescope set in the southern hemisphere. GALAH, acronym which stands for Galactic Archaeology with HERMES, is the primary science driver for the HERMES instrument, a high resolution fibre-fed multi-object spectrometer. It has four non-contiguous

⁹See the ESO website <http://www.eso.org/public/teles-instr/surveytelescopes/> for details.

spectral bands, covering a total of approximately 100 nm between about 470 nm and 790 nm with two resolution modes ($R = 28000$ and $R = 50000$). GALAH aims at obtaining precision multi-element abundances for about 10^6 stars with $V \leq 14$, from high SNR. <http://www.mso.anu.edu.au/galah/home.html>

- **WOCS:** the WIYN Open cluster study is a survey carried out at the WIYN 3.5 m telescope to obtain comprehensive photometric, astrometric, and spectroscopic data for a small number (~ 10) of nearby key clusters (see Ch. 2).

Other surveys are planned for the future, on dedicated facilities. In particular, ESO will host two very high multiplexing high-resolution instruments: MOONS on the VLT and 4MOST on the VISTA telescope. Technical details and a description of the science goals can be found in Cirasuolo et al. (2012) and in de Jong et al. (2012) respectively for MOONS and 4MOST. In the northern hemisphere, a new wide-field multi-object spectrograph for the William Herschel Telescope (4.2 m telescope at the Observatorio del Roque de los Muchachos, on La Palma in the Canary Islands) called WEAVE is planned (see Balcells et al., 2010). It will allow astronomers to take spectra of up to 1000 stars and galaxies in a single exposure. WEAVE will measure the speeds of about one million of the stars mapped by GAIA.

Chapter 4

Photometric study

In this chapter we describe the photometric analysis methods adopted within the BOCCE project (see Ch. 2) and applied to study 10 OCs that are now part of the BOCCE database: Berkeley 27 (Be 27 or Biurakan 11), Berkeley 34 (Be 34 or Biurakan 13), Berkeley 36 (Be 36), NGC 2849, and NGC 6134 are presented in Ch. 5; Berkeley 81 (Be 81), NGC 1817, NGC 2141, plus NGC 2158 and Trumpler 5 are presented in Ch. 6. The first 8 are part of three different scientific papers, Donati et al. (2012), Ahumada et al. (2013), and Donati et al. (2014a), while the last 2 are under study. They have been selected because they are old (older than 0.5 Gyr) and because their position is particularly interesting for studying the metallicity gradient of the Galactic disc. One of them (Be 81) is located toward the Galactic centre, at a Galactocentric distance $R_{GC} \sim 6$ kpc, while the others are set in the outer part at about $R_{GC} \sim 10$ kpc (where the transition of the metallicity gradient is claimed to be) or at larger distances (as Be 34) thus making possible to enlarge the information of the BOCCE database on the whole range of Galactocentric distances. This way we not only gain a larger statistic in the metallicity-Galactocentric distance plane, but also obtain information for a study of the local disc.

One key-aspect of the BOCCE project is homogeneity (see Ch. 2). This implies that the data analysis is always performed using the same methodology. The cluster parameters (namely age, distance, Galactic reddening, and approximate metallicity) and characteristics (percentage of binary systems, differential reddening) are obtained through a detailed analysis of the photometry by using the synthetic colour-magnitude diagram (sCMD, see Sec. 4.2) technique. Accurate metallicity is instead obtained through high resolution spectroscopy of cluster stars. In the following sections we describe in detail the photometric analysis on which most of this thesis work is based on.

4.1 Photometric analysis - DAOPHOT

For each OC we have scientific frames in different filters (usually in B , V , and I , sometimes also in U) and for different exposure times to sufficiently cover the whole magnitude range of the cluster stars. The short exposures are fundamental for precise photometry of bright stars while the fainter stars of the lower MS are recovered with the long exposures. The source detection and relative photometry of each observed frame is performed independently on each B , V , and I image, using the PSF-fitting code DAOPHOTII/ALLSTAR Stetson (1987, 1994). DAOPHOT is a programme widely used by the astrophysical community which is able to automatically analyse the photometric images of star-like objects,

requiring a minimal human intervention. The PSF-model on each scientific frame is derived independently allowing the code to find the best solution. A standard iterative process is adopted: star-like object with counts lower than the saturation regime but higher than a certain threshold (usually about 10 sigma above the background level but depending on the object and the photometric quality of the images) are retained for the PSF analysis. In the next iterations neighbour stars or bad cases (extended objects or stars with bad pixels) are discarded from the analysis and subtracted from the image using the preliminary PSF model. This means that at each iteration the PSF analysis improves its quality because defects or noise sources are statistically taken into account. The procedure stops when convergence is reached. Once the best PSF is found then all the detected sources on the frames are evaluated with the same PSF model. DAOPHOT is used also for aperture photometry to compute aperture corrections to the PSF-fitting photometry.

The robustness of the programme allows its exploitation in automated routines for the artificial star experiment and guarantees the homogeneity required by the project.

4.2 The synthetic CMD technique

For a better understanding of the observational CMD diagrams in terms of a combination of the various effects which shape their morphology (e.g. stellar evolution, field contamination, photometric errors, completeness of the photometric data set, differential reddening, and binaries), we use the sCMD technique. As described in Tosi et al. (1991) and Bragaglia & Tosi (2006), this technique consists in a numerical MonteCarlo code which simulates the HR diagram of a composite stellar population through random extractions of mass-age pairs according to an assumed Initial Mass Function (IMF), Star Formation (SF) law, and time interval of the SF activity. The OCs can be considered simple stellar populations. Consequently, a single burst lasting 5 Myr (i.e., approximately an instantaneous burst relative to the age of most of the studied clusters) with a homogeneous chemical composition are considered. Each extracted synthetic star is placed in the CMD by a suitable interpolation from the adopted stellar evolution tracks and adopting the Bessell et al. (1998) tables for photometric conversion to the relevant arbitrary, but reasonable, photometric system. The absolute magnitude is converted to a provisional apparent magnitude by applying (arbitrary) reddening and distance modulus. The synthetic stars extracted for any provisional magnitude and photometric band are assigned the photometric error derived for the actual stars of the same apparent magnitude. Then, they are randomly retained or rejected on the basis of the incompleteness factors of the actual data, derived from extensive artificial star tests (see Sec. 4.3).

Once the number of objects populating the whole CMD or portions of it are equal to the observed ones, the procedure is stopped. In this process the contamination of field stars is taken into account, i.e. the adopted number of cluster stars for the simulation is the number of stars in the cluster field corrected for the number of stars in an external field. For this reason an accurate photometry of a comparison field is required to better understand the CMD diagrams. The goodness of the model predictions is obtained thorough comparison with the observational LFs, the overall morphology of the observational CMD, the star counts at particular evolutionary phases (the main sequence turn-off, MSTO, the “red hook”, RH, the Main Sequence Termination Point, MSTP, the RGB, the base of the RGB, BRGB, and the RC). The most valuable age indicator are the Turn Off (TO) point, that is the bluest point after the over-all contraction, and the RC luminosity; however, at least in the case of OCs, these phases may be very poorly populated, and identifying them is not a

trivial game, especially if a strong field stars contamination is present. A model can be considered satisfactory when it can reproduce all the feature of the observational LFs and CMDs. However, due to the uncertainties on the photometry and the theoretical parameters (stellar evolutionary tracks) and to the intrinsic variability of the field contamination, the precision of the method is limited by the quality of the data and cannot provide strictly unique results. The degeneracy of the parameters causes several different solutions to be satisfactory within the errors, nevertheless our method allows to significantly reduce the range of acceptable parameters.

In this way we derive age, distance, and reddening of the cluster and indicate the metallicity of the evolutionary models which is in better agreement with the data. If multi-filter photometry is available it is possible to better discriminate models with different metallicity, since only models of the right metallicity can fit the observed CMDs in all passbands (see Tosi et al., 2007). In principle, the metallicity of the best-fit model should be indicative of the cluster metallicity, but this depends significantly on some of the stellar models assumptions, such as opacity, chemical mixture, solar abundances, etc.

A quantitative estimation of unresolved binary systems can be obtained with this method. The synthetic CMDs can be generated assuming that all the synthetic stars are single objects or that a (arbitrary) fraction of them are member of binary systems with random mass ratio. The effect of unresolved binary systems on the V magnitude and $B - V$ colour was first addressed by Maeder (1974) and more recently discussed by Hurley & Tout (1998). Bragaglia & Tosi (2006) recalculated the effect of unresolved binaries using the Padova isochrones (Bertelli et al., 1994). Their figure 4, which is reported here in Fig. 4.1, shows the magnitude and colour variations of MS objects of solar metallicity as a function of the mass ratio between the secondary and the primary component of the unresolved system. Again, the comparison of the resulting morphology and thickness of the synthetic MSs of each cluster with the observed ones allows to derive information on its most likely fraction of binaries¹.

With the sCMD it is possible to constrain the differential reddening on the cluster face². The net effect of the differential reddening is to spread the CMD sequences along the reddening vector direction, thickening their appearance. The sCMD technique must consider it as an additional parameter for an accurate analysis of the observations.

The advantage of the synthetic CMD method with respect to a classical isochrone fitting to derive the cluster parameters is evident. With the synthetic CMD the number of stars predicted by the adopted stellar tracks in each evolutionary phase (directly related to the stellar lifetimes in that phase), the effects of the photometry (errors, incompleteness), and other factors (unresolved binaries, differential reddening) on the morphology and spread of the various CMD sequences are taken into account. This clearly provides a larger number of constraints and leads to a better selection of the solution, if not to its uniqueness. For instance, an isochrone may appear to well fit the data, but then the corresponding distribution of the number of stars on the MS or at its TO may be completely at odds with the empirical ones, and the case must be rejected or be given a lower ranking with respect to other models (see Kalirai & Tosi, 2004). This could happen quite often when studying OCs which usually are loosely populated and with relevant field contamination. In

¹Whenever possible (e.g. in case of precise photometry) a quantitative estimation of binaries is performed with a statistical method in order to reduce the parameter space explored with the sCMD. The general method consists in counting the observed stars which lie on and off the MS in the empirical CMD and then compare with a blank field to get a rough estimate of the binary fraction (see Ch. 5 and 6 for details).

²If deep and precise photometry is available, the differential reddening can be quantified statistically comparing the MS stars' colours and magnitudes as a function of their spatial location (see Ch.6 for details), thus reducing the parameters to be estimated with the sCMD technique.

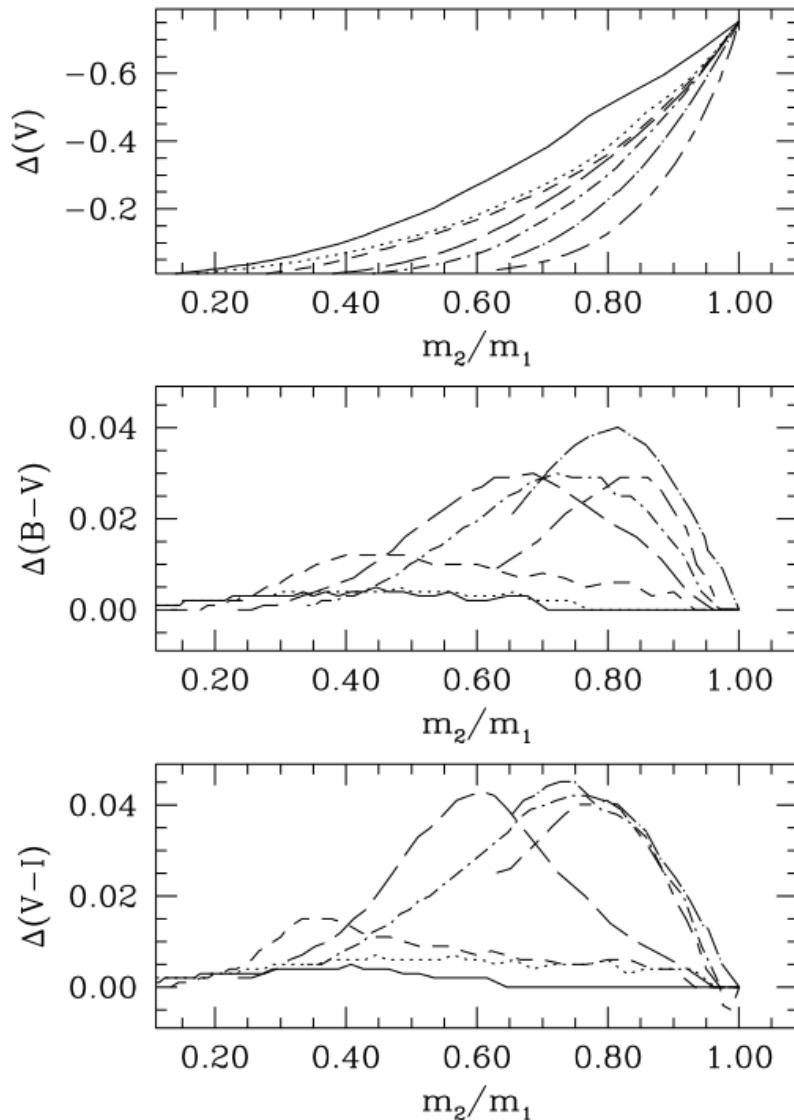


Figure 4.1: Effect of unresolved binaries on the apparent magnitude and colour as a function of the mass ratio between the secondary and primary component of the system and for various masses of the primary star. Line symbols refer to primaries of different initial mass (in the range $26\text{--}0.95M_{\odot}$). The shown variations refer to solar-metallicity MS stars from the Padova isochrones (Bertelli et al., 1994). Reproduced from Bragaglia & Tosi (2006).

such conditions the synthetic CMD technique is much more effective and accurate than the isochrone fitting method.

Different sets of evolutionary tracks are considered to test the effect of different input physics on the derived parameters. Several synthetic CMDs are simulated for each cluster, one for each adopted stellar evolutionary model. The three types of stellar models applied to all clusters are the tracks of Ventura et al. (1998) (hereafter FST models) with high ($\eta = 0.03$), moderate ($\eta = 0.02$), and no overshooting ($\eta = 0.0$); the tracks of the Padova group (Bressan et al., 1993; Fagotto et al., 1994, hereafter BBC) with overshooting; and the tracks of the Frascati group (hereafter the FRA models; Dominguez et al., 1999) with

no overshooting. All the results in the BOCCE project and presented here are obtained consistently using the same version of the FST, FRA, and BBC models quoted above. Updating the analyses by using more recent models is feasible but it must be extended to all the OC sample for maintaining the homogeneity.

The solar-metallicity considered for tracks throughout BOCCE is $Z=0.02$, because they are the ones calibrated by their authors on the Sun, independently of the circumstance that nowadays the actual solar metallicity is suggested to be lower (Asplund et al., 2009). All models assume that the stars were formed following a single slope ($x=1.35$) Salpeter IMF over the whole mass range covered by the adopted tracks (generally $0.6-100 M_{\odot}$). The single-burst SF and these simplistic assumptions on the IMF do not affect the results, as demonstrated by several checks made within BOCCE assuming both different burst durations and different IMFs.

4.3 The artificial star experiment

Synthetically reproducing the complete process of photometric measurements is the only way to properly characterise the final photometric catalogue in terms of internal error and level of completeness. The photometric error contributes in spreading the CMD sequences while the completeness analysis quantifies the efficiency of the data reduction procedure in the identification of star-like objects at different magnitude level. In order to obtain an accurate comparison with the observational CMDs, the sCMD technique takes into account these “instrumental” effects. While limiting the precision of the analysis they could lead to misinterpretation if underestimated. In the present context a large number of artificial star experiments are crucial. For each frame centred on the clusters the adopted procedure for the artificial star experiments, is the following:

1. A ridge line covering the whole range of magnitudes in the CMDs is defined by visual inspection

2. The V magnitude of artificial stars is randomly extracted from a V Luminosity Function (LF) modelled to reproduce the observed LF for bright stars and to provide large numbers of faint stars down to below the detection limits of our observations. We need to simulate a large number of stars in the range of magnitude where significant losses due to incompleteness are expected in order to have a robust statistic. Furthermore, the actual choice of the LF of the artificial stars is not important in the present case since we want to quantify how efficient is the photometric measurement. At each extracted V magnitude the correct B and I magnitudes are determined by interpolation on the cluster ridge line. Thus the (input) artificial stars lie all on the cluster ridge line on the CMDs.

3. It is of the utmost importance that the artificial stars do not interfere with each other, since in that case the output of the experiments would be biased by artificial crowding, not present in the original frame. To avoid this potentially serious bias we divide the frames into grids of cells of known width (about 60 pixels but depending on the crowding level of the field and in order to have a fraction of artificial stars not exceeding the 20% of real stars) and we randomly position only one artificial star per cell for each run. In addition, we constrain each artificial star to have a minimum distance (about 20 pixels or at least three times the FWHM) from the edges of the cell. In this way we can control the minimum distance between adjacent artificial stars. At each run the absolute position of the grid is randomly changed in a way that, after a large number of experiments, the stars are uniformly distributed in coordinates.

4. The stars are simulated with the DAOPHOT PSF model for the fit, including any

spatial variation of the shape of the PSF, and are added on the original frame. Each star is added to the B , V , and I single long-exposure frames (we are confident to have 100% completeness for bright magnitudes). The measurement process is repeated in the exactly same way as the original measures.

5. The simulations are repeated until the desired total number of artificial stars is reached. The final result is a list containing the input and output values of positions (X , Y) and magnitudes (B , V , I).

Depending on the case, tens to hundreds of thousand artificial stars are produced for each frame. We only focus on the frames centred on the clusters, assuming the same results hold for the other frame. Even if this could be a simplistic assumption it is sufficient in the case of the OCs, where the crowding is not dramatic, as for example in GCs, even for the central frames. The whole procedure is driven by an automated pipeline taking advantage of the large degree of automation of DAOPHOT. In Fig. 4.2 we show an example of the results obtained by such an experiment: the differences between input magnitudes and output magnitudes are reported as a function of input magnitude for the artificial stars simulated and recovered in the case of NGC 2141 chosen as an example case.

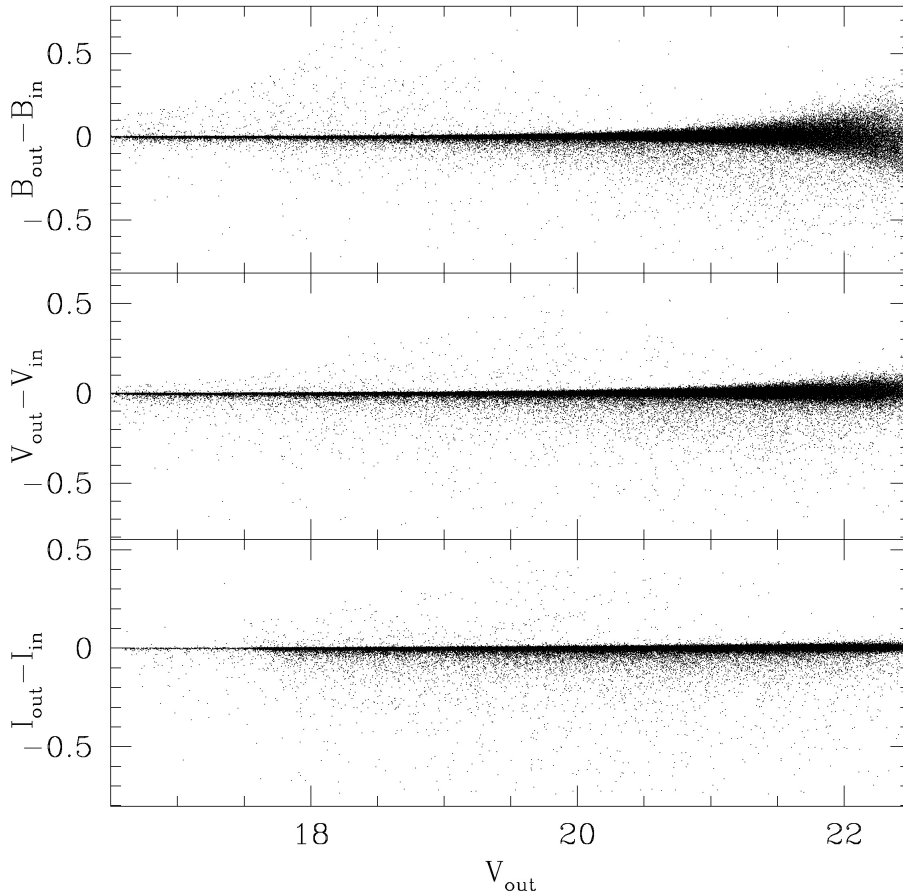


Figure 4.2: Differences between the input and output magnitudes of the artificial stars versus output V magnitudes for the B (top panel), V (middle panel), and I (bottom panel) passbands, for the observations of NGC 2141 (see Ch. 6 for details).

About 250000 stars were simulated in this case and about 150000 were recovered. The plots show that our measures are very accurate: for instance, the average $\sigma(B_{out} - B_{in})$, $\sigma(V_{out} - V_{in})$ and $\sigma(I_{out} - I_{in})$ are lower than 0.05 mag for $V_{out} < 23$. The distributions of magnitude differences are not symmetrical: there is an almost uniform cloud of stars in the lower half of each plot. These stars have been recovered with a significantly brighter magnitude than that assigned in input. They are the artificial stars that blended with real stars of similar (or larger) brightness. The points in the upper half, instead, are probably due to less accurate PSF fitting and are due to stars recovered fainter than the input value.

Chapter 5

Five Open Clusters on a small FoV

This chapter describes the photometric analysis for five OCs of the BOCCE project studied during my thesis. Be 27, Be 34, Be 36, NGC 2849, and NGC 6134 are old OCs, all observed with small FoV at ESO telescopes, and important to trace the properties of the early epochs of the disc evolution. The results obtained for Be 27, Be 34, and Be 36 are published in Donati et al. (2012) and the ones obtained for NGC 2849 and NGC 6134 in Ahumada et al. (2013).

5.1 Be 27, Be 34, Be 36

The three clusters Be 27 (with Galactic coordinates $l = 207.8^\circ, b = 2.6^\circ$), Be 34 ($l = 214.2^\circ, b = 1.9^\circ$), and Be 36 ($l = 227.5^\circ, b = -0.6^\circ$) are all located in the anti-centre direction, very close to the Galactic plane and have an age older than 1 Gyr. They were chosen because they all lie beyond a Galactocentric distance of 10 kpc, hence they can be useful to understand the properties of the outer disc. In particular they are located in the region where the radial metallicity distribution changes its slope and where more clusters should be studied to better understand why this happens (see, e.g., Sestito et al. 2008; Friel et al. 2010; Andreuzzi et al. 2011; Lépine et al. 2011). These OCs have already been studied to different degrees in the past: the resulting parameters sometimes agree with each other and sometimes not. We present here their *BVI* photometry, used to improve upon previous determinations of their parameters using the sCMD.

All three clusters have been studied by Hasegawa et al. (2004) as part of a survey of 14 anti-centre clusters; they obtained *BVI* photometry with a 0.65-m telescope. Be 27 has also been studied by Carraro & Costa (2007) using *VI* photometry acquired at a 0.9-m telescope. Be 34 and Be 36 have been observed also by Ortolani et al. (2005) at a 3.5-m telescope using the *BV* filters. As we will see in detail in next section, our data are then superior in filter coverage and/or telescope used. In all the three papers, the clusters parameters have been derived using isochrone fitting and their results are summarised in Tab. 5.1.

5.1.1 The Data

Observations

The three clusters were observed in service mode at the ESO 3.58-metre New Technology Telescope (NTT) of the La Silla Observatory (Chile) with the instrument SUp erb Seeing Imager (SUSI2) in 2005 and 2006. The instrument was composed by a mosaic of two EEV

Table 5.1: Literature values for the clusters Be 27, Be 34, and Be 36

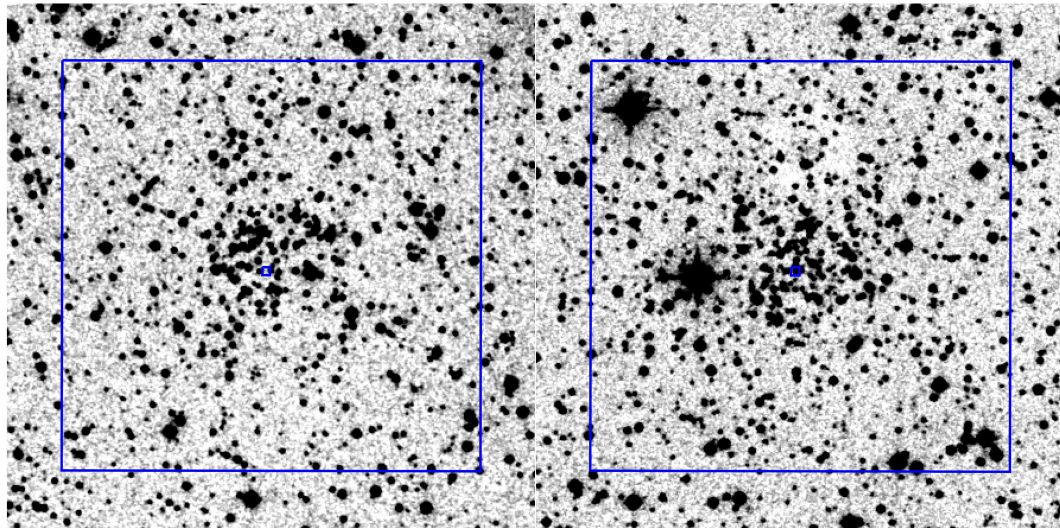
Cluster	E(B-V)	$(m - M)_0$	age (Gyr)	metallicity	Reference
Be 27/Biu 11	0.24	14.25	2	$Z = 0.03$	Hasegawa et al. (2004)
	0.35	14.30	2	$Z = 0.02$	Carraro & Costa (2007)
Be 34/Biu 13	0.48	15.80	2.8	$Z = 0.02$	Hasegawa et al. (2004)
	0.30/0.41	15.4/15.62	2.3/2.3	$Z = 0.02/0.008$	Ortolani et al. (2005)
Be 36	0.44	15.30	3.4	$Z = 0.02$	Hasegawa et al. (2004)
	0.250.36	14.70/14.85	4/4	$Z = 0.02/0.008$	Ortolani et al. (2005)

CCDs (2048×4096 pixels) placed in a row. The field of view (FoV) of SUSI2 is equivalent to 5.5×5.5 arcmin², with a pixel scale of 0.085 arcsec pixel⁻¹; for these observations the instrument was set in the 2×2 binned mode (pixel scale 0.161 arcsec). The data were collected with the B, V, and I Bessel filters. The clusters were positioned at the geometric centre of the mosaic with the rotator in the default position; two of them were also observed with the instrument rotated 90 deg clockwise in order to recover stars falling in the mosaic gap. Digitized Sky Survey (DSS) images of the SUSI2 FoV for the pointings of Be 27, Be 34, and Be 36 are shown in Fig. 5.1. The observations log-book for the three clusters is presented in Tab. 5.2. Comparison fields were also observed for decontamination purposes, located 30 arcmin away from the cluster centre (see Tab. 5.2). The seeing was below $1.5''$ for all images and below $1''$ for many. For each cluster observations in photometric condition were obtained which allowed a proper calibration using the photometric standard fields SA98, SA101-262, PG0918, and RU152 (Landolt, 1992).

Table 5.2: Log of observations.

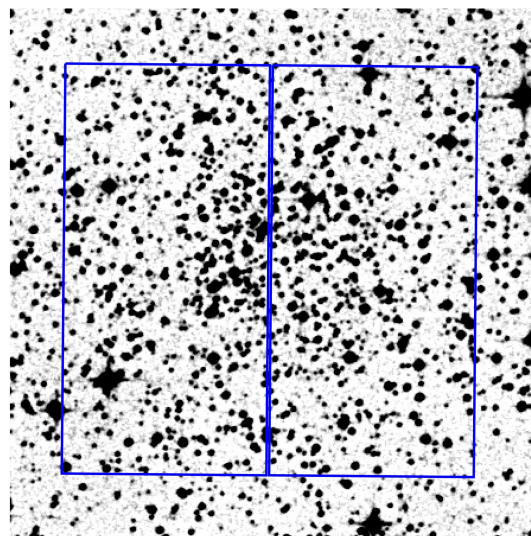
Cluster	RA (J2000)	Dec (J2000)	Date	Rot*	B exptime	V exptime	I exptime
Be 27	6 51 21	+05 46 00	Nov, 29 2005	a	10s, 44s, 540s	5s, 270s	5s, 270s
				b	10s, 540s	5s, 270s	5s, 270s
			Feb, 19 2006	a	50s, 100s	50s, 50s	50s, 50s
				b	100s	50s	50s
Be 27 ext	6 51 21	+05 18 00	Nov, 29 2005	a	2×10 s, 560s	5s, 280s	5s, 280s
			Feb, 19 2006	a	100s	50s	50s
Be 34	7 00 23	-00 14 11	Nov, 29 2005	b	10s, 103s, 540s	5s, 270s	5s, 270s
			Jan, 26 2006	a	10s, 540s	2×5 s, 270s	2×5 s, 270s
				b	4×10 s, 2×540 s	4×5 s, 2×270 s	4×5 s, 2×270 s
			Feb, 24 2006	a	100s	50s	50s
b	100s	50s		50s			
Be 34 ext	7 00 23	-00 50 11	Nov, 29 2005	a	10s, 77s, 560s	5s, 280s	5s, 280s
			Feb, 24 2006	a	100s	50s	50s
Be 36	7 16 24	-13 11 50	Jan, 26 2006	a	10s, 540s	5s, 270s	2×5 s, 270s
			Feb, 25 2006	a	100s	50s	50s
			Mar, 20 2006	a	100s	50s	50s
Be 36 ext	7 16 24	-13 42 00	Jan, 26 2006	a	10s, 560s	5s, 280s	5s, 280s
			Feb, 25 2006	a	100s	50s	50s
			Mar, 20 2006	a	100s	50s	50s

* Angle of the rotator: “a” means default position, “b” means 90 deg clockwise.



(a) Be 27

(b) Be 34



(c) Be 36

Figure 5.1: DSS image of the FoVs centred on the clusters. The box is the composite FoV of SUSI2 obtained with the rotator in different positions: only the stars inside the smaller central box in (a) and (b) fell in the mosaic gap. In case (c), only the default orientation was used and the FoV has a gap apparent in the figure.

Data reduction

Bias and flat field corrections were done using a standard analysis with IRAF¹. The source detection and relative photometry were performed independently on each B, V, and I image, using the PSF-fitting code DAOPHOTII/ALLSTAR. For each frame a sample (20 to 70) of isolated and bright stars was selected to compute the PSF. The profile-fitting algorithm determines a spatially variable PSF to include a quadratic dependence on the x and y coordinates in order to minimise geometrical distortion biases. Different exposure times let us recover efficiently bright and faint stars.

The next step was to remove any systematic difference between the magnitude scale of all the frames. The stars in each frame were first matched to the ones taken in photometric conditions using DAOMATCH and DAOMASTER. Then the average of the independent measures obtained from the different images were adopted as the final values of the instrumental magnitude. The uncertainty is derived through the artificial star experiment (see Ch. 4 and next paragraphs).

About 20 images (6 – 7 per filter) of the standard areas were observed during each photometric night and the magnitude of the standard stars was measured. Three sets of calibration equations were derived, as the targets were observed in different nights. The results are reported in Tab. 5.3.

Table 5.3: Calibration equations. B , V , and I are the magnitudes in the standard Johnson-Cousins system while b , v , and i are the instrumental magnitudes.

Cluster	Date	Equation	r.m.s.
Be 27	Feb, 19 2006	$B = b - 0.143(b - v) + 0.275$	0.017
		$V = v - 0.016(b - v) + 0.562$	0.024
		$V = v - 0.019(v - i) + 0.540$	0.023
		$I = i - 0.016(v - i) - 0.450$	0.019
Be 34	Feb, 24 2006	$B = b - 0.125(b - v) + 0.312$	0.023
		$V = v - 0.010(b - v) + 0.620$	0.023
		$V = v - 0.014(v - i) + 0.602$	0.019
		$I = i - 0.035(v - i) - 0.376$	0.022
Be 36	Feb, 25 2006	$B = b - 0.129(b - v) + 0.318$	0.015
		$V = v - 0.016(b - v) + 0.631$	0.019
		$V = v - 0.015(v - i) + 0.606$	0.018
		$I = i - 0.024(v - i) - 0.367$	0.018

As the photometry of the standard stars was computed using aperture photometry, the instrumental magnitudes of the scientific targets were corrected to take into account the differences between aperture and PSF magnitudes (using about 20 isolated stars), then calibrated to the standard Johnson-Cousins system. Two different calibration equations were derived for the V magnitude: one using the $(B - V)$ colour index and the other one using the $(V - I)$ colour index. The difference between the two calibrations is, on average, well below one hundredth of magnitude with a small dispersion and a very shallow dependence on colour.

The *Guide Star Catalogue 2.3* (see Lasker et al., 2008) was used to find an accurate astrometric solution to transform the instrumental pixels positions into J2000 celestial co-

¹IRAF is the Image Reduction and Analysis Facility, a general purpose software system for the reduction and analysis of astronomical data. IRAF is written and supported by the IRAF programming group at the National Optical Astronomy Observatories (NOAO) in Tucson, Arizona.

Table 5.4: Completeness of the photometry for the three clusters.

mag	compl <i>B</i>	compl <i>V</i>	compl <i>I</i>	Be 27			Be 34			Be 36		
				compl <i>B</i>	compl <i>V</i>	compl <i>I</i>	compl <i>B</i>	compl <i>V</i>	compl <i>I</i>	compl <i>B</i>	compl <i>V</i>	compl <i>I</i>
16.0	100±6	99±5	100±4	100±6	100±6	99±5	100±6	99±5	99±4			
16.5	99±6	98±3	100±3	100±5	100±5	99±4	100±5	98±5	98±4			
17.0	99±4	99±3	99±3	100±5	98±4	98±3	99±5	99±4	98±3			
17.5	99±3	98±2	98±3	98±4	98±4	97±3	99±5	99±4	98±2			
18.0	98±3	99±2	98±2	99±4	98±3	97±2	100±4	98±3	97±2			
18.5	98±2	97±2	96±2	98±3	98±3	96±2	98±4	97±2	98±2			
19.0	98±2	97±2	96±2	99±3	97±2	94±2	97±3	98±2	96±2			
19.5	97±2	96±2	96±2	98±2	97±2	94±2	98±2	97±2	95±2			
20.0	98±2	96±2	93±2	97±2	96±2	90±2	98±2	96±2	94±2			
20.5	96±2	95±2	88±2	96±2	95±2	74±2	96±2	95±2	88±2			
21.0	95±2	93±2	80±2	95±2	92±2	38±3	96±2	94±2	75±2			
21.5	94±2	88±2	59±2	92±2	87±2	5±7	94±2	89±2	42±3			
22.0	88±2	78±2	36±3	72±2	50±3	0	84±2	71±2	7±6			
22.5	74±2	59±2	13±5	17±4	8±6	0	34±3	23±3	0			
23.0	52±2	35±2	2±11	3±10	1±18	0	4±8	2±11	0			

ordinates. More than 200 stars were used for each frame as astrometric standards and the final transformations, obtained with the code CataXcorr², has an r.m.s. scatter less than 0.2'' in both RA and Dec.

The final step of the data reduction process consisted in recovering the completeness level of the photometry using the extensive artificial stars experiment (see Ch. 4). About 50000 stars have been artificially added and uniformly distributed on the deepest frames in groups of about 120 stars at a time, to avoid changing the actual crowding conditions. For each iteration of the artificial stars experiment the frames were reduced using the same reduction process described above. The fraction of recovered stars at different magnitude levels represents the completeness of our photometry; values are presented in Tab. 5.4.

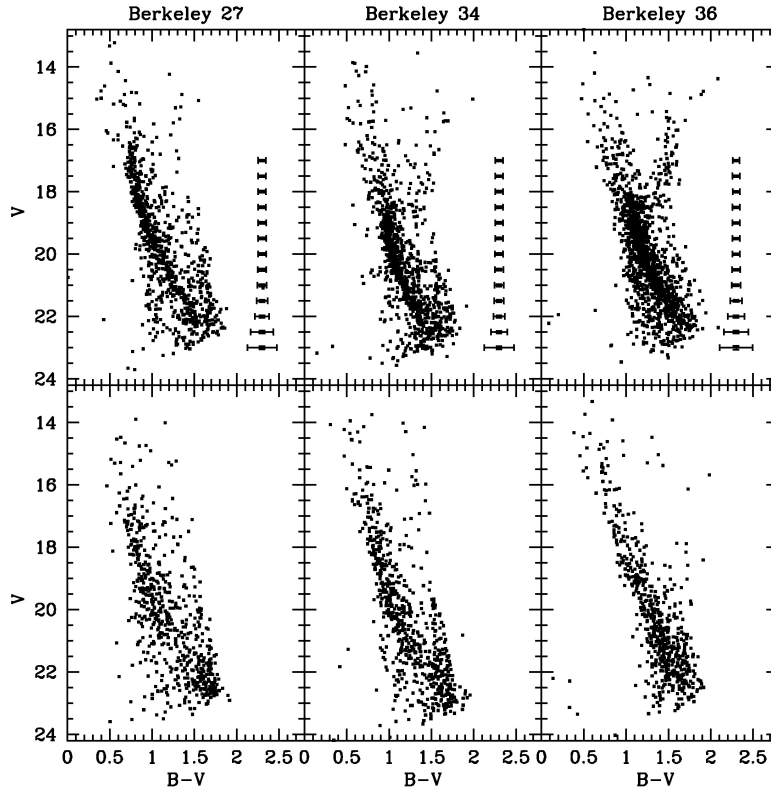
The resulting CMDs for the cluster stars and the comparison field stars are shown in Figs. 5.2 (*V, B-V* plane) and 5.2 (*V, V-I* plane). Error bars indicate the global photometric error that takes into account the instrumental error and the uncertainties on the calibration procedures. They range from about 0.03 mag at the bright limit to less than 0.1 mag around *V* = 24. The three OCs main evolutionary phases are visible despite the important field contamination. In particular, the MS is easily recognisable although its broad shape does not help in defining its features. The detailed analysis of the CMDs morphology is described in Sec. 5.1.3. The photometric catalogues are available through the CDS³.

²CataXcorr was developed by Paolo Montegriffo at INAF - Osservatorio Astronomico di Bologna.

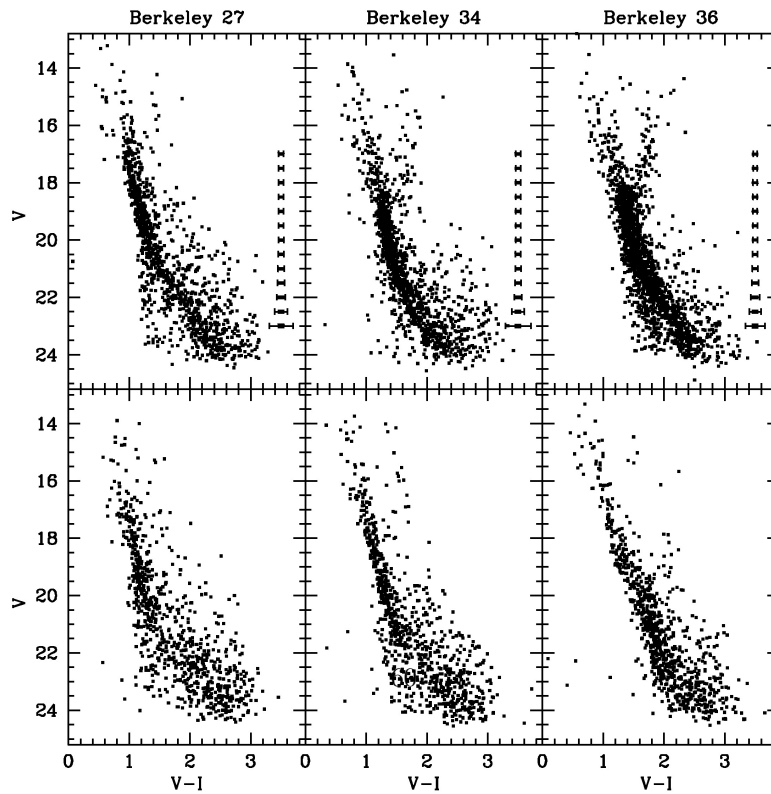
³The Strasbourg Astronomical Data Center, see <http://cds.u-strasbg.fr/>.

Figure 5.2: (a) Upper panels: CMDs of Be 27, Be 34, and Be 36 showing V vs $(B - V)$. Lower panels: CMDs of the corresponding comparison field. Global photometric errors are shown on the right side of the clusters CMDs. (b) The same but for V vs $(V - I)$.

(a)



(b)



Comparison with previous data

As said in Sec. 5.1, Be 27, Be 34, and Be 36 were previously observed by various authors. The WEBDA was exploited to obtain the best literature data available. We show a comparison only with the data from Carraro & Costa (2007) which contains V and I photometry for Be 27 and with the data from Ortolani et al. (2005) that has B and V photometry for Be 34 and Be 36 (see Figs. 5.3, 5.4, and 5.5).

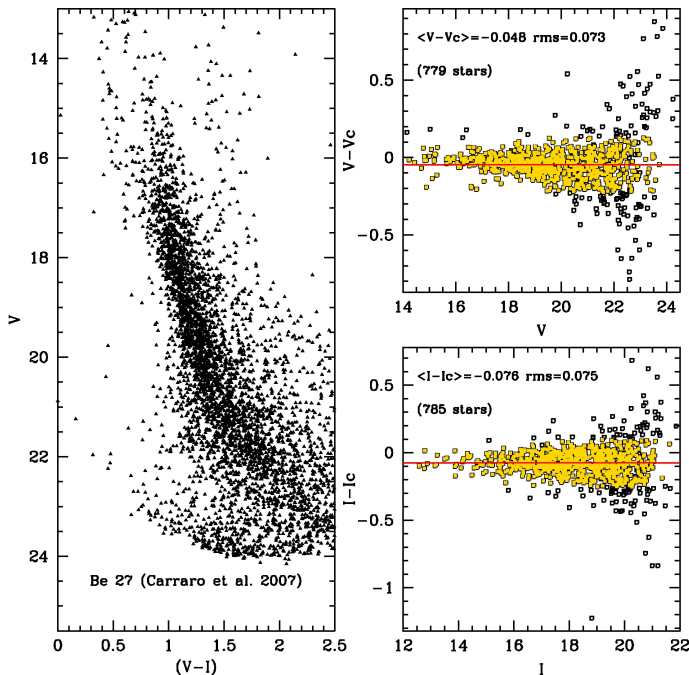


Figure 5.3: Left panel: CMD of Be 27 by Carraro & Costa (2007). Right panel: differences between our photometry and theirs in V (upper panel) and I (lower panel). In the comparison panels the black points are all stars in common, while the filled, yellow symbols indicate stars used to compute the mean differences (within 2σ from the average).

The differences found in B , V , and I are reported in figures. In general we find small offsets with literature data and only in some cases large deviations (see the cases of Be 34 and Be 36 in Figs. 5.4 and 5.5). The explanation of such differences is not straightforward as it is not possible to definitely distinguish if they are due to our photometry or theirs.

5.1.2 Clusters' centre

Occasionally the cluster centre indicated in the WEBDA or DAML02 is offset from the true one, even by a few arcminutes, so we checked if this was the case for the three OCs. For each object we computed its centre as the barycentre of the stars spatial distribution on the basis of a simple statistical approach. The three clusters are all distant objects, so their apparent diameter is relatively small, giving us the chance to distinguish the central part even with the small FoV of SUSI2. From the DAML02 catalogue we know that the apparent diameter of the clusters (based on visual inspection) is about 2 arcmin for Be 34 and 5 arcmin for Be 36, while for Berkeley 27 the recent study by Carraro & Costa (2007) indicates a cluster radius of 3 arcmin. This means that two of our OCs are fully contained in the SUSI2 FoV, while Be 27 is slightly larger.

To identify the centre, first we restricted our analysis only to stars which belong to the upper part of the CMDs (selecting those with $V \leq 22$) to have a sample of objects strongly dominated by cluster stars with a relatively small contamination of field stars. Then we

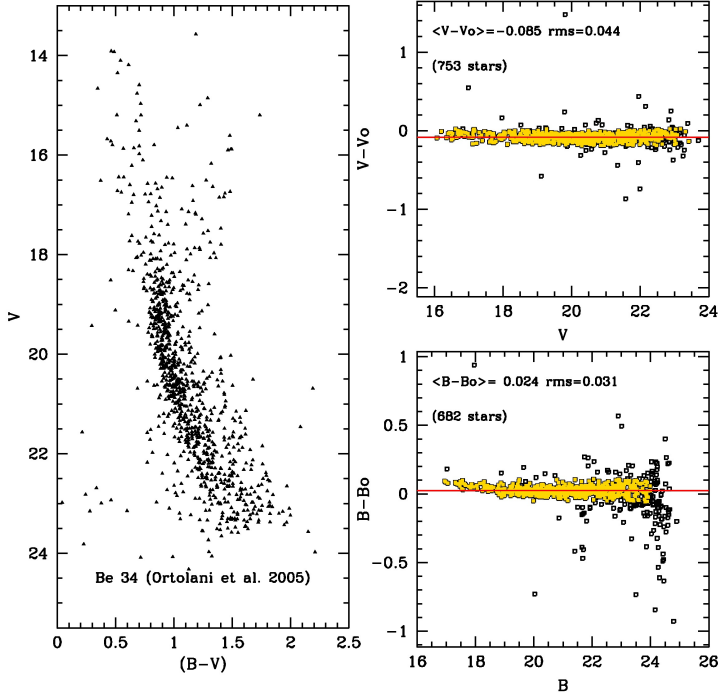


Figure 5.4: Left panel: CMD of Be 34 by Ortolani et al. (2005). Right panel: comparison with our data for V (upper panel) and B (lower panel) magnitudes. In the comparison panels the black points are all stars in common, while the filled, yellow symbols indicate stars used to compute the mean differences (within 2σ from the average).

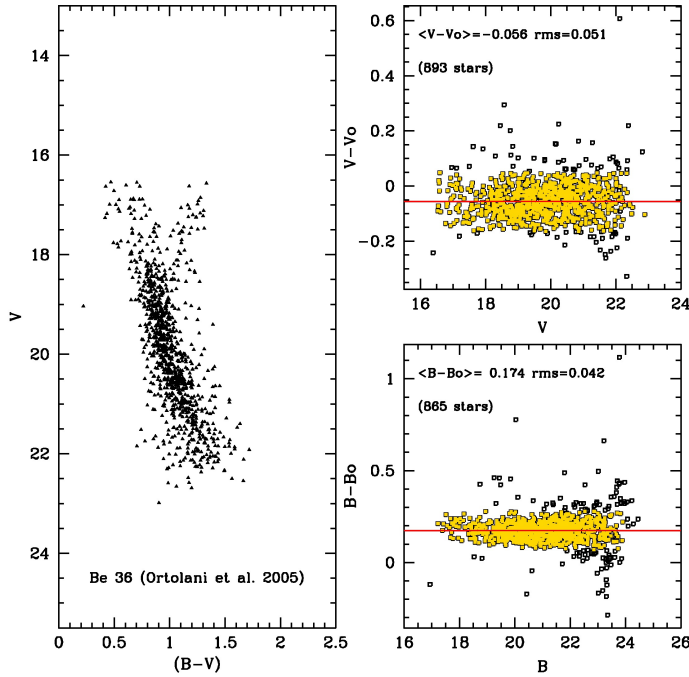


Figure 5.5: Left panel: CMD of Be 36 by Ortolani et al. (2005) of the stars we could cross-identify with our catalogue. Right panel: comparison with our data. In the comparison panels the black points are all stars in common, while the filled, yellow symbols indicate stars used to compute the mean differences (within 2σ from the average).

performed a spatial selection: we computed the smallest intervals in coordinates RA and Dec that contain 70% of stars and, with this smaller group, we iterated the computation to define a spatial region used to refine our analysis. The cluster centre is then computed as the barycentre of the final group of stars. The procedure is repeated for different selections in magnitude and the corresponding results averaged together as best estimate of the cluster centre. The results are shown in Tab. 5.5. They are slightly different from the literature ones, especially for Be 36.

Table 5.5: J2000 RA and Dec coordinates for the three clusters. The second and third columns are the computed coordinates. The last two columns the previous determinations.

Cluster	Centre		Previous Determination ^a	
	RA	Dec	RA	Dec
Be 27	06 51 21	+05 46 07	06 51 18	+05 46 00
Be 34	07 00 23	-00 13 56	07 00 24	-00 15 00
Be 36	07 16 24	-13 11 35	07 16 06	-13 06 00

^aSource: WEBDA.

5.1.3 Clusters parameters using synthetic colour-magnitude diagrams

The estimations of age, metallicity, distance, mean Galactic reddening, and binary fraction have been obtained comparing the observational CMDs with a library of synthetic ones, built using synthetic stellar populations as described in Sec. 4.2.

Adopting the same approach described in Cignoni et al. (2011), we first evaluated the parameters that do not depend on the evolutionary model analysis, as the binary fraction and the differential reddening. The binary fraction is estimated from the information on colour and magnitude of the cluster stars then fine-tuned, together with the differential reddening parameter, in order to match the MS width. In the analysis described in the next paragraphs the adopted differential reddening is considered as an upper limit and added as a random positive constant to the mean Galactic reddening. In the case of the OCs observed with larger FoV we adopted a statistical method to directly measure the differential reddening (see Sec. 6.1.3). The luminosity of the MSTP and of the RC are effectively used to constrain the age. The estimated luminosity of the base of the RGB (BRGB), the RGB inclination and colour, and RC colour are used to select the best fit to the observational CMDs in order to estimate the mean Galactic reddening $E(B - V)$ and distance modulus $(m - M)_0$, and to fine tune the metallicity. The best estimate of the mean Galactic reddening is defined when the bluest upper part of the sCMD MS matches the corresponding part of the observed CMD MS; the observed distance modulus is identified when the MSTP level and colour are reproduced in the synthetic CMD. We took into account the information of the complete *BVI* photometry to constrain the metallicity (see Tosi et al., 2007) and reduce the parameter space of our analysis: the best metallicity is defined when it is possible to reproduce at the same time the observed $B - V$ and $V - I$ CMD with the synthetic ones using the same distance modulus, reddening, and age. To deal with $(B - V)$ and $(V - I)$ colours we adopted the normal extinction law where $E(V - I) = 1.25 \times E(B - V) \times [1 + 0.06 \times (B - V)_0 + 0.014 \times E(B - V)]$ (Dean et al., 1978).

This procedure relies mostly on the MS fitting and the RC fitting. Hence, the main uncertainties on the results are due to the fact that the MS inclination and RC morphology and luminosity are quite sensitive to the input physics of the model and to the adopted

colour transformations, and the uncertainties in defining the RC stars are not negligible for poorly populated clusters, increasing the probability of confusion with RGB and field stars biasing the age determination. In this context the “best” solution parameters are chosen as the ones which fit most of the visible MS shape and the assumed RC level.

We estimated the errors on the cluster parameters (mean Galactic reddening, distance modulus, and cluster age) considering the instrumental photometric error and the uncertainties of the fit analysis. The net effect of the former is an uncertainty on the luminosity level and colour of the indicators adopted. Then we select the best fitting synthetic CMD and take into account in the error budget the dispersion of the cluster parameters estimates for the different solutions. The uncertainties are taken to be of the form:

$$\begin{aligned}\sigma_{E(B-V)}^2 &\sim \sigma_{(B-V)}^2 + \sigma_{fit}^2 \\ \sigma_{(m-M)_0}^2 &\sim \sigma_V^2 + R_V^2 \sigma_{E(B-V)}^2 + \sigma_{fit}^2 \\ \sigma_{age}^2 &\sim \sigma_{fit}^2.\end{aligned}$$

The typical photometric error for the reddening is ~ 0.04 and for the distance modulus ~ 0.1 (we considered negligible the error on R_V); the dispersion for the fit analysis depends mainly on the uncertainty on the RC level and on the coarseness of the isochrone grid. It is of the order of ~ 0.02 for the reddening, and ranges between 0.01 and 0.05 for the distance modulus, and about 0.2-1 Gyr for the age.

Berkeley 27

Be 27 is a poorly populated cluster: the contrast of member stars with the comparison field ones outlines the cluster MS but other evolutionary phases are not easily recognisable. For a more robust analysis we studied the inner part of the cluster which is less contaminated by field interlopers. Fig. 5.6 shows the CMDs for different circular areas around the cluster centre: the left panels are the CMDs for the smallest area (distance from the centre $r < 0.8'$) and only the MS is clearly visible. We indicate the RH level (solid arrow on the left): the MS shows a little bend toward the red just below the RH then reaches its reddest point at $V \sim 16.5$. The two blue stars at $(B - V) \sim 0.45$ and $V \sim 16$ are probably cluster blue straggler stars (very common in OCs, see e.g., Ahumada & Lapasset 2007 for a recent catalogue). The central panels of the same figure show the CMD for stars with a distance from the cluster centre smaller than $1.5'$ and the right one for a distance $r < 2.2'$. Concerning the RC stars there is no firm evidence from the CMDs; we define the most probable RC locus (solid arrow on the right) choosing the two stars at magnitude $V \sim 15.2$ and colour $(B - V) \sim 1.3 - 1.4$: these stars are close to the centre, hence they are more likely cluster members and have a very small difference both in $B - V$ and $V - I$ colours; in addition, our choice is in agreement with the analysis by Carraro & Costa (2007). The RC stars are very few but still more abundant than the comparison field stars (see CMDs in Fig. 5.7 for a circular area of $r = 2.2'$). The uncertainty in defining the magnitude level of the RC directly affects the precision of the age estimate. We chose to use the CMD for $r < 2.2'$ in the further analysis to limit the field contamination.

The MS appears broader than expected from photometric errors. This is probably due to two factors: one is a large fraction of binaries and the other is the presence of differential reddening. For our simulations we needed to assume a differential reddening of $\Delta E(B - V) = 0.05$ mag in addition to the mean Galactic reddening.

A rough estimate of the binary fraction was obtained following the method described in Cignoni et al. (2011): we defined two CMD boxes, one which encloses MS stars and

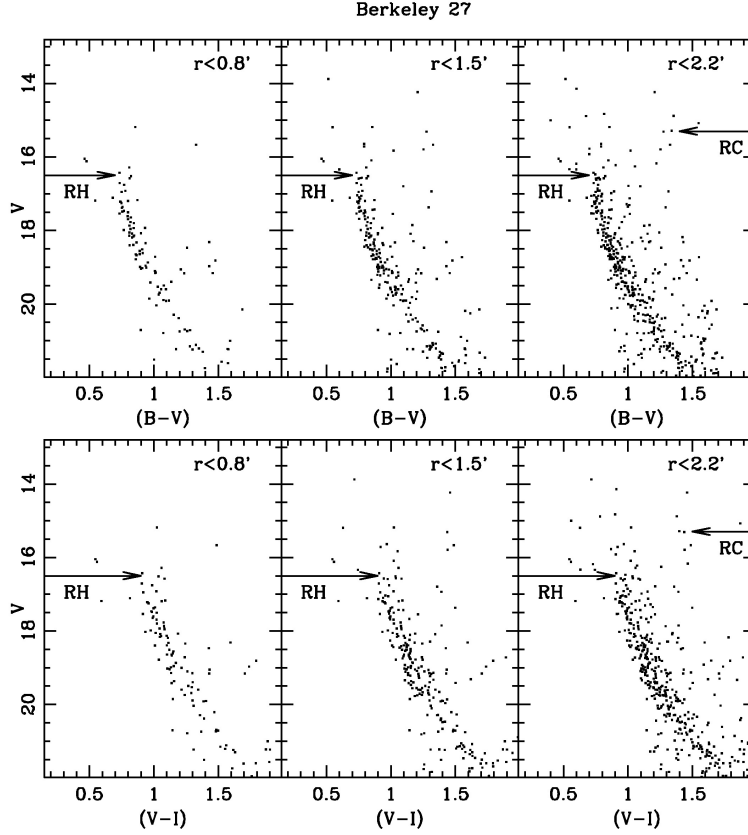


Figure 5.6: Upper panels show the V vs $(B - V)$ CMDs of Be 27 for different distances r from the cluster centre. Lower panels: the same but for the V vs $(V - I)$ CMDs. In the plots the level of RH (solid arrow on the left) and RC (solid arrow on the right) are also indicated.

the other red-ward of the MS in order to cover the binary sequence (see dashed and dot-dashed lines in Fig. 5.7). To remove the field contamination we subtracted the contribution of field stars falling inside the same CMD boxes of an equal area of the control field. We performed the same computation on regions smaller and larger than $2.2'$, finally ending with an estimate between 20% and 30%. The dispersion on the estimate is mostly due to the spatial fluctuations across the control field. Moreover these fractions are underestimated: we are missing binaries hosting low mass star, whose properties are close to those of single stars. However, a mean fraction of 25% appears a reasonable trade-off and will be assumed for all the simulations.

We performed the simulations looking for the best combination of parameters keeping fixed the binary fraction and differential reddening derived above. The interval of confidence for the cluster age turns out between 1.2 and 1.8 Gyr. Concerning the metallicity, we found that all models with solar metallicity can not fit the stellar population both in $(B - V)$ and $(V - I)$ colours. Therefore we concentrated our efforts on solutions with $Z < 0.02$.

The FST models with $Z = 0.006$ and $Z = 0.01$ (overshooting parameter $\eta = 0.2$) fit reasonably well the RH and RC luminosity levels. The synthetic MS is slightly redder than the observed one in the magnitude range $18.5 < V < 20$ mag and this is probably due to the fact that the synthetic MS shape is too curved before the RH point. In terms of cluster

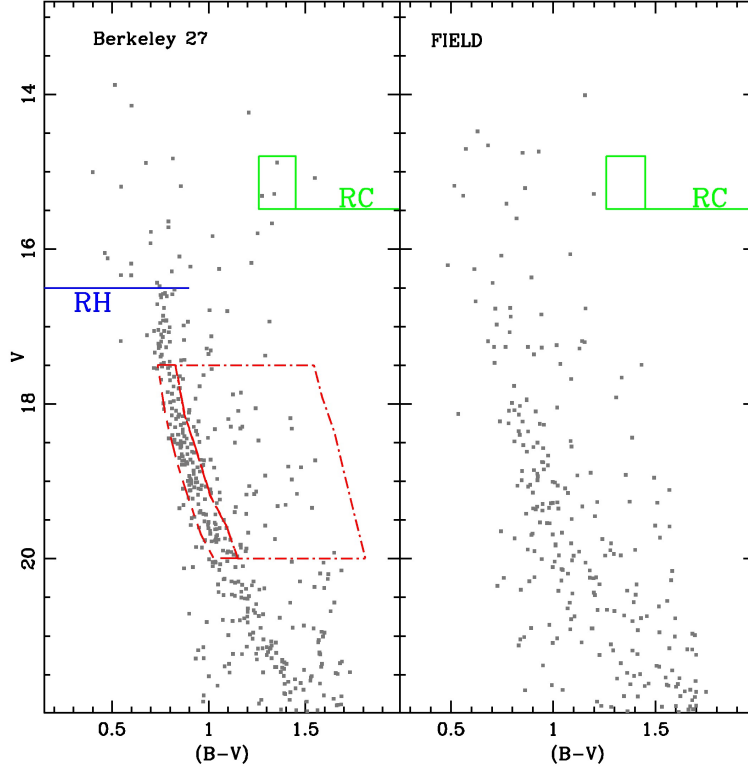


Figure 5.7: Left panel: CMD of Be 27 for stars falling inside a region of 2.2 arcmin from the cluster centre. We indicate the luminosity level of the RH and the RC. The dotted and the dot-dashed boxes are, respectively, used to estimate the fraction of single and binary stars. Right panel: CMD of the comparison field of an equal area.

parameters $Z = 0.006$ implies a cluster age of 1.5 ± 0.2 Gyr, $E(B - V) = 0.50 \pm 0.04$, and a distance modulus $(m - M)_0 = 13.20 \pm 0.13$; $Z = 0.01$ implies a cluster age of 1.5 ± 0.2 Gyr, $E(B - V) = 0.44 \pm 0.04$, and a distance modulus $(m - M)_0 = 13.27 \pm 0.13$. We can not firmly choose between the two metallicities $Z = 0.006$ and $Z = 0.01$: from the comparison of $(B - V)$ and $(V - I)$ CMDs with the observed ones we find a good match in both cases. This means that the metallicity estimate suffers more uncertainties, as we can not obtain a unique and independent evaluation from the BVI photometry but only put an upper limit. On the other hand, the circumstance that with both metallicities we obtain the same age and distance modulus (obviously not the same reddening) emphasises the robustness of their values.

Of the BBC models we used the ones with $Z = 0.004$ and $Z = 0.008$. In the first case we obtain the best match assuming a cluster age of 1.7 ± 0.2 Gyr, a reddening of $E(B - V) = 0.52 \pm 0.04$ and a distance modulus of $(m - M)_0 = 13.05 \pm 0.13$. Both the RC and RH levels have a good fit, matching also the RC colour. As for the FST models, we find a slightly redder MS for $V > 19$ mag. The difference remains also with the other tracks with $Z = 0.008$. For this metallicity we estimate a cluster age of 1.7 ± 0.2 Gyr, $E(B - V) = 0.44 \pm 0.04$, and a distance modulus of $(m - M)_0 = 13.10 \pm 0.13$. Also for the BBC models we can only put an upper limit to the cluster metallicity using $(B - V)$

and $(V - I)$ CMDs comparison, and constrain the metallicity estimate in terms of the best synthetic CMD fit. Again for age and distance we get stable solutions.

With the FRA models we used metallicity $Z = 0.006$ and $Z = 0.01$. In the former case we can match the RH and RC levels with a reasonable fit of the upper part of the MS while the lower part ($V > 18.5$) has a redder $(B - V)$ colour. We determine a cluster age of 1.2 ± 0.2 Gyr, $E(B - V) = 0.54 \pm 0.04$, and $(m - M)_0 = 13.1 \pm 0.13$. For the latter case we obtain a fit that shares the same problems of the previous one: the RH and RC levels are well matched but the lower part of the synthetic MS is redder for $V > 18.5$. Accepting these differences we confirm a cluster age of 1.2 ± 0.2 Gyr with $E(B - V) = 0.50 \pm 0.04$, and $(m - M)_0 = 13.10 \pm 0.13$. For the FRA models the higher metallicity ($Z = 0.01$) gives a slightly better match both in $(B - V)$ and $(V - I)$, reproducing better the RH phase. As usual, the ages derived from the FRA models are lower than those from both the BBC and the FST ones. This is because the FRANEC tracks do not include overshooting from convective cores, while the other two sets do.

Fig. 5.8 shows the comparison between the observed CMD (top left) and the best fits obtained with the three sets of tracks. The results of the analysis are summarised in Tab. 5.6.

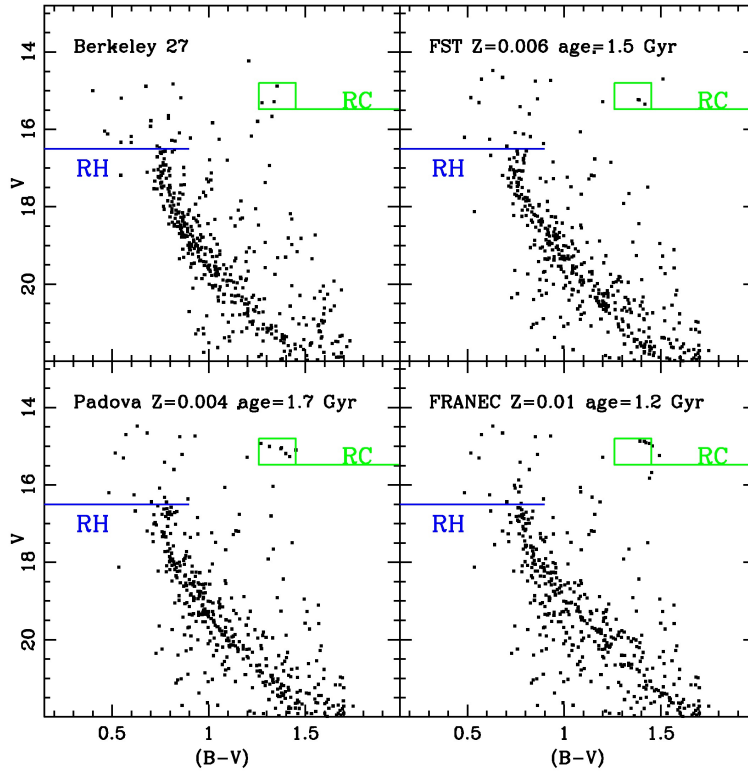


Figure 5.8: Top left panel: CMD of stars inside $2.2'$ radius area of Be 27. The top right panel shows the best fitting CMD obtained with FST model: $Z = 0.006$, age 1.5 Gyr, $E(B - V) = 0.50$, and $(m - M)_0 = 13.2$; the bottom left panel is the synthetic CMD obtained with BBC track: $Z = 0.004$, age 1.7 Gyr, $E(B - V) = 0.52$, and $(m - M)_0 = 13.05$; finally, the bottom right CMD has been obtained with FRA model: $Z = 0.01$, age 1.2 Gyr, $E(B - V) = 0.50$ and $(m - M)_0 = 13.1$.

From this analysis it turns out that the FST models are the ones that best fit the observed CMD as they provide a better match of the MS shape. This restricts the age to 1.5 ± 0.2 Gyr. Consequently the Galactic reddening is between 0.40 and 0.50 mag which nicely compares with the Schlegel et al. (1998) estimate of 0.49 mag, while the distance modulus is between 13.2 and 13.3.

To Be 27 Carraro & Costa (2007) assign an age of 2 Gyr, older than our estimates but still compatible with the results obtained with BBC models (the ones used by the authors). This difference is mainly due to the identification of the RC level. The cluster in fact lacks a clear RGB and clump, leaving more uncertainties on the age determination. Restricting the comparison to the BBC models, the chosen metallicity used for the fit can explain the difference for the reddening estimate, as the photometry offset between our data and theirs is of the order of 0.03 mag for $(V - I)$: for higher metallicities the fit requires lower reddening values as the isochrone has a redder colour. We find a distance modulus larger (about 0.4 mag) and this is mainly due to the age adopted (the offset in photometry is only of the order of 0.05 mag): the higher the age the fainter the magnitude of the TO, therefore a good fit is obtained with a smaller value of the distance modulus.

Berkeley 34

The CMD of Be 34 is much richer than that of Be 27. In Fig. 5.9 we show the $(B - V)$ and $(V - I)$ CMDs for different circular areas centred on the cluster. The plots on the left are a selection of the very central part of Be 34 (distance r lower than $0.8'$): the MS is well visible and we indicate the RH level, positioned near $V=18.5$ mag and the MSTP level, set near $V \sim 18.0$ mag. In the central ($r < 1.5'$) and right ($r < 2.5'$) panels the MS is better delineated but with a heavier contamination of field stars. We identify two different equally probable locations for the RC: one is the bright small group of three stars at $V \sim 15.7$ mag and $(B - V) \sim 1.7$ (dashed arrow on the right), the second is the fainter group (4 and more sparse stars) at $V \sim 16.7$ and $(B - V) \sim 1.55$ (solid arrow on the right). The uncertainty on the RC level comes from the fact that this evolutionary phase is very scarcely populated. In the first case we would estimate an older age for the cluster, as the magnitude difference between the MSTP and the RC levels is larger.

In Fig. 5.9 we show, in the left panel, the CMD of stars selected in a region within $2.5'$ from the cluster centre (we used this selection for the following analysis) and in the right panel the comparison field of an equal area. We indicate also the RH, MSTP, and RC magnitude levels. The RGB is difficult to recognise. It is populated by a little bunch of stars that runs red-ward of $(B - V)=1.5$ and brighter than $V=18.0$. We identify the base of the RGB (BRGB) at level $V=18.6$ (see Fig. 5.10). In the comparison field there is no star with $(B - V) > 1.5$ and no counterpart at the RC levels defined above.

As for Be 27, the MS appears broader than expected from the photometric errors: presumably differential reddening and binaries play a non negligible role in shaping the MS appearance. For our simulations we took into account a differential reddening of at least 0.05 mag. The percentage of binaries was computed using the same approach done for Be 27, finding an average fraction of 27%.

In order to put limits on the cluster age and metallicity, the CMD of the region within $2.5'$ is compared with our synthetic CMDs. We found that models with metallicity $Z < 0.02$ are in agreement with both $(B - V)$ and $(V - I)$ therefore we discarded models with solar metallicity.

If we adopt the brighter RC level estimation we find that the synthetic CMDs can match well the indicators levels (RH, MSTP and RC) but with a worse fit for the lower

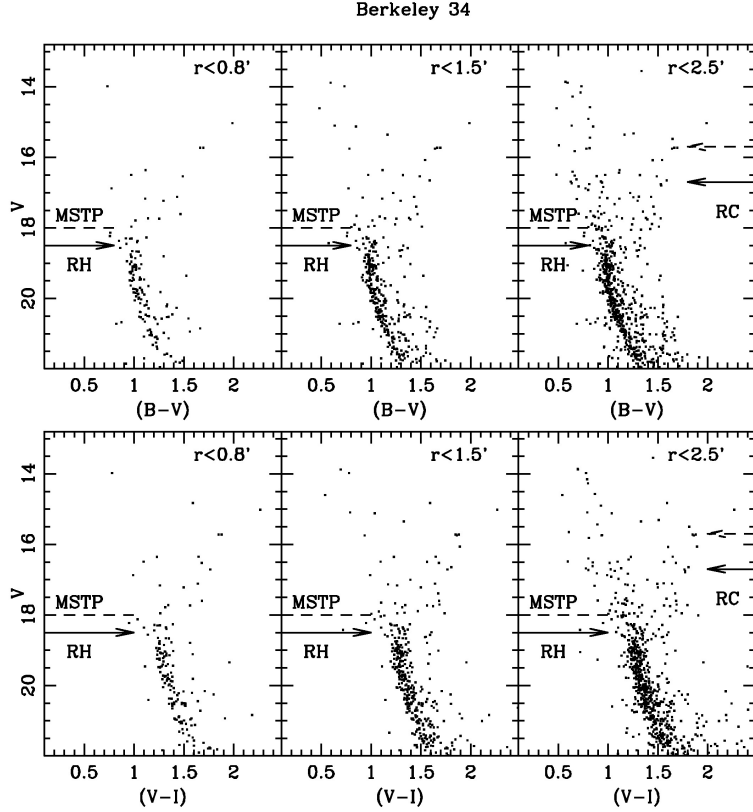


Figure 5.9: Upper panels show the V vs $(B - V)$ CMDs of Be 34 for different distances r from the cluster centre. Lower panels: the same but for the V vs $(V - I)$ CMDs. In the plots are also indicated the levels of RH (solid arrow on the left) and MSTP (dashed line). We indicate also the two RC levels identified: dashed (rejected) and solid (adopted) arrows on the right.

MS ($V > 18.0$) and for the RGB and RC colours (too blue). Even if the colour indicators are prone to greater uncertainties, as explained at the beginning of this section, in our opinion these discrepancies come from an incorrect age estimation: as the age of the stellar population increases the colour extension of the sub giant branch (SGB) becomes shorter. We thus took into account also this age sensitive indicator, looking for a reasonable match of the distance in colour between the MS and the BRGB. In addition these solutions cannot fit the very bright ($V \sim 15$) and red ($B - V \sim 2.0$) star, that seems to be an RGB cluster member. Our final choice is therefore to identify the RC at $V \sim 17.2$ and $(B - V) \sim 1.55$.

For the FST models (with overshooting parameter $\eta = 0.2$) we find a reasonable agreement between synthetic and observed CMDs for a cluster age of 2.1 ± 0.2 Gyr with both metallicities $Z = 0.006$ and $Z = 0.01$. The RH, MSTP, BRGB, and RC levels are well matched with a proper fit of the MS and of the RGB shapes. The better match is obtained with the model with $Z = 0.01$: the bright red member mentioned above suggests an RGB inclination which better matches the metal-rich model. The chosen binary fraction seems in agreement with the observations: the broad lower part of the MS is well reproduced. The reddening and distance modulus assigned for the model with $Z = 0.006$ are $E(B - V) = 0.62 \pm 0.04$ and $(m - M)_0 = 14.2 \pm 0.13$. For $Z = 0.01$ we estimated

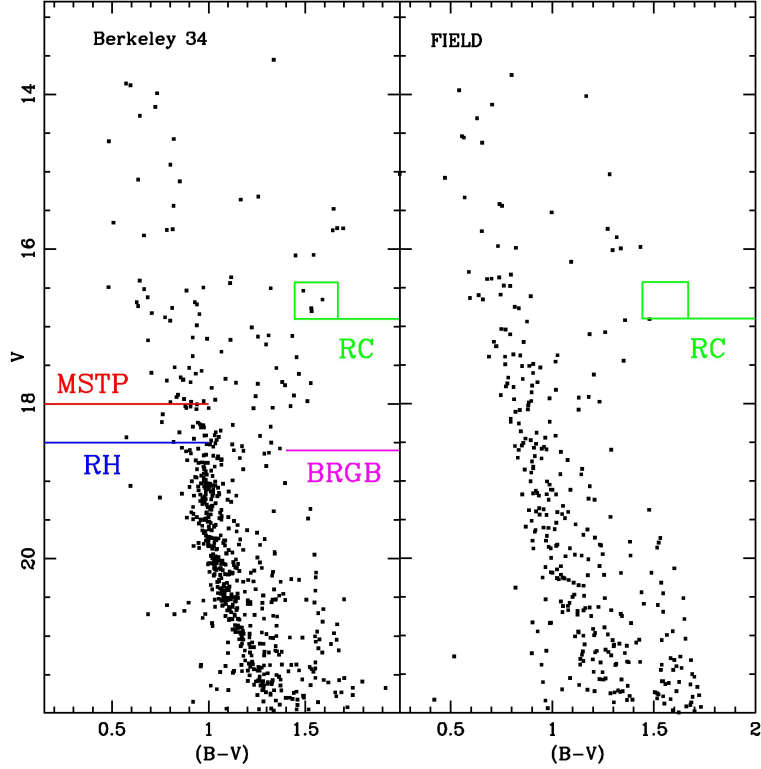


Figure 5.10: Left panel: CMD of Be 34 for stars falling inside a region of 2.5 arcmin from the cluster centre. We indicate the luminosity level of the RH, the MSTP, the RC, and the BRGB. Right panel: CMD of the comparison field of an equal area.

$E(B - V) = 0.57 \pm 0.04$ and $(m - M)_0 = 14.3 \pm 0.13$. From this analysis we find that the models with $Z = 0.006$ and $Z = 0.01$ provide good matches both in the $(B - V)$ and in the $(V - I)$ CMDs, leaving open the choice between these two metallicities.

Using the BBC tracks with $Z = 0.004$ and $Z = 0.008$ we obtain in both cases a good match for RH, MSTP, and BRGB magnitudes and colours, as well as a reasonable fit for the MS shape and RGB colour and inclination. Also in this case the best match is obtained using the metal-richer model. For $Z = 0.004$ we infer a cluster age of 2.5 ± 0.2 Gyr, $E(B - V) = 0.64 \pm 0.04$, and a distance modulus $(m - M)_0 = 14.1 \pm 0.13$. With $Z = 0.008$ we derive a cluster age of 2.3 ± 0.2 Gyr, $E(B - V) = 0.59 \pm 0.04$, and a distance modulus $(m - M)_0 = 14.2 \pm 0.13$. Also for the BBC models with sub-solar metallicity we obtain a good match in the $(B - V)$ and in the $(V - I)$ CMDs, hence we can not firmly choose between $Z = 0.004$ and $Z = 0.008$.

With the FRA models we obtain a younger age estimate for the cluster. These models in fact do not consider overshooting and this naturally leads to a lower age prediction. The younger age required to fit the luminosity constraints results in a synthetic CMD that has a too red RGB and a too faint BRGB. For $Z = 0.006$ we estimate a cluster age of 1.6 ± 0.2 Gyr, $E(B - V) = 0.67 \pm 0.04$, and a distance modulus $(m - M)_0 = 14.2 \pm 0.13$. With $Z = 0.01$ we obtain a cluster age of 1.6 ± 0.2 Gyr, $E(B - V) = 0.65 \pm 0.04$, and a distance modulus $(m - M)_0 = 14.2 \pm 0.13$. In this case the higher metallicity ($Z = 0.01$) gives a slightly better

match both in $(B - V)$ and $(V - I)$, with a better fit of the upper MS morphology.

Fig. 5.11 shows the best fitting CMD for each set of tracks and the corresponding parameters. We prefer the FST models as they give a better description of the CMD morphology as a whole. We find in fact that the BBC models predict a MS shape too curved before the RH point. The FRA models, instead, give a good match of the magnitude indicators but a worse fit for the MS shape and RGB inclination. With this assumption the age of Be 34 is estimated as 2.1 Gyr, with a range in reddening between 0.57 and 0.62 (similar to the Schlegel et al., 1998, value of 0.68)⁴ and a distance modulus between 14.2 and 14.3. The results of the analysis are summarised in Tab. 5.6.

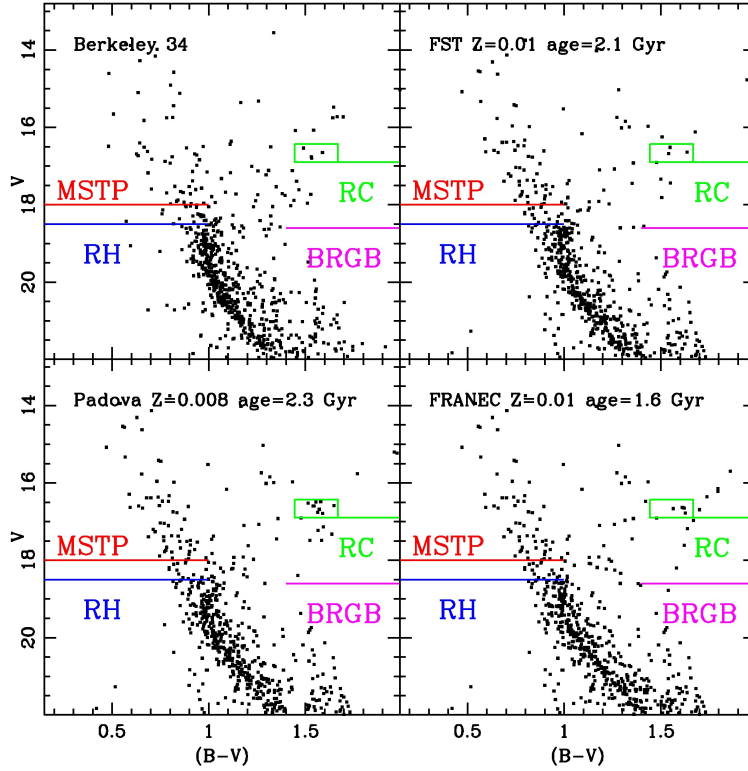


Figure 5.11: Top left panel: CMD of stars inside $2.5'$ radius area of Be 34. The top right panel shows the best fitting CMD obtained with FST model: $Z = 0.01$, age 2.1 Gyr, $E(B - V) = 0.57$ and $(m - M)_0 = 14.3$; the bottom left panel is the synthetic CMD obtained with BBC track: $Z = 0.008$, age 2.3 Gyr, $E(B - V) = 0.59$, and $(m - M)_0 = 14.2$; finally, the bottom right CMD has been obtained with FRA model: $Z = 0.01$, age 1.6 Gyr, $E(B - V) = 0.65$ and $(m - M)_0 = 14.2$.

Ortolani et al. (2005) assign to this cluster an age of 2.3 Gyr, which is in agreement with our estimation. In particular it coincides with the one we obtained with the BBC models (the ones used by them). However, their choice of RC level does not seem to agree with either one of our two possibilities. A non negligible difference is found in the reddening and distance modulus determination. In the first case the discrepancy can be explained

⁴Unfortunately, given the very low latitude of all three OCs, these reddening values cannot be trusted to give the real asymptotic reddening, and cannot give a firm constraint as in more favourable cases.

in terms of differences between our photometries (see Sec. 2.4). For the distance modulus the differences in the photometries can not explain such discrepancy: we notice that they chose a MSTP level about half magnitude brighter with respect to our analysis, hence they determined a smaller distance modulus.

Berkeley 36

Be 36 is the richest cluster of the group. The CMDs in Fig. 5.12 clearly show the MS, the MSTP ($V \sim 18.1$), and the RGB for different distances from the cluster centre. The contamination from field stars is evident particularly in the central and right panel: the MS is blurred and the region above the MSTP is dominated by field interlopers (together with the cluster blue straggler stars). Also for this cluster we restricted our analysis to a small area of $2.3'$ of radius to maximise the membership likelihood. Even within this restricted area we can still notice an important field contamination but without losing the evidence of the CMD features: the MSTP at $V \sim 18.1$ and the BRGB at the magnitude level of $V \sim 18.6$ (see Fig. 5.13). We also notice a small gap at $V \sim 18.7$ which could be associated to an RH phase; however, further investigations discarded this hypothesis. The RGB is quite evident, running red-ward of $(B - V) = 1.5$ and reaching $V \sim 14.5$ with a very red member at $B - V \sim 2.2$. The field contamination along the RGB seems very modest, from

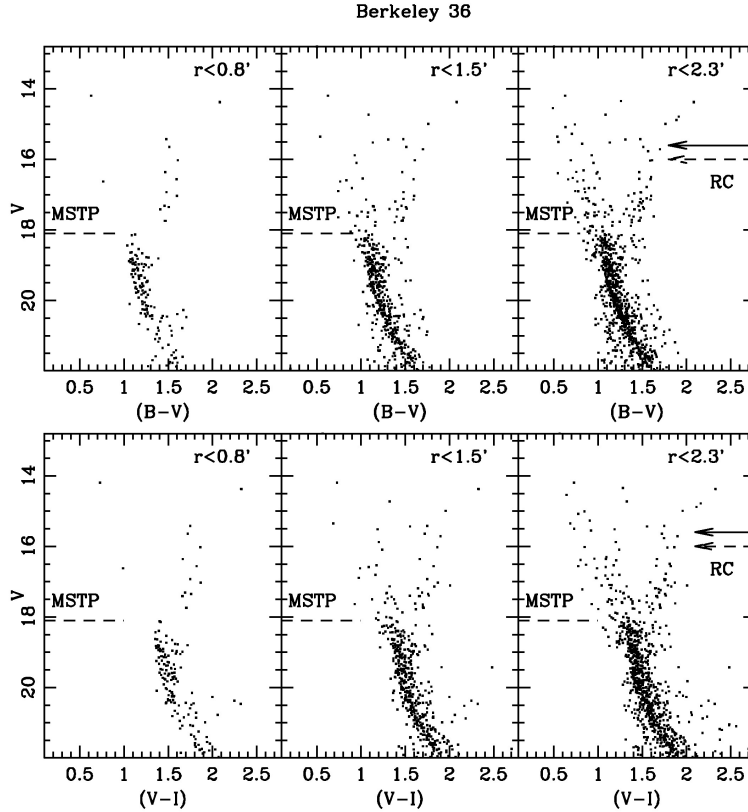


Figure 5.12: Upper panels show the V vs $(B - V)$ CMDs of Be 36 for different distances r from the cluster centre. Lower panels: the same but for the V vs $(V - I)$ CMDs. In the plots we indicate the levels of MSTP (dashed line) and RC. The dashed arrow is for the rejected level (see text) and the solid arrow is for the adopted RC level.

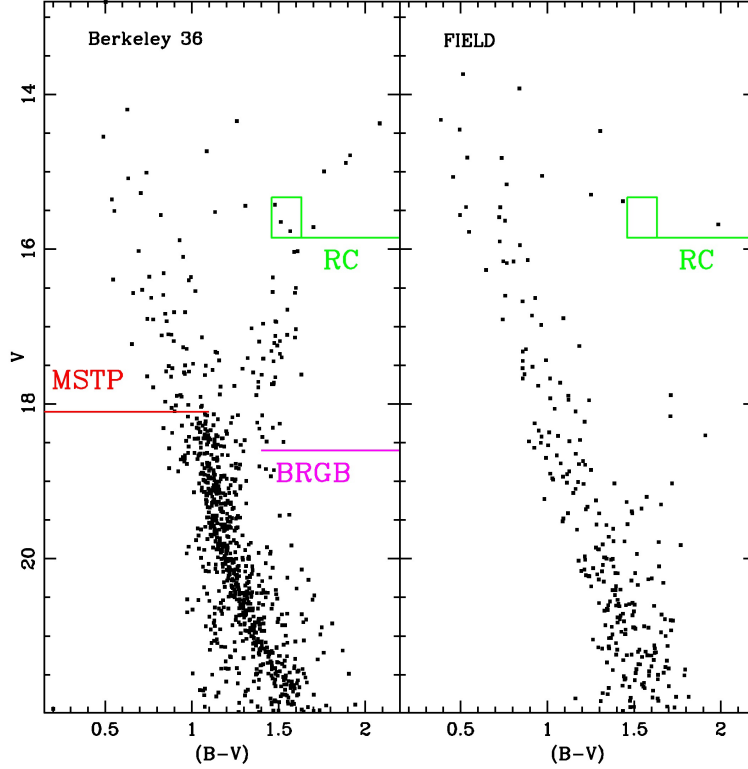


Figure 5.13: *Left panel*: CMD of Be 36 for stars falling inside a region of 2.3 arcmin from the cluster centre. We indicate the luminosity level of the MSTP, BRGB, and the RC. *Right panel*: CMD of an equal area of the comparison field.

comparison to an equal area of the external field (Fig. 5.13). Yet, the RC level is not so evident: we adopted as RC the small group of stars (two) located at $V \sim 16.0$ (in Fig. 5.12 we indicate with the dashed arrow the probable RC). However, even though we obtained a good fit of the RC and MSTP levels and of the MS shape, we could not obtain a good description of the RGB phase, too red in the synthetic CMDs. This is due to a too extended SGB phase, suggesting that we are adopting a too young age for the cluster. To help choose the best solution ever without a firm evidence of RC stars, we compared the CMD of Be 36 with those of two of the oldest clusters inside the BOCCE project: Berkeley 17 (Be 17) and Berkeley 32 (Be 32). Be 17 is among the oldest OCs of the Galaxy, with an age in the range 8.5-9.0 Gyr (Bragaglia et al., 2006a) while Be 32 is 5-5.5 Gyr old (Tosi et al., 2007). They both have sub-solar metallicity, as expected for Be 36 from previous analysis.

In Fig. 5.14 we show a comparison of the CMDs of Be 32, Be 36, and Be 17. In the left and right panels we present the CMDs of Be 32 and Be 17 using absolute magnitude M_V and intrinsic colour $(B-V)_0$. We used different limits on the magnitude (y-axis) to visually align the luminosity level of the evolutionary MSTP phase of the clusters, preserving the magnitude and colour range in order to properly compare the CMDs. We also show the isochrones which best fit the clusters according to our analysis (dashed line for Be 32 and solid line for Be 17). We overplot them on the CMD of Be 36 after a proper alignment in colour and magnitude. While both isochrones fit well the upper and lower MS, they bracket

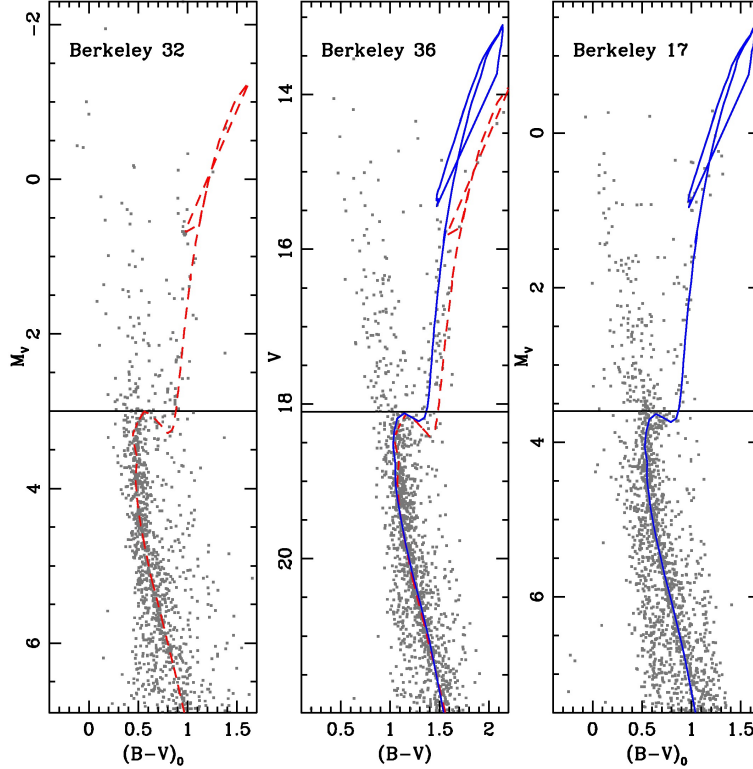


Figure 5.14: *Left panel:* CMD $M_V, (B - V)_0$ of Be 32. The dashed line is the best fit solution described in Tosi et al. (2007): $Z = 0.008$, age 5.2 Gyr, $E(B - V) = 0.12$, and $(m - M)_0 = 12.6$ for the BBC models. *Central panel:* CMD of Be 36 with the overplot of the best fit isochrones of Be 32 (dashed line) and Be 17 (solid line). *Right panel:* CMD $M_V, (B - V)_0$ of Be 17. The solid line is the best fit solution for the BBC models described in Bragaglia et al. (2006a): $Z = 0.008$, age 8.5 Gyr, $E(B - V) = 0.62$, and $(m - M)_0 = 12.2$. We used different limits on the magnitude (y-axis) for the three plots in order to visually align the evolutionary MSTP phase of the clusters but preserving the magnitude and colour range for a easier comparison. The solid horizontal lines set the MSTP level.

the RGB of Be 36 on the red and blue side.

This indicates that Be 36 is in an evolutionary status intermediate between that of Be 32 and Be 17. In particular, we can discard a cluster age younger than about 5 Gyr, as it would imply a more extended SGB and a redder RGB, while the older isochrone shown in the comparison sets a upper limit (8.5 Gyr) to the cluster age. Assuming the ages of Be 32 and Be 17 as limits for Be 36, the corresponding most probable RC locus for this cluster is at $V \sim 15.5$ and $(B - V) \sim 1.55$ (solid arrow on the right in Fig. 5.12). The three stars enclosed in the box in Fig. 5.13 are very few but likely to be cluster members as they are positioned near the cluster centre.

Having so decided the RC position and an age range, we applied the usual method of analysis, taking into account the very scattered characteristic of the CMD. We adopted a higher differential reddening of 0.15, the only viable solution to reproduce the MS spread, and a binary fraction of 25%. Given the more scattered appearance, these values have larger

uncertainties than for the two other clusters. Keeping fixed these parameters we investigated the possibility to fit simultaneously the MSTP, BRGB, and RC luminosities by adjusting the age, the mean Galactic reddening, and the distance modulus.

Also for Be 36 we restricted our analysis to models with sub-solar metallicity: a metallicity of $Z = 0.02$ can not match at the same time $B - V$ and $V - I$, predicting a RGB with a strong inclination in the upper part. In contrast with what was found for Be 27 and Be 34, all the explored models predict a lower MS slightly bluer than observed. We could not use the FRANEC models as they have incomplete evolutionary tracks for ages older than 5 Gyr for subsolar metallicities. Fig. 5.15 displays the best fitting CMD for each set of tracks compared with the observational CMD (upper panel). The results of the analysis are summarised in Tab. 5.6.

The FST models can reproduce quite well the magnitudes and colours of the indicators, even though they predict a bluer MS for $V > 21$. We find a better match for models with $Z = 0.006$. For $Z = 0.01$, when the synthetic $B - V$ CMD is correct, the $V - I$ always turns out to be slightly bluer than observed. The best solution is obtained for the models with $Z = 0.006$, a cluster age of 7.0 ± 1.0 Gyr, a mean reddening of $E(B - V) = 0.53 \pm 0.04$, and a distance modulus $(m - M)_0 = 13.15 \pm 0.13$. For $Z = 0.01$ we find the same age of 7.0 ± 1.0 Gyr, $E(B - V) = 0.48 \pm 0.04$, and $(m - M)_0 = 13.19 \pm 0.08$.

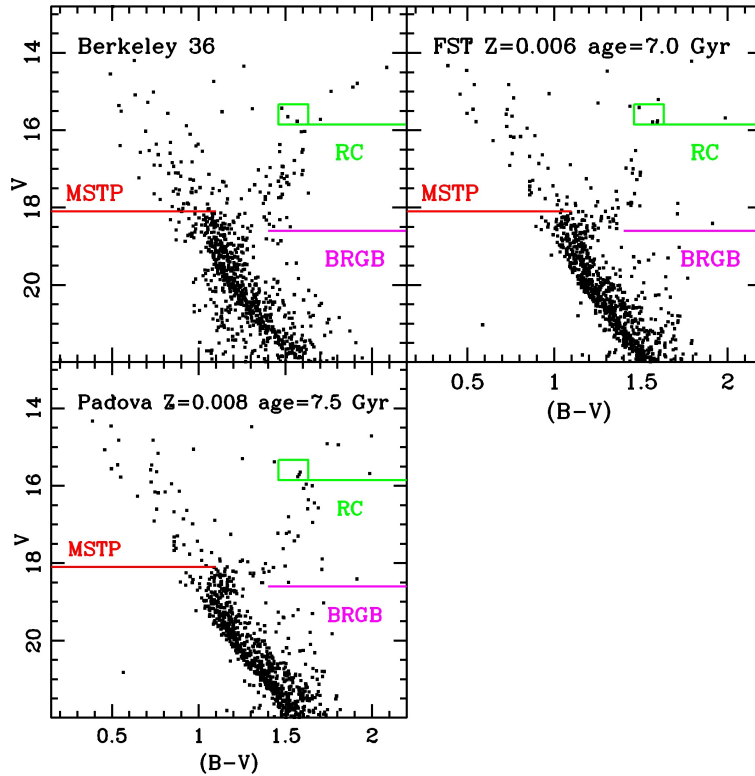


Figure 5.15: Top panel: CMD of stars inside $2.3'$ radius area of Be 36. The central panel shows the best fitting CMD obtained with the FST models: $Z = 0.006$, age 7.0 Gyr, $E(B - V) = 0.53$ and $(m - M)_0 = 13.15$; the bottom panel is the synthetic CMD obtained with the BBC tracks: $Z = 0.008$, age 7.5 Gyr, $E(B - V) = 0.51$, and $(m - M)_0 = 13.1$.

Using the BBC models we find a good match for the MSTP, BRGB and RC levels with a better description of the MS (bluer only for $V > 21.5$). The best matches are obtained with models with $Z = 0.008$, when the synthetic CMDs can match the observed one both in $B - V$ and $V - I$ at the same time. We find a cluster age of 7.5 ± 1.0 Gyr, $E(B - V) = 0.51 \pm 0.04$, and $(m - M)_0 = 13.1 \pm 0.13$; the synthetic CMD obtained with these parameters reproduces quite well the MS and RGB shape and colour, even if it can not reproduce correctly the over-density observed at $V \sim 17$ along the RGB.

The comparison with previous results (Ortolani et al., 2005) shows a significant discrepancy in the cluster age and therefore in the determination of cluster reddening and observed distance modulus. This is in part due to the choice of the MSTP level and in part to the disagreement in the photometries (see Sec. 2.4). Concerning the age they set the MSTP level half a magnitude brighter than our estimation, adopting the same RC level we use for the analysis. This implies a younger age and a smaller distance modulus estimations. The difference in the reddening estimates is mainly due to the remarkable disagreement in the photometries.

Table 5.6: Cluster parameters derived using different models.

Model	age (Gyr)	Z	$(m - M)_0$ (mag)	$E(B - V)$ (mag)	d_\odot (kpc)	R_{GC}^a (kpc)	z (pc)
Be 27							
BBC	1.7	0.004	13.05	0.52	4.07	11.76	184.8
FST	1.5	0.006	13.20	0.50	4.37	12.03	198.0
FRA	1.2	0.010	13.10	0.50	4.17	11.85	189.1
Be 34							
BBC	2.3	0.008	14.20	0.59	6.91	14.26	229.4
FST	2.1	0.010	14.30	0.57	7.24	14.57	240.2
FRA	1.6	0.010	14.20	0.65	6.91	14.26	229.4
Be 36							
BBC	7.5	0.008	13.1	0.51	4.17	11.24	-43.7
FST	7.0	0.006	13.15	0.53	4.27	11.32	-44.7

^a $R_\odot = 8$ kpc is used to compute R_{GC}

5.2 NGC 2849, NGC 6134

The analysis of these two clusters is described in Ahumada et al. (2013) and here the main results of the analysis are reported. NGC 2849 is a relatively compact cluster with an apparent diameter of $\sim 3'$. It is located in the third Galactic quadrant in the Vela constellation ($l = 265.27^\circ$, $b = +6.36^\circ$). NGC 6134 is located near the Galactic plane in the Norma constellation, at less than 26° from the Galactic centre direction ($l = 334.92^\circ$; $b = -0.20^\circ$). In Tab. 5.7 are summarised the results of previous studies.

Table 5.7: Literature values for the clusters NGC 2849 and NGC 6134.

E(B-V)	$(m - M)_0/D_\odot$	age (Gyr)	metallicity	Reference
NGC 2849				
0.46–0.57	14.02±0.4	0.63	$Z = 0.02$	Ahumada (2003)
0.50±0.04	13.93±0.17	0.63±0.13	$[\text{Fe}/\text{H}] = -0.23 \pm 0.12$	Kyeong et al. (2004)
NGC 6134				
0.45	0.7 kpc	0.7	-	Lindoff (1972)
0.46±0.03	9.8	0.9	-	Kjeldsen & Frandsen (1991)
0.35 ± 0.02	0.76 kpc	-	$[\text{Fe}/\text{H}] = -0.05 \pm 0.12$	Claria & Mermilliod (1992)
0.365 ± 0.04	-	0.69 ± 0.10	$[\text{Fe}/\text{H}] = +0.28 \pm 0.02$	Bruntt et al. (1999)
0.29–0.37	1.08±0.05 kpc	1.25	-	Ahumada (2002)
0.355 ± 0.005	-	-	$[\text{Fe}/\text{H}] = +0.15 \pm 0.03$	Carretta et al. (2004)

5.2.1 Observations and data reduction

NGC 2849 was observed on May 10 1997 with the Dutch telescope of 0.91 m, located at La Silla Observatory (ESO, Chile). The TK512CB CCD Tektronix of 580×520 pixels was mounted at the direct camera. The observed FoV was 4.2×3.8 arcmin². The filters used were *B* (ESO#419), *V* (ESO#420), and *I* (ESO#465). We observed the centre of the cluster (FC) and a region (FN) located $\sim 2'$ to the north of FC (see Fig. 5.16). Seeing values were lower than $1.5''$; both FC and FN were observed with airmass values less than 1.45. We also observed standard stars from Landolt (1992) to calibrate the instrumental magnitudes to the standard system.

In Fig. 5.16 we present also the observed region of NGC 6134. It was observed on May 15-16 2001 with the Danish Faint Object Spectrograph and Camera (DFOSC) mounted at the Danish 1.54 m telescope, La Silla Observatory (ESO, Chile). The FoV of the instrument is 14.0×13.7 arcmin². The observations were taken with the filters *U* (ESO#632), *B* (ESO#450), *V* (ESO#451) and *I* (ESO#425). Despite the poor seeing values ($\sim 2''$ to $\sim 3''$) during the first night (N1), we also observed an external field (Ext) distant $\sim 40'$ from the cluster centre to be used for comparison and field fore/background contamination. The second night (N2) was photometric and seeing values ranged from $1.1''$ to $1.4''$. All the observations were obtained with airmasses lower than 1.22 as we see from Table 1. To calibrate instrumental magnitudes to the standard system we observed two regions from Landolt's (1992) list.

The standard data reduction applied to photometric images of the BOCCE OCs was applied also for these two clusters. For the clusters and their external fields we constructed the point spread function (PSF) determined from well-isolated stars in each frame (see Sec. 4.1 for the description of the method used).

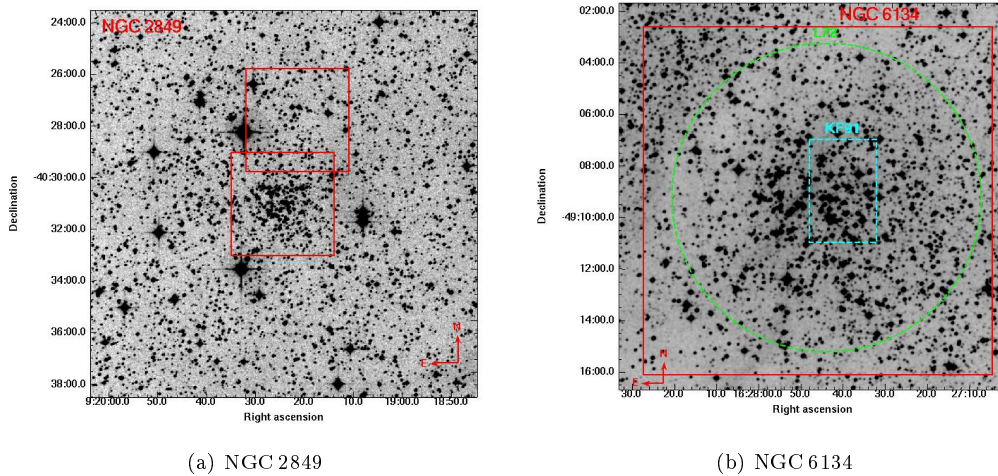


Figure 5.16: DSS images of NGC 2849 and NGC 6134. (a) Centre of NGC 2849 (FC) and a region at the north (FN). Red squares indicate the observed zones. The map is $15' \times 15'$. North is up and east is left. (b) image of NGC 6134. The red square indicates the field observed by us, the cyan square indicates the field observed by Kjeldsen & Frandsen (1991), and the green circle indicates the field observed by Lindoff (1972). The map is $15' \times 15'$. North is up and east is left. The external field, not shown here, is about $40'$ south of the cluster centre.

The x and y coordinates of the final catalogue obtained for each cluster were then aligned to the astrometric catalogue Guide Star Catalogue-II (GSC II) to obtain equatorial coordinates. These catalogues are made available only in electronic form through the CDS portal.

The completeness of our photometry for both clusters was derived using the usual method of artificial stars. Tab. 5.8 shows the completeness factor for the FC and FN regions of NGC 2849, while Tab. 5.9 shows that for NGC 6134 and its external field. For magnitudes brighter than 15.5 mag, the completeness is 100 per cent.

Table 5.8: Completeness for NGC 2849 in the *BVI* filters.

Mag	Compl <i>V</i>		Compl <i>B</i>		Compl <i>I</i>	
	FC	FN	FC	FN	FC	FN
15.5	0.980	0.994	0.974	1.000	1.000	1.000
16.5	0.974	0.994	0.980	0.990	0.959	0.990
17.5	0.957	0.983	0.977	0.983	0.958	0.996
18.5	0.947	0.963	0.952	0.974	0.928	0.968
19.5	0.905	0.946	0.939	0.968	0.862	0.910
20.5	0.857	0.905	0.894	0.935	0.658	0.796
21.5	0.620	0.724	0.743	0.867	0.240	0.300
22.5	0.226	0.306	0.390	0.470	0.020	0.030
23.5	0.023	0.021	0.044	0.077	0.000	0.000
24.5	0.000	0.000	0.001	0.001	0.000	0.000

Table 5.9: Completeness for NGC 6134 and its external field in the different filters.

Mag	Compl <i>U</i>		Compl <i>B</i>		Compl <i>V</i>		Compl <i>I</i>	
	Cluster	Ext	Cluster	Ext	Cluster	Ext	Cluster	Ext
15.5	0.995	1.000	1.000	1.000	1.000	1.000	0.972	1.000
16.5	0.996	1.000	1.000	1.000	1.000	0.973	0.954	1.000
17.5	0.988	0.989	0.973	0.966	0.920	0.907	0.996	
18.5	0.980	0.970	0.945	0.955	0.871	0.815	0.799	
19.5	0.966	0.973	0.910	0.914	0.765	0.604	0.558	
20.5	0.860	0.932	0.824	0.863	0.609	0.144	0.277	
21.5	0.252	0.889	0.698	0.723	0.371	0.008	0.059	
22.5	0.002	0.637	0.375	0.261	0.088	0.000	0.011	
23.5	0.000	0.075	0.043	0.009	0.005	0.000	0.000	
24.5	0.000	0.004	0.004	0.000	0.000	0.000	0.000	

5.2.2 Colour-Magnitude Diagrams

A more detailed discussion of the evolutionary sequences and the properties of both clusters can be found in next sections, we present here a short description of the main features.

Fig. 5.17 shows the V , $B-V$ and V , $V-I$ diagrams for the centre of NGC 2849 (FC, upper panels) and for the more external field (FN, lower panels). We see that V reaches as deep as 22 mag, and for FC the main sequence (MS) and the turn-off (TO at $V \sim 15.8$, $B - V \sim 1.2$, $V - I \sim 1.3$) are clearly visible. To better discriminate between cluster and field stars, in Fig. 5.18 we present V , $B-V$ CMDs for different radial distances for FC and FN stars. In the external part we see what seems the main sequence of field disc stars, without a clear TO or evolved stars, while for the inner regions the structure of the OC is clearly visible, with a defined MS TO and a red clump (RC).

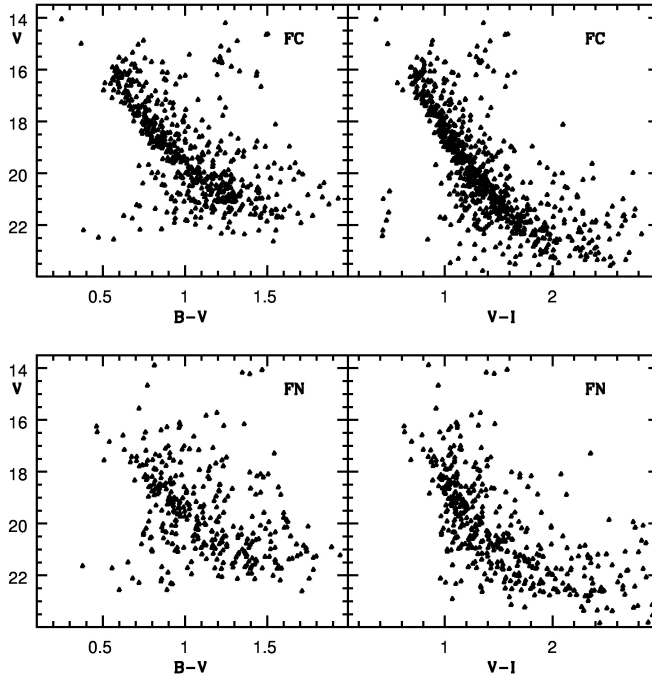


Figure 5.17: V , $B-V$ and V , $V-I$ CMDs for NGC 2849 (FC, upper panels) and an the northern field (FN, lower panels).

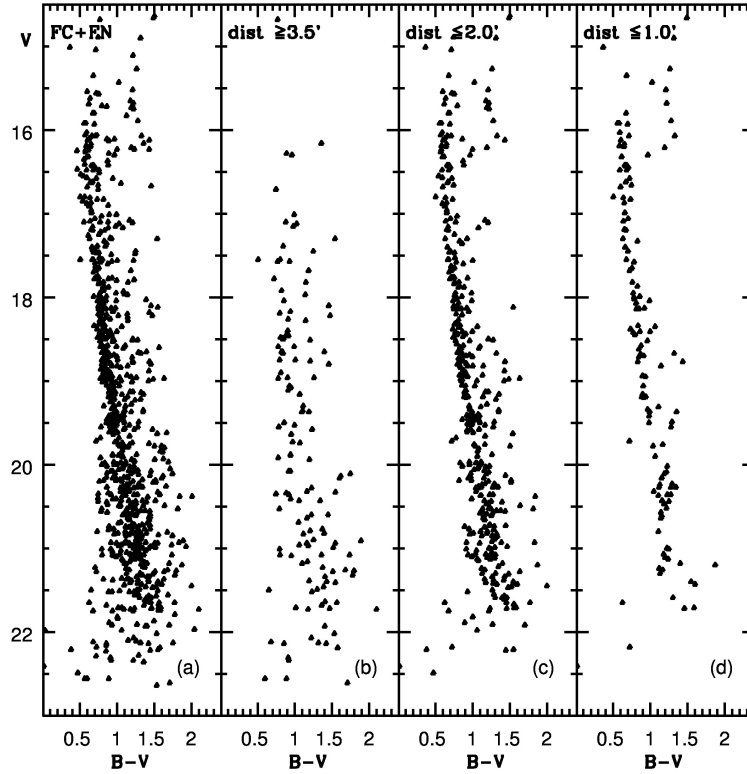


Figure 5.18: Radial V , $B-V$ diagrams for NGC 2849. FC and FN stars (a), stars in the external part, with distances $\geq 3.5'$ (b), distances $\leq 2.0'$ (c) and distances $\leq 1.0'$ (d). The centre of the stars distribution is assumed as the FC centre.

For NGC 6134, Fig. 5.19 presents V , $B-V$, V , $V-I$ and U , $U-B$ diagrams for the cluster (upper panels); for the external field we only present two CMDs: V , $B-V$ and V , $V-I$ (lower panels). In the upper panels we see not only a very well defined MS extending as deep as $V \sim 22$, but also the RC near $V = 12$, $B-V = 1.4$, and $V-I = 1.7$. We see that for $V \leq 13$ mag the external field (lower panels) is practically empty, and for $V \leq 15$ mag the external CMD is scarcely populated. In Fig. 5.20 we plot the CMD of NGC 6134 for subregions with different distance from the cluster centre. As usual, the main evolutionary features are better delineated in the inner regions, but the cluster is still evident at about $7'$ from its centre.

In the external field of NGC 6134 (Fig. 5.19) we see another sequence from $V \sim 20$, $B-V \sim 3.2$ to $V \sim 14$, $B-V \sim 2.0$, parallel to the MS. This sequence is due to the population of the disc, and in particular to RC stars at different distances and/or reddening (see e.g. Cignoni et al., 2008). One can immediately appreciate the different behaviour of this feature in the central and comparison fields; unfortunately we seem to have chosen a line of sight with somewhat different properties from the cluster's. Fortunately, this is true only for the fainter magnitudes; TO and RC are well constrained and the comparison to synthetic models is not hampered.

Another exotic feature of this cluster appears in the radial CMDs of Fig. 5.20. The central part of the cluster, i.e., for radii smaller than 2.0 arcmin, shows a striking MS gap at

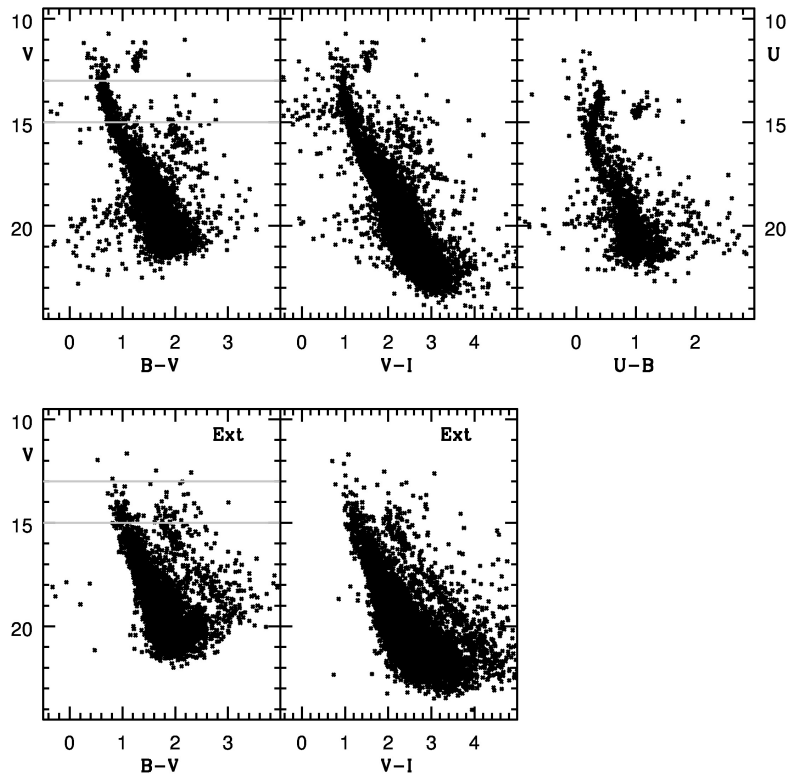


Figure 5.19: V , $B-V$ and V , $V-I$ CMDs for NGC 6134 (upper panels) and an external field (Ext, lower panels). The U , $U-B$ diagram is showed only for the cluster due to the absence of U data for the external field.

$V \sim 15$, $B - V \sim 0.9 - 1.0$, which partially disappears moving outwards. This gap is not a result of mismatches in our photometry. It was first detected by Kjeldsen & Frandsen (1991), who also discussed a similar case in the intermediate age OC IC 4651. The gap is a genuine cluster feature, masked at larger radii by the proportionally increasing contamination by foreground and background stars.

Similar gaps have been found also in very well studied systems, but their detection has been often complicated by low-number statistics, completeness issues, and field contamination. For instance, de Bruijne et al. (2000) identified two gaps at $B-V \sim 0.38$ and ~ 0.48 in the MS of the Hyades, an OC with age and metallicity (about 0.7 Gyr, $[\text{Fe}/\text{H}] = +0.17$, and negligible reddening according to the WEBDA) similar to NGC 6134. The redder gap had also been noted before by Bohm-Vitense (1995). D’Antona et al. (2002) could explain the bluer gap adopting the FST model tracks to simulate the Hyades; however they found that another explanation is needed for the redder gap. Furthermore, Subramaniam & Bhatt (2007) found an indication of a MS gap at $(B-V)_0 \sim 0.38$ in the young (400 Myr) cluster NGC 7245 and Giorgi et al. (2002) found a pronounced gap in the very young (50 Myr) OC NGC 2571 at $0.15 < (B-V)_0 < 0.25$ demonstrating that this gap is not produced by a random process but is a real lack of stars in a given magnitude interval. Balaguer-Núñez et al. (2005) applied a significance test to several OCs with evidence of multiple MS gaps, namely NGC 2548, Pleiades, Hyades, NGC 1817, and M67, finding no clear correlation with

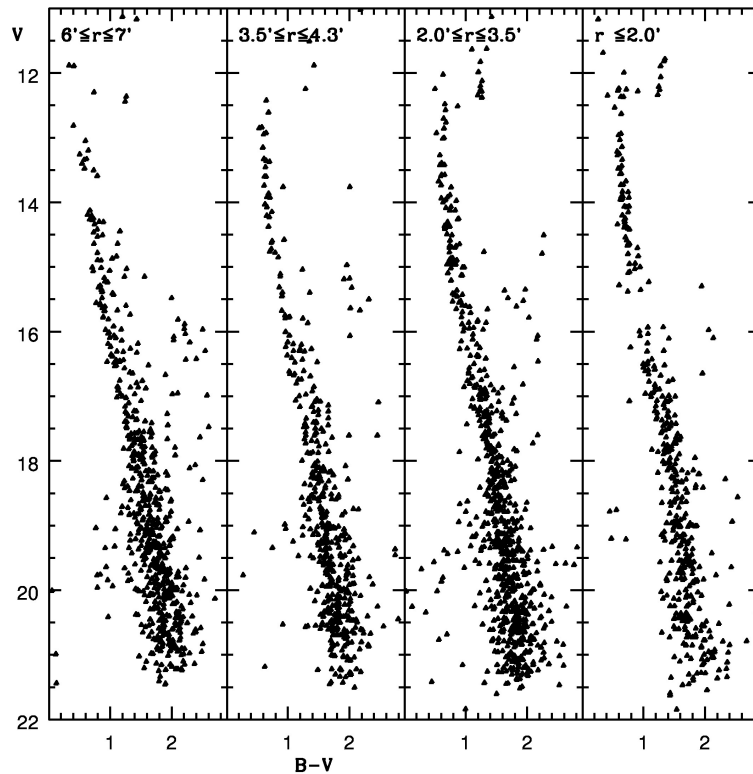


Figure 5.20: V , $B-V$ diagrams for NGC 6134 in consecutive annular regions of approximately equal area around the adopted cluster centre.

age and metallicity. The same authors suggested that all these gaps could be classified into four main loci with colours $(B-V)_0 \sim 0.3, 0.4, 0.7, 0.9$, respectively.

Among field stars, the existence of MS gaps is still debated. Using very precise temperatures (computed from line depth ratios) for 248 F-K field dwarfs of about solar metallicity with Hipparcos parallaxes, Kovtyukh et al. (2004) found a gap at $(B-V)_0 \sim 0.7$ (which is close, but not identical, to the locus of our gap). Interestingly, the authors noted that this gap is located near the hot edge of the lithium depression (where lithium is depleted by orders of magnitude) in the field dwarfs, with dwarfs on the red side of the gap showing a large spread in lithium abundance and dwarfs located on the blue side showing low abundances. Given the dependence of the surface Li abundance to the thickness of the convective envelope, Kovtyukh et al. (2004) suggested a connection between this MS gap and convection.

5.2.3 Clusters Parameters

We derived the main clusters parameters using the synthetic CMD method (see Sec. 4.2). In order to lift or reduce the age-metallicity-reddening degeneracy, only those parameters that can actually reproduce the observed data in both V , $V-I$ and V , $B-V$ planes are considered acceptable solutions (see however Sec. 4.2).

NGC 2849

To help visualising the data-model comparison, colour edges and magnitude levels of significant stellar phases are indicated on the observational CMD in Fig. 5.21 with lines of different colours: the bluest MS point (“blue edge”, BE), the colour and luminosity of the reddest MS point (“Red Hook”, RH), and bona fide RC stars.

Our simulations indicate that photometric errors and binaries alone cannot explain the MS width. A differential reddening $\Delta E(B - V)$ in the range $\sim 0.05 - 0.1$ mag would be enough to reproduce both the MS width and the RC shape. Given this uncertainty, the current data do not allow us to reach a firm conclusion about the binary fraction. Hence, we keep this parameter fixed at 30%. “Reasonable” values often found in past analyses range between 25% and 30% for this parameter.

Fig. 5.21 show the best-match FST, BBC, and FRA synthetic CMDs (clockwise from the top-right panel) computed for solar metallicity. All models fit reasonably well both the $V, V-I$ and $V, B-V$ CMDs with approximately the same reddening. The only drawbacks are *i*) the RC colour, which always appears slightly redder (and sparser for the BBC model) than the observational counterpart, probably suggesting a residual metallicity mismatch, and *ii*) the predicted number of RC stars, which outnumbers the observed one, but up to a factor of two.

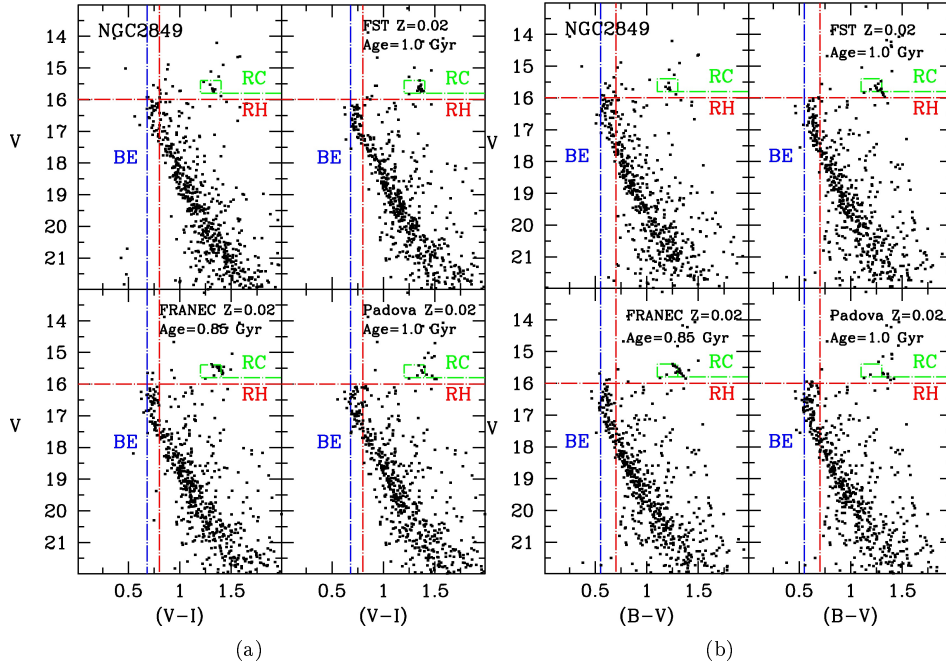


Figure 5.21: (a) The upper-left panel shows the $V, V-I$ CMD for NGC 2849. The magnitude and colours of main evolutionary features are indicated with red (RH), green (RC), and blue (BE) dot-dashed lines. The other panels, clockwise from this, show the best fitting synthetic CMDs for the following parameters: FST $Z = 0.02$, age 1.0 Gyr, $E(B - V) = 0.325 \pm 0.025$ and $(m - M)_0 = 13.8$; BBC $Z = 0.02$, age 1.0 Gyr, $E(B - V) = 0.285 \pm 0.025$ and $(m - M)_0 = 13.9$; FRA $Z = 0.02$, age 0.85 Gyr, $E(B - V) = 0.315 \pm 0.025$ and $(m - M)_0 = 13.95$. The adopted percentage of binaries (with random mass ratio) is always 30%. (b) The same but for the $V, B-V$.

Our best estimate of the age of NGC 2849 is between 0.85 Gyr (FRA solution; models without overshooting always predict smaller values in this age range) and 1.00 Gyr (FST and BBC solutions). Both are slightly higher than the 0.6 Gyr found by Kyeong et al. (2004); however, their data are much shallower and the isochrone they chose does not seem to reproduce the RC. The results are summarised in Tab. 5.10.

NGC 6134

NGC 6134 is more populous than NGC 2849, providing a better opportunity to compare data and models. Unfortunately, we cannot take full advantage of the external field because its CMD (see Fig. 5.19) is clearly different from the field contamination in NGC 6134’s CMD, as already remarked in Sec. 5.2.2. While the NGC 6134 contamination shows a mildly visible RC population located 2-3 mag below the cluster RC and 1 mag to the right of the cluster MS, the comparison field CMD shows a clear stripe of RC stars running parallel to the MS, from $V=14$ down to the completeness limit. Such a difference is intriguing because it contrasts with a standard thin disc model. NGC 6134’s field is slightly closer to the Galactic plane, hence its contamination was expected higher and more reddened than the external field’s. A possible explanation may be that the reddening plane is tilted with respect to the Galactic plane. Indeed, Joshi (2005) finds that, around the Galactic longitude of NGC 6134, the plane defined by the reddening material might be inclined below the formal plane. In this way, the external field may be closer to the “reddening plane” than NGC 6134’s field and, therefore, affected by reddening for a longer distance. However it still remains difficult to explain why the external field is globally more populated.

As for NGC 2849, the most relevant evolutionary phases are indicated with lines of different colours in Fig. 5.22. A visual inspection of the figure reveals a BE around $B - V \sim 0.57$, a RH around $V \sim 12.5$ and $B - V \sim 0.57$, and a well defined RC concentrated around $V = 12.25$.

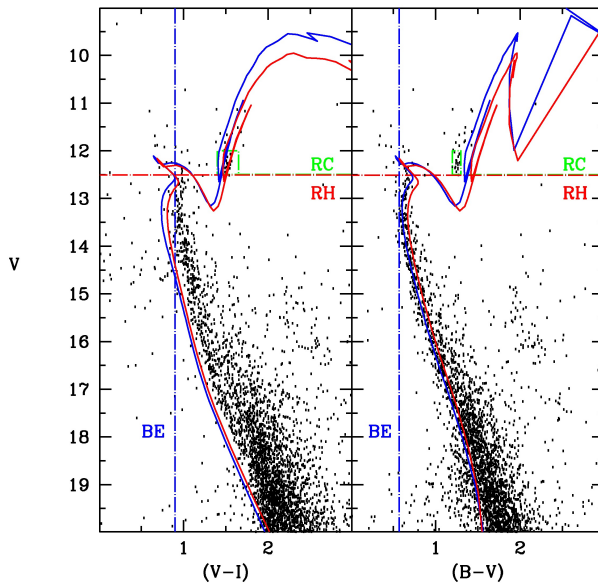


Figure 5.22: V , $V-I$ and V , $B-V$ for NGC 6134. Magnitude and colours of main evolutionary features follow the same nomenclature of Fig. 5.21. The solid lines show the Padova isochrones (Marigo et al., 2008) for 1 Gyr and $Z = 0.02$ (red) or $Z = 0.03$ (blue).

We find that no synthetic model for any of the three sets of tracks was able to simultaneously reproduce both the $B-V$ and $V-I$ colours of all the evolutionary phases. When models

are tuned to fit the MS in $B-V$, the synthetic $V-I$ colours turn out to be systematically too blue. We also tried newer Padova isochrones (Marigo et al., 2008) with updated physical inputs and colour transformations, but the improvement was not significant (see Fig. 5.22). Moreover, the same effect was found also using the BaSTI (e.g., Pietrinferni et al., 2004) and Victoria (VandenBerg et al., 2006) sets of stellar models (the corresponding isochrones are not shown in figure for clarity).

A similar problem had already been found for other clusters of the BOCCE project, including NGC 2849. However, in all those cases the mismatch was clearly a function of the assumed metallicity: larger for metallicities too different from the actual one, and increasingly small when approaching the right Z . In this case, the size of the discrepancy doesn't change with metallicity. We believe that the discrepancy can probably be attributed to the inability of past and present atmosphere models to reproduce real colours at high metallicity (i.e., low temperature), or, less probably, to a calibration issue with the I -magnitude (see below), or even less probably, to some difference in the reddening law toward this particular cluster. We further discuss this problem in Sec. 4.2.2.

Given the difficulty to define the metallicity and the reddening from the simultaneous fit of the $B-V$ and $V-I$ CMDs, we limited our analysis to constraining the age and distance of NGC 6134, assuming the spectroscopic abundance and the reddening derived from the $U-B$ vs $B-V$ diagram (see below). Then the most likely age and distance are determined by the simulated CMD which best fits the magnitude and colour difference between the RC and TO⁵. We chose to use only the V , $B-V$ CMD for this computation. There is no guarantee that the colour transformations, if they truly are the culprits, work better in this colour. However, these are the filters we always have for all the BOCCE clusters, so we stick to them to maximise the homogeneity of treatment.

There is some dispersion in literature reddening values for NGC 6134 (see Introduction). Because, as already mentioned, the metallicity and age of the Hyades are similar, we compared our data with UBV photoelectric data from Johnson & Knuckles (1955) to derive a value for the reddening, using the two-colours diagram. In Fig. 5.23 we show the $B-V$, $U-B$

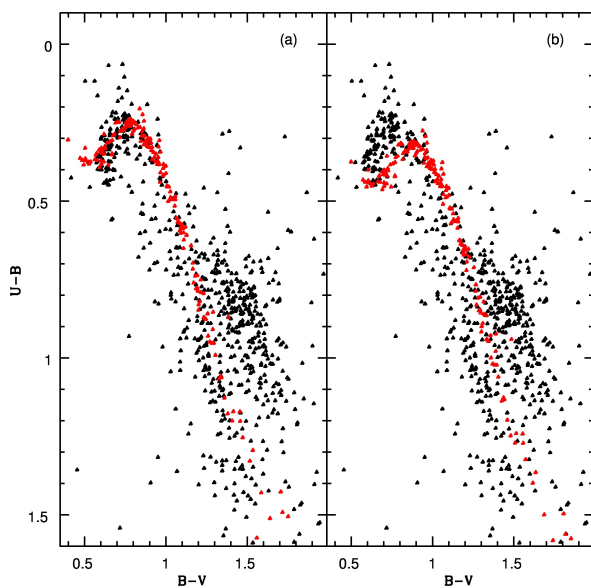


Figure 5.23: $U-B$, $B-V$ diagrams for NGC 6134 (black points) and the Hyades (red points). We plot stars with distances $\leq 4'$ from the cluster centre dereddened using two different colour excesses: $E(B-V) = 0.35$ (left-hand panel) and $E(B-V) = 0.45$ (right-hand panel). The fit is much better with the former value.

⁵These differential features are less affected by reddening and metallicity.

diagram for NGC 6134 stars with distances less than $4'$ from the centre (in black) and for the Hyades stars (red). The Hyades reddening is very low, $E(B-V) \leq 0.01$ (Taylor, 2006). In Fig. 5.23 we dereddened our data using two values, $E(B-V) = 0.35$ and 0.45 , which represent the ones most commonly found in literature. They correspond to $E(U-B) = 0.25$ and 0.32 , according to the relation $E(U-B)/E(B-V) = 0.70 + 0.05 E(B-V)$ (Fitzgerald, 1970). The figure clearly shows that the lower reddening gives a much better fit, so it should be preferred. We note that this is also very close to the reddening derived by Carretta et al. (2004) in a totally independent way, based on spectroscopically determined temperatures and relations with intrinsic colours.

For all simulations we assumed a fraction of binaries of 30% and only the V , $B-V$ is used for the fit. The adopted metallicities are the closest to the spectroscopic value. Fig. 5.24

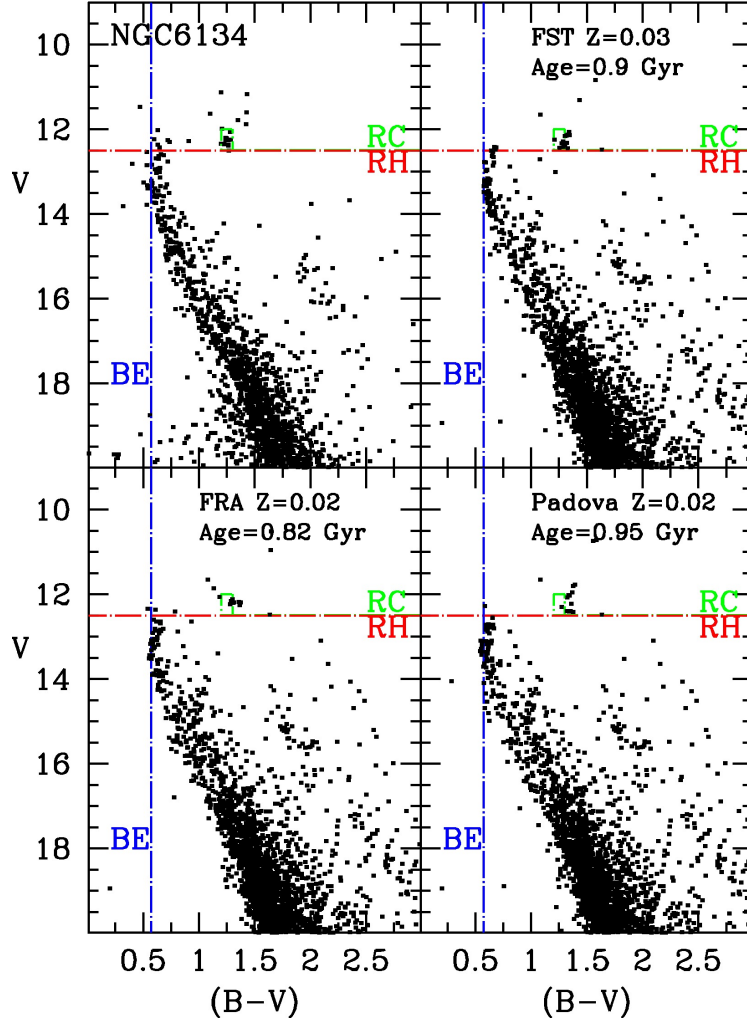


Figure 5.24: V , $B-V$ CMD for NGC 6134. Magnitude and colours of main evolutionary features follow the same nomenclature of Fig. 5.21. The other panels, clockwise from this, show the best fitting synthetic CMDs for the following parameters: FST $Z = 0.03$, age 0.9 Gyr, $E(B-V) = 0.33$, and $(m-M)_0 = 10.5$; BBC $Z = 0.02$, age 0.95 Gyr, $E(B-V) = 0.33$, and $(m-M)_0 = 10.5$; FRA $Z = 0.02$, age 0.82 Gyr, $E(B-V) = 0.35$, and $(m-M)_0 = 10.5$. The adopted percentage of binaries (with random mass ratio) is always 30%.

shows the best fitting CMDs according to the FST (top right panel), PADOVA (bottom right panel), and FRANEC (bottom left panel) models. The results are summarised in Tab. 5.10. Our best age estimate is between 0.82 and 0.95 Gyr.

Table 5.10: Cluster parameters derived using different models.

Model	age (Gyr)	Z	$(m - M)_0$ (mag)	$E(B - V)$ (mag)	d_\odot (kpc)	R_{GC}^a (kpc)	z (pc)
NGC 2849							
BBC	1.00	0.020	13.90	0.285	6.03	10.40	667.5
FST	1.00	0.020	13.80	0.325	5.75	10.23	637.4
FRA	0.85	0.020	13.95	0.315	6.16	10.49	683.0
NGC 6134							
BBC	0.95	0.020	10.50	0.33	1.26	6.88	-4.4
FST	0.90	0.030	10.50	0.33	1.26	6.88	-4.4
FRA	0.82	0.020	10.50	0.35	1.26	6.88	-4.4

^a $R_\odot = 8$ kpc is used to compute R_{GC}

OCs colours: a more general issue

Before discussing the possibility that all the considered evolutionary models are unable to consistently fit the observed CMDs in all colours, we need to exclude that there is a problem with our I photometry. Unfortunately, no direct comparison with literature photometry is possible in this filter (see Sec. 2.3), so we took a more devious route. Suspecting that problems could arise at high metallicity, we selected other OCs of super-solar metallicity according to high resolution spectroscopy and with B, V, I photometry available. We then compared data and models. Using the WEBDA, we finally selected five metal rich OCs of different ages, namely NGC 2477, NGC 2539, NGC 7142, NGC 2112, and NGC 6705 (M11)⁶.

Fig. 5.25 shows the $V, B-V$ (left panels) and $V, V-I$ (right panels) CMDs compared to the corresponding best fitting Padova isochrones (obtained from the official website <http://stev.oapd.inaf.it/cmd>, see Marigo et al. 2008). The isochrones are taken already transformed from luminosity and temperature to magnitude and colour, at variance with what we usually do with the evolutionary tracks, where we apply our own transformations. The age is taken from the literature, while the metallicity is fixed at $Z = 0.03$ (red isochrones, but for comparison also solar isochrones are shown). Distance and reddening are estimated by matching the $V, B-V$ CMD, while no attempt is done to fit the $V, V-I$ one (the relation $E(V-I) = 1.3 \times E(B-V)$ is used). This comparison highlights two important biases. First, most of these OCs exhibit the same problem observed in NGC 6134: when isochrones match well in $B-V$, they systematically fail in $V-I$, with the exception of NGC 6705. Second, in the $V, B-V$ CMDs most models deviate systematically from the observed MS at faint magnitudes. Moreover, in some OCs the two biases may be at work simultaneously (see e.g., NGC 2112) and the oldest OCs (those with the coolest TOs) in the sample, NGC 2112 and NGC 7142, show the largest discrepancies. This may be a hint of an atmosphere issue.

One caveat to these results could be that the slightly different metallicity of each OC may account for a part of the mismatch. However, also the adoption of a solar metallicity (see

⁶Their $[Fe/H]$ values are: +0.07 (NGC 2477, Bragaglia et al., 2008); +0.08 (NGC 2539, Santos et al., 2009); +0.14 (NGC 7142, Jacobson et al., 2008); +0.16 (NGC 2121, Carraro et al., 2008); +0.17 (NGC 6705, Gonzalez & Wallerstein, 2000). We did not attempt any homogenisation of the metallicity scales, the only relevant information is that all these OCs have super-solar metal abundance.

the blue isochrones in Fig. 5.25) instead of $Z = 0.03$ does not change our conclusions. Given the similarity of results for the BaSTI and Victoria isochrones in the case of NGC 6134, we did not attempt a similar test with them.

When taken together these findings are a strong warning against any blind attempt to match the CMD without a multicolour analysis. Theoretical predictions will require a much firmer evaluation of colour-temperature relations.

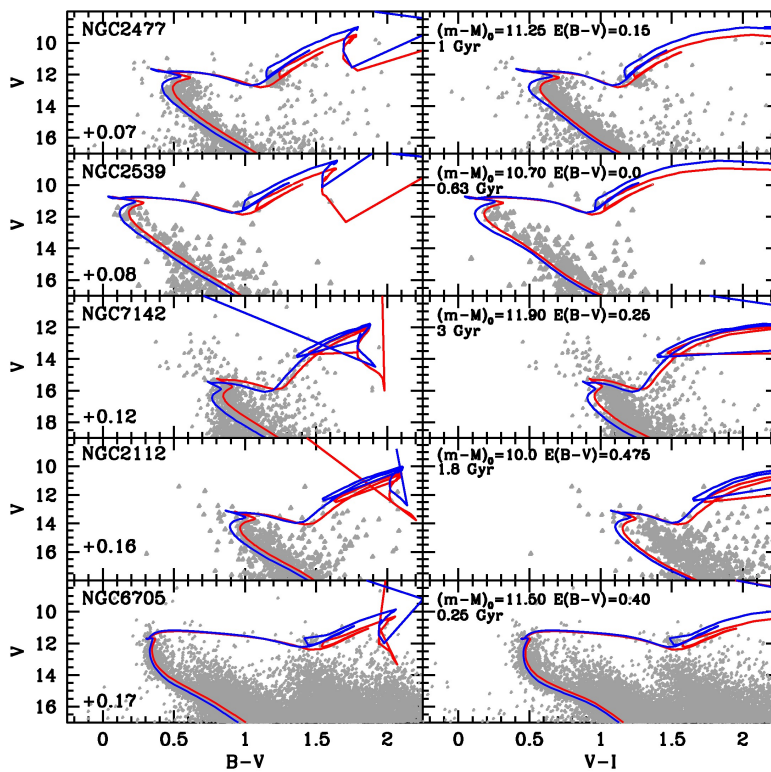


Figure 5.25: CMDs of five metal rich OCs, $V, B-V$ on the left, $V, V-I$ on the right, with overlaid the best fitting isochrones (see text for details).

Chapter 6

The advantage of wide-fields for Open Clusters

This chapter describes the photometric analysis for the last five OCs of the BOCCE project studied during my thesis. Be 81, NGC 1817, NGC 2141, NGC 2158, and Tr 5 are old OCs observed with large FoVs that permitted to determine accurate cluster's structural properties. The results obtained for Be 81, NGC 1817, and NGC 2141 are published in Donati et al. (2014a) while NGC 2158 and Tr 5 are under study. The properties of the OCs of the BOCCE project with complete photometric analysis (34, including the eight described in the present thesis), are summarised and discussed in the context of the Galactic disc in Ch. 8.

6.1 Berkeley 81, NGC 1817, NGC 2141

In the following we discuss the photometric analysis of three OCs that were observed on a large field of view (about $20' \times 20'$) with the Large Binocular Camera (LBC) at the 8-meter class telescope Large Binocular Telescope (LBT, see Giallongo et al. 2008): NGC 1817 (Galactic coordinates $l = 207.8^\circ, b = 2.6^\circ$), NGC 2141 ($l = 214.2^\circ, b = 1.9^\circ$), and Berkeley 81 (Be 81, $l = 227.5^\circ, b = -0.6^\circ$). These clusters have been chosen also because they could be targets of the Gaia-ESO Survey (see Ch. 3 for a description).

NGC 2141 and NGC 1817 are anti-centre clusters, whilst Be 81 lies towards the Galactic centre¹, so they are particularly interesting to study the radial distribution of the disc properties. In Table 6.1 we report a summary of all the parameters available in the literature for the three clusters showing that a more precise analysis is called for.

NGC 1817 - Its richness, distance from the Galactic plane (-400 pc), and metallicity make this cluster particularly interesting. In fact, NGC 1817 has been the target of many photometric studies, starting from Arp & Cuffey (1962) and Purgathofer (1961), who obtained shallow photographic CMDs, including only stars at the MSTO and some giants. Harris & Harris (1977) acquired photographic *UBV* data, providing a well defined MS and RC, and derived distance, reddening (see Table 6.1), age similar to the Hyades, and a low metallicity. Balaguer-Núñez et al. (2004) performed deep, wide field photometry in the Strömrgren system ($uvby - H\beta$) and exploited the proper motion and membership analysis

¹On the basis of the distance moduli derived in the following sections their distances from the Galactic centre are $R_{GC} \simeq 9.5$ kpc for NGC 1817, $R_{GC} \simeq 12$ kpc for NGC 2141, and $R_{GC} \simeq 5.7$ kpc for Be 81.

by Balaguer-Núñez et al. (1998). A subsolar metallicity was derived by Parisi et al. (2005) on the basis of Washington photometry.

Spectroscopic analyses were made using low resolution spectra by Friel & Janes (1993) and high resolution ones by Jacobson et al. (2009), Jacobson et al. (2011b), and Reddy et al. (2012) for different cluster stars. Despite showing different results all these studies point to a slightly subsolar metallicity (see Table 6.1). Crucial information on radial velocities (RVs), membership, and binary stars were given by Mermilliod et al. (2003, 2007), and Mermilliod et al. (2008).

NGC 2141 - It is a rich cluster, subject of several studies in the past. Burkhead et al. (1972) obtained photoelectric and photographic *UBV* data, barely reaching below the MSTO; they determined the distance modulus and reddening listed in Table 6.1, and an age intermediate between those of M67 and NGC 2477. Rosvick (1995) used *VI* filters and observed a smaller area with *JHK*. Her CMD reached about four magnitudes below the MSTO, and showed a large scatter, interpreted in terms of both field star contamination and differential reddening. Rosvick (1995) determined the reddening, distance modulus, metallicity and age listed in Table 6.1 from a fit with the Bertelli et al. (1994) isochrones. The latest photometric data for this cluster have been presented by Carraro et al. (2001), who acquired *BV* and *JK* data. Their optical CMD extends to $V \sim 21.5$, while the IR CMD reaches about two magnitudes below the MSTO. They estimated the metallicity from the IR photometry, deriving best-fit age and distance, based on the Girardi et al. (2000a) isochrones (see Table 6.1).

Table 6.1: List of the main properties of the three clusters found in literature. The true distance modulus $(m - M)_0$ is evaluated from literature values after applying the same extinction law adopted in this analysis ($R_V = 3.1$).

Cluster	E(B-V)	$(m - M)_0$	age	metallicity	Reference	
NGC 1817	0.28	11.3±0.4	~Hyades	less than Hyades	Harris & Harris (1977)	
		10.9±0.6	1.1 Gyr	[Fe/H] = -0.34 ± 0.26	Balaguer-Núñez et al. (2004)	
	0.27				[Fe/H] = -0.33 ± 0.09	Parisi et al. (2005)
					[Fe/H] = -0.38 ± 0.04	Friel & Janes (1993)
					[Fe/H] = -0.07 ± 0.04	Jacobson et al. (2009)
					[Fe/H] = -0.16 ± 0.03	Jacobson et al. (2011b)
NGC 2141	0.3	13.17	NGC2477<age<M67		Burkhead et al. (1972)	
		13.08±0.16	2.5 Gyr	Z=0.004-0.008	Rosvick (1995)	
	0.40	12.90±0.15	2.5 Gyr		[Fe/H] = -0.43 ± 0.07	Carraro et al. (2001)
					[Fe/H] = -0.39 ± 0.11	Friel & Janes (1993)
					[Fe/H] = -0.18 ± 0.15	Yong et al. (2005)
					[Fe/H] = $+0.00 \pm 0.16$	Jacobson et al. (2009)
Berkeley 81	1.0	12.5	1 Gyr	solar	Sagar & Griffiths (1998)	
				[Fe/H] = -0.15 ± 0.11	Warren & Cole (2009)	

Spectroscopic analyses of cluster stars were made by different authors: Friel & Janes (1993), Minniti (1995) used low resolution spectra while Yong et al. (2005) and Jacobson et al. (2009) high resolution ones. They found different values for the cluster metallicity from solar to sub-solar (see Table 6.1). Jacobson et al. (2009) discussed the possible sources for the discrepancy and thoroughly analysed the literature findings. In summary, this cluster has a metallicity near solar or slightly lower, and this information will be used here to constrain the choice of the cluster's parameter.

Berkeley 81 - *BVI* photometry of part of Be 81 has been presented by Sagar & Griffiths (1998). They argued for the absence of significant differential reddening from the CMDs of

different regions, and attributed the width of the MS to the presence of field stars, binaries, and variables. They derived a cluster radius of 2.7 ± 0.2 arcmin, and the reddening, distance modulus and age listed in Table 6.1, using the Bertelli et al. (1994) isochrones with solar metallicity.

The metallicity of Be 81 was determined from calcium triplet (CaT) spectroscopy by Warren & Cole (2009). Their subsolar value is however quite uncertain, since they were unable to convincingly define the cluster mean RV, due to the huge contamination by field stars. The Gaia-ESO Survey spectra will thus be crucial to infer its actual metallicity.

6.1.1 The Data

The three clusters were observed in service mode at the LBT on Mt. Graham (Arizona) with LBC in 2011 (see Tab. 6.2 for details). There are two LBCs, one optimised for the UV-blue filters and one for the red-IR ones, mounted at each prime focus of the LBT. Each LBC uses four EEV chips (2048×4608 pixels) placed three in a row, and the fourth above them and rotated by 90 deg (see Figure 6.1). The field of view (FoV) of LBC is equivalent to $22' \times 25'$, with a pixel sampling of $0.23''$. The clusters were positioned in the central chip (# 2) of the LBCs CCD mosaic (see Fig. 6.1). We observed in the *B* filter with the LBC-Blue camera and in *V* and *I* with the LBC-Red one. No dithering pattern was adopted. Tab. 6.2 gives the log of the observations. The seeing was good (about $1''$), and the airmass of the exposures was in the range 1.0-1.3. Landolt fields were observed to perform our own calibration to the Johnson-Cousins system.

Table 6.2: Logbook of the observations. The listed coordinates refer to the telescope pointings.

Cluster	RA J2000	Dec J2000	Date	B Exp. time	V Exp. time	I Exp. time	seeing "
NGC 1817	05 12 41 16	44 30 24	Oct 2011	1s, 3×5s, 3×90s	1s, 3×5s, 3×60s	1s, 3×5s, 3×60s	$1''$
NGC 2141	06 02 57 10	27 27 21	Oct 2011	1s, 3×5s, 3×90s	1s, 3×5s, 3×60s	1s, 3×5s, 3×60s	$1''$
Be 81	19 01 41 -00	27 40 20	Oct 2011	1s, 3×5s, 3×90s	1s, 3×5s, 3×60s	1s, 3×5s, 3×60s	$1''$

Data reduction

The raw LBC images were corrected for bias and flat field, and the overscan region was trimmed using a pipeline specifically developed for LBC image prereduction by the Large Survey Center (LSC) team at the Rome Astronomical Observatory². The source detection and relative photometry was performed independently on each *B*, *V*, and *I* image, using the PSF-fitting code DAOPHOTII/ALLSTAR. We sampled the PSF using the highest degree of spatial variability allowed by the programme because the images are affected by severe spatial distortion. Giallongo et al. (2008) showed that the geometric distortion, of pin-cushion type, is always below 1.75% even at the edge of the field. At any rate, for our purposes we mostly use the inner area of the FoV where a distortion up to only 1% is expected. Moreover, the energy concentration of the instrumental PSF is very good: 80% of the energy is enclosed in a single CCD pixel in the *B* band and in 2×2 pixels in the *V*, *I* bands.

The brightest stars, saturated in the deepest images, were efficiently recovered from the short exposure images. The weighted average of the independent measures obtained from the different images were adopted as the final values of the instrumental magnitude

²LSC website: <http://lsc.oa-roma.inaf.it/>

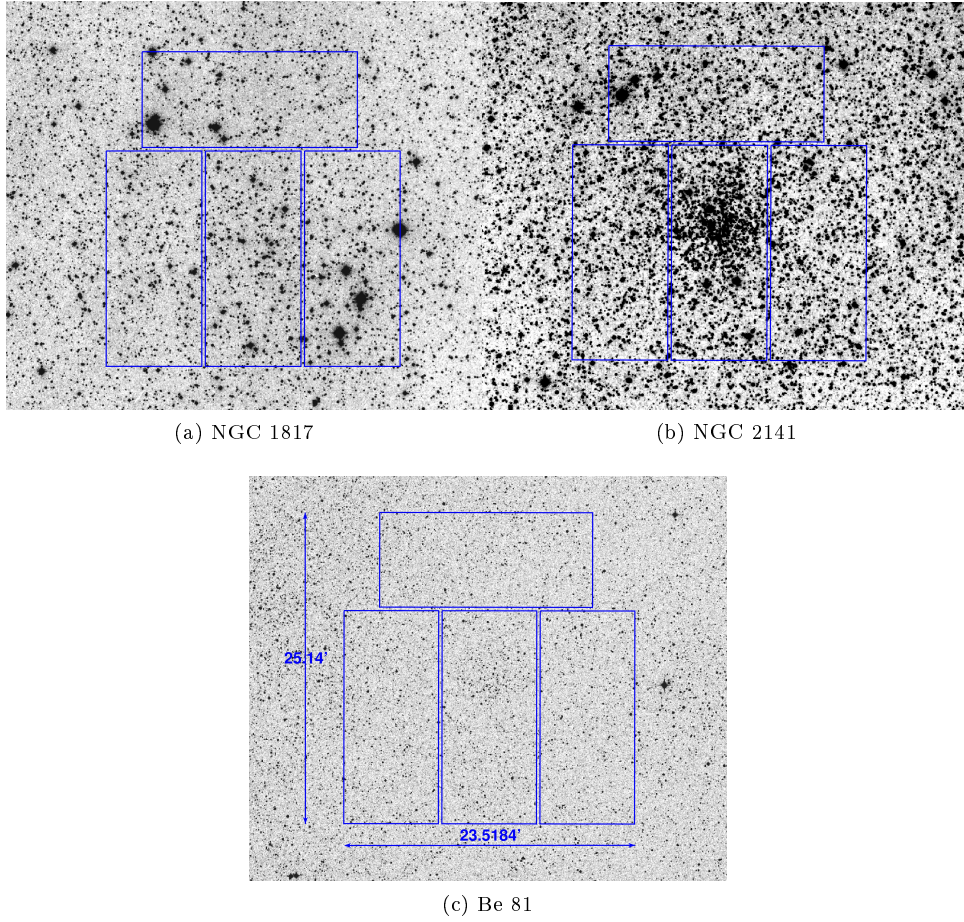


Figure 6.1: The field of views of the three clusters, NGC 1817, NGC 2141, and Be 81. In (c) we indicate the dimension of the FoV in arcminutes. All these images were downloaded from the DSS SAO catalogue in the GSSS bandpass 6 (V495). North is up and East is left.

(basing the weight on the error). More than 200 stars from the 2MASS catalogue (Skrutskie et al., 2006) were used as astrometric standards to find an accurate astrometric solution and transform the instrumental positions, in pixels, into J2000 celestial coordinates for each chip. To this aim we adopted the code CataXcorr. The r.m.s. scatter of the solution was about $0.1''$ in both RA and Dec.

We derived the completeness level of the photometry by means of extensive artificial stars experiments. About 10^5 artificial stars were used to derive photometric errors and completeness in B , V , and I exposures for the central chip. The results are shown in Tab. 6.3.

Table 6.3: Completeness level for calibrated B , V , and I magnitudes.

bin	NGC 1817 ($d < 5'$)			NGC 2141 ($d < 4'$)			Be 81 ($d < 2'$)		
	B	V	I	B	V	I	B	V	I
16.5	-	100.0 ± 1.0	-	-	100.0 ± 1.3	$100.0 \pm -$	-	-	100.0 ± 3.0
17.0	100.0 ± 1.7	100.0 ± 1.8	100.0 ± 1.2	-	97.1 ± 1.4	100.0 ± 1.2	-	100.0 ± 6.0	84.9 ± 2.9
17.5	100.0 ± 1.4	100.0 ± 1.5	95.3 ± 1.1	-	97.1 ± 1.4	95.7 ± 1.1	-	97.7 ± 5.5	77.6 ± 2.2
18.0	100.0 ± 1.9	96.1 ± 1.4	94.4 ± 1.0	100.0 ± 1.2	97.4 ± 1.2	94.7 ± 1.0	100.0 ± 8.2	94.2 ± 3.9	78.1 ± 1.9
18.5	100.0 ± 1.6	95.4 ± 1.4	92.5 ± 1.0	97.1 ± 1.4	96.7 ± 1.2	93.7 ± 0.9	98.5 ± 7.5	93.4 ± 3.6	69.6 ± 1.4
19.0	96.0 ± 1.6	95.9 ± 1.3	87.5 ± 0.9	96.8 ± 1.2	95.9 ± 1.2	90.8 ± 0.9	95.2 ± 4.5	92.2 ± 2.9	64.9 ± 1.1
19.5	95.5 ± 1.5	95.0 ± 1.3	83.7 ± 0.8	96.6 ± 1.3	94.6 ± 1.1	81.1 ± 0.8	93.4 ± 3.9	89.9 ± 2.5	54.6 ± 0.9
20.0	95.5 ± 1.5	94.4 ± 1.2	68.9 ± 0.8	96.0 ± 1.2	93.7 ± 1.1	69.4 ± 0.7	93.2 ± 3.5	88.4 ± 2.1	35.0 ± 0.6
20.5	95.5 ± 1.4	92.4 ± 1.2	28.5 ± 0.4	94.6 ± 1.2	91.4 ± 1.0	28.0 ± 0.4	92.0 ± 3.0	82.4 ± 1.6	9.7 ± 0.3
21.0	95.1 ± 1.4	88.8 ± 1.1	3.0 ± 0.1	94.7 ± 1.2	83.5 ± 1.0	1.6 ± 0.1	88.6 ± 2.5	77.7 ± 1.3	1.1 ± 0.1
21.5	94.7 ± 1.4	84.0 ± 1.0	0.2 ± 0.0	92.0 ± 1.1	74.7 ± 0.9	0.1 ± 0.0	88.1 ± 2.1	69.4 ± 1.1	0.2 ± 0.0
22.0	92.3 ± 1.3	78.5 ± 0.9	$0.0 \pm -$	88.3 ± 1.1	60.5 ± 0.8	-	81.4 ± 1.7	51.4 ± 0.8	-
22.5	89.8 ± 1.2	64.8 ± 0.8	-	80.5 ± 1.0	25.5 ± 0.4	-	78.0 ± 1.4	21.1 ± 0.5	-
23.0	85.2 ± 1.0	31.2 ± 0.5	-	74.9 ± 1.0	2.6 ± 0.1	-	71.6 ± 1.2	3.1 ± 0.2	-
23.5	81.5 ± 1.0	4.6 ± 0.2	-	64.5 ± 0.9	0.1 ± 0.0	-	58.4 ± 1.0	0.2 ± 0.0	-
24.0	72.5 ± 0.9	$0.3 \pm -$	-	40.7 ± 0.7	-	-	36.2 ± 0.7	-	-
24.5	47.4 ± 0.6	-	-	6.9 ± 0.2	-	-	8.2 ± 0.3	-	-
25.0	8.0 ± 0.2	-	-	0.3 ± 0.0	-	-	0.3 ± 0.1	-	-
25.5	0.3 ± 0.0	-	-	-	-	-	-	-	-

Calibration and comparison with previous data

The calibration to the Johnson-Cousins photometric system was obtained using standard stars (Landolt, 1992) obtained in the same observing nights. Landolt fields SA98, SA101, SA113L1, and L92 were observed at different airmasses: in the range 1.2-1.9 during the nights of Oct. 20 2011 and Oct. 21 2011, and in the range 1.2-1.5 during the third night. It was not possible to derive a calibration equation for each chip. So, we used the same one for all the four CCDs.

Comparing the calibrated V obtained from $(b - v)$ with that obtained with $(v - i)$, we find a small difference of ≤ 0.02 mag, which tends to worsen towards fainter magnitudes (see Fig. 6.2).

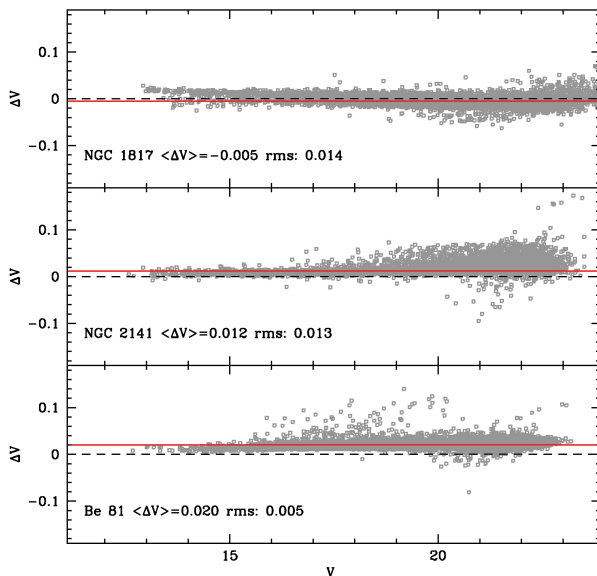


Figure 6.2: Comparison of the V calibrated from $(b - v)$ and $(v - i)$ colours with respect to the V magnitude for the three clusters (from top to bottom NGC 1817, NGC 2141, and Be 81). The labelled values $\langle \Delta V \rangle$ are the medians of all the stars shown for each plot.

In Figs. 6.3, 6.4, and 6.5 we show the comparisons of our photometry with the literature ones (downloaded through WEBDA) for NGC 1817, NGC 2141, and Be 81. In the case of NGC 1817, we find a small offset: about 0.04 mag in B and 0.03 in V , corresponding to an offset of 0.01 mag in $B - V$. More worrisome are the comparisons obtained for NGC 2141 and Be 81, showing an offset of up to 0.1 mag. The explanation for such differences is not straightforward, since we can only perform relative comparisons, with no absolute reference point. There must be issues related to the adopted calibration equations, but it is not possible to identify in which data set. We have further investigated this problem using photoelectric measurements, when available. This was feasible for NGC 1817 and NGC 2141, thanks to the photoelectric data by Harris & Harris (1977), Purgathofer (1964), and Burkhead et al. (1972), but not for Be 81. The results are shown in Fig. 6.6. The agreement between our photometry and photoelectric standards is good for both clusters, showing only a tiny offset, smaller than 0.02 mag in most cases and only slightly worse for the B of NGC 1817.

For NGC 1817 we were also able to compare our photometry with the Sloan Digital Sky Survey (SDSS) (see York et al., 2000) using the transformation by Lupton³ to convert their magnitudes into the Johnson-Cousins system. The results are shown in Fig. 6.7. The

³<http://www.sdss.org/dr4/algorithm/sdssUBVRITransform.html#Lupton2005>

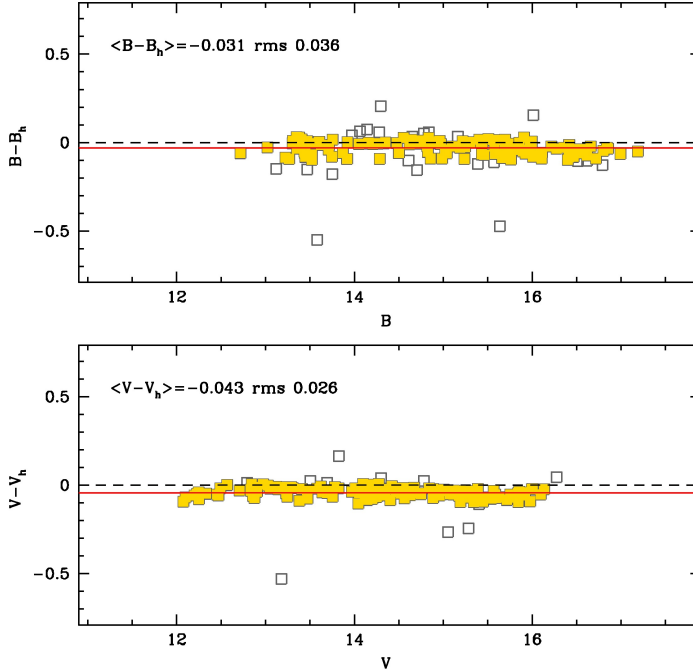


Figure 6.3: Comparison of our photometry with the one by Harris et al. (1977) for NGC 1817. The average difference is computed using the golden points, retained after one sigma-clipping has been applied.

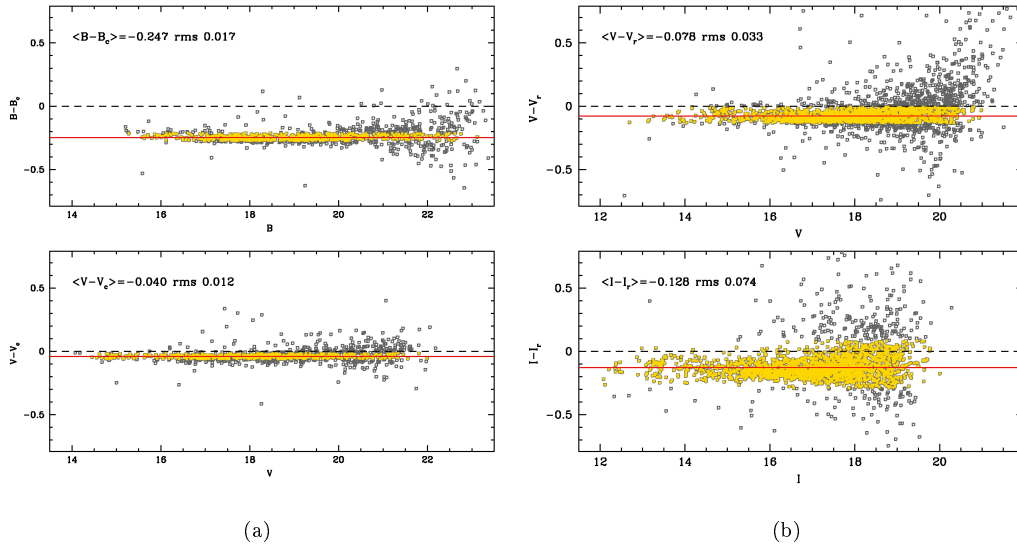


Figure 6.4: Same as Fig. 6.3, but for NGC 2141. (a) we compare B and V with the photometry of Carraro et al. (2001), in (b) V and I with Rosvick et al. (1995).

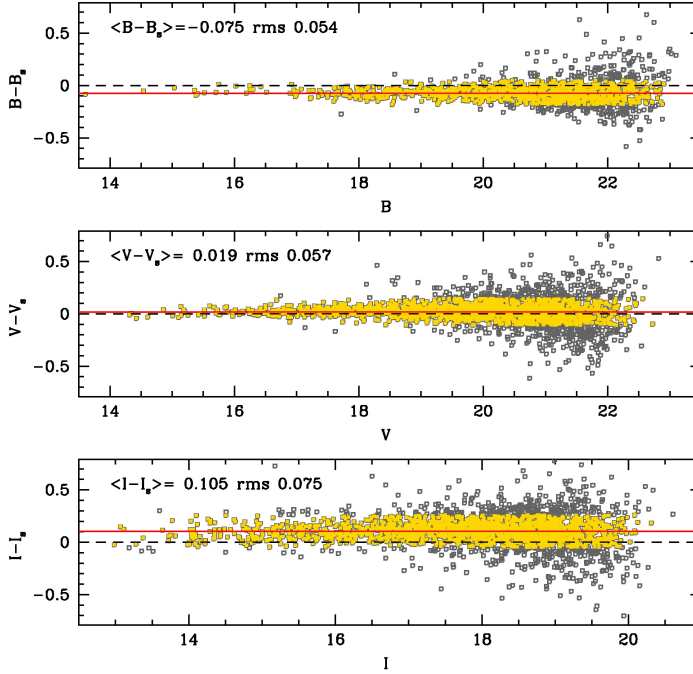


Figure 6.5: Same as Fig. 6.3, but for Be81 compared to Sagar et al. (1998).

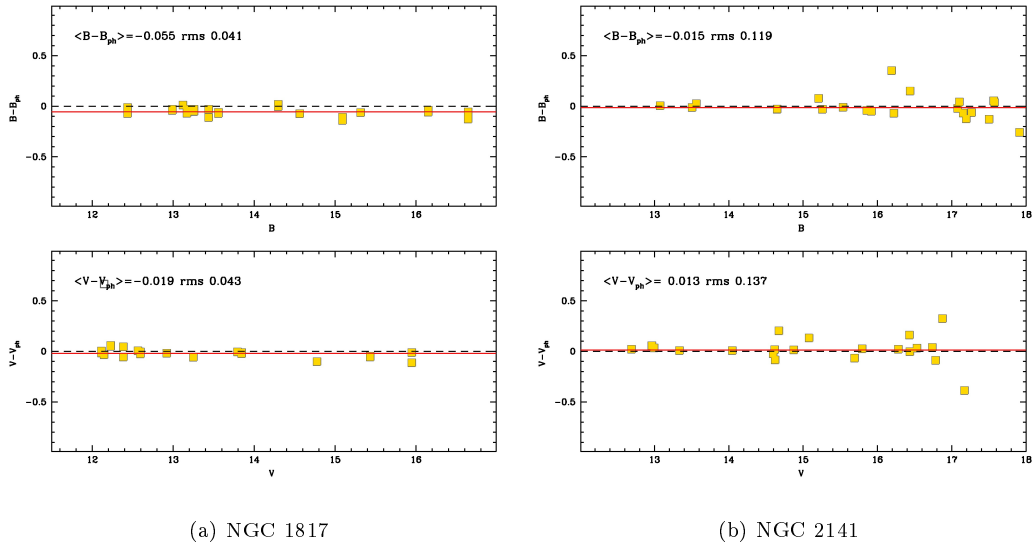


Figure 6.6: Comparison of the B and V calibrated photometry with the photoelectric photometry. In (a) the results for NGC 1817, in (b) the case of NGC 2141.

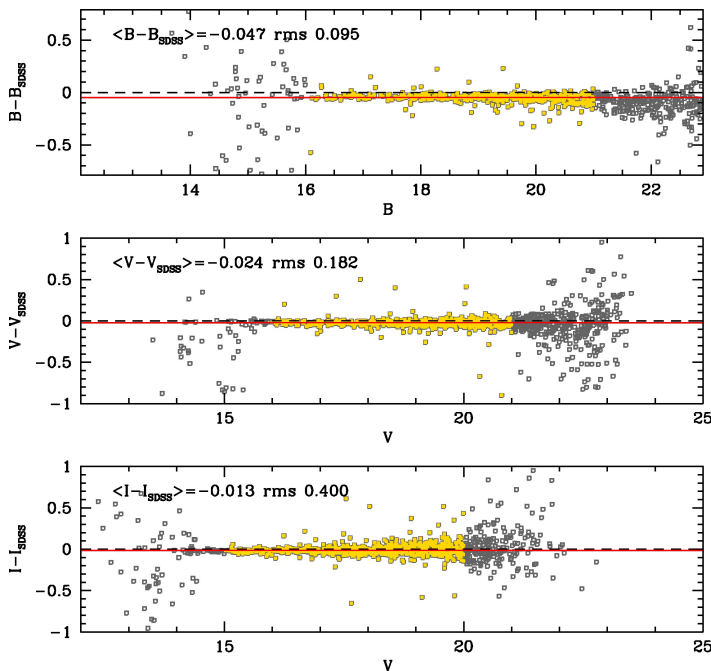


Figure 6.7: Comparison of the BVI with SDSS $ugriz$ magnitudes calibrated to the Johnson-Cousins system for NGC 1817. The median of the difference (red line) is computed using the golden points: we excluded bright and possibly saturated stars and faint star, we used stars in common only with chip#2 and flagged with Q SDSS parameter equal to 3.

median of the difference in B is about 0.05 mag, and is lower than 0.03 in V and I . This translates in colour differences smaller than 0.03 mag.

In summary, we find that our photometry for NGC 1817 is in good agreement with the literature, and in particular with both photoelectric measurements and SDSS data. For NGC 2141 we find a poor comparison with literature CCD data but a very good agreement with photoelectric measurements, which makes us confident of our results. For Be 81 there were no further checks feasible, but, given the robustness of the calibrations adopted for the other two clusters, we believe the third is correct too.

The colour magnitude diagram

The CMDs obtained for the three clusters are shown in Figs. 6.8 and 6.9, with errors in colour and magnitude indicated. The errors are evaluated using the artificial stars tests. They are random standard errors, with no consideration of possible sources of systematics. In the upper panels only the more central regions are plotted, while more external regions are used for comparison to estimate the field contamination. For Be 81 the size of the LBC FoV makes this possible, but NGC 2141 is present also in the outer parts of the FoV, and NGC 1817 is so extended that it fills all the four CCDs. The differences between the CMDs of the three OCs are quite evident.

NGC 1817 is a young and luminous cluster, but not as rich as NGC 2141. Its size is probably larger than the LBT FoV, given the presence of probable cluster RC (at $V \sim 12$ mag) and MS stars in the outer parts of our frames. The brighter MS and RC stars were saturated in I even in short exposures and we miss them in the $V, V - I$ CMD. On the other hand we obtained a very good description of the MS, which extends for about 10 mag in V .

NGC 2141 shows a very rich MS and a populated RC at $V \sim 15$ mag. The RGB is visible at $B - V \sim 1.6 - 2.0$ up to $V = 13$ and there are a few probable SGB stars at its base.

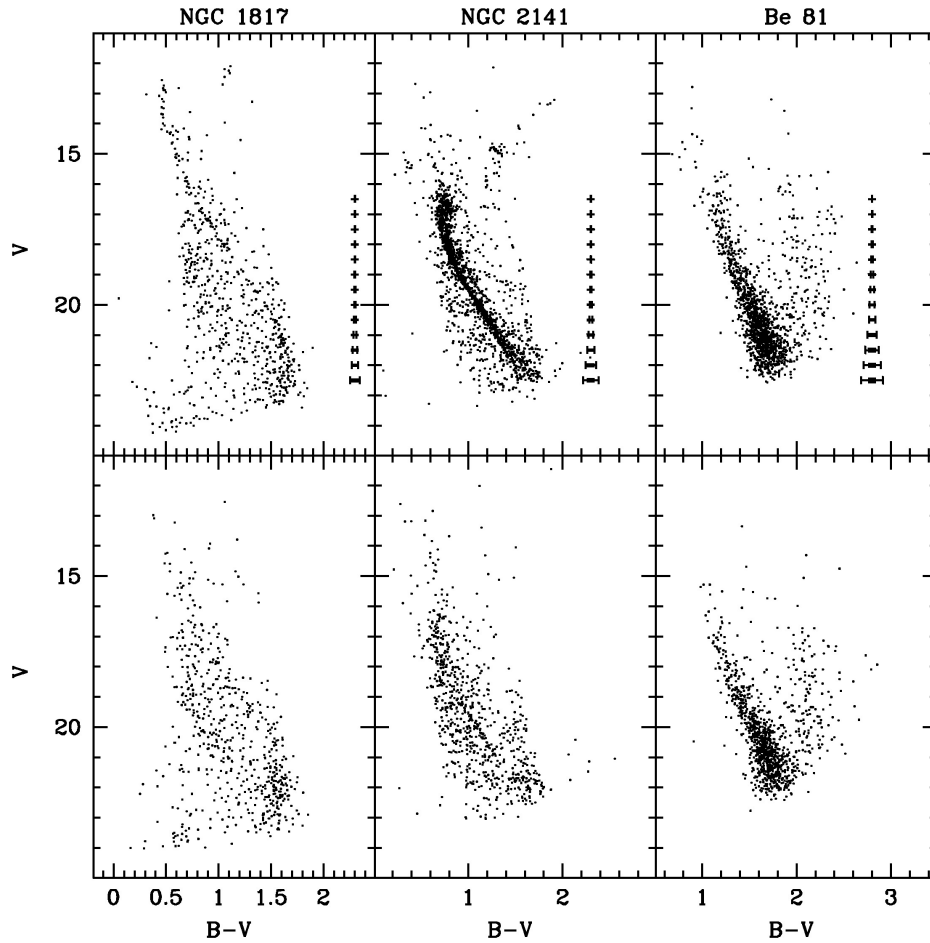
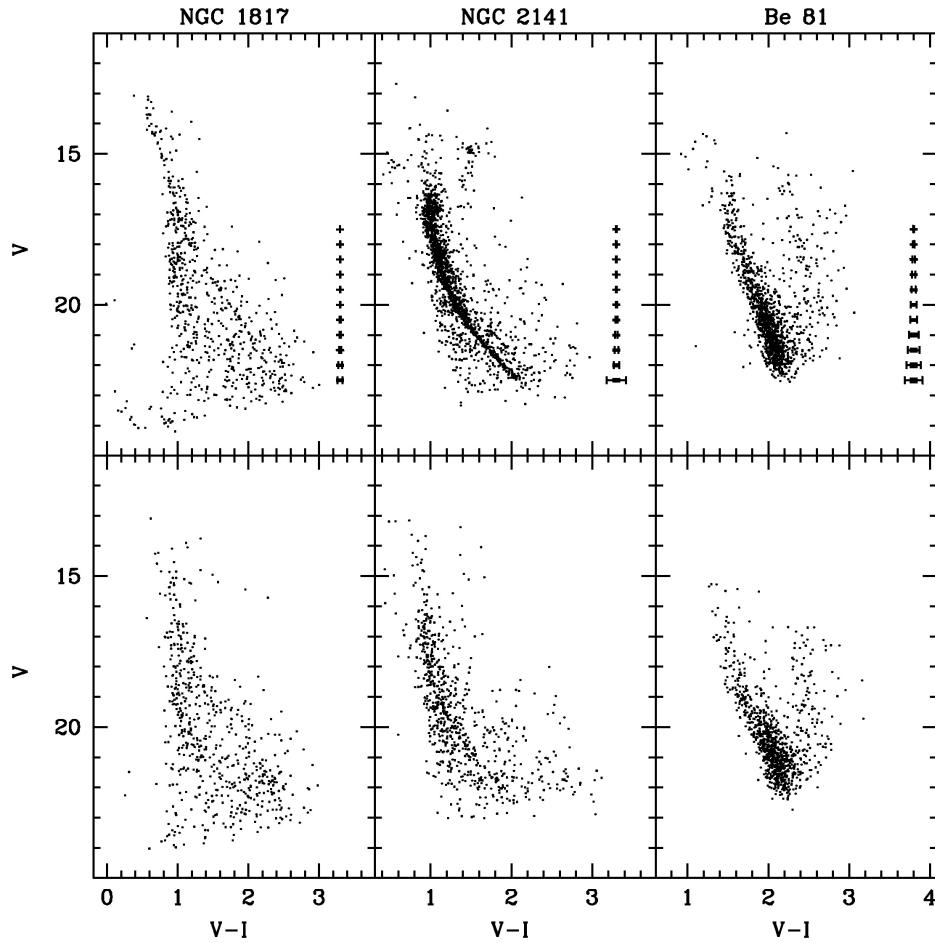


Figure 6.8: *Upper panels:* $V, B-V$ CMDs for the inner part of NGC 1817 ($d < 5'$), NGC 2141 ($d < 3'$), and Be 81 ($d < 2.5'$). The errors on colour and magnitudes are indicated by error-bars and derived using the artificial stars tests. *Lower panels:* $V, B-V$ CMDs for an external area with the same dimension.

The binary sequence (redder and brighter than the MS) is very clear and neat. The TO is extended in colour, with a “golf club” shape common to other young OCs (see Sec. 6.1.3). A small clump of stars bluer and brighter than MS stars ($V \sim 15.5$, $B - V \sim 0.3$) is visible, probably blue-stragglers.

Be 81 is heavily contaminated by field stars, and is hardly distinguishable, even using the control field for comparison. However, there is a mild excess of stars at $V \sim 16.5$ and $B - V \sim 1.9$, which is not present in the outer field, and can be considered the cluster signature, probably its RC.

Figure 6.9: As Fig. 6.8, but for $V, V - I$.

Radial Velocity

For NGC 1817 and NGC 2141, we have identified the stars in our catalogue with literature RVs from high-resolution spectroscopy. They are all evolved stars, mainly on the RC but also on the bright RGB. They are listed in Tab. 6.4, and are displayed with larger symbols in the CMDs of Fig. 6.10.

For Be 81, Warren & Cole (2009) observed stars in the CaT spectral region, but we opted not to use their data because of the large uncertainty in the membership attribution.

6.1.2 Centre of gravity and density profile

Exploiting the deep and precise photometry obtained with LBT and its large field of view, we re-determined the centre of each cluster following the approach described in Sec. 5.1.2. The root mean square (rms) on the centre coordinates is about $5''$.

The most uncertain determination is for NGC 1817. It is a nearby cluster, hence its projected angular dimensions are larger than the LBT's FoV. Moreover it is not richly populated and it does not seem particularly concentrated, circumstances that both hamper the analysis. We thus applied the same method on the 2MASS catalogue to check the results

Table 6.4: Stars in common with Jacobson et al. (2009, 2011b) and Yong et al. (2005) in NGC 1817 and NGC 2141.

ID	RA	Dec	V	B - V	V - I	ID _{webda}	RV	flag
NGC 1817 - stars in common with Jacobson et al. (2011b)								
1429	78.0807757	16.6801860	12.116	1.052	-	8	64.8	M
1431	78.0260996	16.6376011	12.232	1.025	-	81	65.1	M
1432	78.0190940	16.6740782	12.237	1.227	-	90	27.8	NM
1434	78.0271406	16.7457104	12.389	1.048	-	177	65.2	M
1435	78.0444686	16.6419862	12.494	1.027	-	79	65.8	M
1436	78.0960056	16.5669407	12.480	1.268	-	155	14.5	NM
1438	78.0772008	16.6959836	12.597	0.960	-	12	62.7	M
1440	78.0941116	16.6357254	12.713	1.034	-	40	65.1	M
1448	78.0939209	16.7331841	13.282	1.322	-	53	50.4	M?
2922	78.1881838	16.5799475	13.808	0.844	0.976	219	-26.1	NM
3106	78.1092441	16.5988226	12.079	1.039	-	72	66.5	M
3108	78.1890040	16.7280692	12.106	1.115	-	2049	65.0	M
3109	78.1498523	16.7244935	12.206	1.059	-	19	35.2	M?,SB
3110	78.2087521	16.6804613	12.253	1.100	-	127	65.1	M
3111	78.1601438	16.7064247	12.336	1.110	-	22	63.7	M
3112	78.2283968	16.6160611	12.361	1.126	-	2050	65.7	M
3113	78.1356504	16.6660230	12.460	1.059	-	30	65.0	M
3116	78.1717679	16.5846748	12.590	1.019	-	286	66.9	M
3118	78.2083091	16.7333221	12.710	1.042	-	121	64.6	M
3121	78.1291901	16.8236832	12.815	1.055	-	185	65.3	M
3124	78.1221863	16.5986027	12.882	1.034	-	71	65.9	M
3126	78.1834030	16.6199452	12.931	1.179	-	138	8.4	NM
4510	78.3186789	16.6698094	13.663	1.066	1.192	471	48.1	NM
4511	78.2917601	16.7518247	13.468	0.867	0.964	1722	15.1	NM
4513	78.3164620	16.7476535	13.566	0.793	0.929	482	15.6	NM
4518	78.3029299	16.7208041	13.736	0.881	0.955	477	40.3	NM
4670	78.2593664	16.6553140	12.288	1.090	-	211	65.1	M
6178	78.0818374	16.9064095	12.235	1.059	-	1292	65.5	M
NGC 2141 - ^a Jacobson et al. (2009), ^b Yong et al. (2005)								
6770	90.7115940	10.5078007	13.341	1.761	-	1007 ^a	25.5	M
						1007 ^b	24.4	M
6590	90.7427760	10.4441398	14.178	1.546	1.715	2066 ^b	24.8	M
6604	90.7345371	10.4851441	14.777	1.385	1.606	1286 ^b	23.0	M
6644	90.7511372	10.4788874	15.082	1.359	1.572	1333 ^b	23.5	M
6771	90.7564588	10.4763049	13.337	1.871	-	1348 ^b	24.6	M
6776	90.7500858	10.5398554	14.081	1.500	-	514 ^b	23.3	M
6777	90.7814610	10.4469925	14.145	1.537	-	1821 ^b	24.8	M

on a larger field of view (30' of radius). We find a very similar answer, with a difference of only about half arcminute in both RA and Dec. We therefore adopted the value obtained from our photometry, which is more precise and deeper than 2MASS, and allows us to include stars on the fainter MS. The results are summarised in Tab. 6.5.

Following the approach adopted by Cignoni et al. (2011), the projected number density profile is determined by dividing the entire data-set in N concentric annuli, each one partitioned in four subsectors (although only two or three subsectors are used, if the available data sample only a portion of the annulus). The number of stars in each subsector is counted and the density is obtained by dividing this value by the sector area. The stellar density in each annulus is then obtained as the average of the subsector densities, and the uncertainty is estimated from the variance among the subsectors. Also in this case, only stars within a limited range of magnitudes are considered in order to avoid spurious effects due to photometric incompleteness.

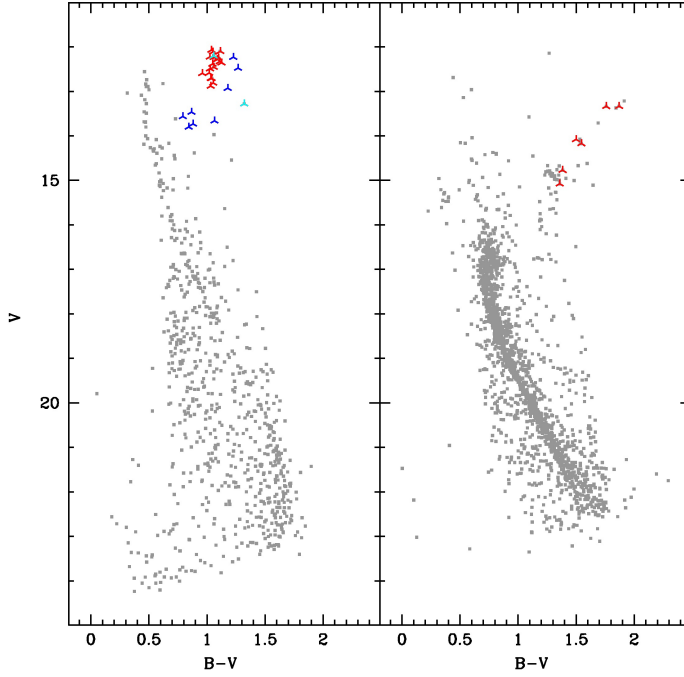


Figure 6.10: *Left panel:* CMD of NGC 1817 inside 5'. *Right panel:* CMD of NGC 2141 inside 4'. The shaped points are the targets with RV measurements listed in Tab. 6.4. In red the sure members, in blue the non members, in cyan the stars with uncertain membership.

Table 6.5: Clusters centres and structural parameters. The r.m.s. on the centre determination is about 5''.

Cluster	RA ^a (h:m:s)	Dec ^a (°:!::'')	RA (h:m:s)	Dec (°:!::'')	c	r_c (arcsec)	r_h (arcsec)	r_t (arcsec)
NGC 1817	05:12:15	16:41:24	05:12:38.33	16:43:48.85	-	-	-	-
NGC 2141	06:02:55	10:26:48	06:02:57.71	10:27:14.43	1.0	120	234	1219
Be 81	19:01:40	-0:27:22	19:01:42.82	-0:27:07.67	0.6	95	128	388

^aPrevious centre estimates from the DAML02 catalogue.

The observed stellar density profiles are shown in Fig. 6.11 for the clusters Be 81 and NGC 2141. For these two OCs the collected data-set covers the entire cluster extension, reaching the outermost region where the Galactic field stars represent the dominant contribution with respect to the cluster. This is not the case for NGC 1817, which is not fully covered by the LBT's FoV. As done for the centre determination, we tried to evaluate its density profile on a larger area using 2MASS, SDSS, and literature catalogues, but the looseness of the cluster and its proximity to a nearby OC (NGC 1807, even if Balaguer-Núñez et al. 2004 showed that NGC 1807 is not a physical cluster) jeopardise the analysis. Unable to reach a satisfying conclusion, we preferred to limit the analysis to Be 81 and NGC 2141. The results are summarised in Tab. 6.5.

In order to reproduce the observed profile, isotropic, single-mass King models (King, 1966) have been computed adopting the Sigurdsson & Phinney (1995) code. The best fit models are shown as solid curves are shown in Fig. 6.11 together with the observed density profiles. In each figure we also show the values of concentration ($c = \log_{10}(r_t/r_c)$), core radius (r_c), half-mass radius (r_h), and tidal radius (r_t) as obtained from the best-fit model. The residual of the fit of the model to each observed point is shown in the lower panel of

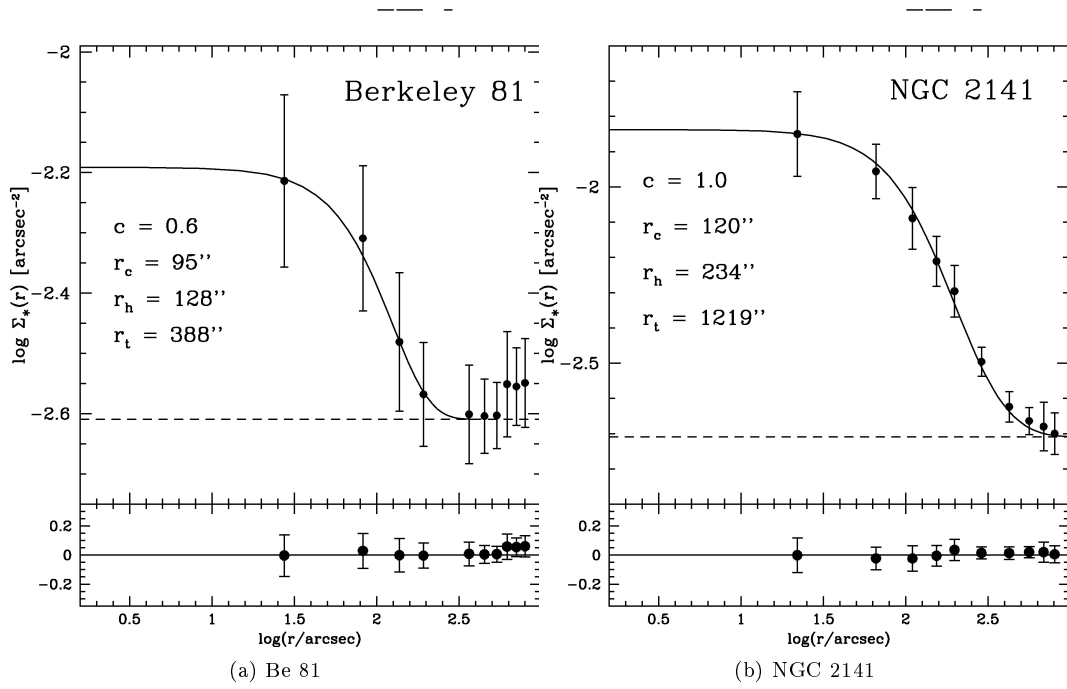


Figure 6.11: King profiles for (a) Be 81 and (b) NGC 2141.

each density plot.

Clearly, Be 81 is a small, low-mass and very sparse OC. The density profile is hence affected by larger statistical uncertainty. Nevertheless, the residuals of the model fit are quite small, at least in the most central part, where the star counts are dominated by the cluster’s members.

6.1.3 Differential reddening

As noted in Sec. 6.1.1, NGC 2141 shows a “golf club” shaped MSTO. We can exclude that this observed feature is due to the photometric error, which is too small to explain the colour extension. Carraro et al. (2001) propose a metallicity spread as best explanation, but this circumstance is very unlikely in OCs. In literature there are other similar examples of Milky Way OCs and Magellanic Clouds clusters showing an extended MSTO (see e.g. Tr 20 in the MW presented in Ch. 7, and about 10 young globular clusters in the LMC, Milone et al. 2009). Another possible explanation is stellar rotation. For instance, Bastian & de Mink (2009) find that fast rotators at the TO phase have a redder and fainter colour, and can be responsible for the “golf club” shape. Girardi et al. (2011), instead, exclude that rotation can have such an effect. Also binary systems, which have redder colour and brighter magnitude than single stars, could explain the broadening of the MS, as could an age spread. The latter, however, has never been convincingly observed in OCs. A more plausible explanation can be differential reddening (DR). Different absorptions on the cluster field due to different extinction paths along the line of sight result in different shifts in colour and magnitude. This circumstance can also explain the elongated shape of the RC, when RC stars are spread along one single direction.

Most likely, DR is not negligible also over the field of Be 81, that is located very close to the Galactic plane (about 130 pc below the disc, see Sec. 6.1.4) and toward the Galactic

centre. Its high average reddening, $E(B - V) \sim 1.0$ mag, favours the chances for DR. However, Be 81 is severely contaminated by field stars, and this makes it very hard to measure DR. For NGC 1817 there is no direct evidence of DR from the observational CMD (see Fig. 6.8).

To evaluate the effect of DR for NGC 2141 we adopt the following approach, using a revision of the method described in Milone et al. (2012), adapted to the case of the OCs, which are less populated and more contaminated by field stars than the globular clusters. The main steps of the process are the following:

- we draw a fiducial line along the MS, and use it as a reference locus for the DR estimate;
- we draw a box on the MS: all stars falling in this box are used to estimate the DR. The box is chosen to select stars on the blue side of the MS, and to avoid as many binaries as possible, since they also produce a shift to the red of the sequence. We also keep far from the MSTO and the fainter part of the MS, where errors are larger and field stars confuse the picture;
- for each star in the catalogue we pick the 30 nearest and brightest stars inside the MS box and compute their median distance along the reddening vector direction from the fiducial line in the CMD plane. This distance is used to correct colour and magnitude for DR;
- after the correction for the first DR estimate is applied star-by-star, the algorithm starts a new loop and this procedure is repeated until a convergence is reached. The convergence criterion is a user-defined percentage of stars for which the DR correction is lower than the average r.m.s. on these estimates;
- once a final value for the DR is obtained for each star, a binning is performed in the spatial plane. The spatial scale must be compatible with the average distance of the 30 neighbour stars selected and used for the DR estimate. In our case it is less than 1 arcmin^2 , as described in the following paragraphs. At this point the outliers are rejected, i.e., stars whose DR estimate is larger than the average error, and stars whose distance to the 30 neighbours is larger than average.
- a final and robust value for the DR is then computed as the average value of the DR corrections associated to the stars falling in the same bin and the error on this estimate is the associated rms. The values obtained are not absolute values but relative to the fiducial line.

We estimated the DR in the $B - V$ colour. The direction of the reddening vector is derived assuming the standard extinction law ($R_V = 3.1$, $E(V - I) = 1.25 \times E(B - V)$) described in Dean et al. (1978). The fiducial line is defined using the CMD of the inner part of the cluster (all the stars inside $4'$) and is chosen as the ridge line along the MS. Several attempts have been made to avoid fiducial lines that, during the estimates of the DR, lead to corrections that artificially and significantly change the magnitude and colour of the age-sensitive indicators (e.g. RC, MSTO). We want in fact to keep RC, MSTO and the blue envelope of the MS as close as possible to the original position in the CMD, to avoid spurious interpretations of the cluster parameters due to DR corrections. When defining the MS box we avoided the broad and bended region of the TO, where the morphology could hamper the correct interpretation, and the fainter part of the MS, where the photometric

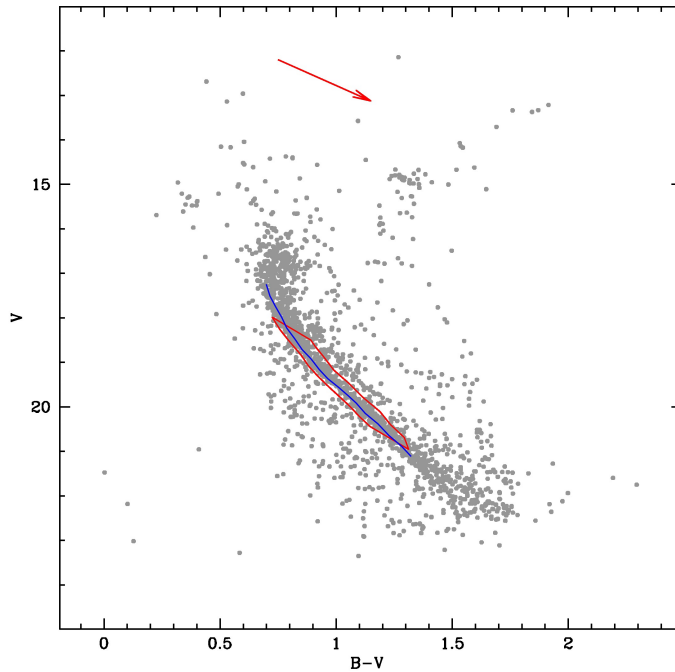


Figure 6.12: CMD of NGC 2141 inside 4 arcmin. The red box and the blue line indicate the MS box and the fiducial line for the DR estimate. The red arrow indicates the reddening vector, both in size and direction.

error is more important. The box and the fiducial line used are highlighted in Fig. 6.12 with colours.

Taking into account the star counts of the inner and outer parts of the cluster (see Sec. 6.1.2) we decided to limit the DR correction to stars within a $4'$ radius (approximately the half mass radius). For the outer regions the contamination of field stars becomes not negligible (the contrast density counts with respect to the field plateau drops below 50%) and any attempt to estimate the DR is severely affected by field interlopers. The spatial smoothing applied to have a more robust statistic is $0'.4 \times 0'.4$ in right ascension and declination. As final caveat, we stress that photometric errors, undetected binary systems, and residual contamination from the field could affect the DR estimation, since they all produce a broadening of the MS. Our results are then an upper limit to the DR.

In Fig. 6.13 we show the map of the DR obtained in terms of $\Delta E(B - V)$ with respect to the fiducial line. It ranges from ~ -0.04 to $\sim +0.1$. In the same figure we show the corresponding map of the error associated to our estimates. The discrete appearance of these maps is due to two reasons: the poor sampling of a circular area with polygonal bins and the avoidance of interpolation in the corners, where the poor statistics could lead to uncertain estimates.

The overall effect of the DR correction on the CMD appearance is shown in Fig. 6.14. The MS and MSTO region appear tighter, reducing substantially the broadening. In the figure, only the upper MS stars corrected for DR are highlighted in black, but the lower MS benefits from the DR correction too. The RC stars, apparently aligned along the direction of the reddening vector in the original CMD (see the left panel in Fig. 6.14), appear more clumped after the DR correction, thus supporting the DR hypothesis. Also the RGB looks better defined. Furthermore, our DR estimate does not change the luminosity level and colour of age sensitive indicators such as the MSTO, or the bright edge of the MS, the RH phase. We list in our catalogue for NGC 2141 both the original magnitudes and the DR

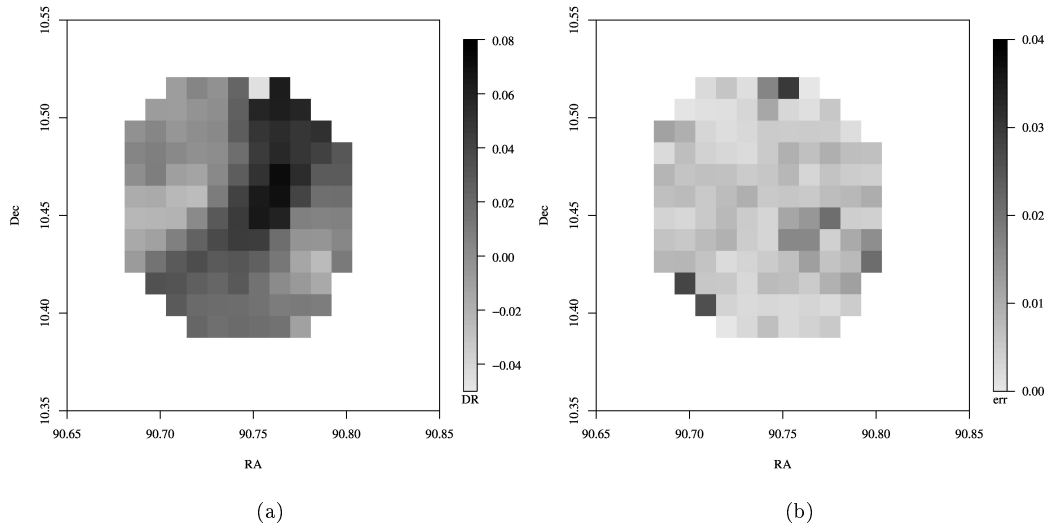


Figure 6.13: (a) Colour deviations from the reference line due to the effect of DR, mapped on a $0'.4 \times 0'.4$ grid for stars inside $4'$ from the centre. The correction is expressed in gray-scale colours, see the legend on the right side. (b) Corresponding error map.

corrected ones.

We cannot apply the same analysis to Be 81 because it is severely contaminated by field interlopers even in the inner regions. For instance, in the central $2'$ (approximately the half-mass radius estimated in Sec. 6.1.2), the density contrast is only 25%. Hence, in its

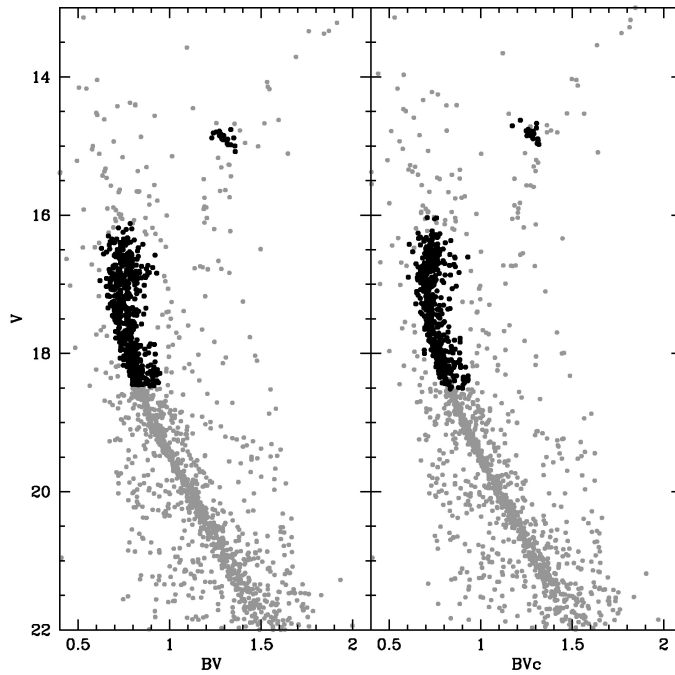


Figure 6.14: CMDs for NGC 2141 inside 4 arcmin. *Left panel:* observational CMD. *Right panel:* CMD after correction for DR. The stars in the upper part of the MS and in the RC phase are highlighted in black to better show the effect of the correction.

case the algorithm would be driven by stars not belonging to the cluster rather than MS stars, seriously weakening the results. We thus prefer to evaluate the effect of DR on Be 81 with the synthetic CMD technique described in the next section.

6.1.4 Synthetic CMD

As described in Sec. 4.2, the cluster parameters are determined by the best fit solution that can best reproduce the age-sensitive indicators (RH, RC, RGB, and MSTP).

The binary fraction is estimated with the same methodology discussed previously. The DR is taken into account and the synthetic CMD technique applied to the DR corrected photometry. The best fit to all the above indicators provides the best choice for age, reddening, and distance modulus. To infer the metallicity it is crucial to analyse together all the *BVI* photometry. To deal with $(B - V)$ and $(V - I)$ colours we adopted the normal extinction law (Dean et al., 1978).

We estimated the errors on the cluster parameters considering both the instrumental photometric errors and the uncertainties of the fit analysis, as described in Sec. 5.1.3.

NGC 1817

With the deep LBT photometry we can reach magnitude $V \sim 23$ in the $B - V$ CMD, describing very well the MS. The RC is well visible at $V \simeq 12.3$, as shown in Fig. 6.15. In the same figure we show the comparison with an external region of the same area. We can see the signature of the cluster (mainly MS stars) also in the outer parts of the image. As explained in Sec. 6.1.2, we could not cover the whole extension of the cluster with the instrument's FoV. There is a clear signature of RC stars, confirmed by the studies on the RV of spectroscopic targets (see Sec. 6.1.1 and Fig. 6.10); the upper part of the MS is poorly populated so it is difficult to reach a statistically firm conclusion on the locus of the RH. We place this phase at magnitude $V \simeq 13$. A well defined binary sequence is visible redward of the MS.

To estimate the binary fraction we defined two CMD boxes, one which encloses MS stars and the other redward of the MS in order to cover the binary sequence (see dashed lines in Fig. 6.15). To remove the field contamination we subtracted the contribution of field stars falling inside the same CMD boxes in a portion of the control field with same area. We performed the same computation on regions smaller and larger than $5'$, finally ending with an estimate between 20% and 30%. The dispersion on the estimate is mostly due to the spatial fluctuations across the control field. Notice that the derived binary fractions may be underestimated, since we possibly miss systems with very low mass secondary, whose luminosity doesn't alter significantly that of the primary. A mean fraction of 25% has been assumed for all the simulations presented here.

We limit the differential reddening to 0.02 mag because we find no direct evidence of it in this cluster.

After fixing these two parameters we use the synthetic CMD technique to estimate the age, reddening, and distance modulus of the cluster. For the simulations we used all the stars inside $5'$ from the centre.

Using the BBC models we find that a subsolar metallicity is required to describe with the same model both the $V, B - V$ and $V, V - I$ observational CMDs. In particular the best match is obtained for $Z = 0.008$ ($[\text{Fe}/\text{H}] \simeq -0.40$), an age of 1.1 Gyr, $E(B - V) = 0.23$, and $(m - M)_0 = 11.1$.

In the case of the FST models we converge to similar results, finding the best solution

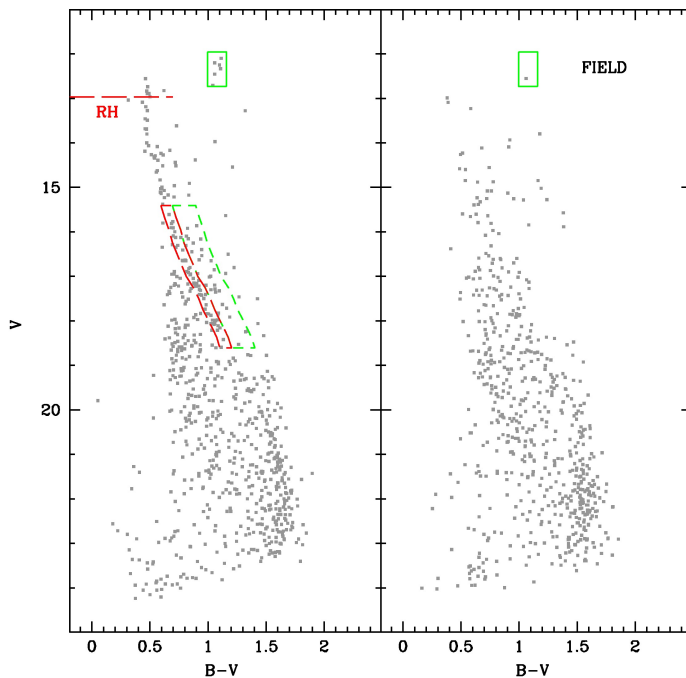


Figure 6.15: Left panel: $V, B - V$ CMD for the inner part of NGC 1817 (inside $5'$). The age indicators RC (green box) and RH (red line) are shown. The red and green boxes on the MS and redward of it are used to estimate the percentage of binaries. Right panel: CMD of the comparison field of the same area. The same RC box adopted in the left panel is shown here.

for a metallicity lower than solar. We chose $Z = 0.01$, an age of 1.05 Gyr, $E(B - V) = 0.21$, and $(m - M)_0 = 10.98$.

For the FRA models we find the best fit for $Z = 0.01$, age of 0.8 Gyr, $E(B - V) = 0.34$, and $(m - M)_0 = 10.88$. The age is younger than with the other two models, as expected since these evolution tracks do not include overshooting. We reproduce the magnitude of the age sensitive indicators (RH and RC), but we don't match the RC colour and the MS shape and colour. In particular, the FRA models cannot reproduce the correct inclination of the MS for $V > 16$.

Fig. 6.16 shows the comparison between the observational CMD (top left) and the best fits obtained with the three sets of tracks.

The LFs (see Fig. 6.17) show a satisfying agreement. There are small departures between the observational and synthetic LFs probably due to the poor statistics in star counts. For example the observational CMD (Fig. 6.15) shows a lack of stars at $V \sim 19$ which is not reproduced in any synthetic CMDs.

From this analysis it turns out that the BBC and FST models provide a better description of the observational CMDs. This restricts the best age to 1.05-1.1 Gyr. Consequently the Galactic reddening is about 0.22^4 , while the distance modulus is between 10.98 and 11.1. The results are summarised in Tab. 6.6.

Balaguer-Núñez et al. (2004) estimate an age of about 1.1 Gyr, a reddening of 0.21 and a distance modulus of 10.9. Our results are in excellent agreement with theirs. The metallicity of the cluster has been studied in detail by different spectroscopic analysis of cluster stars. They all point toward lower than solar abundances (see Tab. 6.1). Our photometric analysis suggests a metallicity ranging from -0.40 to -0.30 in agreement with Balaguer-Núñez et al. (2004); Parisi et al. (2005); Friel & Janes (1993).

⁴The Schlegel et al. (1998) estimate is 0.43 mag, but this is the asymptotic value in that direction, while the cluster is nearby

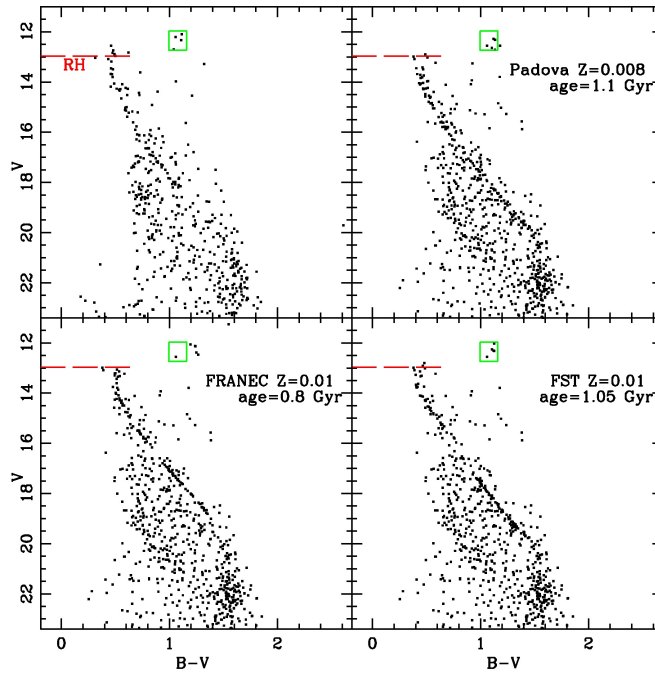


Figure 6.16: Top left panel: CMD of stars inside $5'$ radius area of NGC 1817. Clockwise from the top right panel: the best fitting synthetic CMD obtained with BBC, FST, and FRA models.

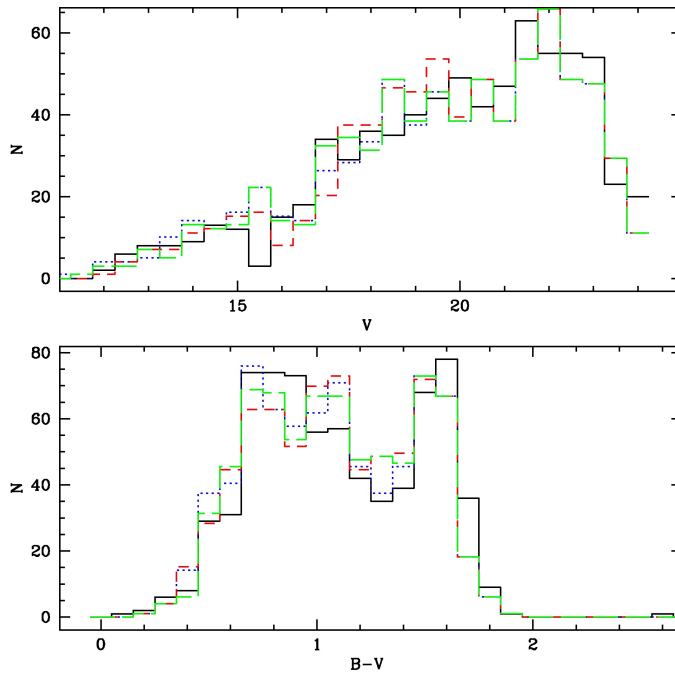


Figure 6.17: Luminosity functions in magnitude V (upper panel) and colour $B - V$ (lower panel) of NGC 1817. The solid black line is obtained from the observational CMD, the blue dotted line from the BBC synthetic CMD, the red dashed line from the FST synthetic CMD, and the green dot-dashed line from the FRA synthetic CMD.

NGC 2141

NGC 2141 shows clearly all its evolutionary sequences. In Fig. 6.18 we show the comparison of the inner part of the cluster (inside $4'$, corresponding to the half-mass radius of the cluster) with an external region of the same area. Even in the outer parts of the instrument FoV the cluster is clearly present, with an evident star excess at $V \sim 20$ aligned along the MS direction, and a mild excess at brighter magnitudes. We identify the RH at $V \simeq 16.4$, the MSTP at $V \simeq 16$, and the RC at $V \simeq 15$ and $B - V \simeq 1.3$. We find an indication of stars in the SGB phase at the base of the RGB and identify the BRGB at $V \simeq 17$.

We evaluated the fraction of binaries as for NGC 1817, and find an average fraction of 16%. For the simulations we use the photometry corrected for DR (see Sec. 6.1.3), and adopt a DR of 0.02 mag to take into account the intrinsic scatter in the correction.

Keeping fixed these parameters we estimate the cluster age and metallicity comparing the observational CMD for stars inside $4'$ from the cluster centre with our synthetic CMDs. We find that only models with metallicity $Z < 0.02$ are in agreement with both $(B - V)$ and $(V - I)$, therefore we discard models with solar metallicity.

For the BBC models we obtain the best match using the metallicity $Z = 0.008$ ($[\text{Fe}/\text{H}] \sim -0.4$). Our synthetic CMD reproduces the magnitude and colour of all the age indicators, reproducing very well the MS, the binary sequence, and the RGB. The corresponding cluster parameters are: age 1.9 Gyr, $E(B - V) = 0.36$, and $(m - M)_0 = 13.2$.

With the FST models we find a good match for $Z = 0.006$, age 1.7 Gyr, $E(B - V) = 0.45$, and $(m - M)_0 = 13.06$. Also in this case the synthetic CMDs can reproduce well the MS, the binary sequence, and the RGB even if the RC colour is slightly redder than observed.

In the case of the FRA models, the best fit is obtained for $Z = 0.01$, age of 1.25 Gyr, $E(B - V) = 0.45$, and $(m - M)_0 = 13.19$. Despite being able of matching the luminosity of the age sensitive indicators, the colour of one of them, the RC, is much redder than observed.

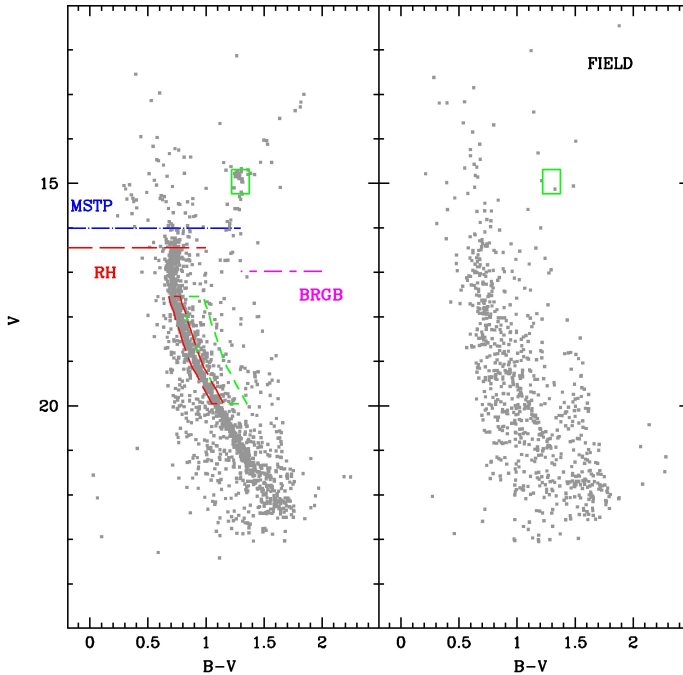


Figure 6.18: Left panel: $V, B - V$ CMD for the inner part of NGC 2141 (inside $4'$) corrected for DR. The age indicators RC (green box), RH (red line), MSTP (blue line), and BRGB (magenta line) are shown. The red and green boxes on the MS and redward the MS are used to estimate the percentage of binaries. Right panel: CMD of the comparison field of the same area. The cluster is still visible, even if as a minor component.

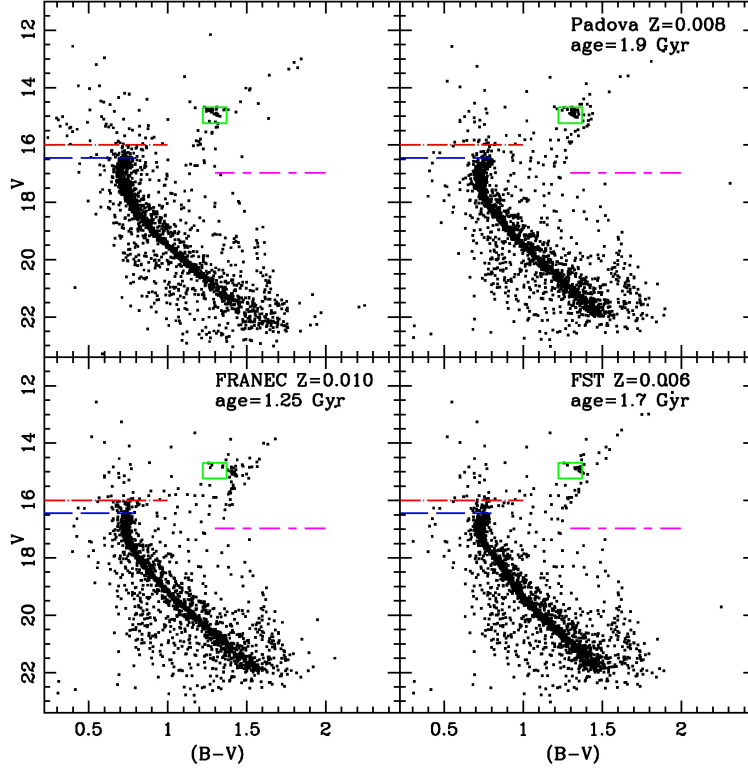


Figure 6.19: Same as Fig. 6.16 but for NGC 2141. The observational CMD in the top left panel is for stars inside a $4'$ radius area.

Moreover, the MS shape is poorly reproduced for faint magnitudes ($V > 19$).

Fig. 6.19 shows the comparison between the observed CMD (top left) and the best fits obtained with the three sets of tracks. From this analysis the BBC models provide a better match of the MS shape and of the colour and magnitude of the age indicators. The results are summarised in Tab. 6.6.

Looking at the luminosity functions of the observational and synthetic CMDs (see Fig. 6.20) we clearly see that the peak of the synthetic distribution is fainter than the observational one. In the comparison field (shown in Fig. 6.18) there are clearly MS stars around $V \sim 20$. This may be due to evaporation, i.e., the typical tendency of low mass stars of moving out of the cluster. Another possible explanation is related to the Initial Mass Function (IMF). The best models predicts a mass of about $0.8 M_{\odot}$ at $V \sim 20$, in the mass range where Salpeter's IMF (Salpeter, 1955) overestimates the mass fraction. Since the synthetic CMDs are generated assuming Salpeter's IMF, they are likely to overpredict low mass stars.

Comparing with literature results we find a lower age with respect to both Rosvick (1995) and Carraro et al. (2001). In both cases the authors chose a TO fainter than ours by about 0.5 mag (at about the same level of our RH), and a RC slightly brighter than ours (see Fig. 5 in Rosvick 1995). Since the age is primarily constrained by the magnitude difference between the RC and the MSTO, the large difference in age is explained by the choice of these two age indicators. We confirm a sub-solar metallicity as suggested by the two papers.

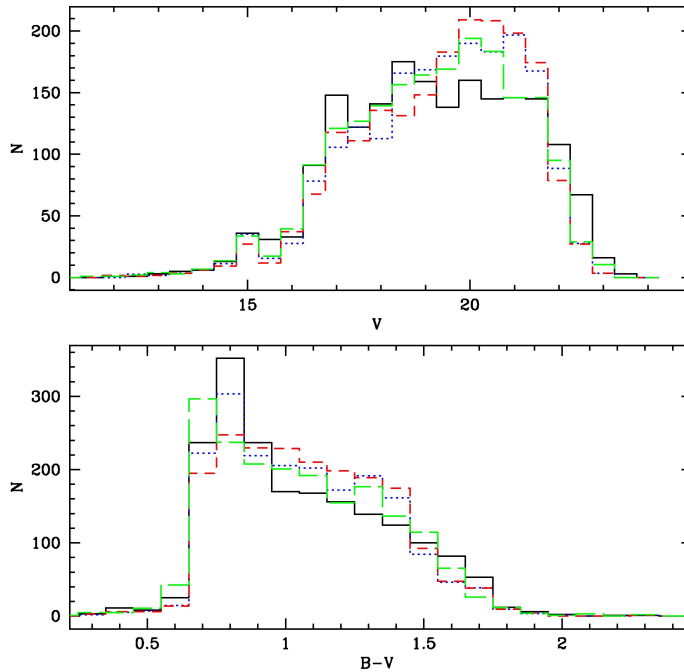


Figure 6.20: Same as Fig. 6.16 but for NGC 2141.

Be 81

Be 81 is highly contaminated by field interlopers, condition that makes the interpretation of the cluster features more difficult. For a more robust analysis we studied the inner part of the cluster, where the contrast density with respect to the background density (see Sec. 6.1.2) is higher and the cluster members should be more evident. From Fig. 6.21 an excess at the brighter MS end ($V \simeq 15.6$) and on the probable RC locus ($V \simeq 16.3$, $B - V \simeq 1.8$) is visible for the central part with respect to an external control region. These features have been evaluated for different inner regions and for different choices of comparison field of the same area. We are confident in adopting these features as age sensitive indicators.

The binary sequence for this cluster is not evident from the CMDs because of the high contamination and possibly DR, and for the simulations we adopted a conservative value of 25% as found on average in many OCs.

We expect a not negligible DR. The MS appears more extended in colour than expected from the photometric error and the probable RC stars have scattered colour and magnitude. After several tests, we decided to adopt a DR of 0.15 for the simulations, with a sensitivity of 0.03. Lower or higher values imply a too tight or too extended MS in the synthetic CMDs.

We find that the cluster footprints (MS and RC) can be reproduced by a solar metallicity, for which we obtain a good match in both V , $B - V$ and V , $V - I$ CMDs. With all the models we can reproduce the magnitude of the age sensitive indicators (RH and RC) and the overall shape of the observational CMD (see Fig. 6.22). The colour of the RC is well recovered by FST and FRA models. Because of the high contamination from field stars and the effect of severe DR we cannot detail our analysis further.

With the BBC models we find an age of 0.9 Gyr, an average reddening $E(B - V) = 0.91$, and a distance modulus $(m - M)_0 = 12.4$. In the case of FST models the best match is for an age of 1.0 Gyr, $E(B - V) = 0.90$, and $(m - M)_0 = 12.37$. With FRA we estimate an age of 0.75 Gyr, $E(B - V) = 0.92$, and $(m - M)_0 = 12.45$.

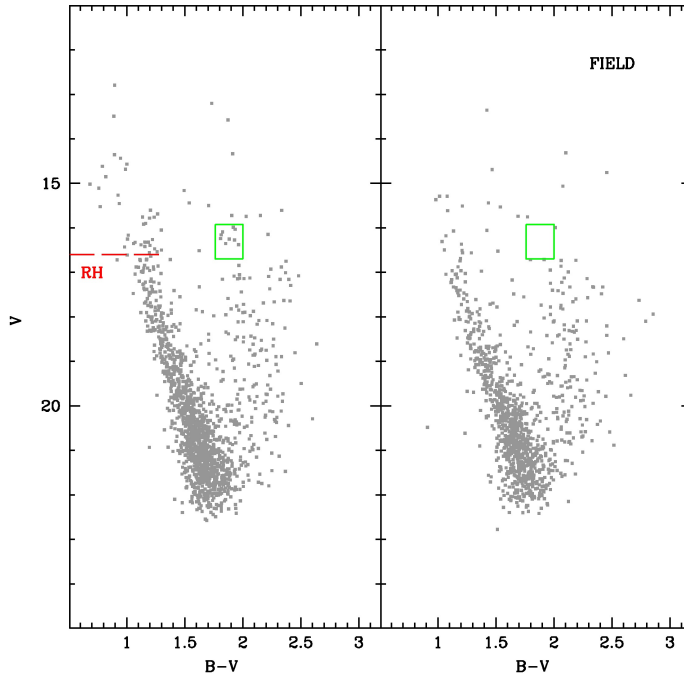


Figure 6.21: Left panel: $V, B - V$ CMD for the inner part of Be 81 (inside $2'$). The age indicators RC (green box) and RH (red line) are shown. Right panel: CMD of the comparison field of the same area. No RC stars appear in the external part of the field.

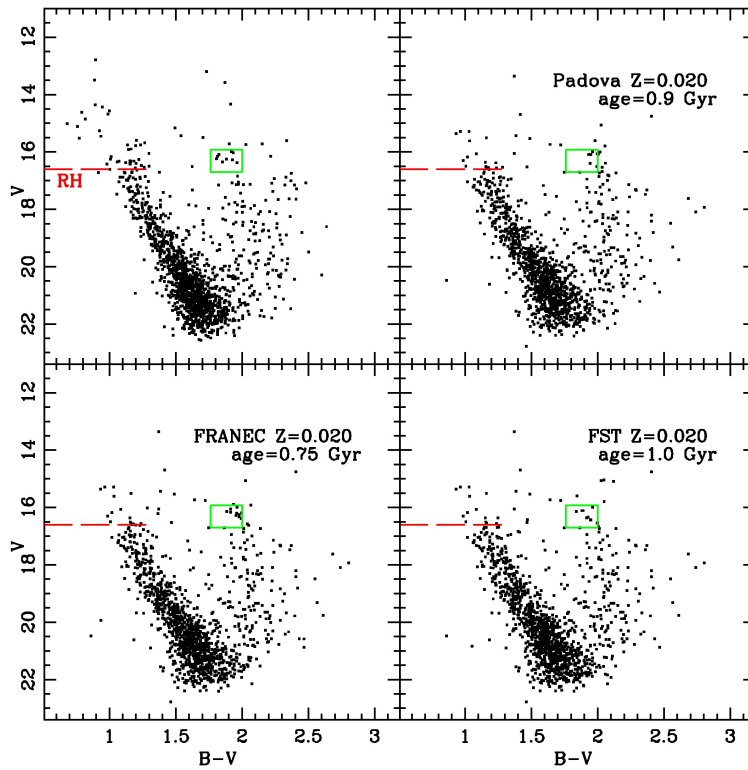


Figure 6.22: Same as Fig. 6.16 but for Be 81. The observations CMD in the top left panel is of stars inside a $2'$ radius area, corresponding to the half mass radius of the cluster.

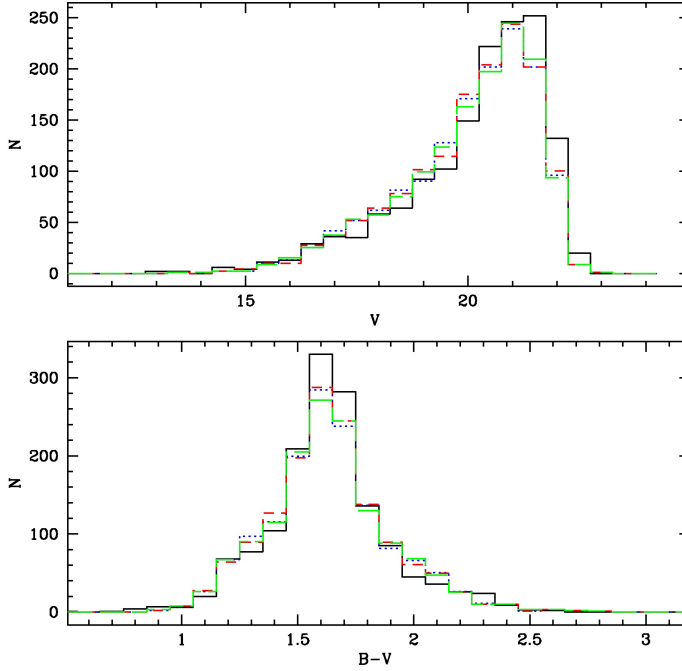


Figure 6.23: Same as Fig. 6.16 but for Be 81.

The comparison of the observational and synthetic LFs is very good both in magnitude and in colour, as shown in Fig. 6.23.

We find a good agreement with the results presented by Sagar & Griffiths (1998). We estimate a lower average DR (about 0.1 mag lower) but this can be explained by the differences in our photometries (see Sec. 6.1.1). On the other hand they exclude that DR be the explanation of the observed broad MS, pointing out that the severe contamination of field stars pollutes the cluster sequences and drives the CMD appearance. We investigated further this hypothesis using the synthetic CMD technique and choosing different external areas inside our FoV. We find that the lower MS ($V > 19$) is always dominated by field contamination and the signature of the cluster is not evident. Hence we evaluated the DR effect from the brighter part of the MS. It is true that there are many field interlopers even for $V < 19$, but low DRs always imply a too tight synthetic MS and RC with respect to the observations. Hence we suggest that DR is not negligible across the FoV of Be 81. Firmer conclusions, especially on the cluster metallicity, will be obtained from the analysis of the Gaia-ESO Survey spectra. Both radial velocity measurements and chemical abundance estimates will be fundamental to distinguish cluster members from field stars, cleaning the cluster sequences by interlopers.

The clusters' mass

The synthetic CMD technique can also be used to evaluate the total mass of the clusters summing the masses of all the synthetically generated stars still alive. In order to do that properly we normalised the synthetic population to the star counts inside one r_h and with magnitude V for which 100% completeness is achieved. The contamination of field stars is taken into account for the normalisation. The derived mass inside one r_h is then multiplied by two to have an estimate of the total mass. The results quoted in Tab. 6.6 are obtained with MonteCarlo experiments. We generated 300 hundred synthetics for each cluster taking

Table 6.6: Cluster parameters derived using different models.

Model	age (Gyr)	Z	$(m - M)_0$ (mag)	$E(B - V)$ (mag)	d_\odot (kpc)	R_{GC}^a (kpc)	z (pc)	M_{TO} (M_\odot)	M_{tot} (M_\odot)
NGC 1817									
BBC	1.1	0.008	11.10	0.23	1.66	9.61	-373.2	1.8	-
FST	1.05	0.010	10.98	0.21	1.57	9.53	-353.2	1.9	-
FRA	0.80	0.010	10.88	0.34	1.50	9.46	-337.3	2.0	-
NGC 2141									
BBC	1.9	0.008	13.20	0.36	4.37	12.21	-440.9	1.5	5600 ± 300
FST	1.7	0.006	13.06	0.45	4.09	11.95	-413.4	1.6	6160 ± 400
FRA	1.25	0.010	13.19	0.45	4.34	12.19	-438.9	1.7	4480 ± 300
Be 81									
BBC	0.9	0.020	12.40	0.91	3.02	5.74	-131.3	2.1	1540 ± 100
FST	1.0	0.020	12.37	0.90	2.98	5.77	-129.5	2.1	1624 ± 100
FRA	0.75	0.020	12.45	0.92	3.09	5.69	-134.4	2.2	1232 ± 100

^a $R_\odot = 8$ kpc is used to compute R_{GC}

into account the uncertainty on the normalisation star counts and the error on the distance modulus and differential reddening parameters. The first one is considered as a poissonian error on the counts, hence it affects the number of stars extracted to populate the synthetic. The errors on the distance modulus and reddening (quoted in Sec. 6.1.4) affect the mass limit at which the synthetic population is normalised. We use the median of the distribution obtained and its r.m.s. as the reference estimate for the total mass of the cluster.

We can perform this evaluation only for NGC 2141 and Be 81, the two clusters for which we could estimate the King profile (see Sec. 6.1.2). For NGC 2141 we adopted $V < 16.75$ as magnitude limit to normalise the synthetic population. This limit corresponds to the faintest magnitude at which completeness is still 100% (see Tab. 6.3). For Be 81 we adopted $V < 17.25$ as magnitude limit. Using brighter magnitude limits comparable mass estimates are found within the errors.

These computations provide about $1000M_\odot$ for Be 81 and $\sim 4000M_\odot$ for NGC 2141. These mass estimates are a lower limit to the total cluster mass. In fact the stellar models we are using to make synthetic populations have a lower mass limit of $0.6 M_\odot$, hence all the stars with lower mass are not taken into account. To get the actual cluster mass we then need to extrapolate along the IMF down to $0.1 M_\odot$. This implies multiplying by a factor of two the mass if we adopt Salpeter's IMF (Salpeter, 1955) and by a factor of 1.4 if we adopt Kroupa's (Kroupa, 2002). Since the latter is supposed to best describe the real IMF, we conclude that Be 81 has a mass of about $1400M_\odot$ and NGC 2141 of $5600M_\odot$. These are the values listed in Tab. 6.6.

6.2 Ongoing work

Eleven OCs more, for which we have already photometric images, will be shortly added to the BOCCE database. We acquired photometric data for Berkeley 30, Berkeley 98, Berkeley 99, NGC 2158, NGC 2225, NGC 2355, NGC 2204, and Trumpler 5 (Tr 5) on large FoVs (LBC@LBT and WFI instruments) and for Berkeley 19, and NGC 2266 on small FoVs (OIG@TNG instrument). The first six are part of two proposals at LBT (PI Bragaglia and PI Donati). I am currently working on the analysis of two OCs of the group: NGC 2158 and Trumpler 5, both older than 1 Gyr. NGC 2158 was observed with LBC@LBT on February 2012 with B , V , and I filters, and the technical aspects of the instrument and the observations scheme are the same described in Sec. 6.1.1. Tr 5, instead, was observed using the Wide Field Imager mounted at the 2.2-m MPG/ESO Telescope of the La Silla Observatory (Chile), in November 2001. The WFI instrument is a mosaic composed by 8 CCDs covering a FoV equal to 34×33 arcmin². The dataset consists in images in U , B , and V filters. For this cluster I am also working on additional high resolution spectra of 3 RC stars that have been observed with the spectrograph UVES@VLT in order to derive chemical abundances and cluster's metallicity.

6.2.1 NGC 2158

NGC 2158 is an old cluster located at RA=06:07:26 and Dec=24:05:52 ($l=186.64$ and $b=1.79$). This cluster is relatively well studied both with photometric and spectroscopic observations, even if with contradictory results for its parameters (see e.g. Carraro et al. 2002; Jacobson et al. 2009 for extensive discussions of the different conclusions). In fact, for this cluster the derived parameters show a dichotomy: either the cluster has a metallicity close to solar and is heavily reddened or it is less reddened and metal-poorer. We hope to help solving this ambiguity with our analysis.

Photometry

The photometric data analysis follows the same scheme adopted for the other LBT clusters and described in Sec. 6.1.1. However, no standard stars have been observed the same night, hence it was not possible to obtain independent calibration equations. We could only tie our data to the photometric catalogue available in literature (Carraro et al., 2002, hereafter C02). As done for NGC 1817 in Sec. 6.1.1, we checked the calibration with SDSS data, transforming the SDSS photometry into the Johnson-Cousins system. Surprisingly, we found significant differences between the $V - I$ colour of C02 and the one from SDSS. In Fig. 6.24 we show in black the CMDs obtained with the data of C02 and in blue the SDSS stars in the field of NGC 2158. While in the $(V, B - V)$ empirical CMD the calibration obtained with C02 and the SDSS photometry are in good agreement, in the $(V, V - I)$ plane there is a systematic difference of about 0.2 mag. In order to understand the issue we asked for further observations of NGC 2158 to obtain an independent calibration. The LBT observations provided us with deep and precise photometry (about 3 magnitude deeper in V with respect to C02) and it would be very important to assess accurate cluster's parameters as done for the other LBT clusters described in this chapter.

Nevertheless, looking at the $(V, B - V)$ CMD, where C02 and SDSS photometry agree, we can describe the principal morphological features of the cluster. In Fig. 6.25 we show the CMDs in the $B - V$ colour and for different distances from the cluster's centre.

The RH is located at $V \simeq 16.7$ and $B - V \simeq 0.9$, as evident by looking at the inner region. The stars in the RGB phases are easily recognisable and extending up to $V \sim 13$

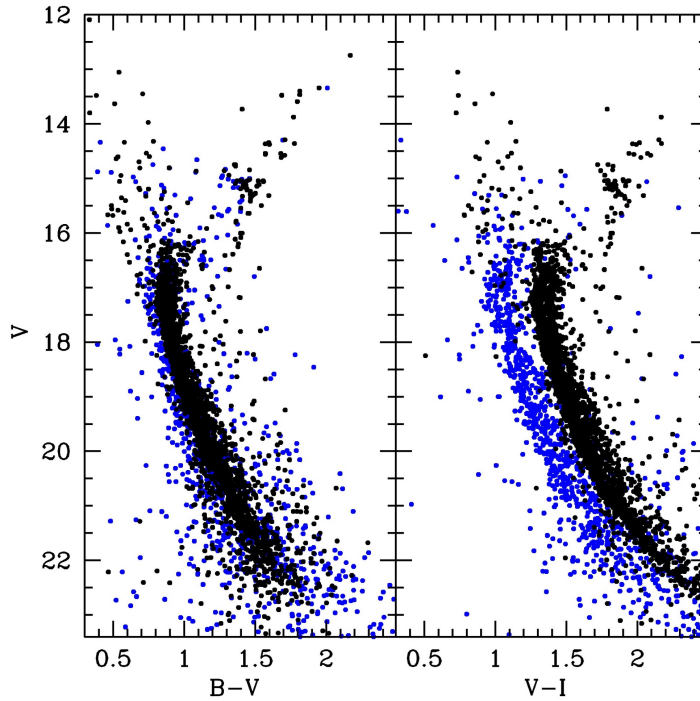


Figure 6.24: Empirical CMDs of NGC 2158. The black points are our data calibrated using C02 as reference catalogue. The blue points are the SDSS photometry in the cluster's field, transformed to Johnson-Cousins filters. In the right panel the systematic difference in colour between the two datasets is evident.

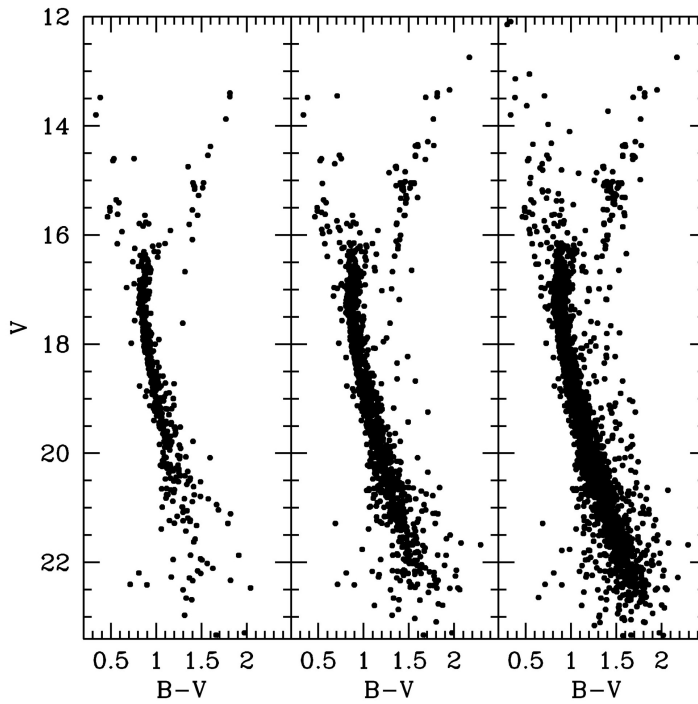


Figure 6.25: Empirical CMD of NGC 2158 for different area. *Left panel:* stars inside 1'; *middle panel:* stars inside 2'; *right panel:* stars inside 3'.5'.

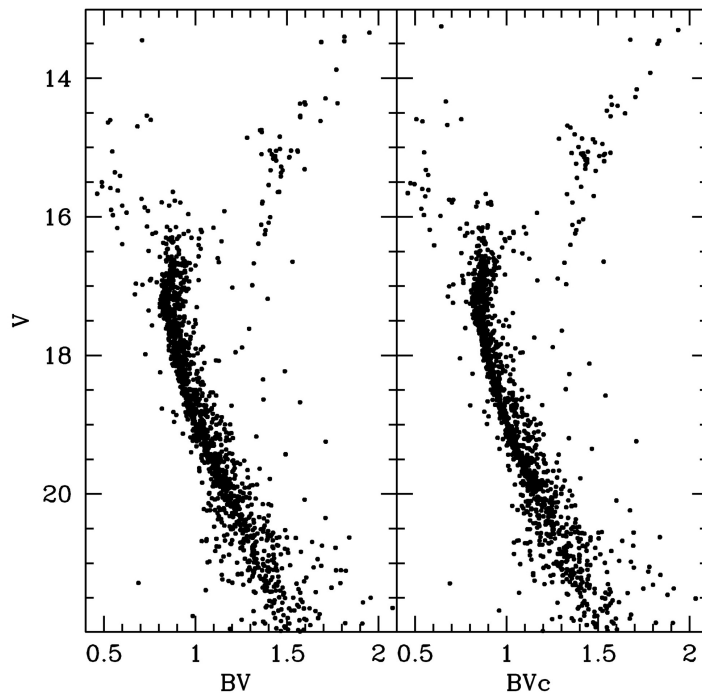


Figure 6.26: CMDs of NGC 2158 inside $2'$. *Left panel:* empirical CMD. *Right panel:* CMD corrected for DR.

but much more numerous when larger areas are considered. Several blue straggler stars, brighter and bluer than the upper MS of the CMD, appear clearly, especially in the CMD of the inner region where the field contamination is not relevant. The RC is manifest at $V \simeq 15.2$ and $B - V \simeq 1.4$ and appears clearly stretched. We argued, as in the case of NGC 2141 (see Sec. 6.1.3), that the DR across the face of the cluster might be conspicuous. The extended shape of the upper MS is in favour of this hypothesis.

Then, we quantified the DR to investigate if the CMD appearance improves after correcting for it, i.e. if the stretched shape of the RC and the spread visible in the upper MS reduce. We adopted the same procedure described in Sec. 6.1.3 and found that the DR ranges between -0.10 mag and 0.15 mag with respect to the average Galactic reddening ($E(B - V) \simeq 0.6$ from C02). In Fig. 6.26 we compare the observational CMD and the one corrected for DR. The improvement is evident: the RC stars are less stretched and appear more clumped; the MS is more defined and tight, the spread visible in the observational CMD is less pronounced in the corrected one.

6.2.2 Trumpler 5

Trumpler 5 is a massive and old OC in the anticentre direction ($l = 202.81$, $b = 1.01$). It is interesting because it is metal-poor ($[Fe/H] \leq -0.3$ dex, according both to photometric and low-resolution spectroscopic measures) and located at a Galactocentric distance of 10-13 kpc where a transition from a radially-decreasing metallicity to a flat(ter) distribution seems to happen (see Ch. 1).

As usual, its properties (age, distance, reddening) show a large dispersion (see table 1 in Kim et al. 2009 for a comprehensive list of values prior to our work).

Photometry

The photometric data were reduced following the same procedure adopted for the clusters described so far. However, our final catalogue is still provisional because it requires a detailed analysis of the well known photometric distortion of the WFI instrument. As described e.g. in Koch et al. (2004), the CCD mosaic has not a uniform response to incident light, and varies sensibly from CCD to CCD. Unfortunately, we do not have enough standard stars to obtain individual calibration equations for all chips, moreover, we cannot use available photometric catalogues in literature to solve the issue because they cover small FoVs, not sufficient for the full data set. In the following discussion we focus on chip #2, centred on the cluster, for which we could obtain a self-consistent calibration in agreement with the one of Kaluzny (1998).

In Fig. 6.27 we show the CMDs for Tr 5 for different distances from the cluster centre. It is a rich cluster, showing a neat sub-giant and giant branches. Notwithstanding the heavy field contamination, several blue stragglers stars are identifiable bluer than $B - V \sim 1.0$ and brighter than $V \sim 17$. The RC is extended and located at $V \sim 15.0$ and $B - V \sim 1.5$. The structure of the upper MS is blurred and difficult to define. Also for this cluster we argue that DR across the cluster face is significant and represents the main explanation of the CMD appearance.

We applied the same technique adopted in other OCs to evaluate the DR. We found that DR can vary a lot (we investigated the inner $6'$ from the cluster centre, where the density of stars is about 50% higher than the external region of our field of view), ranging from -0.1 mag up to 0.3 mag with respect to the average intergalactic reddening ($E(B - V) = 0.58$, Kaluzny 1998). After applying the correction for DR, the MS, SGB, and RGB appear tighter and the RC appears more clumped (see Fig. 6.28).

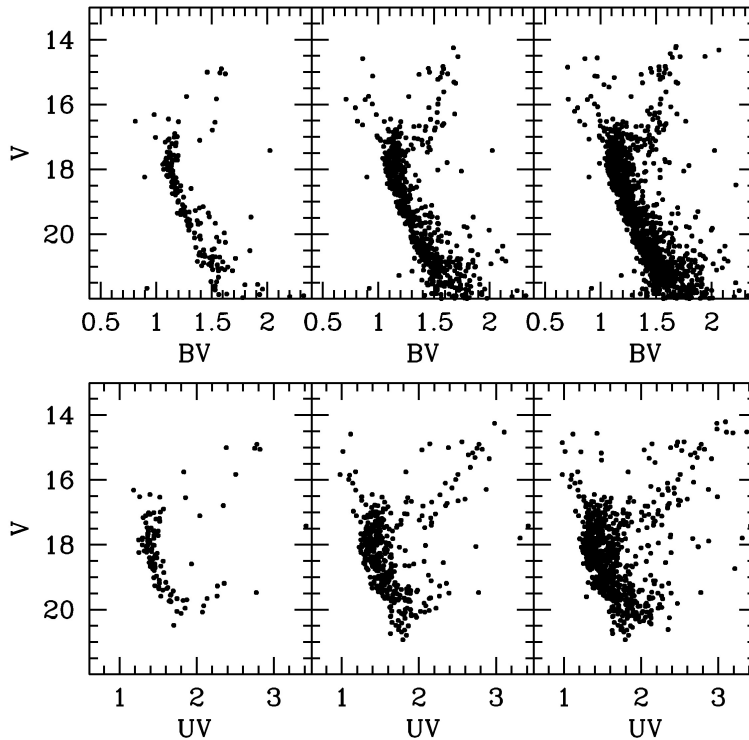


Figure 6.27: CMDs for Tr 5 in the $B - V$ (upper panels) and $U - V$ (lower panels) colours and for different distances from the cluster centre (from the left to right: $d < 1'$, $d < 2'$, and $d < 3'$).

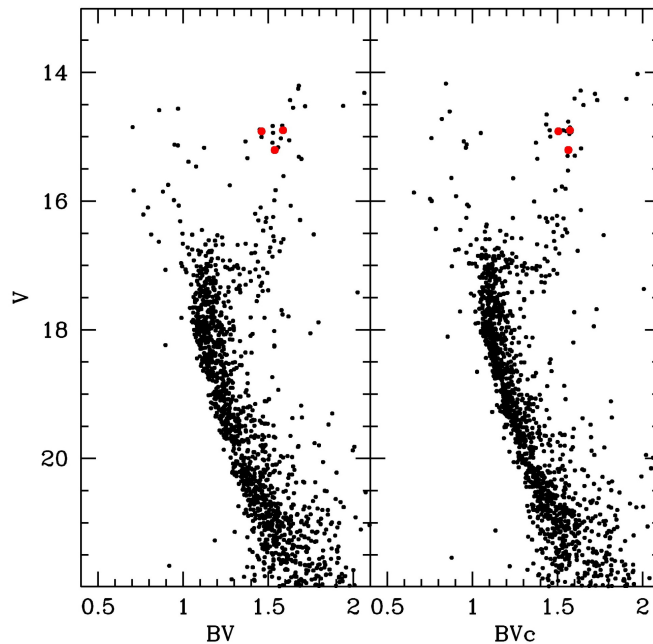


Figure 6.28: On the left the observational CMD for Tr 5. On the right the CMD after the correction for DR is applied. The red points are the three spectroscopic targets, part of this study.

The estimation of the cluster’s parameters through the sCMD technique is still provisional, waiting for a solution of the issue of the photometry for the whole CCD mosaic. The results we got for the BBC models (using tracks with $Z = 0.008$) are age of 2.7 Gyr, $E(B - V) = 0.66 \pm 0.04$, and $(m - M)_0 = 12.30 \pm 0.1$.

Spectroscopy

The spectra of three RC stars were acquired in service mode at the ESO Very Large Telescope (VLT) with the high-resolution spectrograph UVES (ESO programme 074.D-0344, PI Pancino). They were analysed using the DOO pipeline, an automated version of DAOSPEC (Stetson & Pancino, 2008), described in details in Cantat-Gaudin et al. (2013) and in Ch. 7. The EWs obtained with DOOp were used for the classical curve of growth analysis. The GALA programme (Mucciarelli et al., 2013) was used to derive the stellar atmosphere parameters and the elemental abundances. We obtained for the three stars an average abundance of $[\text{Fe}/\text{H}]$ of about -0.4 dex. The positions of the three stars are shown in Fig. 6.28. Looking at spectroscopic analyses available in literature, Cole et al. (2004) obtained an average metallicity of $[\text{Fe}/\text{H}] = -0.56 \pm 0.11$, making Tr 5 one of the metal-poorer known OC. Carrera et al. (2007), instead, found $[\text{Fe}/\text{H}] = -0.36 \pm 0.05$, much more similar to our estimate. They both employed the IR calcium triplet (CaT) calibrated to well known GCs and OCs to estimate the iron abundance.

We plan to present the complete and detailed results both for the photometry and the spectroscopy in a paper, in preparation.

Chapter 7

First Gaia-ESO Survey data

The Gaia-ESO Survey started on 31 December 2011 (see Ch. 3). Its scientific outcome will be unprecedented thanks to the ambitious aims of the project. Only a large scientific collaboration, involving many scientists of different research groups from all over the world can guarantee its success. It is not only a matter of man power, which, indeed, is crucial to handle all the tasks of the survey (see Ch. 3), but also a matter of dealing with specific scientific requirements.

One of the basic requirements is the data analysis of the many spectra observed. Ordinarily, the spectroscopic analyses are carried out on a few spectra at a time, as a results of observations planned on stars of the same type. Moreover, they are usually spectra of the same spectral resolution and spectral range. The grand design of the survey, instead, targets stars of different spectral type and tunes the observations according to different aims. Hence, the analysis of the spectra requires adaptability to deal with widely different data and different quality. Furthermore, it has to be efficient in managing a considerable amount of spectra in a row.

WG10 and WG11 are the two working packages in charge of analysing the spectra of F, G, and K spectral type stars. As described in Ch. 3, WG10 and WG11 coordinate and combine the analyses of several nodes, each one of them providing independent results. I cooperate with the two WGs as member of the EPInArBo node, sharing the analysis of HRS spectra of field stars, which are mainly stars in the MSTO phase, and OCs' stars, which are mainly giant stars (cool and with the typical metallicity range of the thin disc), and intermediate-high resolution spectra of clusters' stars, which are mainly MS metal-rich dwarf stars.

The outcomes of the analysis are the measurements of the EWs of the absorption lines of each spectra, the estimates of the stellar atmosphere parameters (namely effective temperature, T_{eff} , surface gravity, $\log g$, metallicity, $[\text{Fe}/\text{H}]^1$, and microturbulence, ξ) for each target, and the chemical abundances for a selected list of elements. Within the EPInArBo node the EWs are measured with a dedicated pipeline (DOOp) while atmosphere parameters and chemical abundances are obtained through the classical method of the curve of growth analysis performed by the FAMA programme.

In this chapter I describe the tools used for the spectra analyses (DOOp and FAMA) and then focus on the first scientific results obtained for the old OCs observed by the Gaia-ESO Survey and part of the first data release. In particular I will focus on the OC Trumpler 20,

¹ $[\text{Fe}/\text{H}]$ is the iron abundance with respect to the solar value, and defined as $[\text{Fe}/\text{H}] = \log \frac{n(\text{Fe } I)}{n(\text{H})} - \log \frac{n(\text{Fe } I)_{\odot}}{n(\text{H})_{\odot}}$.

object of the analysis described in Donati et al. (2014b), and briefly present the outcomes for the other old OCs.

7.1 DOOp

DOOp (described in Cantat-Gaudin et al. 2013) is an acronym that stands for *DAOSPEC Option Optimiser pipeline*. It uses DAOSPEC (Stetson & Pancino, 2008, hereafter SP08) to measure the EWs and optimises its key parameters in order to make the measurements as robust and repeatable as possible. It was built as part of the PhD theses work by Tristan Cantat-Gaudin and myself. I will make a short synopsis of the main characteristics of DAOSPEC in the next section in order to better understand the DOO pipeline.

7.1.1 DAOSPEC: a brief description

DAOSPEC is an automated FORTRAN programme to measure EWs of absorption lines in high-resolution (typically, higher than 20000) and high signal to noise (SNR higher than 30) spectra of stellar atmospheres. The measured lines are matched with a user-provided line list. The code employs a fixed full width at half maximum (FWHM, or scaled with wavelength for echelle spectra) to facilitate deblending, and estimates the continuum with Legendre polynomials after all the fitted lines are removed from the spectrum. This makes DAOSPEC especially useful on crowded spectra.

One important feature of DAOSPEC (see Fig. 4 in SP08) is that the continuum on which the EW fits are based is not the *true continuum* of the spectrum (i.e., the continuous star emission after all the lines are excluded), but an *effective continuum*, which is the true continuum depressed by a statistical estimate of the contaminating lines (the unresolved or undetected ones, producing a sort of line blanketing). This greatly improves the estimate of the unblended EW of each line in crowded spectra, as demonstrated in Sec. 3.2.1 of SP08, but it is often perceived as being too low by those who are used to employing traditional interactive methods for the continuum fitting procedure. The discrepancy between the true continuum and the effective continuum increases with line crowding (i.e., spectrum metallicity, especially for giants) and with decreasing SNR or resolution of the spectra.

FWHM and continuum placement are strictly correlated: if the continuum level of a spectrum is altered, so is the FWHM of each line. This is why the three most important parameters for a successful use of DAOSPEC are: (1) the FWHM estimate; (2) the continuum placement; and (3) the residual core flux parameter, which is the flux at the core of saturated lines, expressed in percent of the local continuum level. Therefore, DOOp is designed to provide the best fine-tuning of these three parameters.

The DAOSPEC code relies on statistical evaluation to consistently estimate the FWHM of the lines and places the effective continuum across the whole spectral range, which means that it performs better on wider ranges than on smaller ones. When dealing with spectra from an echelle spectrograph that delivers individual orders, it is safer to use a merged spectrum rather than measuring each order separately. This applies of course also to DOOp.

7.1.2 DOO pipeline

The DOOp code is an algorithm which optimises the parameters of DAOSPEC in order to get the best measurements of EWs. The fine tuning of the parameters is obtained through a fully automatic and iterative procedure and is tailored to the intrinsic characteristic of

the spectrum that is going to be analysed. This procedure is performed by different scripts written in BASH² and IRAF built around DAOSPEC.

The DAOSPEC parameters on which DOOp focuses are the following:

- short wavelength limit (SH)
- long wavelength limit (LO)
- minimum radial velocity (MI)
- maximum radial velocity (MA)
- residual core flux (RE)
- FWHM (FW)

An exhaustive description of these parameters can be found in SP08 or in the DAOSPEC manual publicly available³. Here we describe briefly their meaning. The SH and LO parameters specify the spectral range over which DAOSPEC will measure equivalent widths. The MI and MA parameters set the velocity range in which DAOSPEC is allowed to estimate the radial velocity (RV) of the star. Imposing a restricted range of possible RV through MI and MA reduces the risk of mismatching the lines (for instance in spectra with very few or very broad lines) and helps to find the right value. It also reduces the computation time. The RE parameter tells the program the residual flux at the core of the deepest line in the spectrum. The FW sets the estimate of the resolution of the spectrum in units of pixel. All the other DAOSPEC parameters are set to default values but some of them must be specified in the input file of DOOp (see Sec. 7.1.2).

Among these, the most important is the order of the polynomial (OR) used to fit the continuum. This parameter is not optimised by DOOp, and is kept fixed to the value provided by the user. The OR parameter should be chosen with care and in the next section we discuss its importance and its impact on the EW measurement.

The choice of continuum fitting when analysing a stellar spectrum is always of great importance. A good model of the continuum must follow the main large-scale features in a spectrum, and a general rule of thumb is to use a polynomial of an order similar to the number of waves seen in the spectrum. For a large wavelength range, one must use a polynomial of higher order. Different choices of continuum can result in differences in EWs of up to 2 mÅ for some lines, as illustrated in Cantat-Gaudin et al. (2013) when comparing measurements with literature values obtained with DOOp.

Basic functioning

The work flow of the pipeline is summarised in Fig. 7.1. The pipeline reads two input files. One is needed to set the basic options of the algorithm of the whole pipeline, such as the names of the output files and the convergence parameters for Module 2 (described later in this section). The other input file contains the list of spectra to analyse and a set of six parameters for each of them. The first five parameters are the DAOSPEC parameters OR (order of the polynomial for continuum fitting), FW (first guess of the FWHM), FI (=1 if this FWHM must be kept fixed, =0 if it must be optimised), RE (residual core flux) and

²BASH is a Unix shell, a free software in common with all the operating systems based on UNIX and Linux.

³www3.cadc-ccda.hia-ihp.nrc-cnrc.gc.ca/community/STETSON/daospec or www.bo.astro.it/~pancino/projects/daospec.html

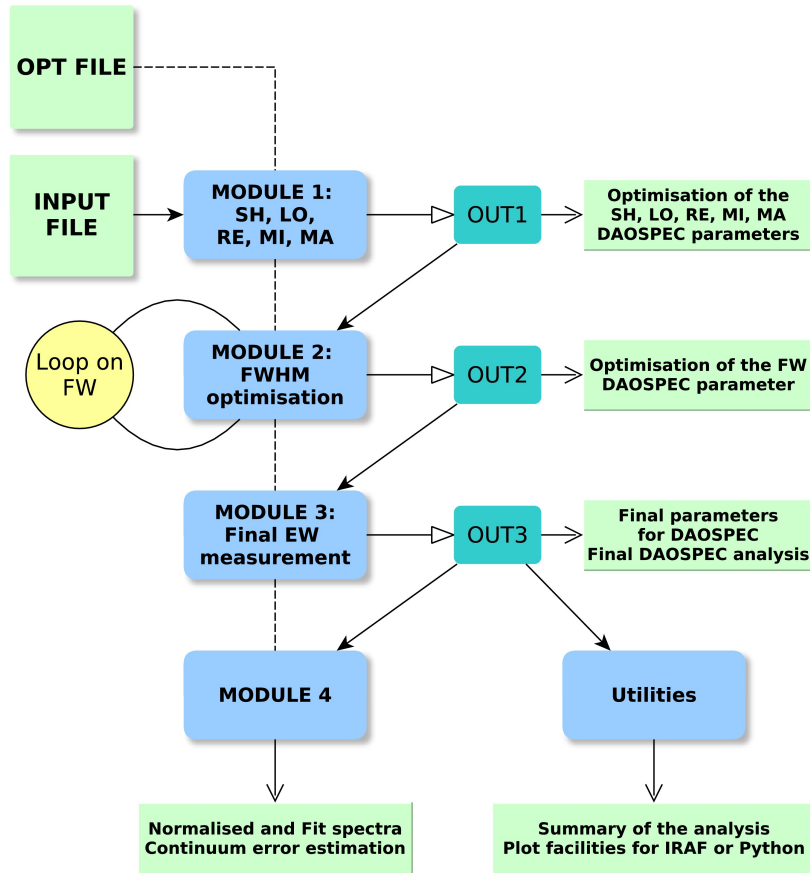


Figure 7.1: The tasks performed by DOOp are organised in several modules. The figure shows the dependencies of the modules and their main results.

RV (radial velocity). If RE and RV are known their value can be given by the user to save computation time, otherwise setting a value of 0 means they will be derived by the pipeline. The last parameter sets which algorithm the pipeline must use to optimise the FWHM. At the moment two possibilities are allowed (see next paragraphs). All the parameters must be explicitly specified. To ensure that DOOp performs well on a list of spectra it is always better to analyse together spectra of the same resolution, that were collected with the same instrument.

After these two files are set, DOOp is ready to work. The measurements will be carried out by four modules performing different tasks:

- **Module 1:** this module provides the SH, LO, RE, MI, and MA parameters, as well as the first EW estimates. The SH, LO, and RE values are determined calling IRAF twice with two different IRAF scripts. The first looks for the starting and ending wavelength of the spectrum avoiding glitches and bad values that may be found at the spectrum borders, setting the two parameters as the first/last wavelength for which the spectrum has a non-negative value. The second looks for the strongest lines in the spectrum ($H\alpha$, $H\beta$, Mg b triplet, Ca II triplet for the Gaia-ESO spectra) to set properly the RE parameter. If negative values are found, or if none of these strong lines are

detected, a default value is imposed. The MI and MA parameters are set accordingly to the input RV: if 0, then a wide range is imposed, otherwise a smaller range is used. These ranges can be defined by the user ($\pm 500 \text{ km s}^{-1}$ and $\pm 10 \text{ km s}^{-1}$ are typically reasonable values). At the end of Module 1 a first EW measurement is performed on the spectra for which DAOSPEC did not encounter computational problems. This measurement is not the best one, as not all the parameters are optimised.

- Module 2: this module provides the best FWHM parameter for DAOSPEC. For each analysed spectrum, an initial value of FWHM is needed. If the user wishes to optimise the FWHM, DAOSPEC runs once and Module 2 compares the output FWHM to the input (user-given) value. If a convergence criterion (by default, the output value has to be within 3% of the input) is not reached, then DAOSPEC runs again, using the output value as a new initial guess. The user can choose how many of the spectra in the list have to reach convergence (in percent). In some cases, the spectra under analysis are known a priori to present the same FWHM but its estimate is made difficult in some spectra (for instance because of different signal-to-noise ratios). In such a case it can be sufficient to reach convergence for only 50 or 70% of them and use the median value of the FWHM to measure the others (which is done by Module 3). In the most general case of a batch containing spectra of potentially different FWHMs (because the spectra were obtained with different instruments or because of rotating stars) it is recommended to require 100% of the spectra to reach convergence of the FWHM, so that this parameter is estimated in an independent way for each spectrum. If after 30 iterations the FWHM has not converged for some spectra, Module 3 will take care of them.
- Module 3: this module determines the FWHM that will be used for the final EW measurements. It computes the median FWHM of all the spectra for which it converged. Depending on the choice of the user, it will use this median value for the spectra that did not converge, or for all the spectra in the batch *including those that converged*. This second option may be more suitable if all the spectra are known a priori to have the same FWHM. Of course, the spectra for which the user had required to use a fixed FWHM (by setting FI=1) are measured using the FWHM given by the user. The output of DAOSPEC at the end of Module 3 are *the final EW measurements of DOOp*.
- Module 4 is designed to perform two different tasks. One is to provide the fit and normalised spectra in FITS format, because DAOSPEC only provides the continuum and residual FITS files. The other task is to provide EW measurements obtained by over- and underestimating the continuum level. The amount by which the continuum will be shifted is proportional to the dispersion of the residuals in the final DAOSPEC fit. The results coming out of these experiments can be used to quantify the error in the EW measurement due to the placement of the continuum. For UVES/FLAMES spectra (R=47000), the dispersion of the residuals of the fit ranges typically from 3% for a SNR of 30, to 1% or less for a SNR above 100. Altering the continuum placement by these amounts can lead to differences of 10 and 3 mÅ respectively, although this is certainly a conservative estimate and can depend on other factors such as the metallicity of the star. A description of how the EWs are changed when altering the continuum placement is done by SP08 in their Sec. 3.4.3 and Fig. 2. Module 4 uses IRAF scripts to obtain the FITS files, while DAOSPEC is called to perform the EW measurements on the spectra with artificially imposed continuum levels. This module

works with the output produced by Module 3.

- Utilities: together with the main algorithm of the pipeline, small scripts are provided to perform standard operations on the output files obtained by Module 3. They are presently used to produce the input files for the abundance analysis programs GALA (Mucciarelli et al., 2013) and FAMA (Magrini et al., 2013a) and to print out a summary of the analysis, including a log of the possible errors. With a provided script, the user can easily visualise and compare the spectra and their corresponding fit.

One advantage of the pipeline is that it can be easily customised. For example, if only the RV measurement is needed, one can set the pipeline to use only Module 1. If, instead, one wants to test the effect of changing the continuum order while keeping all the other parameters fixed, it is also possible. Furthermore, if the user prefers to pre-normalise their spectra using a personal routine, indicating a continuum order of -1 tells DAOSPEC not to perform any normalisation.

The performances of DOOp are tested and described in Cantat-Gaudin et al. (2013). In Fig. 7.2 the continuum placement and the fit obtained with DOOp for a benchmark stars used as a test-case are shown as an example. DOOp, along with a user guide, is available to the community via its web page: <http://web.oapd.inaf.it/GaiaESO/DOOp>.

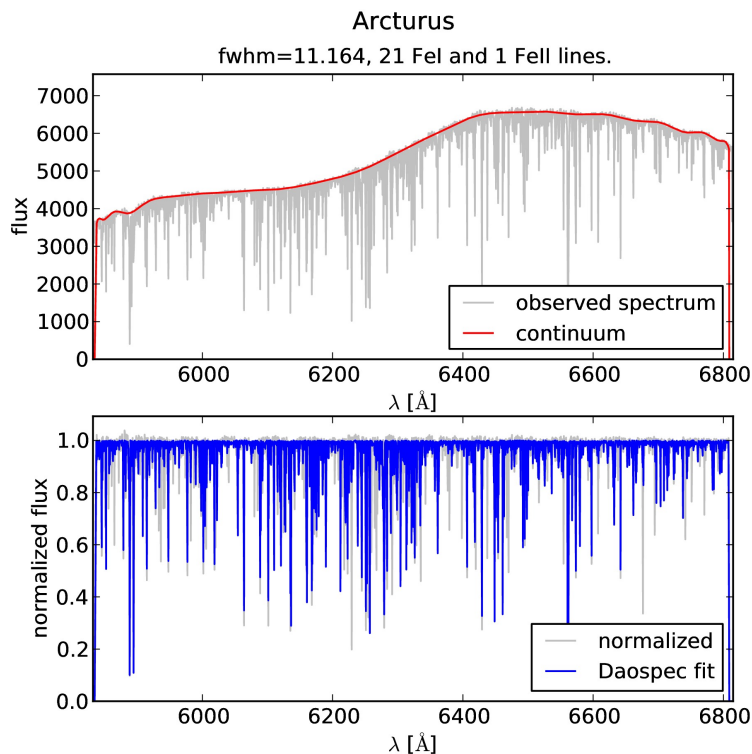


Figure 7.2: UVES-POP spectrum of Arcturus seen through the graphical interface of DOOp. *Top*: original spectrum and fitted continuum. The flux is given in arbitrary units, as the instrument response was not corrected for. Information is displayed on the FWHM of the lines and the number of lines that were identified from the line list. *Bottom*: normalised spectrum and fit.

7.2 FAMA and the traditional EW analysis

FAMA (the acronym stands for Fast Automatic Moog Analysis) is described in details in Magrini et al. (2013a). It is a programme which uses MOOG (Snedden, 1973; Sneden et al., 2012) to automatically derive the stellar atmosphere parameters and the chemical abundances, given a set of EWs. It is designed to perform the classical analysis of MOOG

(see next paragraphs) for a large number of stars without any human intervention during the phase of determination of atmospheric parameters and abundances.

The classical use of MOOG is to assist in the determination of these quantities following the basic equations of one-dimensional local thermodynamic equilibrium (1D LTE) stellar line analysis, in addition to a variety of line analysis and spectrum synthesis tasks. The classical version of MOOG makes use of the ABFIND driver with a model atmosphere to derive the stellar parameters and the abundances. MOOG needs a continuous human intervention to adjust the stellar parameters satisfying three requirements: the ionisation balance, the excitation balance, and the minimisation of the trend between abundance and the observed (or predicted) reduced EWs $[\log(\text{EW}/\lambda)]^4$. Each of these three well-known steps allows to fix one of the stellar parameters:

- Temperature is obtained by eliminating trends between abundance of the chemical elements and the respective excitation potentials (EP). If we assume a wrong T_{eff} in the analysis of a given stellar spectrum, we need different abundances for matching the observed profile of transitions with different values of EP. A wrong, too large value of T_{eff} will introduce an anticorrelation between abundances and EP while a positive correlation is expected in the case of the adoption of a value of T_{eff} that is too small.
- Gravity is optimised by assuming the ionisation equilibrium condition, i.e. requiring that for a given species, the same abundance (within the uncertainties) is obtained from lines of two ionisation states (typically, neutral and singly ionised lines). Because gravity is a direct measure of the pressure of the photosphere, variations of $\log g$ lead to variations in the ionised lines (which are very sensitive to electronic pressure), while the neutral lines are basically insensitive to this parameter.
- Microturbulence velocity is set by minimising the slope of the relationship between abundance and the logarithm of the reduced EWs. The microturbulent velocity is a quantity incorporated in the Doppler width of the profile of a line, introduced to increase the strength of the lines near or on the flat part of the curve of growth to reconcile them with the observations. ξ preferentially affects the moderately/strong lines, while the weak ones are less affected.

However, the atmospheric parameters are correlated with each other. A variation of T_{eff} implies a variation of ξ . Also, variations of T_{eff} and ξ will change the abundances derived from different levels of ionisation (hence, the gravity) in different ways. Because the determination of the atmospheric parameters is usually done with an iterative process, it could take a relatively long time to complete the analysis of a single star. This is acceptable if the number of stars is limited. When dealing with a large sample FAMA is very efficient, automatically performing the iterative process. It is able to minimise the slopes of the correlations in a coherent way that considers the quality of the spectra and of the EWs measurement.

7.2.1 FAMA in a nutshell

FAMA can be run by feeding it with two files for each spectrum. One is the file with the EWs measurements (obtained, in our case, with DOOp) and the other is the file containing the

⁴In theory, it might be possible to use all the known elements to satisfy the three equilibria, provided that their corresponding absorption lines can be identified. Usually, Fe is the most used one. Many absorption lines of Fe I and several of Fe II are well known and relatively easily identifiable and measurable in the optical wavelength range, covering a sufficiently large range in EPs and in EWs.

first-guess atmosphere parameters (T_{eff} , $\log g$, ξ , and $[\text{Fe}/\text{H}]$)⁵. The programme is designed to look for the three conditions that satisfy the LTE requirements i.e. excitation equilibrium, ionisation equilibrium, and the trend between $\log n(\text{Fe I})$ and $\log(\text{EW}/\lambda)$, by using Fe absorption lines through a series of recursive steps that follow a hierarchical algorithm. The T_{eff} value is the controlling parameter for the ultimate solution and is the one to be set first: the guess on T_{eff} is adjusted by an amount that depends on how far the initial T_{eff} is from the excitation equilibrium. Subsequently the surface gravity is modified by an initial amount that depends on the difference between $\log n(\text{Fe I})$ and $\log n(\text{Fe II})$. Finally, ξ is varied on the basis of the slope of reduced EW versus $\log n(\text{Fe I})$. This is repeated for three cycles. In each cycle, the minimisation requirements on the slopes and neutral/ionised iron abundances are varied and become stricter with each cycle. In particular, the minimisation requirements for the first cycle are three times larger than those of the last cycle, and those of the second cycle are two times larger. The value of the smallest minimisation requirement is calculated using the information on the quality of the EW measurements. Since the EW measurements are affected by errors, it is not reasonable to minimise the slopes to infinitely low values, yielding zero slopes. This would have no physical justification and would lead to finding local minima in the three-dimensional space of T_{eff} , $\log g$, and ξ . Thus, the minimum reachable slopes in FAMA are strictly linked to the quality of the spectra. This is correct in the approximation that the main contribution to the dispersion is due to the errors in the EW measurement rather than to an inaccuracy in atomic parameters, such as e.g. the line strengths ($\log gf$). During the first iteration, the EWs of Fe I and Fe II are treated with a σ -clipping, a procedure that allows to remove EWs producing abundances more discrepant than $n\sigma$ from the average abundance. The σ -clipping thresholds may be easily changed according to necessity. In Fig. 7.3 (figure 3 of Magrini et al. 2013a) the final control plot of FAMA plotting the excitation and ionisation equilibria and the trend between $\log n(\text{Fe I})$ and $\log(\text{EW}/\lambda)$ achieved by the programme is shown for the Sun spectrum as example.

To ensure that the final solution is independent from the initial parameters, FAMA is however designed to repeat the complete convergence path up to six times. At each step, the requirements of minimisation of the three slopes become stricter and they are parametrised by the so-called quality parameter (QP, adjustable to specific requirements). Each step starts with initial parameters that are the convergence point of the previous step and with the original EW list. The sequence of several steps is necessary, because it allows to move toward the final set of stellar parameters while maintaining the initial line list. After the last step when the final stellar parameters are obtained, the EWs of all elements are passed to MOOG, a σ -clipping is performed on them, and a final evaluation of the error is done.

The errors on the final stellar parameters are obtained evaluating a maximum and a minimum acceptable value for each one, fixing the slopes of the excitation equilibrium, the slope of the trend between $\log n(\text{Fe I})$ and reduced EWs, and the difference between Fe I and Fe II abundances to the maximum and minimum values allowed by the dispersion of the abundances. Concerning the error in the final individual element abundances, there are two types of errors which are considered by FAMA: i) the statistical uncertainties due to the random errors in the EW measurements and to uncertainties on the atomic parameters; and ii) the errors on the abundances generated by the uncertainties in the determination of the atmospheric parameters. The first source of errors is simply evaluated during the analysis with MOOG by the standard deviation around the average value of the abundance of each elements. The second source of error is instead evaluated recomputing the element

⁵These can already be close to the final values, e.g. for stars in a cluster, but FAMA can reach convergence even starting from widely wrong initial guesses.

abundances with the stellar parameters corresponding to the minimum and maximum slope and Fe I and Fe II difference. Their difference with respect to the abundances computed with the best parameters gives us an estimate of the error due to the uncertainties in stellar parameters.

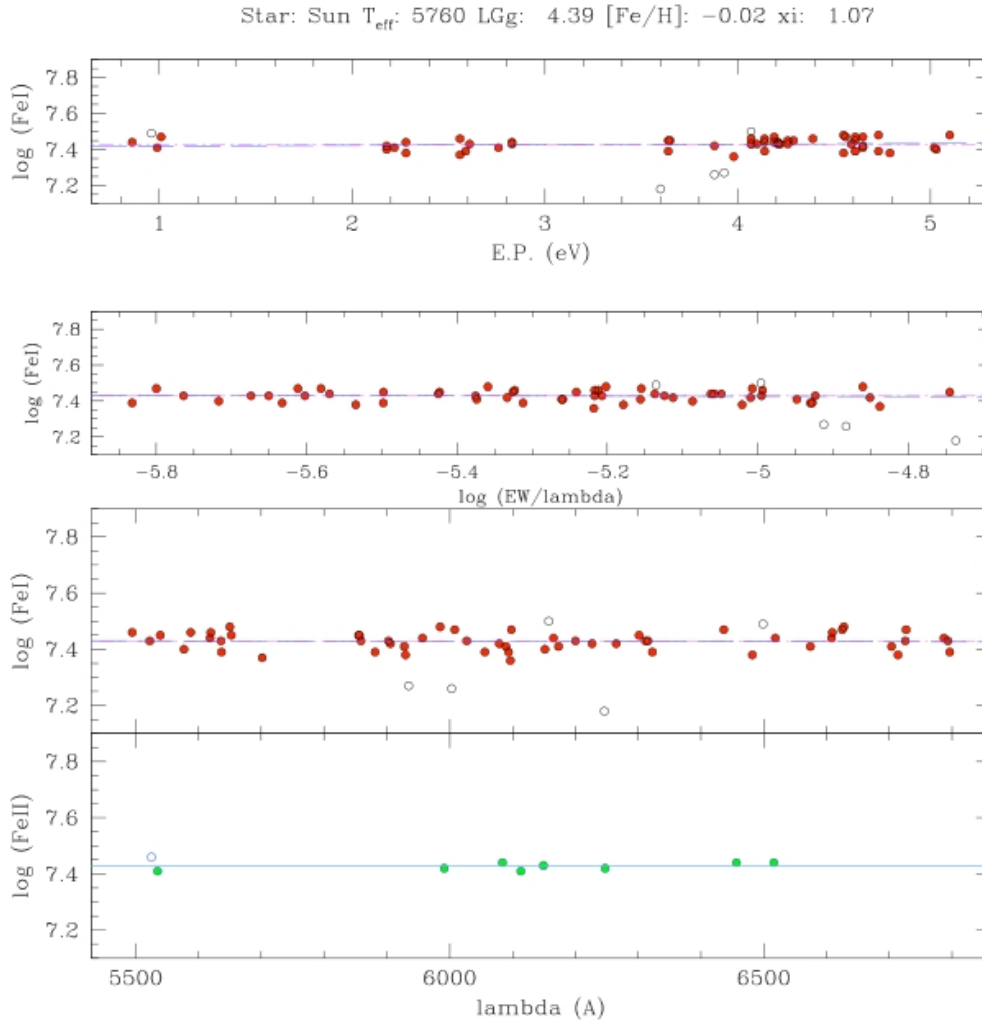


Figure 7.3: Example of the final control plot of FAMA. In the first three panels, the filled (red) circles are the abundances from the Fe I EWs accepted after the σ -clipping, while the empty circles are those rejected. In the first two panels the excitation and microturbulence equilibria are shown. The blue long-dashed line is the zero-slope curve, and the dashed magenta line is the slope of the final convergence point. In the third panel the dependence on iron abundances on λ is shown, and in the fourth panel, the ionisation equilibrium is presented with the green circles being the Fe II abundances used for gravity determination. The cyan horizontal line in the last panel is the average Fe II abundance, while the magenta line (which coincides with the blue one) is the average Fe I. Reproduced from Magrini et al. (2013a).

7.3 Trumpler 20, NGC 4815, M 11

The target stars of the OCs of the Gaia-ESO Survey are selected within WG4, as described in Ch. 3. After the first 6 months of observations the results for the old OCs Trumpler 20 (Tr 20), NGC 6705 (or M 11), and NGC 4815 were made available as produced by the first internal data release (GESviDR1Final). The targets for these clusters, described with more details in the following sections, are giant stars (observed mainly with the UVES spectrograph) and MS stars (observed mainly with the GIRAFFE spectrograph).

The three OCs are all located within the Solar circle. Their parameters and chemical properties are studied in details in four different papers summarised in the following sections. The goal of these studies is *a)* to determine with better accuracy the cluster fundamental parameters (age, distance, and metallicity) from the best-fitting isochrones of the latest evolutionary models, taking into account the effect of differential reddening (if relevant) and the spectroscopic information from the Gaia-ESO Survey for cluster membership and chemical abundances; *b)* to determine the RV distribution of the clusters using mostly the GIRAFFE spectra; *c)* to constrain the metallicity of the clusters by accurate chemical abundances analysis using mostly the UVES spectra; *d)* to compare the chemical patterns of each object with well studied MW components (MW field stars).

These OCs are set in a region still poorly investigated but of great importance for our understanding of the mechanisms of disc/bulge formation as well as for studying the radial metallicity gradient (see Ch. 1). Being close to the Galactic centre, the three clusters might have suffered from strong tidal effects, as well as frequent interactions with molecular clouds, and thus they can provide important constraints to the cluster survival in a ‘hostile’ environment (see e.g. Lada & Lada, 2003).

7.3.1 Tr 20

The detailed analysis of this cluster is presented in Donati et al. (2014b). Photometric data and the Gaia-ESO Survey results are combined together to obtain accurate cluster’s parameters.

7.3.2 Observational data

The photometric catalogues considered in the following analysis are the ones described in Platais et al. (2008), hereafter P08, and Carraro et al. (2010), hereafter C10, that we retrieved from the CDS and WEBDA. By using the CATAPACK programme, we were able to cross-identify the stars in common between the two catalogues and compare their photometry. The difference between P08 and C10 is on average -0.052 ± 0.045 in V , $+0.057 \pm 0.025$ in $(B - V)$, and -0.146 ± 0.032 in $(V - I)$ (in the sense of C10-P08).

Because of the smaller difference, we decided to give preference to the $(B - V)$ colour with respect to the $(V - I)$ one throughout the analysis. The impact on the derivation of the cluster properties of the use of the two catalogues is discussed in Sec. 7.3.5.

Many stars of Tr 20 have been observed within the Gaia-ESO Survey, using the GIRAFFE HR15N setup and the UVES 580nm setup. The targets were selected to lie on or near the evolutionary sequences of the CMD. Concerning the cluster MS, stars with colour between the blue envelope of the MS and about 0.3 mag redder were considered potential targets, with a higher priority given to stars closer to the cluster centre. The cluster RC is evident and rich, and all stars in this phase were considered potential targets. Some potential subgiant stars were also targeted. The GIRAFFE targets were chosen mainly on the MS and on the possible subgiant branch (SGB), the RGB, and the RC, while the UVES targets fall

mostly on the RC. In Fig. 7.4 we show their spatial position and their locus on the CMD. The SNR ratio of the spectra depends mainly on the luminosity of the targets, spanning from about 10 for the fainter targets up to 300 for the most luminous. The median SNR is about 30 for the GIRAFFE targets and 60 for those of UVES.

The Gaia-ESO Survey observations of Tr 20 have been obtained in Spring 2012 and 2013. We observed 42 stars on the RC with the UVES fibres, while 527 MS and giant stars were observed with the GIRAFFE fibres. Only 13 UVES targets were fully analysed as part of the first internal data release (GESviDR1Final) of the survey, which encompassed the first six months of observations, while for the other targets a full analysis will be available in the next releases. However, the RV is available for all the Gaia-ESO Survey stars and for the 954 archive spectra (ESO programme 083.D-0671, PI C. Melo) with the GIRAFFE HR09B setup, described in Platais et al. (2012) (hereafter P12) and re-analysed inside the Gaia-ESO

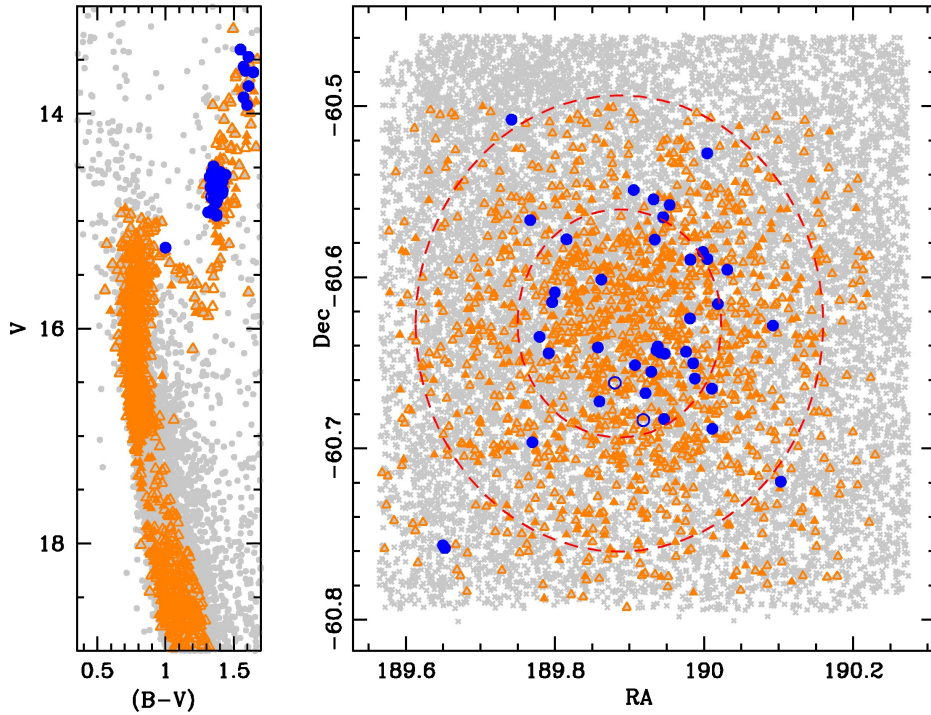


Figure 7.4: *Left panel:* CMD of the GES targets for Tr 20 with a distance from the centre $d < 8'$. *Right panel:* Spatial distribution of the GES targets; the red dashed circles define the regions for $d < 4'$ and $d < 8'$ from the centre. In both panels, the orange triangles are GIRAFFE targets, while the blue filled circles are UVES; filled symbols are candidate members for RV (see Sec. 5). The stars in the photometric catalogue are plotted in grey.

Survey. This very large sample greatly benefits the analysis of the RV distribution. In our sample, 40 stars were observed both with UVES and GIRAFFE; 110 stars with the two GIRAFFE setups; 10 with all the setups. More information on the observations is given in Table 7.1. In Table 3 of Donati et al. (2014b), only available online through CDS, we list the relevant information for all the spectra (obtained with the three different setups HR09B, HR15N, and UVES) of the targets. With the help of this new spectroscopic information, it is possible to derive the cluster parameters with unprecedented accuracy.

Table 7.1: Summary of the GES and public spectroscopic observations for Tr 20.

Setup used	$\lambda\lambda$ (nm)	Time exp. (min)	# stars
UVES 580nm	476.0-684.0	3×50	525
GIRAFFE HR15N	647.0-679.0	3×50	42
GIRAFFE HR09B	514.3-535.6	60 ^a	954

^aESO public archive data of programme 083.D-0671 (see P12) processed within the GES

7.3.3 Photometric analysis

Centre, mass, and radius

Since RVs are available only for part of the stars, to select probable cluster members we made a broad photometric selection to remove very obvious field polluters from the sample, keeping the MS, MSTO, and RC stars. We determined the position of the cluster centre by an iterative process using the same method described in Sec. 5.1.2. We computed the barycentre of the positions of the stars, then took the 70% of stars closest to this position and recomputed their barycentre, and iterated until convergence on a central position. To avoid selecting too many field stars we tried different magnitude cuts at $V = 16, 17,$ and 18 . This led to similar results: the position we obtain is identical within $0.5'$ around the coordinates $RA=12:39:32:8$, $Dec=-60:37:37:04$ (or, in Galactic coordinates: $l = 301^\circ.47$, $b = 2^\circ.21$). Our coordinates nicely compare to the one found in Seleznev et al. (2010) which used a different method.

Tr 20 is densely populated and stands out against the field stars, which enabled us to follow its density profile. C10 indicated that the completeness of their photometry is better than 90% for magnitudes $V < 19$. To be conservative, we only used stars brighter than $V = 18$. We performed a least-squares fit of a two-parameter King profile (King, 1962),

$$f(r) = \rho_{bg} + \frac{\rho_0}{1 + (r/r_c)^2}, \quad (7.1)$$

where ρ_{bg} the background density, ρ_0 the central density, and r_c the core radius are left as free parameters. The observed profile and the best-fit are shown in Fig. 7.5. Using a three-parameter King model that also takes into account a tidal radius does not improve the goodness of fit. This means that the tidal radius of Tr 20 is larger than our field of view, and the region where the density profile starts to decrease faster is too far out for our data.

Since the model fitting provides a value for the background stellar density, we were able to remove its contribution to the star counts. The density profile was integrated to obtain the total number of stars contained in the cluster. Assuming a Salpeter mass function and the best-fitting PARSEC isochrone (see Sec. 7.3.5), we produced a synthetic population that

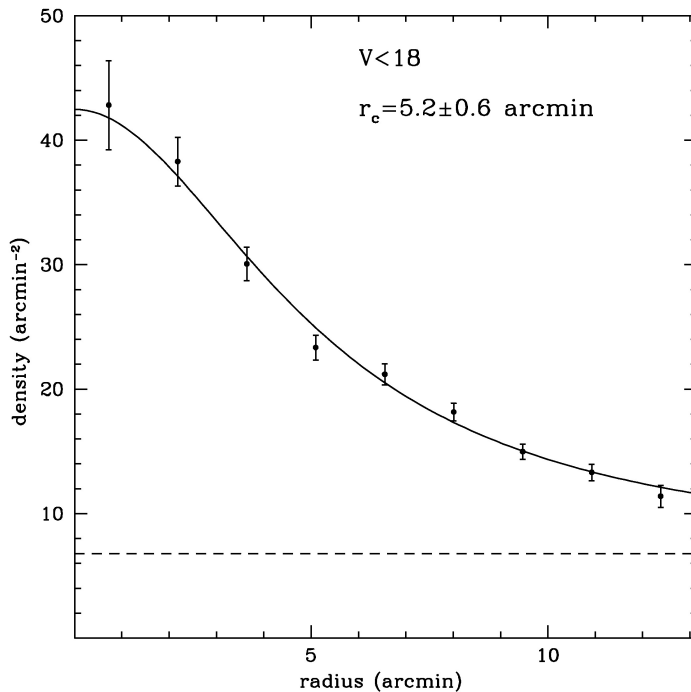


Figure 7.5: Density profile of Tr 20 using stars with $V < 18$. The error bars are the random errors. The best-fit is a two-parametric King model of core radius 5.2 ± 0.6 arcmin.

contains the same number of stars as Tr 20 in the magnitude range $V < 18$. We added all the masses of stars down to $0.08 M_{\odot}$ (according to the IMF) and found a total mass of about $6800 M_{\odot}$. Varying the age of the isochrone within the uncertainties gives an estimate of the error on the total mass. This whole operation was also performed by selecting stars brighter than $V = 17$ and $V = 16$, which yielded very similar results. Finally, we estimated the total mass of Tr 20 to be $6700 \pm 800 M_{\odot}$. We can draw a more conservative estimate by adding the contribution of the random errors to the star counts. Considering the Poissonian uncertainty, we find a mass between the extreme values of 5500 and $8000 M_{\odot}$.

Differential reddening

The position of Tr 20 in the Galactic disc and its high reddening estimates strongly suggest differential reddening (DR, as discussed by P12). As discussed in Sec. 6.1.3, the main effect of DR on the CMD appearance is that it broadens the sequences. This is mainly due to the presence of patchy dust structures in the field of view, which cause different extinctions along the line of sight. Photometric errors have a similar effect on the CMD appearance, but the broadened MS of Tr 20 cannot be explained only with errors since they are too small in the two photometric studies considered, as discussed in the original papers.

Other explanations of the broadened MS and elongated RC cannot be a priori ruled out. For example, as pointed out in Sec. 6.1.3, age spread during the star formation process, unresolved binary systems, metallicity spread, and stellar rotation can produce, in principle, observational effects very similar to DR. Among all, the metallicity spread is the less likely interpretation because there is no evidence among the OCs of inhomogeneities in the overall metallicity. Concerning rotation, hot early-type stars, such as those near the MSTO, can be fast rotators, as demonstrated by P12 and as seen from the Gaia-ESO Survey GIRAFFE spectra. However, the rotation has a mild effect on the CMD appearance (see P12), confirming the study of Girardi et al. (2011), who excluded rotation as a possible explanation

of the extended TOs observed sometimes in LMC clusters.

An estimate of the DR for Tr 20 has been performed in P12. They used about 200 slow-rotator stars (located in the upper MS) and evaluated their distance, along the reddening vector direction, from a hand-defined blue envelope of the MS. They smoothed the measurements on a grid using a scale of $1'$ and adopting for each bin the median of the nearest few measurements that fell in the same bin of the grid. They demonstrated that the effect of DR on the cluster face is not negligible, but we were unable to use their individual DR values because they are not publicly available at the moment.

We decided to apply the same method described in Sec. 6.1.3. We used the photometry of C10 because it reaches fainter magnitudes, so that the MS is well described on a wider magnitude range. We estimated the DR in the $B - V$ colour, since the C10 and P08 photometric data agree better in this colour than in $V - I$ (see Sec. 7.3.2). The direction of the reddening vector was derived assuming the standard extinction law ($R_V = 3.1$) described in Dean et al. (1978). The fiducial line was defined using the CMD of the inner part of the cluster (all the stars in C10 inside $4'$ to clearly identify the cluster signature against the field contamination) and was chosen as the ridge line along the MS. In Fig. 7.6 the box and the fiducial line used are highlighted. Several attempts were made to avoid fiducial lines that during estimation of the DR led to corrections that artificially and noticeably changed the magnitude and colour of the age-sensitive indicators. We aimed to keep the RC, MSTO, and the blue envelope of the MS as close as possible to the observational CMD to limit spurious interpretations of the cluster parameters due to DR corrections. When defining the MS box, we avoided the broadened and curved region of the TO, where the morphology might hamper a correct interpretation, and the fainter part of the MS, where the photometric error is larger.

Taking into account the star counts of the inner and outer parts of the cluster (see Sec. 7.3.3), we decided to limit the application of correction for DR to stars inside a region of $6'$ of radius. For the outer parts the contamination of field stars becomes significant (the

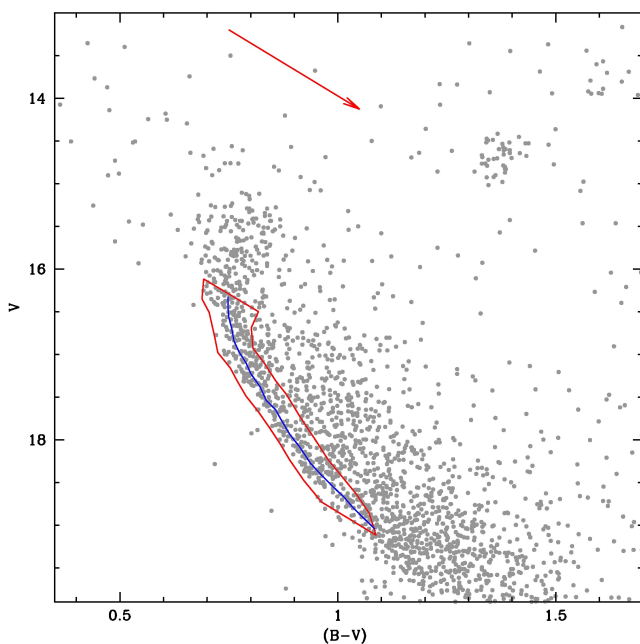


Figure 7.6: CMD of Tr 20 inside $4'$. The red box and the blue line indicate the MS box and the fiducial line for the DR estimate. The red arrow indicates the reddening vector, both in direction and size.

contrast density counts with respect to the field plateau drops below 50%) and any attempt to estimate the DR is severely affected by field interlopers. For all the stars inside $6'$, a value of DR was computed using the 30 nearest stars falling in the MS box. Then spatial smoothing was applied to obtain a more robust statistic, adopting a binning of $50''$ in right ascension and declination.

In Fig. 7.7 (panel a) we show the map of the DR obtained in terms of $\Delta E(B - V)$ with respect to the fiducial line. It ranges from about -0.07 to about $+0.10$. In particular, a region of low reddening is clearly identifiable. Comparing our results with those presented in Fig. 3 of P12, we obtain qualitatively the same result, with a region of lower DR in the north-western part. We found an excursion in the DR estimates of about 0.15 mag, similar to the 0.1 mag discussed in P12. Our higher value can be explained by the fact that we did not impose a blue envelope, allowing negative correction for DR, while P12 fixed the DR at zero for stars bluer than their reference line. In Fig. 7.7 (panel b) we show the corresponding map of the error associated to our estimates. The discrete appearance of these maps is due to two facts: the poorness in sampling a circular area using polygonal bins and the avoidance of interpolation in the corners, where the poor statistics may produce weak estimates. The table with the DR estimates is available through the CDS.

The overall effect of the DR on the CMD appearance is shown in Fig. 7.8. The MS and MSTO regions appear tighter, reducing the broadening of these phases substantially. This improvement is highlighted in black in the figure for the upper MS, but the lower part also benefits from the DR correction. The RC stars are more clumped, highlighting the peculiar morphology of this phase (see Sec. 7.3.3). Our DR estimate did not change the luminosity level and colour of age-sensitive indicators such as the MSTO, the bright limit of the MS, or the red-hook (RH) phase, limiting artifacts in estimates of the cluster parameters. The main difference to the method used in P12 is that we used many more stars to estimate the DR,

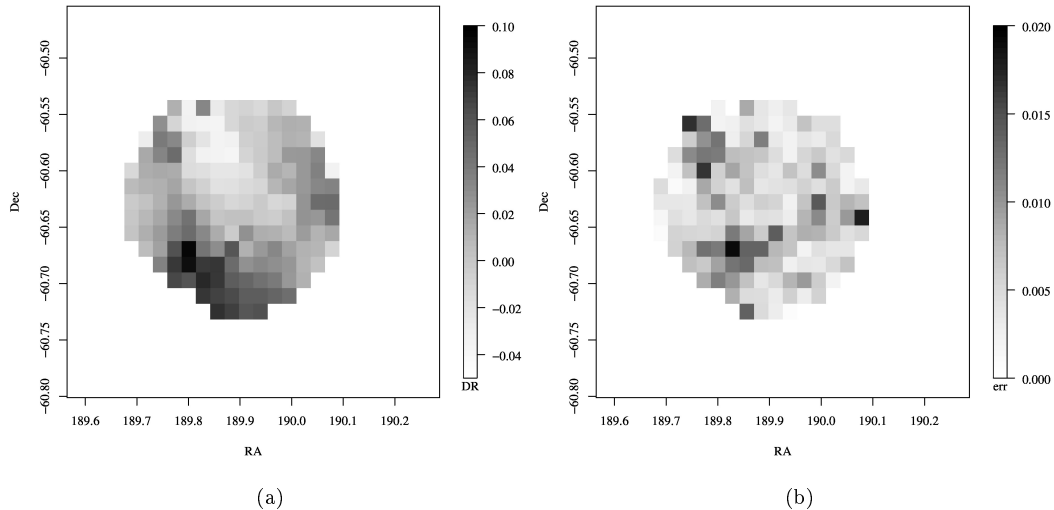


Figure 7.7: (a) Colour deviations from the reference line due to the effect of DR, mapped on a $50'' \times 50''$ grid for stars inside $6'$ from the centre. (b) Corresponding error map for the computed colour deviations from the reference line. The grayscale on the right side of each panel indicates the level of each parameter plotted.

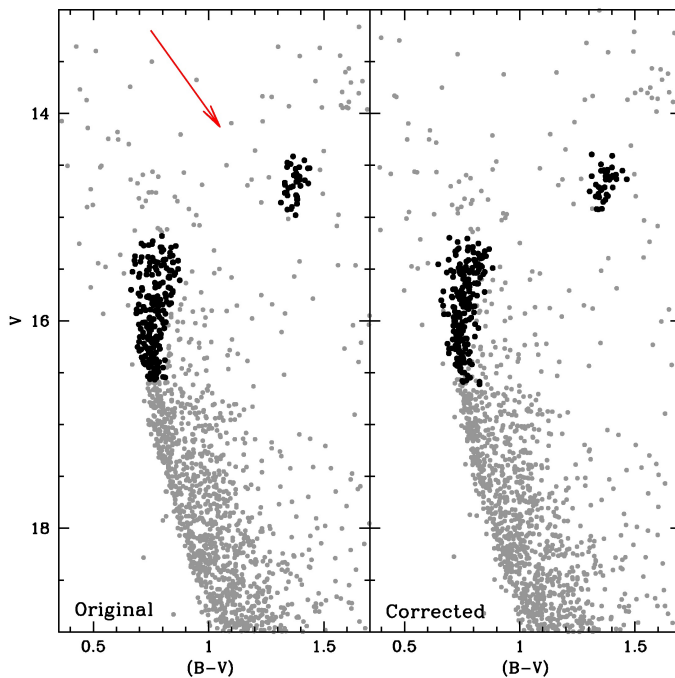


Figure 7.8: CMDs for Tr 20 stars (photometry from C10) with distance from the cluster centre $d < 4'$. *Left panel*: original photometry. The red arrow shows the direction of the reddening vector. *Right panel*: photometry corrected for DR. The TO and RC regions are plotted in black to clearly show the effect of the correction for DR.

which is therefore supported by a robust statistic. Moreover, we selected stars on the lower MS, avoiding objects at the MSTO. In this part of the CMD other physical mechanisms than DR have a more significant impact on the star magnitude and colour (in particular binaries), and, furthermore, the shape of the MS is much more sensitive to the metallicity and age, limiting the accuracy on both the DR estimates and the definition of the fiducial. On the other hand, the P12 method has the advantage of using only cluster members. Even though we have spectra for 1370 stars, only 520 are candidate members (see Sec. 7.3.4) and 100 fall in the MS box. They are too few for a statistically significant estimate of the DR on the cluster field. However, we can quantify the differences between the two methods for the stars in common. Adopting the same MS box and fiducial, we compared the DR corrections obtained for individual stars using our method and that of P12, without applying spatial smoothing. We found that the average difference is -0.004 mag with a dispersion of 0.02 mag. No systematic differences between the two methods were found, but only a low intrinsic dispersion. As final caveat, we stress that photometric errors, undetected binary systems, and residual contamination from the field might affect the DR estimation because they all produce a broadening of the MS. Our results are therefore an upper limit to the DR.

Red clump

Tr 20 has been known to feature an extended RC at $B - V \simeq 1.45$, spread from $V \simeq 14.5$ to $V \simeq 15$. The de-reddened photometry of Figs. 7.8 and 7.9 shows that this extension is real and is not created by DR, as was found also by P12. Furthermore, when DR is taken into account, the double structure of the RC, which has previously been discussed by C10, becomes more evident (see Fig. 7.9, panel a). Two distinct groups of stars are evident, one extended and fainter, centred on about $V \sim 14.8$, the other more luminous, centred on $V \sim 14.5$. We see, however, that the RC cannot be fitted by a single isochrone

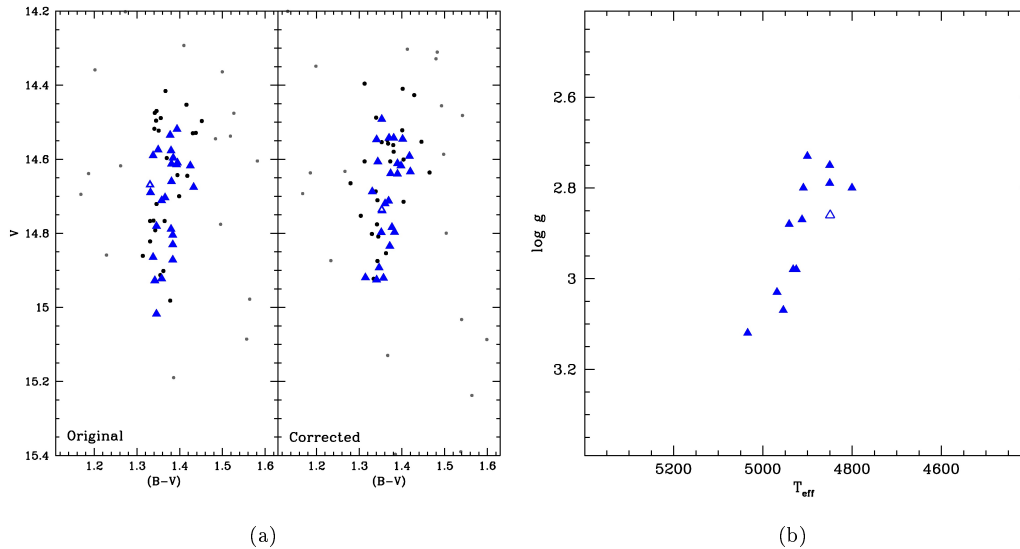


Figure 7.9: (a) As in Fig. 7.8, but for a CMD region centred on the RC position and for stars inside $5'$. The blue triangles are the UVES candidate members. The open triangle is the outlier in chemical abundance (see Table 7.4). (b) the UVES target candidate members in the theoretical $\log g$ vs. T_{eff} plane (only the 13 stars with complete analysis).

(see Sec. 7.3.5). Table 7.4 sums up the spectroscopic properties of the 13 UVES targets that are completely analysed; we list the identification and B , V magnitudes in C10, the Gaia-ESO Survey identifications, coordinates, RVs and the Gaia-ESO Survey atmospheric parameters T_{eff} , $\log g$, $[\text{Fe}/\text{H}]$, and microturbulent velocity ξ values. The numbers in Table 7.4 confirm that the observed targets are giant stars, possibly in the RC phase, and are all very good candidate members for RV. Except for one star, which is however within 3σ from the average metallicity, they also show a remarkable chemical homogeneity, with an average iron abundance $[\text{Fe}/\text{H}] = +0.17$ and a dispersion of only 0.03 dex. In Fig. 7.9 (panel b) we show the 13 UVES targets with abundance analysis in the theoretical plane T_{eff} , $\log g$. They seem to have the same elongated shape as was found in the photometric plane.

Structured RC have been found in other OCs. The works of Mermilliod & Mayor (1989, 1990) and Mermilliod et al. (1997) present about ten intermediate-age MW OCs that show this peculiarity. The first interpretation of these findings, confirmed by the subsequent works of Girardi (1999) and Girardi et al. (2000b), is the possibility that some stars in the RC phase have undergone evolution through helium-core flash, while others have not, because of small differences in the exact core mass. Such differences require a considerable mass spread for clump stars of about $0.2 M_{\odot}$, however, which could in principle result from different mechanisms: *a)* the natural mass range of core-helium burning stars found in single isochrones, although the current models do not have the level of detail necessary to completely explore this possibility; *b)* a broad age spread (broader than 100 Myr), even if never observed in MW OCs; *c)* star-to-star variations in the mass-loss rates during the RGB phase. Recent asteroseismologic studies on the two OCs NGC 6791 and NGC 6819, the latter of which has an age and metallicity similar to Tr 20 (see Miglio et al., 2012; Corsaro et al., 2012), seem to indicate that no extreme mass-loss during RGB phases should be expected; *d)* different stellar rotation history; *e)* dispersion in the overshooting efficiency

in the convective core; *f*) binarity, if interaction and mass transfer or even mergers are considered. Nevertheless, the transition between non-degenerate and degenerate He-core ignition would explain the findings in old OCs (age of about 1.4-1.6 Gyr), but not in other OCs, which are too young to be compatible with this evolutionary explanation. Tr 20 is an old cluster (see Sec. 7.3.5) and agrees beautifully with this hypothesis. On the other hand, we cannot exclude the shape of the MSTO from this reasoning: even when we remove the effect of DR, a spread is still visible in the CMD that could be due to binary systems or to an age spread (more unlikely); both could give rise to a secondary RC.

Alternatively, Carraro et al. (2011) studied NGC 5822 (0.9 Gyr old) and proposed that part of the stars of its apparently double RC might instead be RGB stars. With the abundance analysis of the UVES targets, the stars in the fainter part of the RC have a $\log g$ too large to be fit by the RC phase of the evolutionary models considered in this work. They might possibly be giant stars in the RGB phase, even if they are too warm for the best-fit model (see Sec. 7.3.5, where we derive the cluster parameter with the isochrone fit). In this case, the accurate estimate of lithium abundance might be used to distinguish stars in the RGB phase (lithium should be lower for RC than for RGB stars), but at the moment we do not have this information for our targets.

Understanding the RC of Tr 20 is not easy at all. More investigations are needed to test all the possible hypotheses. About 30 additional giant stars have been observed with UVES, thus it will be possible to obtain a detailed abundance analysis and spectroscopic parameters for a significant fraction of stars that appear in the structured RC of the observational CMDs. Moreover, the Gaia-ESO Survey observations can be used to find binary systems (when combined with archive data), and examine the effect of binaries on the observational CMD quantitatively.

Finally, we note that double RCs are also evident in clusters of the Magellanic Clouds as shown in Glatt et al. (2008) and Milone et al. (2009) and discussed in Girardi et al. (2009). In these high-mass clusters the presence of stars of different age (due to a gap in star formation or a prolonged star formation) looks more probable, similarly to the massive old globular clusters of the MW. However, the transition from non-degenerate and degenerate He ignition is not the universally accepted explanation for them, either. The effect of stellar rotation on the observational CMD (proposed e.g., by Bastian & de Mink 2009 or Li et al. 2012 and refuted by Girardi et al. 2011) or of binary interactions and merging (e.g. Yang et al., 2011) were considered to reproduce the double RCs.

7.3.4 Spectroscopic analysis

We remind that in the following analysis we used the RVs for the entire spectroscopic sample but the abundances for only the 13 RC stars observed with UVES completely analysed.

RV distribution

Using all the RV measurements obtained for the stars observed in Tr 20, it is easy to identify the cluster signature with respect to the field stars. In Fig. 7.10 we show the RV distribution for the entire Gaia-ESO Survey and archive targets (both UVES and GIRAFFE). The typical error on the RV for UVES targets is about 0.4 km s^{-1} , while it ranges from 0.3 km s^{-1} to several km s^{-1} in the worst cases for GIRAFFE targets (see Table 3 of Donati et al. 2014b). We used stars in common between the setups (110 stars are in common between HR09B and HR15N, 40 between HR09B and UVES, 10 between all the setups) to align the GIRAFFE RV estimates to that of UVES, finding that a systematic correction of -0.46 km s^{-1} is needed

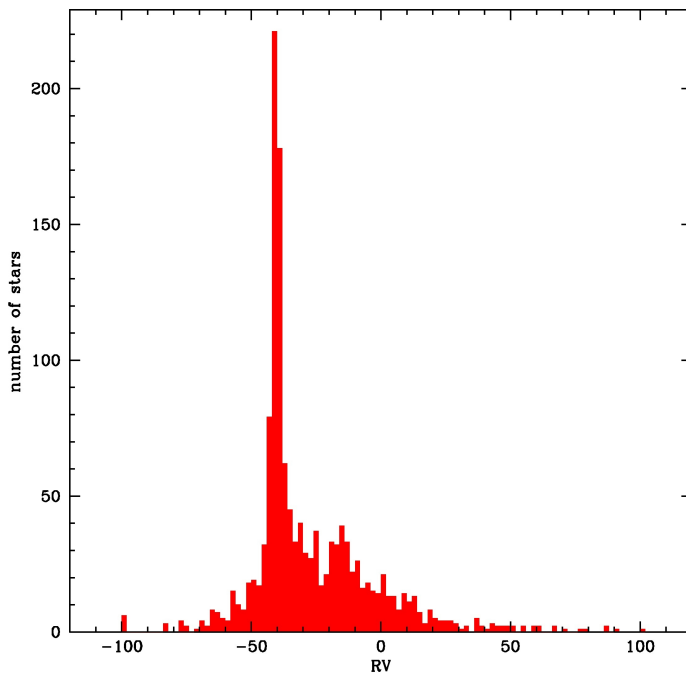


Figure 7.10: RV distribution of all the GES targets (1370 stars). The peak of cluster stars is evident at about -40 km s^{-1} .

for the HR15N spectra and of -0.50 km s^{-1} for the HR09B ones. Since we are not interested in the detailed cluster internal dynamics, but only aim to identify candidate member stars, we did not try harder to homogenise the RVs by using, for instance, sky lines to correct for offsets between the zero points of individual spectra. Stars observed with different setups were considered using the following priorities: we used the UVES RV if available, the average RV between GIRAFFE setups when the star was observed with both HR15N and HR09B, and finally the RV derived from only one setup. We estimated the average RV of the sample by selecting stars at different distances from the cluster centre to verify that consistent values were obtained. The inner part of the cluster has of course a higher percentage of cluster members than more distant fields, hence the estimate of the cluster average RV is more robust against spurious interlopers. On the other hand, statistics are poorer since the targets are spread up to $12'$ from the centre. We decided to choose $8'$ as the limiting distance for this analysis.

For each selection made on distances from the centre, outliers were expunged using the following method: the stars whose RV fell in the smallest RV interval containing 68% (about the percentage of occurrences inside one standard deviation in a normal distribution) of the RV distribution were retained, then candidates were iteratively selected by using a two-sigma-clipping statistics on the median (five iterations were used). With the last selection convergence was reached and the average and the dispersion were computed. The results of this procedure are shown in Fig. 7.11 (left panel). We stress here that our aim is to better define the evolutionary sequences on the CMDs by using only the most probable members. A more reliable membership estimation needs a more conservative approach that also considers binaries that might lie outside our selection criteria even if they belong to the cluster.

The values obtained for different selections in distance agree within 0.2 km s^{-1} ; the estimate obtained in the inner region has a higher dispersion because of the small number of

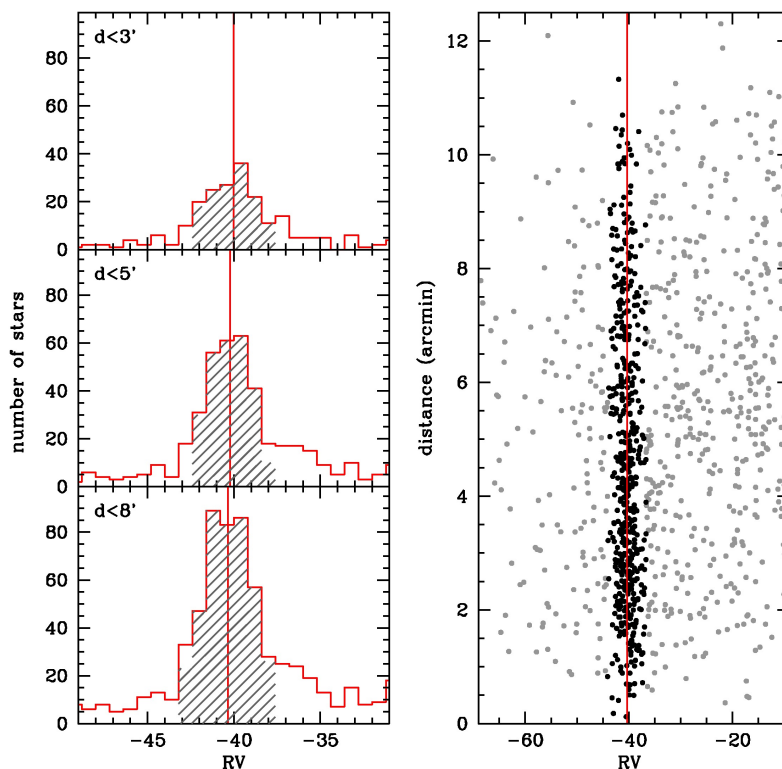


Figure 7.11: *Left panel:* RV distribution of all the GES targets for different distances from the cluster centre. The vertical line is the average RV of stars in the shaded histogram, obtained after an iterative two-sigma-clipping on the median. *Right panel:* distance from the cluster centre versus RV of the targets. The black dots are the stars selected as candidate members using the average RV (red line) and σ obtained from the whole group of targets (bottom histogram, left panel).

stars. The final values for the average RV and standard deviation used are those obtained for stars inside $8'$. The average RV velocity is $\langle RV \rangle = -40.357 \pm 0.003 \text{ km s}^{-1}$ (the r.m.s. of the sample used to compute the average RV was $\sim 1.239 \text{ km s}^{-1}$)⁶. Considering only the 13 UVES targets with abundance analysis, we obtain an average $\langle RV \rangle = -40.26 \pm 0.11 \text{ km s}^{-1}$, in agreement with the whole sample of stars. For comparison, the average velocity found by P08 is -40.8 km s^{-1} (based on five stars), while P12 obtained $-40.40 \pm 0.12 \text{ km s}^{-1}$ by analysing 68 RC targets. Both agree very well with our values.

Our sample of targets encompasses MS and evolved stars, observed with two instruments of different resolution and spectral coverage. We defined the cluster candidate members using the following simple selection criterion: stars with an RV higher or lower than three times the r.m.s. with respect to the cluster average are not considered cluster members. One of the goals of the Gaia-ESO Survey is, in fact, to clean the sequences in the CMDs using membership information and combining Gaia-ESO Survey and archive spectra. From this

⁶ The quoted dispersion is relative to the sample of stars selected to estimate the systemic velocity of the cluster (411 stars); it is indeed a lower limit of the expected dispersion of the cluster RV because in our analysis we did not consider the effect of binaries, for example.

analysis we found that $\sim 38\%$ of the targets (520 stars out of 1370) are good candidate members (see Fig. 7.11, right panel). According to the Besançon model (see Robin et al., 2003), which was computed for the same coordinates of Tr 20, we estimated that indicatively⁷ about 17% of the candidate members for RV may still be field stars. As shown in Figs. 7.4 and 7.13, almost all the targets located in the SGB region were discarded. The same has been found in P12 (see their Fig. 2), and confirms the expectations from theoretical models. The SGB phase has a very short timescale and is evident in very rich clusters, but poorly populated in smaller clusters. We also found that many stars near the MSTO are not candidate members, as P12 did.

Cluster metallicity

In Table 7.4 we summarise the main results of the abundance analysis for the RC stars (a detailed description is provided in Magrini et al., 2013b, and summarised in Sec. 7.3.7, where the metallicity and the abundance ratios of four α -elements -Mg, Si, Ca, and Ti- and of three iron-peak elements -Fe, Cr, and Ni- are discussed). In Fig. 7.12 we show their $[\text{Fe}/\text{H}]$ vs. T_{eff} ; there seems to be a mild correlation, even though errors on quantities reduce the statistic significance. This minor effect is irrelevant for the goals of the present work because we used the metallicity information only to confirm the membership and to choose the appropriate isochrones (see next section). All 13 RC stars are very good candidate members according to their RV (see Sec. 7.3.4) and have a very low dispersion in metallicity. Only J12391577-6034406 (#340) shows a slight discrepancy in the iron abundance relative to the other members. The average metallicity is $\langle [\text{Fe}/\text{H}] \rangle = 0.17$ dex (with a dispersion of 0.03 dex) without this star, and $\langle [\text{Fe}/\text{H}] \rangle = 0.16$ (with a dispersion of 0.05 dex) with it. J12391577-6034406 (#340) is within 3σ from the average. This places Tr 20 in the super solar metallicity regime.

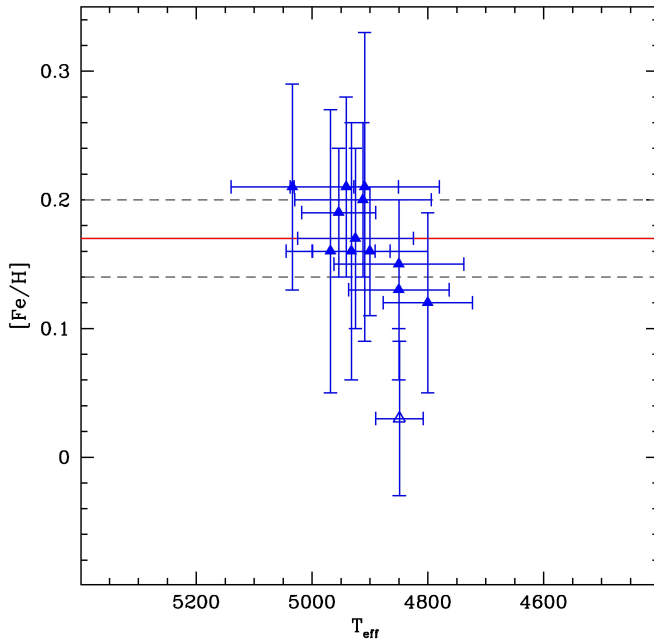


Figure 7.12: UVES targets in the $T_{\text{eff}}, [\text{Fe}/\text{H}]$ plane. The red line is the average metallicity; the dashed lines define the confidence interval.

⁷The Besançon model is not appropriate for small scales such as our case, but can still be used to obtain an approximate description of the field contamination.

We recall that the solar abundances we adopted are those of Grevesse et al. (2007), that is, the iron abundance of the Sun is 7.45. Since this is the same value adopted by P08, our metallicity is significantly higher than their estimate of -0.11 dex, which was based however on only one bright RGB star. Unfortunately, this star is not in common with the Gaia-ESO Survey UVES targets, which were all chosen to lie on or near the RC; this prevents a direct comparison and investigation of systematics between the different analyses. On the other hand, the star analysed by P08 is located in the upper part of the RGB, where 1D atmospheric models have more difficulties in reproducing real stars. In the past it has already been found that for low gravity and temperature the abundance analysis leads to lower iron abundances than for RC stars (see, e.g. Friel et al., 2003; Carretta et al., 2005).

Table 7.4: Information for the 13 UVES targets of Tr 20 with complete abundance analysis.

id	GES id	V (mag)	B (mag)	RA (deg)	Dec (deg)	RV (km s ⁻¹)	T _{eff} (K)	log g (dex)	[Fe/H] (dex)	ξ (km s ⁻¹)
340	12391577-6034406	14.67	16.00	189.8157333	-60.5779569	-40.02±0.42	4849±41	2.86±0.13	0.03±0.06	1.27±0.11
770	12392585-6038279	14.93	16.27	189.8577030	-60.6410769	-42.54±0.42	5034±106	3.12±0.31	0.21±0.08	1.25±0.10
505	12392700-6036053	14.52	15.91	189.8624847	-60.6014733	-40.06±0.42	4800±77	2.80±0.24	0.12±0.07	1.29±0.10
894	12393132-6039422	14.77	16.11	189.8804981	-60.6617437	-35.98±0.42	4954±64	3.07±0.15	0.19±0.05	1.20±0.22
835	12393782-6039051	14.58	15.96	189.9075746	-60.6514254	-40.53±0.42	4909±129	2.80±0.21	0.21±0.12	1.30±0.16
346	12394419-6034412	14.70	16.07	189.9341452	-60.5780773	-41.02±0.42	4941±90	2.88±0.23	0.21±0.07	1.25±0.06
781	12394475-6038339	14.61	16.01	189.9364207	-60.6427569	-39.28±0.42	4850±112	2.75±0.22	0.15±0.05	1.38±0.08
791	12394596-6038389	14.54	15.91	189.9414399	-60.6441467	-39.69±0.42	4912±118	2.87±0.21	0.20±0.06	1.27±0.15
287	12394690-6033540	14.78	16.13	189.9453843	-60.5650194	-40.98±0.42	4968±77	3.03±0.10	0.16±0.11	1.14±0.14
795	12394742-6038411	14.71	16.07	189.9475589	-60.6447566	-39.82±0.42	4900±100	2.73±0.23	0.16±0.05	1.21±0.15
787	12395426-6038369	14.60	15.98	189.9760346	-60.6436069	-42.45±0.42	4925±100	2.98±0.13	0.17±0.07	1.36±0.04
399	12395975-6035072	14.62	16.04	189.9988948	-60.5853363	-42.01±0.42	4850±87	2.79±0.19	0.13±0.07	1.29±0.11
1044	12400278-6041192	14.99	16.37	190.0115263	-60.6886598	-39.04±0.42	4932±67	2.98±0.11	0.16±0.10	1.37±0.05

7.3.5 Cluster parameters

By means of the considerable improvements obtained i) in the photometry with the DR estimation, ii) in the metallicity measurement with the high-resolution spectroscopy, and iii) in the membership with RV determinations, we derived the age, distance, and average reddening of Tr 20 by using the classical approach with isochrone fitting. We adopted three different sets of isochrones to have a less model-dependent solution for the cluster parameters: the PARSEC (Bressan et al., 2012), the BASTI (Pietrinferni et al., 2004), and the Victoria-Regina (VandenBerg et al., 2006) isochrones.

The best-fitting isochrone was chosen by eye examination as that which can describe the main age-sensitive evolutionary phases at the same time: the luminosity and colour of the MSTO, RH, and RC when possible. We used the metallicity resulting from the spectroscopic estimate, that is $[\text{Fe}/\text{H}]=+0.17$, and we converted it to Z taking into account the different solar abundances of the three sets of isochrones. The errors on the estimated parameters are mainly due to the uncertainties in the definition of the age indicators. In particular, the RC has a very peculiar morphology (see Sec. 7.3.3), which drives the main uncertainty on the age. The photometric error does not have a significant impact on the error budget, apart from systematic ones that can stem from the photometric data reduction and calibration. For instance, the differences found in magnitude and colour between P08 and C10 have an impact on the determination of distance modulus and reddening that will be discussed. For homogeneity we derive the cluster parameters using the catalogue from C10 corrected for DR in the $B - V$ colour and discuss the effect of the offset between the photometric data. In Fig. 7.13 we show the results of the best fits, summarised in Table 7.5.

Table 7.5: Results, errors, and estimated systematic uncertainties using different evolutionary models with $[\text{Fe}/\text{H}]\simeq+0.17$ for Tr 20.

Model	age (Gyr)	$(m - M)_0$ (mag)	$E(B - V)$ (mag)	d_\odot (kpc)	R_{GC} (kpc)	z (pc)	M_{TO} (M_\odot)
PARSEC	1.66 ± 0.2	$12.64\pm 0.1(0.2)$	$0.32\pm 0.02(0.05)$	$3.37(0.3)$	$6.87(0.02)$	$130.07(10)$	1.8
BASTI	1.35 ± 0.2	$12.72\pm 0.1(0.2)$	$0.31\pm 0.02(0.05)$	$3.50(0.3)$	$6.86(0.02)$	$134.95(10)$	1.9
VICTORIA	1.46 ± 0.2	$12.70\pm 0.1(0.2)$	$0.35\pm 0.02(0.05)$	$3.47(0.3)$	$6.86(0.02)$	$133.71(10)$	1.9

For the PARSEC set (see Fig. 7.13, left panel), for which $Z_\odot = 0.015$, we adopted $Z = 0.022$. We found that the best age estimate is 1.66 ± 0.2 Gyr, with a reddening $E(B - V) = 0.32 \pm 0.02$ mag, and a true distance modulus $(m - M)_0 = 12.64 \pm 0.1$ mag. The luminosity and colour of the RC are well reproduced, as are those of the RH and upper MS. As has often been found, the lower part of the MS, for $V > 18$, is slightly redder in the model than in the observations.

For the BASTI isochrones (see Fig. 7.13, middle panel) there is a coarse grid in chemical composition, hence we chose two different metallicities, $Z = 0.019$ (i.e. solar) and $Z = 0.03$, which bracket our spectroscopic metallicity. The best-fit of RH and RC is obtained for an age of 1.35 ± 0.2 Gyr. The more metal-rich solution reproduces the RGB and RC phases slightly better, hence the adopted parameters are from this isochrone: $E(B - V) = 0.31 \pm 0.02$ and $(m - M)_0 = 12.72 \pm 0.10$.

The Victoria-Regina isochrones do not include the evolved phases after the RGB for the age of Tr 20. Therefore we chose the best-fitting solution as the one that best matches the MS and MSTO morphologies (see Fig. 7.13, right panel). Moreover, it is only possible to use a coarse grid in terms of metallicity, hence we tried two different metallicity values that bracket our estimate: $[\text{Fe}/\text{H}]=0.13$ and $[\text{Fe}/\text{H}]=0.22$. They both fairly well reproduce the

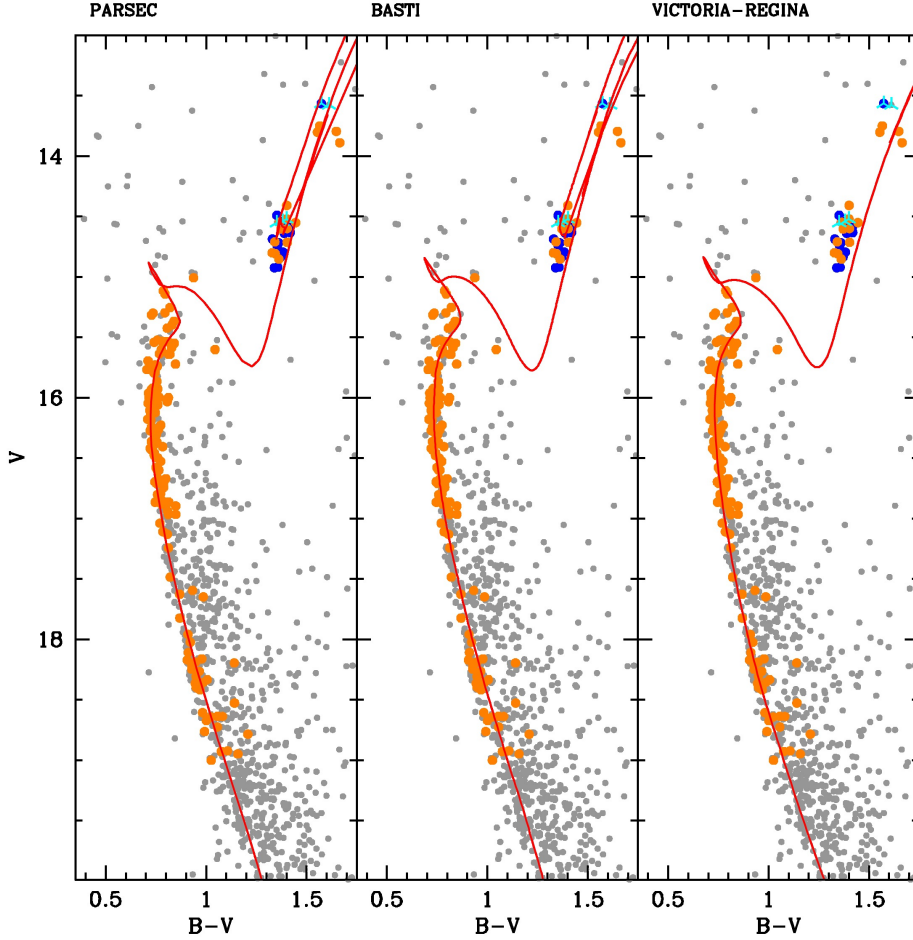


Figure 7.13: CMD obtained for stars inside $3'$ using the photometry from C10 corrected for DR, and the best isochrone fit for different evolutionary models (PARSEC - left; BASTI - middle; Victoria-Regina - right). GES target non-members have been disregarded, while members are highlighted with orange (GIRAFFE) and blue (UVES) points. Cyan points are P08 members. See Table 7.5 for the adopted parameters for the isochrone fitting.

MS ridge-line for an age of 1.46 ± 0.2 Gyr and describe the bending at the MSTO and the slope of the lower MS very well, although we prefer that of the lower metallicity because its RGB is closer to the observations, while the latter has a redder RGB phase. The average reddening and distance modulus for this isochrone are $E(B - V) = 0.35 \pm 0.02$ mag, and $(m - M)_0 = 12.70 \pm 0.1$ mag. With respect to other sets we found that this one reproduces the MS better, though the colour of the RGB is redder than observed. Furthermore, the age is more loosely constrained, since we lack the RC phase.

We repeated this analysis with the Dartmouth isochrones (Dotter et al., 2008) and reached the same conclusions, but for brevity we decided not to detail the analyses as for the other evolutionary tracks. In summary, we found a nice agreement in average reddening and distance modulus for all the model sets. They are similar to what was found by C10. We set the age in the range from 1.35 Gyr to 1.66 Gyr.

Using instead the P08 data, we expect to find some differences in distance modulus and reddening, because the age is mainly constrained by the magnitude difference between the TO and RC luminosities. We found that $E(B - V)$ is about 0.05 mag lower and the distance modulus consequently 0.16 mag higher, which translates into a larger heliocentric distance (by about 0.3 kpc) and a greater height above the MW disc (about 10 pc). The differences with the P08 estimates arise because they used stellar models with subsolar metallicity; in particular, this explains their higher reddening.

The results obtained with the three sets are given in Table 7.5, where we indicate age, distance modulus, reddening, distance from the Sun and the Galactic centre (the $R_{GC,\odot}$ adopted is 8 kpc Malkin 2013), distance from the Galactic plane, and mass of the stars at the MSTO. In parenthesis we quote the systematic errors as an additional uncertainty due to the zero points between the photometric catalogues of C10 and P08.

With the 13 UVES targets it is possible to evaluate the agreement between the models and the data in the theoretical plane $T_{eff}, \log g$ for the first time for this cluster. In Fig. 7.14 we show the best-fitting isochrone for the PARSEC set (continuous line): the RC phase of

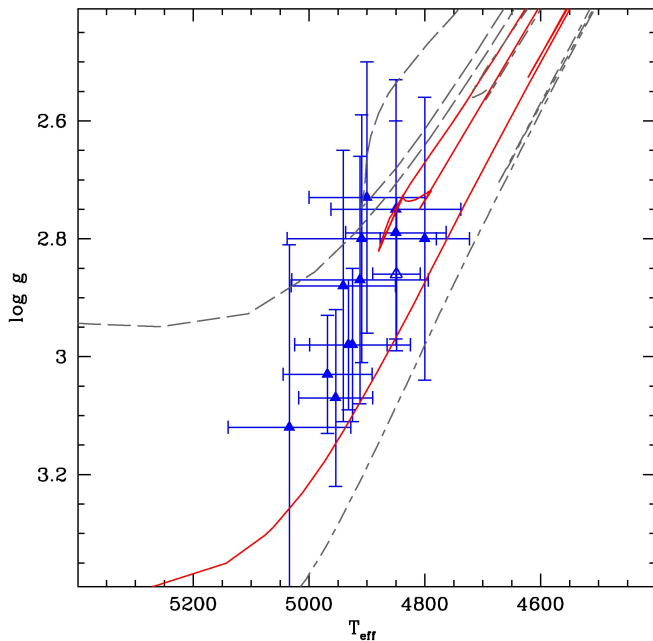


Figure 7.14: Blue triangles are UVES targets. The red line is the PARSEC isochrone for the age 1.66 Gyr. For younger ages (dashed line, age of 0.6 Gyr) or older ones (dot-dashed line, age of 2.5 Gyr) the RC phase moves toward lower $\log g$ values with respect to the data.

the model fits the upper clump of stars quite well, while the lower elongated group cannot be fitted by any age at this metallicity. In the same figure we show for comparison a younger and an older age isochrone (dashed and dot-dashed lines, respectively), for which the clump phase is located at lower $\log g$ with respect to the data, and never reaches $\log g > 3$. These stars might be RGB stars (even if still too warm for the best-fitting model) instead of RC stars. We discussed the peculiar structure of the RC of Tr 20 in detail in Sec. 7.3.3.

Fitting $B - V$ and $V - I$

As already discussed in past Chapters, multi-band photometry can be used to estimate the expected cluster metallicity; in principle, the correct metallicity is the one that produces a good fit with the same isochrone in two different colours with the same parameters (e.g. Tosi et al., 2007). It is very interesting to compare the metallicity obtained from photometry with

the one estimated from spectroscopy. Unfortunately, by applying the standard extinction law to convert $E(B - V)$ to $E(V - I)$ ($E(V - I) = 1.25 \times E(B - V)$), we obtain a poor fit in $V - I$ for the spectroscopic metallicity, after the cluster parameters are fixed in $B - V$. In Fig. 7.15 we show the “best-fitting” isochrone in the $V, V - I$ plane (C10 photometry) after applying the standard extinction law. The same inconsistencies hold, but in the opposite

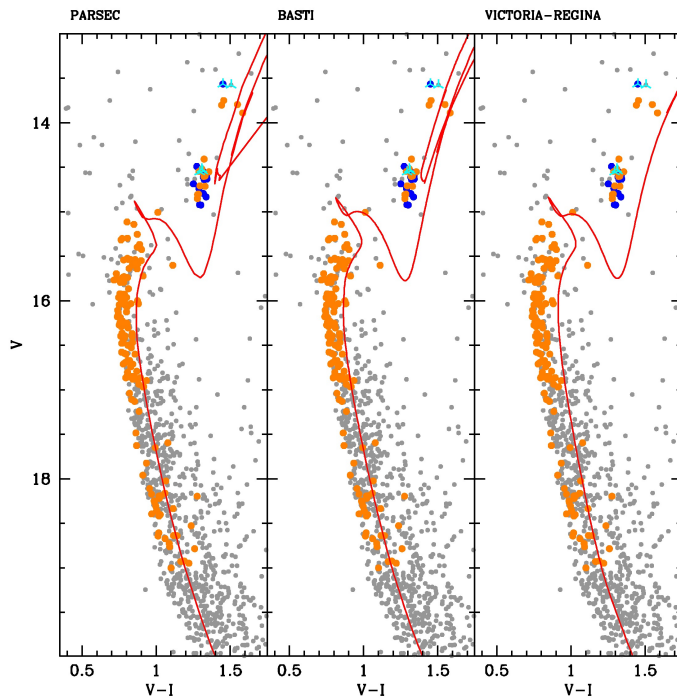


Figure 7.15: Same as in Fig. 7.13, but in the V and $V - I$ CMD, after the standard extinction law has been applied for the isochrones.

way, for the P08 photometry. We tried to find the photometric metallicity that allows a match in both colours. For C10 we derived with a very high metallicity, $Z = 0.05$ or $[\text{Fe}/\text{H}] \sim 0.5$, which seems implausible based on the spectra we analysed. For the photometry of P08 a match was obtained with subsolar metallicity, $Z = 0.01$ or $[\text{Fe}/\text{H}] \sim -0.18$ dex. Both metallicities are in contrast with the accurate spectroscopic value derived for the Gaia-ESO Survey targets.

On the other hand, since Tr 20 is located in the disc between spiral arms, it might be that the standard extinction law is no longer a good approximation. Using a different relation, such as $E(V - I) = 1.62 \times E(B - V)$ (see Cardelli et al., 1989), the agreement in the case of C10 photometry worsens, while for P08 we obtain a good match for the PARSEC and BASTI isochrones, but not for the Victoria isochrones.

This failure in simultaneously fitting the CMDs in two colours has been found in other cases (see e.g. Ahumada et al., 2013, and discussion in Sec. 5.2.3), but no definitive conclusion has been reached. Moreover, in our case we cannot firmly explain the poor match of stellar models in the $B - V$ and $V - I$. One answer can be the already known problem of the photometric transformations from the theoretical to the observational plane. The three models use different transformations, which adds a source of uncertainties to these comparisons. We cannot exclude problems related to the calibration of the photometric data, however, because the catalogues show systematic differences. Lacking better choices, we decided to constrain our analysis by only using the $B - V$ photometry (for which C10 and P08 agree better) and the metallicity from the Gaia-ESO Survey.

7.3.6 NGC 4815 and M 11

The detailed analyses of these clusters will be presented in Friel et al. (submitted) (for NGC 4815) and Cantat-Gaudin & collaborators (in preparation) (for M 11), and follow a similar structure of the analysis presented for Tr 20. I present here a brief description of the results. Photometry and spectroscopy are combined together to provide accurate estimates of clusters parameters. From the RV distribution obtained for GIRAFFE and UVES targets, clusters' candidate members are selected and used to improve the isochrone fitting analysis. The accurate metallicity determination from HRS spectra obtained with UVES are used to constrain the stellar evolutionary models used for the isochrone fitting.

NGC 4815

NGC 4815 is an intermediate age cluster located inside the solar radius, at RA=12:57:59, Dec=64:57:36 and Galactic coordinates $l = 303.6$, $b = -2.1$. It shows distinctly against a crowded field at this low latitude. Located approximately 2.5 kpc away, the line of sight to the cluster passes through both the Sagittarius and the Scutum-Centaurus spiral arms, with the cluster located beyond, but close to, the Sagittarius arm. The cluster has been the subject of several photometric studies, but has not been observed spectroscopically until now.

Targets for Gaia-ESO Survey observations were selected from consideration of the combined photometry from Prisinzano et al. (2001), 2MASS, and two unpublished optical studies, in *BVI* using FORS on the VLT, and *BV* from WFI on the 2.2m. Targets for UVES observations were limited to stars in the region of the RC; 14 of these cluster candidates were observed using the 580nm setup. Targets for GIRAFFE observations were selected to lie along the MS extending from the TO region at $V \sim 14.2$ to 19. The brighter sample of stars, from $V \sim 14.2$ to 17, was observed with GIRAFFE grating HR09B, while those with $16.8 < V < 19$ were observed with grating HR15N. Twenty-one of the fainter stars in the bright magnitude interval were observed with both setups, resulting in a total sample size of GIRAFFE observations of 204 stars.

NGC 4815 observations were taken on 5 nights in April and May 2012. Observations of the setup using GIRAFFE grating HR09B consisted of three 50-minute plus six 25-minute observing blocks. Those with the HR15N grating consisted of three 50-minute plus four 25-minute observing blocks. Signal-to-noise ratios for the final UVES spectra range from 20 to 130, with typical values being ~ 65 . For the GIRAFFE spectra, SNR ratios were typically lower, ranging from 10 to 80, with a median of ~ 30 .

From RVs we estimated the cluster systemic velocity to be 29.4 km s^{-1} (r.m.s. $\sim 4 \text{ km s}^{-1}$). The RV distribution is, however, quite broad, suggesting significant contribution by field stars, which is also indicated by the Besançon Galactic stellar populations model. Selecting stars within 4 km s^{-1} of this mean velocity as potential cluster members results in only 30% of the observed Gaia-ESO Survey targets having velocities consistent with membership.

Stellar abundances from the UVES observations for the 5 evolved stars that are members yield a mean cluster metallicity of $[\text{Fe}/\text{H}] = +0.03 \pm 0.02$ dex (error in the mean). Elemental abundances also show a small dispersion about the mean values, indicating homogeneous chemical composition in the cluster (see Sec. 7.3.7 for more details).

Finally, using the information on radial velocity membership, and with the cluster metallicity constrained by the Gaia-ESO Survey determinations, the published *BV* and *VI* photometry (taken from Carraro & Ortolani 1994 and Prisinzano et al. 2001 respectively) was fit to theoretical isochrones to derive more robust estimates of the cluster parameters. Util-

using three different sets of isochrones (the PARSEC, the Basti, and the Dartmouth one) and fitting both the *VI* and *BV* CMD provided an assessment of uncertainty in these parameters. In Tab. 7.6 we show the results obtained, which are in agreement with previous determinations but based on a more accurate and comprehensive data analysis.

Table 7.6: Results, errors, and estimated systematic uncertainties using different evolutionary models with solar $[\text{Fe}/\text{H}]$ for NGC 4815.

Model	age (Gyr)	$(m - M)_0$ (mag)	$E(B - V)$ (mag)	d_\odot (kpc)	R_{GC} (kpc)	z (pc)	M_{TO} (M_\odot)
PARSEC	0.63±0.1	12.00±0.1	0.65±0.02	2.51	6.93	-92.0	2.5
BASTI	0.50±0.1	12.20±0.1	0.64±0.02	2.75	6.87	-100.8	2.7
DARTMOUTH	0.60±0.1	11.95±0.1	0.59±0.02	2.45	6.95	-89.8	2.5

M 11

M 11 (NGC 6705) is a massive and concentrated OC located 2 kpc from the Sun in the first Galactic quadrant. Its equatorial coordinates are RA=18:51:04, Dec=-06:16:22 (Cantat-Gaudin & collaborators, in preparation), or $l=27.3$ and $b=-2.8$.

During the first six months of observations spectra of about 1000 MS stars were obtained with the GIRAFFE setup HR15N and (only for the brighter and hotter stars near the MSTO) with the HR03, 05, 06, 09, and 14 setups. Furthermore, 49 targets between red giants and MS stars were observed with the UVES setup 580n.

The membership was derived by using the procedure described in Cabrera-Cano & Alfaro (1985). About 500 stars (about half of the sample) are retained as candidate members and the mean radial velocity of these stars is 35.9 km.s^{-1} , with a standard deviation of 2.8 km s^{-1} . The average metallicity obtained from the targets observed with UVES led to an iron abundance of $[\text{Fe}/\text{H}]=0.10$ dex with a dispersion of 0.06 dex. The mean radial velocity for the UVES members is 34.1 km s^{-1} (with a standard deviation of 1.5 km s^{-1}), which is lower than what found for GIRAFFE stars. However, the lack of targets in common between both instruments does not allow for a solid comparison of the systematics between UVES and GIRAFFE (as we did for Tr 20).

By using two different sets of isochrone (PARSEC and Dartmouth), and a careful study of the luminosity function of the inner part of the cluster, the cluster's parameters are determined through isochrone fitting of the *BVI* photometric data described in Cantat-Gaudin & collaborators (in preparation). In Tab. 7.7 we show the results of this analysis.

Table 7.7: Results, errors, and estimated systematic uncertainties using different evolutionary models with $[\text{Fe}/\text{H}]\simeq 0.10$ for M 11.

Model	age (Gyr)	$(m - M)_0$ (mag)	$E(B - V)$ (mag)	d_\odot (kpc)	R_{GC} (kpc)	z (pc)	M_{TO} (M_\odot)
PARSEC	0.32±0.1	11.45±0.1	0.40±0.02	1.95	6.33	-95.25	3.2
DARTMOUTH	0.25±0.1	11.60±0.1	0.40±0.02	2.09	6.22	-102.06	3.5

7.3.7 Chemical patterns

A careful analysis of the chemical patterns of Tr 20, NGC 4815, and M 11 is presented in Magrini et al. (2013b). The homogeneous results of the survey, based only on the HRS spectra obtained with UVES are considered. Four α -elements (Si, Ca, Mg, Ti) and three iron-peak elements (Fe, Ni, Cr) abundances are considered and a comparison is made with what obtained for the field stars targets of the survey and GCE models.

The first step was to check if the abundance ratio in each clusters are homogeneous. We investigated this by comparing the standard deviation of all elements with the average uncertainty in the abundances that is computed averaging the error on abundance ratios of each member star. We considered the cluster homogeneous in a specified element if the intrinsic scatter is lower or comparable to the average error which should be indicative of the expected dispersion. We found that from the Gaia-ESO Survey data the three clusters are essentially homogeneous in all elements and we compared their abundance patterns using the average abundances as representative of the entire cluster. In terms of abundance ratios over iron, these clusters are statistically very similar, but they differ in their global content of metals (see Magrini et al. 2013b for details). The differences found in $[El/H]$ abundances (where El refers to each element analysed) can be considered an intrinsic characteristics of the chemical composition of the ISM from which each cluster was born, since the analysis was performed in a fully homogeneous way. A tentative first conclusion might be that, even if at present Tr 20, NGC 4815 and NGC 6705 are located at similar distances from the Galactic Centre (although NGC 6705 is on the opposite side of the Sun-Galactic Centre line), they did not originate from an ISM with the same composition. In particular, the difference in their mean metallicity is remarkable, NGC 4815 having a much lower metallicity than the other two clusters.

Comparing with the field stars (solar neighbourhood TO stars and inner disc giants), we noted that elemental abundances of stars in OCs are consistent, within the error, with the trends of $[El/Fe]$ versus $[Fe/H]$ for almost all elements in field stars. However, cluster stars show some differences from field stars having the same $[Fe/H]$. The abundance ratios of NGC 6705 are very similar to those of inner-disc/bulge stars, while the abundance patterns of NGC 4815 and Tr 20 do not match perfectly either with the solar neighbourhood stars or with the inner-disc/bulge stars.

We finally compared the field and cluster abundance ratios with two chemical evolution models (Magrini et al. 2009; Romano et al. 2010), finding a general good agreement for the solar neighbourhood. The predictions of the models differ for the inner disc. The α -enhancement of NGC 6705 places it in better agreement with the model curves of Magrini et al. (2009) for Galactocentric radii from 4 to 6 kpc, and, together with its better agreement with the distributions of abundances ratios in the inner-disc/bulge sample, supports an inner birthplace for it.

Chapter 8

BOCCE update

In the context of the BOCCE project, the work of my thesis was devoted to the photometric analysis of eight OCs. The main outcome is a substantial upgrade of the BOCCE database. Now there are 34 OCs with complete photometric studies, and 10 objects more will be included soon. Only 11 clusters out of the 34 have spectroscopic analysis, but 10 have already been observed and are going to be added soon. The main goal of this scientific study is to characterise the properties of the Galactic disc using OCs as proxy (they are indeed valuable disc tracers, as amply demonstrated throughout this thesis). However, about 50 is the minimum number of objects required to sample with a statistical significance the age-distance-metallicity parameters space (see Ch. 2). These three quantities are the main properties of the disc we are interested to trace. Even if a further step is needed to satisfy this requirements, at this stage it is already possible to outline the main results of the BOCCE project. In this chapter I expand the description of the project presented in Ch. 2, discussing what we learnt so far from our OCs' sample. The results of the BOCCE project are all publicly available and can be accessed through the website of the INAF–Osservatorio Astronomico di Bologna <http://www.oabo.inaf.it/> (under the section *Research*); in particular, all the photometric catalogues are available there or at the WEBDA and CDS sites.

8.1 The general properties of the BOCCE OCs

Since the main goal of the project is investigating how the chemical properties of the Galactic disc vary with time and position, the main clusters' parameters we look for are their age, metallicity, and Galactocentric distance. By taking advantage of the homogeneous analysis of photometric imaging (in some cases only in B and V bands, in other also in I , and in a few cases also in U and other bands) and the interpretation of the morphologies of the observational CMDs through the sCMD technique (see Ch. 4), we were able to consistently derive such information. In some cases, deep and precise photometry allowed a statistical analysis of the binary fractions as well as the DR across the clusters' face as, for example, in the case of NGC 2141 described in Ch. 6. The imaging on a relatively large FoV was useful to assess the structural parameters for some clusters (e.g. Be 23, Be 31, and King 8 in Cignoni et al. 2011 or NGC 2141 and Be 81 in 6). However, the metallicity derived from photometry is not as accurate as the one derived with spectroscopy. The spectral analyses of high-resolution spectra of cluster's stars was important to accurately determine the metallicity and the chemical abundances (at the moment for eleven systems).

Age, distance, and metallicity (both the approximate determination with photometry,

the Z values, and the more accurate one with spectroscopy, the $[\text{Fe}/\text{H}]$ values) for the 34 OCs are summarised in Tab. 2.1 while in Fig. 8.1 their distributions are shown. The bulk of the OCs is in the age range of 0.9–3 Gyr. The old tail of the distribution (age > 3 Gyr) is populated by a few objects and more are needed to improve the statistic. The oldest object is Be 17, at 8.5 Gyr. The Galactocentric distances of our clusters span from about 5 to 20 kpc (Be 81 is closest system to the MW centre, Be 29 is the farthest one), and the OCs in the solar neighbourhood ($7 < R_{GC} < 10$ kpc) are about one half. The outer disc ($R_{GC} > 13$ kpc) is relatively poorly sampled but consider that the known clusters in the outer disc are a few (see, e.g. Fig. 1.3a for details). Concerning the metallicity distribution, the values derived from HRS range from -0.5 to $+0.5$ (NGC 2243 is the most metal poor object with $[\text{Fe}/\text{H}] \simeq -0.48$ dex, see Gratton & Contarini 1994, while NGC 6253 is the most metal rich, with $[\text{Fe}/\text{H}] \simeq +0.4$ dex, see Carretta et al. 2007; Sestito et al. 2007). Similar analyses are going to be extended to all the clusters in order to obtain a most accurate and homogeneous sample in HRS, too. In Tab. 8.1 all the OCs for which spectroscopic analysis will be completed in the near future are listed. Accurate spectroscopic analysis is fundamental to derive chemical abundances of various elements in addition to iron. As amply discussed in Ch. 1, α -elements can be used to have strong hints on subtleties of the disc properties. Indeed, oxygen has been suggested to be a superior tracer of the chemical evolution of the disc compared to iron. For these reasons HRS analysis is fundamental to improve our understanding of the disc, in fact the photometric estimates of metallicity are less accurate than HRS and are also limited to a coarse grid of values within our method. They are, however, a good first approximation and will be considered in the following discussion.

The “photometric” properties of the clusters (age, distance, and Z , see Tab. 2.1), refer to the best solutions obtained with sCMD and are mainly based on the BBC models because these are the tracks that more often turned out to best fit to the data. There are (a few) cases, however, in which other stellar models were found to better reproduce the data (see the papers quoted in Tab. 2.1 for details).

It is worth to say that none of the three types of stellar models adopted reproduces perfectly all the CMD features. The differences between predicted and observed features sometimes may be attributed to uncertainties in the data, but in most cases they are the

Table 8.1: List of OCs with available or soon available high-resolution spectroscopic data.

Cluster	Instrument	# of stars
NGC 2204	UVES@VLT	4
NGC 6939	SARG@TNG	4
NGC 7789	SARG@TNG	6
NGC 7790	SARG@TNG	4
NGC 2099	SARG@TNG	4
NGC 2168	SARG@TNG	3
Berkeley 19	SARG@TNG	3
Collinder 110	SARG@TNG	4
NGC 2266	SARG@TNG	5
Berkeley 17	SARG@TNG	3
Forthcoming observing run		
NGC 1817	FIES@NOT	3 (plus 3 already acquired)
NGC 2225	FIES@NOT	3
NGC 2355	FIES@NOT	3

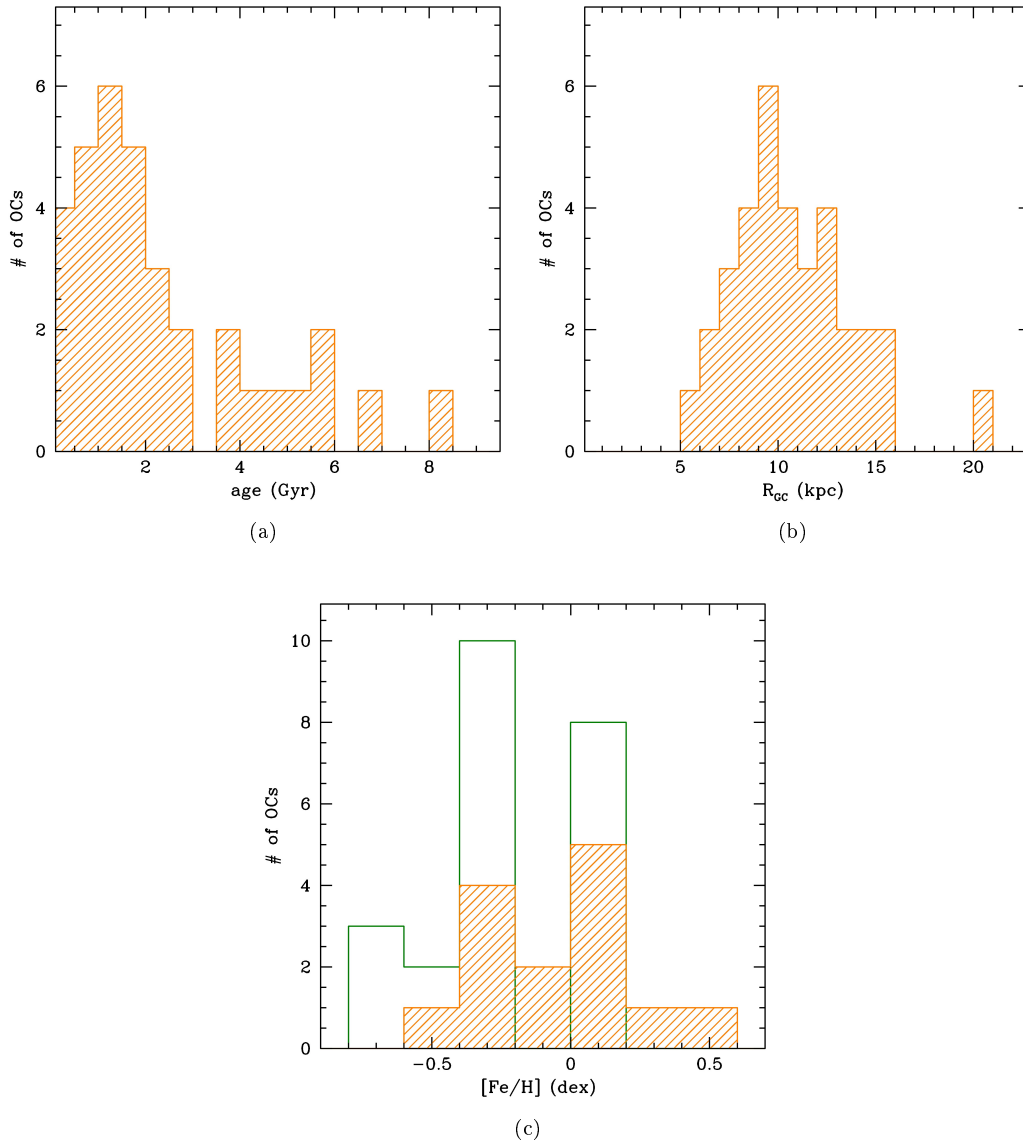


Figure 8.1: Distribution of the 34 BOCCE OCs with complete photometric analysis. (a) Age distribution; (b) Galactocentric distance distribution; (c) [Fe/H] distributions for the OCs with HRS analyses (shaded histogram) and with photometric estimates (empty histogram).

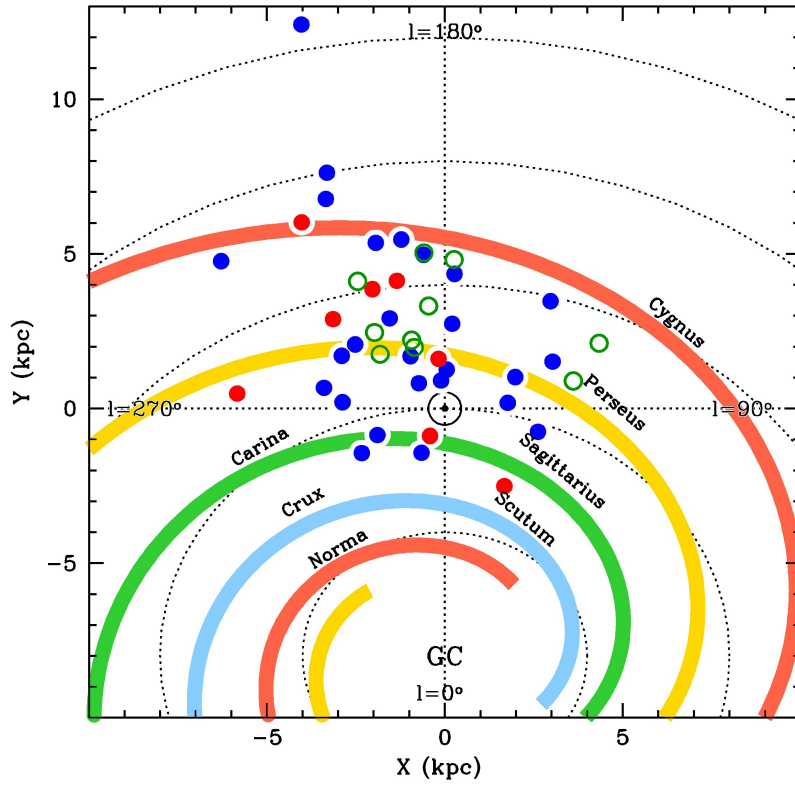
systematic consequence of the stellar model assumptions. This aspect is discussed in details in Bragaglia & Tosi (2006). For example, concerning the FST models, which provide three sets of tracks computed with the same assumptions except for the amount of overshooting from convective cores, the models with overshooting are in general in much better agreement with the data than the models without it. The FRA models often overpopulate the post-MS phases and present a TO morphology that is too hooked at young and intermediate ages, which makes them less viable than other tracks for clusters younger than about 2 Gyr.

One intriguing aspect of the sCMD resulting from different stellar evolution models concerns the slope of the lower MS. Sometimes the photometry is not accurate enough to allow for a safe definition of the MS shape and curvature at faint magnitudes, but there are cases in which the photometry is reliable and the synthetic CMDs (and isochrones) do not reproduce them properly. This can be attributed, as discussed in Bragaglia & Tosi (2006), to some ingredient still missing in the model atmospheres for low mass stars. Indeed, this is likely to be at least one of the causes. For instance, the circumstance that most photometric conversions are applied under *gray* atmosphere assumptions, which are not likely to be applicable to the cold stars with $M_V \geq 8$, is a probable source of inconsistency. Whatever the reason, there is no single set of tracks able to match all CMDs in all colours, at all ages, and for all metallicities. All of them behave quite well in some cases, but not in others.

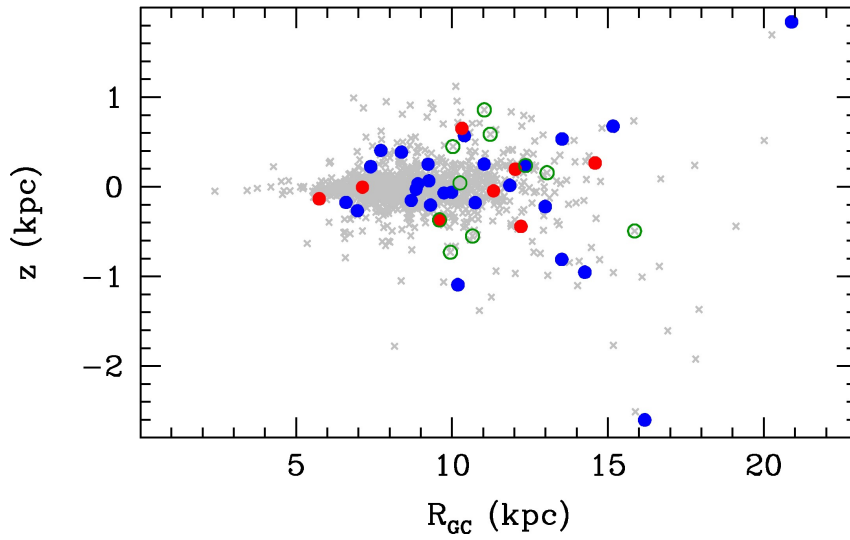
Despite the fact that stellar evolutionary models are constantly updated, for sake of homogeneity all the OCs have been analysed adopting the same assumptions used early in the project. Further improvements on the cluster's parameters can be obtained once all the OCs will be re-analysed with the present-day models. For example, the latest Padova tracks (the PARSEC, Bressan et al. 2012) include updated input physics and would guarantee a more accurate definition of the evolutionary status of the systems. However, we do not expect dramatic variations in the OCs' properties estimates but rather small systematic differences. In other words, we can trust the relative rankings, if not the absolute values. As experienced within the BOCCE project, different input physics have an impact on the age determination, which reflects on the distance parameters. Models that predict younger ages suggest larger distances and vice-versa. Rather than set aside the current set of tracks it would be interesting to add the latest models to the present ones, thus improving the robustness of the results and to quantify, in terms of the variation of clusters' parameters, the different predictions of each one of them.

The cluster's positions projected on the MW disc and in the R_{GC} - z (height above the MW disc) plane are shown in Fig. 8.2. In panel (a) of the figure the four main spiral arms, as delineated by Vallée (2005), are also displayed. The Sun is assumed to be located at 8 kpc from the Galactic centre. The 34 OCs are shown with filled circles (the eight OCs described in this thesis are in red), while those with ongoing photometric analysis (listed in Tab. 8.2) are represented by open circles. In panel (b) the same colour scheme is adopted to distinguish the OCs, while the data from DAML02 are added in the background for comparison.

With the derived reddening and distance modulus, the observational CMDs can be plotted as absolute magnitude versus intrinsic colour. Fig. 8.3 shows the CMDs of all the OCs in the BOCCE database analysed so far. They are plotted in order of decreasing age rightward from the top left panel. The appearance of the CMDs clearly reflects both the Galactic locations of the clusters and the telescope performances. Many clusters were observed with CCDs mounted at 1 m class telescopes (the 1.5m Danish and the 0.9m Dutch telescopes in La Silla, Chile, the 1.5 m Bologna Observatory telescope in Loiano, Italy, and the Palomar 60 inch (1.5 m) telescope in the USA). There are, however, several OCs observed with 4-m (CFHT, NTT, TNG) or 8-m (LBT) class telescopes. Field star contamination appears in



(a)



(b)

Figure 8.2: In panel (a) the positions on the Galactic plane of the OCs in our sample is shown. In panel (b) their distribution in the R_{GC} - z (height above the MW disc). Filled circles represent published OCs (the red ones are part of this thesis), open circles work in progress. The gray points are data taken from DAML02. In panel (a) we show the positions of the Sun (\odot symbol) and the Galactic centre and a sketch of the spiral arms as described in Vallée (2005).

Table 8.2: Forthcoming BOCCE OCs. Information is taken from DAML02.

Cluster	Telescope	RA (hh:mm:ss)	Dec (dd:mm:ss)	l (deg)	b (deg)	d_{\odot} (pc)	$E(B - V)$ (mag)	$\log(\text{age})$
Trumpler 5	WFI@2.2	06:36:42	+09 26 00	202.86	+01.05	2400	0.60	9.70
NGC 2158	LBC@LBT	06:07:25	+24:05:48	186.63	+01.78	5071	0.36	9.02
Berkeley 30	LBC@LBT	06:57:42	+03:13:00	210.78	+02.90	4790	0.50	8.48
Berkeley 98	LBC@LBT	22:42:38	+52:23:16	103.86	-05.65	3739	0.13	9.40
Berkeley 99	LBC@LBT	23:21:36	+71:45:00	115.95	+10.11	4900	0.30	9.50
NGC 2225	LBC@LBT	06:26:36	-09:38:18	218.78	-09.86	3200	0.35	9.11
NGC 2355	LBC@LBT	07:16:59	+13:45:00	203.39	+11.80	2200	0.12	8.85
Berkeley 19	OIG@TNG	05:24:06	+29:36:00	176.90	-03.59	7870	0.40	9.49
NGC 2266	OIG@TNG	06:43:19	+26:58:12	187.79	+10.29	3285	0.10	8.80
NGC 2204	WFI@2.2	06:15:33	-18:39:54	226.01	-16.11	2629	0.08	8.89

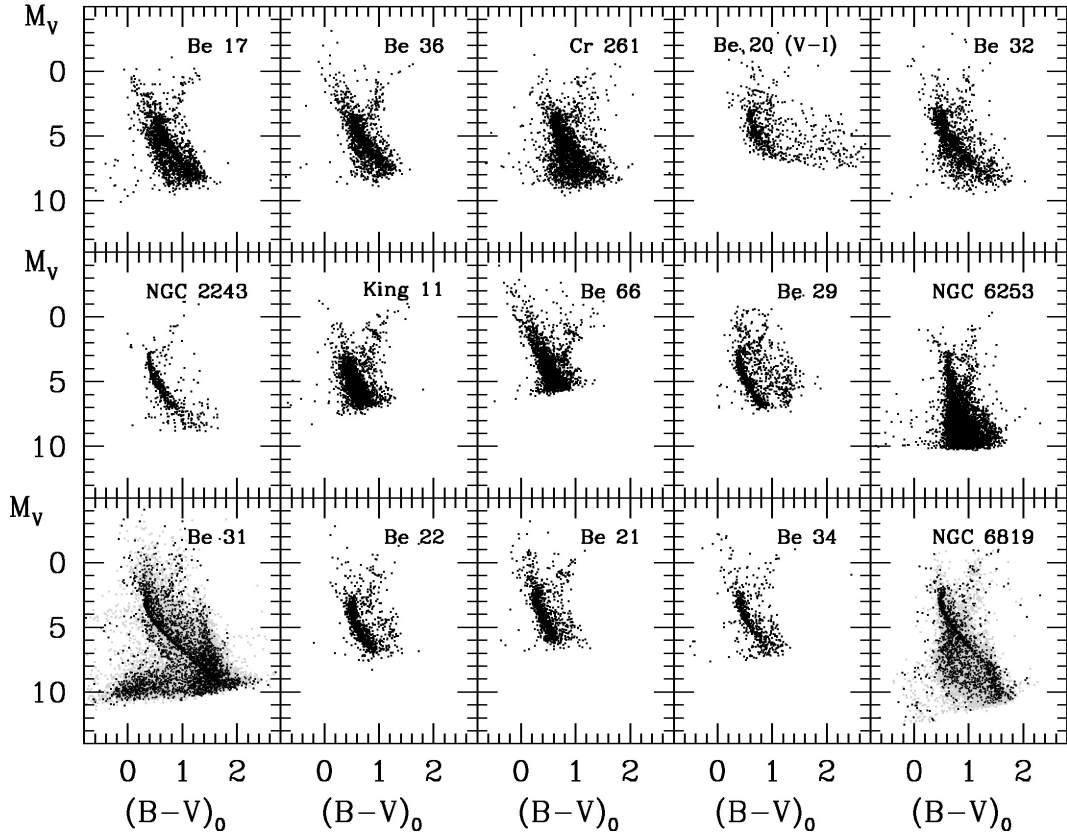
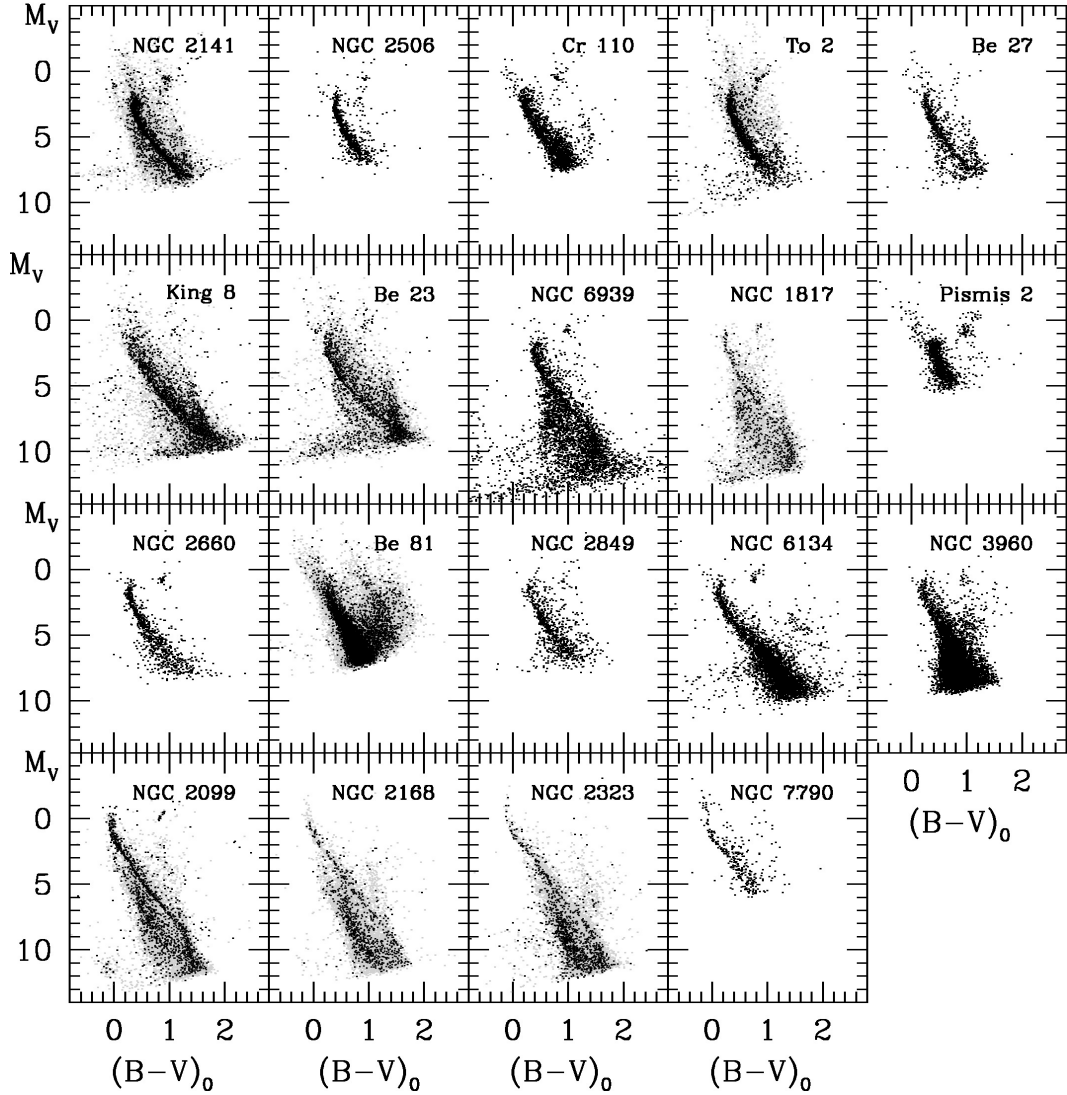


Figure 8.3: $(M_V, B - V_0)$ CMDs of 15 out of 34 OCs in absolute magnitude and intrinsic colour. They are plotted in order of decreasing age rightward from the top left panel. Note that for Be 20 we have only VI data. For OCs observed with large FoV the outer region (arbitrary chosen outside of 5 arcmin radius in most cases) is plotted in gray while the inner one is in black to appreciate better the genuine clusters' sequences. *Continued on next page.*

Figure 8.3: ($M_V, B - V_0$) CMDs of the 19 younger BOCCE clusters.

all CMDs. Its prominence depends on the sky area sampled, but in general the clusters seen in the direction of the Galactic anticentre (like the one presented in Ch. 5 and 6, Be 27, Be 34, and Be 36, and NGC 1817 and NGC 2141) are less affected by foreground/background contamination than those located toward the centre (e.g. NGC 6253, Cr 261, and Be 81). The proximity of populous spiral arms and the presence of overdensities such as the disc warp and/or accreted satellite streams can be a further explanation of the different field contamination observed for different clusters (like the cases discussed in Cignoni et al. 2008, 2011; Ahumada et al. 2013).

The shape and luminosity of the cornerstones for the parameter derivation (upper MS, TO, and RC) may be significantly altered by the presence of line-of-sight intruders. Unfortunately, studies of radial velocities or proper motions of the individual stars are not always present or as accurate as needed, and often the only means to estimate cluster membership is by comparison with nearby blank fields. Decontamination is even more crucial if one also aims at deriving the cluster IMF or the SF rate. Thus, as also discussed in Ch. 2, it

is very important to acquire the photometry of appropriate comparison fields, even if this requires additional observing time and a careful choice of the field position. The lack of observations of an external field can prevent a reliable estimate of the background/foreground contamination.

DR over the cluster face and binary systems can also alter the overall morphology of the empirical CMDs. A varying reddening widens the whole MS by a given amount $\Delta E(B - V)$, while unresolved binaries produce a secondary sequence redder/brighter than the single-stars MS, intersecting it above the TO region. In practice, DR and binarism are distinguishable from each other because the former implies a smooth spread of the MS from the TO down to its faintest portions, while unresolved binaries, even if distributed with random mass ratios, imply a split of the MS and the appearance of a bright “tail” (up to 0.75 mag brighter, corresponding to equal-mass binaries) on top of the TO. The synthetic CMD method allows one to quantify DR and binary fraction more safely than with simple isochrone fitting. However, not all the clusters clearly show the signature of DR and or of binary sequences. For the OCs presented in Ch. 5 and 6 both aspects were considered and estimated using different methods in addition to the synthetic CMD technique to reduce the parameter space explored with it (as done for several other OCs, like e.g. Cignoni et al. 2011). The binary fraction was estimated via a statistical method, counting stars on and off MS in the cluster field and in the blank one. Fractions of the order of 20% to 30% have been found, in concordance with what found for other BOCCE clusters. In three cases (NGC 2141, NGC 2158, and Tr 5, the two last still unpublished) the DR was estimated using a statistical approach as well (see Sec. 6.1.3). In general, we found that DR can range between 0.1-0.2 mag around the average reddening and that clusters with high Galactic reddening have larger ranges of DR, as expected.

The photometric analysis is also valuable for determining structural parameters. This analysis was not performed for all OCs, partly because outside the main goal of the project, partly because in some cases the observations were limited to small FoVs. Only for the farthest clusters (like, e.g. Be 29 and Be 22), that have the smaller apparent sizes and can be sufficiently covered with small FoVs (see Fig. 2.3), and those observed with large FoVs the exercise is feasible. For example, for NGC 2141 and Be 81, two of the three OCs described in Ch. 6 observed with LBT, it was possible to determine the density profile to large distances from the cluster’s centre. The data were then interpreted using a King model as done for Be 23, Be 31, and King 8 in Cignoni et al. (2011) and their core and tidal radii derived. In the case of NGC 2141 and Be 81, it has been possible to give an estimate of their total present-day mass. Such information is interesting to have an exhaustive description of the OCs’ properties. For example, investigating the mass distribution of old and young OCs could provide important hints on the internal dynamical evolution of OCs as well as the correlation of this property with the environment in which they form.

In the reference frame of intrinsic colour and absolute magnitude adopted in Fig. 8.3, the TO brightness obviously anti-correlates with the cluster age, while the clump luminosity at first sight is roughly constant, although actually inversely proportional to the chemical abundance. At first-order approximation, the magnitude difference ΔV between TO and clump is thus an age indicator. A safe use of this indicator requires a careful and homogeneous definition of the reference TO and clump points, which are affected by photometric uncertainties, including blending of unresolved stars, small-number statistics, and background/foreground contamination. In practice, the identification of the reference points differs from one author to the other (see e.g. Janes & Phelps 1994; Carraro et al. 1998; Salaris et al. 2004). In Bragaglia & Tosi (2006) a first attempt in finding a relation between age and ΔV was made. However they concluded that a larger sample, and better defined metal abundances, have

to be employed to find an accurate relation. The current dataset is doubled with respect to theirs, but the metallicity estimates from HRS are still available only for a part of them.

8.2 BOCCE OCs as tracers of the disc properties

We compared our results with the one listed in DAML02. We concentrated mainly on the age, distance, and reddening because many metallicities quoted in DAML02 are from our project. Looking at Fig. 8.4, there is a large spread in the difference between our and their values, especially for old ages. The relative variation of the estimates is confined within 50% and, even if there is no significant systematic difference, this is indeed a quite large spread. It is particularly worrying at old ages where, in principle, the methods used to determine the cluster age (see Ch. 1 for a brief description) should have the smallest relative error. We stress that the DAML02 data are not homogenised and we are comparing analyses obtained with different methods from ours.

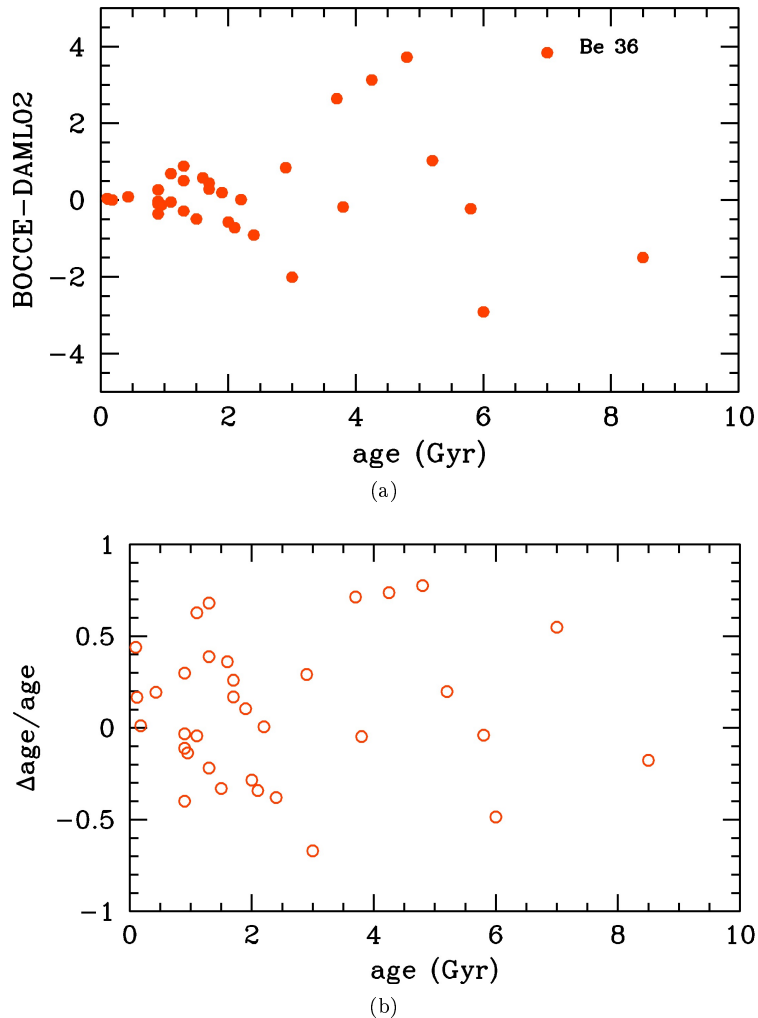


Figure 8.4: Comparison of age estimates for the OCs in common with the DAML02 catalogue. In panel (a) the differences in age are plotted against our age; in panel (b) the relative difference is considered.

Such uncertainties reflect in the distance estimates (see Fig. 8.5). Again, there is no significant trend in the differences between our values and the ones from DAML02 and in most cases they are within 1 kpc. However, for some systems they are large. Be 36 is one of the systems identified in the figure among the ones which show the largest differences. The analysis of this cluster is described in Ch. 5; Be 36 turned out to be much older than previous estimates (see also Fig. 8.4 where is indicated), therefore we also derived a significantly different distance from literature values. Concerning the comparison of the inter-Galactic reddening the differences are all around zero and within 0.2 mag. Only the striking case of Pismis 2 stands out, but such a large difference could be due to a typo in the DAML02 catalogue.

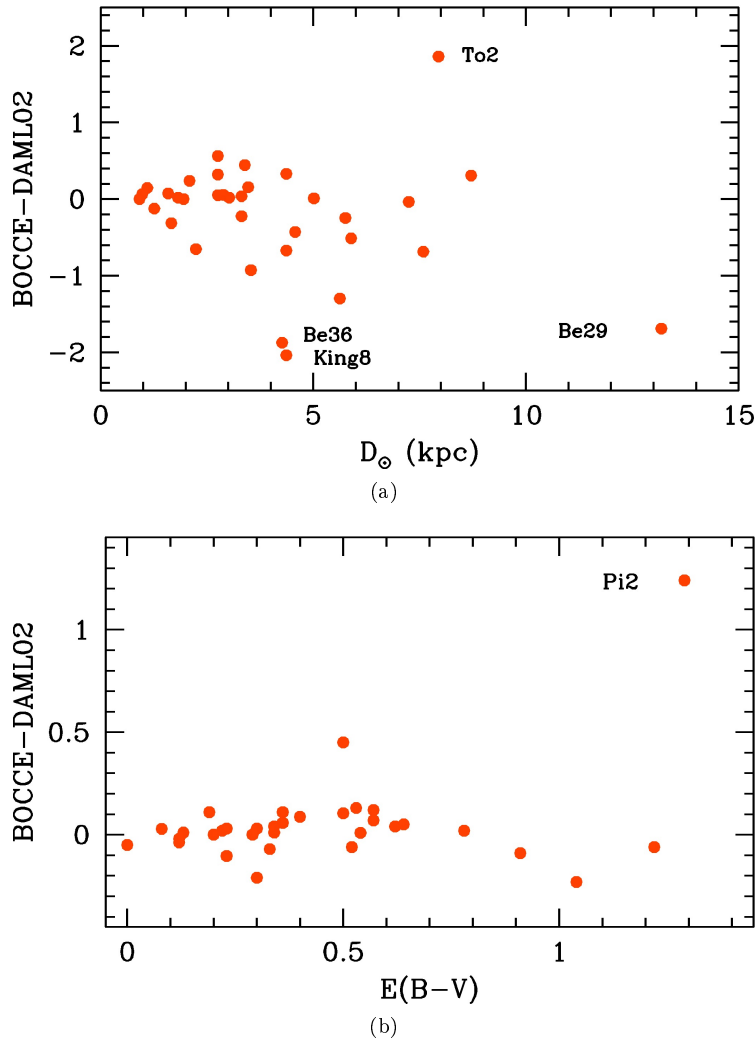


Figure 8.5: The same as Fig. 8.4 but for the distance from the Sun (a) and the reddening (b).

We then investigated if there are relations (or lack thereof) between age, Galactocentric distance, and metallicity plotting these quantities in Fig. 8.6 and 8.7. The gray dots in background are data taken from DAML02 for comparison. We recall, however, that the metallicity derived from photometry should not be taken as a precise measure of the actual

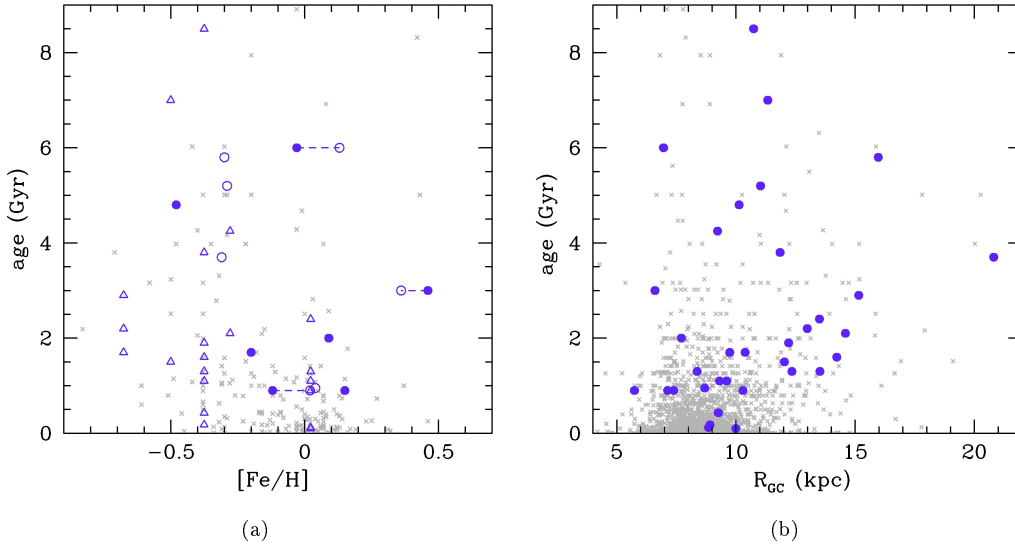


Figure 8.6: Distributions of the OCs in the (a) metallicity-age plane and (b) age vs. Galactocentric distance plane. Coloured points are the BOCCE OCs, gray dots are data taken from DAML02. Filled and open circles in (a) and (b) panels are OCs with metallicity determined from HRS using two different methods adopted in BOCCE (see Ch. 2). OCs with two different HRS estimates are connected with a line. The triangles are OCs with metallicity from photometry.

cluster’s metallicity. Looking at the BOCCE data, Fig. 8.7 shows that the only relation clearly existing between the derived quantities is the metallicity dependence on Galactocentric distance, while there is no apparent relation between age and metallicity or age and Galactocentric distance (Fig. 8.6). From the plots it is evident that there is a large dispersion in age at any distance bin as well as at any metallicity bin. However, very old clusters (older than 2 Gyr) are about half the OCs analysed (see also Fig. 8.1 where the age distribution is shown) and more are needed for a more robust statistic.

The properties of our sample are similar to those of the DAML02 catalogue in all the considered quantities. DAML02 shows in general a much larger dispersion but this is mainly due to the multiple origins of its dataset, which collects the results of different studies without homogenising them. Finally, we compared our metallicity with the values in Heiter et al. (2014). They collected all the available HRS analyses of OCs’ stars and combined them with a careful and detailed homogenisation to obtain a single metallicity value for each cluster. The black crosses in panel (b) of Fig. 8.7 are the results they show in the paper. It seems that there is small systematic difference between our dataset and theirs, with our metallicities slightly smaller. However, we are more interested in confirming that we reproduce the same general appearance of the radial metallicity gradient rather than investigating cluster-to-cluster variations of the metallicity estimates, also because theirs are not independent of ours.

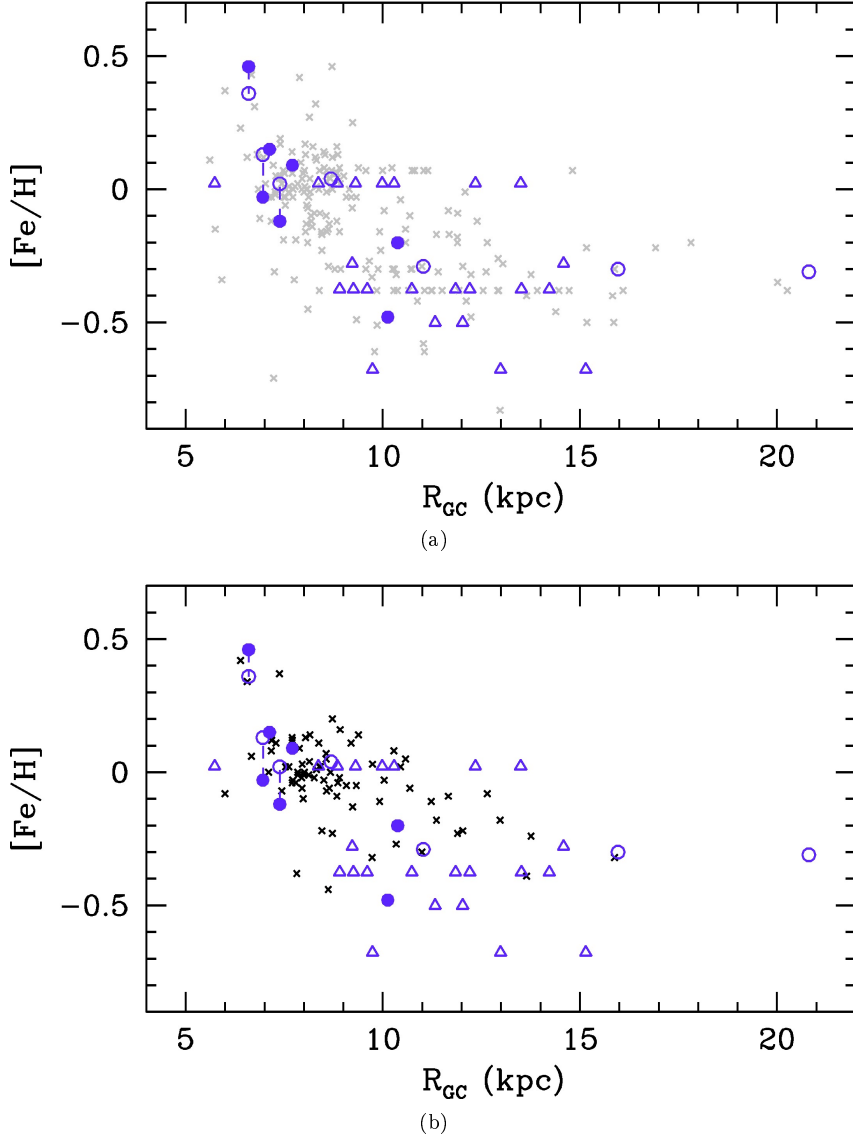


Figure 8.7: Distribution of the OCs in the metallicity vs. Galactocentric distance plane. Coloured points are the BOCCE OCs, gray dots in (a) are data taken from DAML02, black dots in (b) are data taken from Heiter et al. (2014). Filled and open circles in (a) and (b) panels are OCs with metallicity determined from HRS using two different methods adopted in BOCCE (see Ch. 2). OCs with two different HRS estimates are connected with a line. The triangles are OCs with metallicity from photometry.

8.2.1 Do we really see a radial metallicity gradient in the Galactic disc?

Fig. 8.8 shows the distribution of metallicity of our sample with respect to Galactocentric distance. Following the discussion in literature, we made two tentative interpretations: either two different radial gradients, steeper in the inner part and flatter in the outer part of the disc (panel a), or a step-like distribution (panel b).

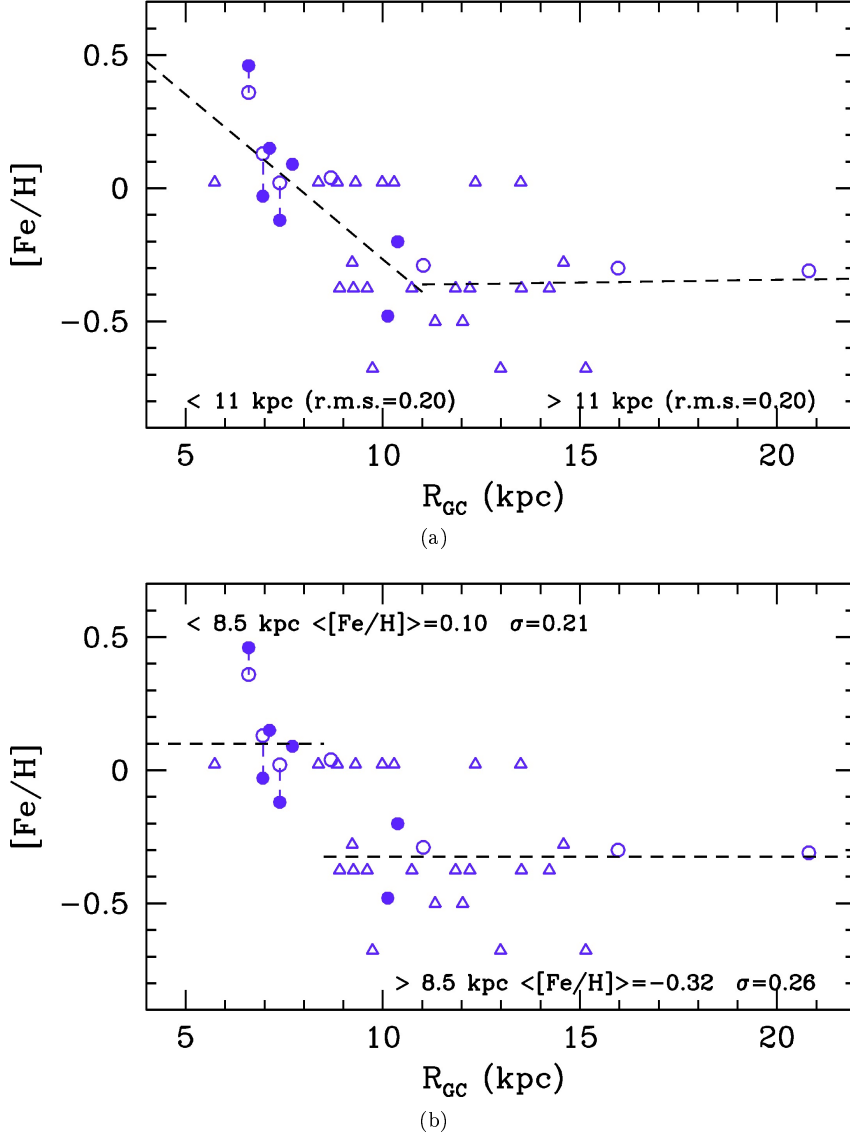


Figure 8.8: Distributions of the 34 OCs in the metallicity vs. Galactocentric distance plane. Filled and open circles are OCs with metallicity determined from HRS using two different methods adopted in BOCCE. OCs with two different HRS estimates are connected with a dashed line. The triangles are OCs with metallicity from photometry. In panel (a) a tentative fit (dashed black lines) of the inner disc ($R_{GC} < 11$ kpc) and of the outer disc ($R_{GC} > 11$ kpc) is shown. In panel (b) the average metallicity estimates inside and outside Galactocentric distances of 8.5 kpc are indicated with horizontal lines.

In the first case, we adopted $R_{GC} = 11$ kpc as Galactocentric distance at which the gradient of the outer disc begins to flatten. We found a inner negative gradient of about $-0.12 \text{ dex kpc}^{-1}$ and a slope compatible with 0 in the outer part. Had we used a different separation in distance (we tried $R_{GC} = 9, 10, 12,$ and 13 kpc), our conclusions would not have changed much, confirming a negative gradient in the range -0.11 to $-0.14 \text{ dex kpc}^{-1}$ in the inner disc and flat in the outer part. Our results compare well with other studies even if we find in general a slightly steeper inner gradient and flatter outer one. For example, Pancino et al. (2010) found a slope of $-0.06 \text{ dex kpc}^{-1}$ for clusters within $R_{GC} < 11$ kpc, Andreuzzi et al. (2011) $-0.07 \text{ dex kpc}^{-1}$ and 0 separating inner and outer disc at 12 kpc, and Yong et al. (2012) found $-0.09 \text{ dex kpc}^{-1}$ in the inner part and $-0.02 \text{ dex kpc}^{-1}$ in the outer part. However, such comparison is only provisional at this stage, as the clusters used in each work are different and our metallicities are not all based on HRS.

We investigated also if there is a significant variation of the gradient with the age of the clusters. In Fig. 8.9 we overimposed the gradient found with the whole sample to OCs selected in different age bins. The r.m.s of the selected clusters with respect to the fit are shown. At present, there are no significant suggestions of change with time of the gradient within our data. The fit found with the whole sample is coherent with different

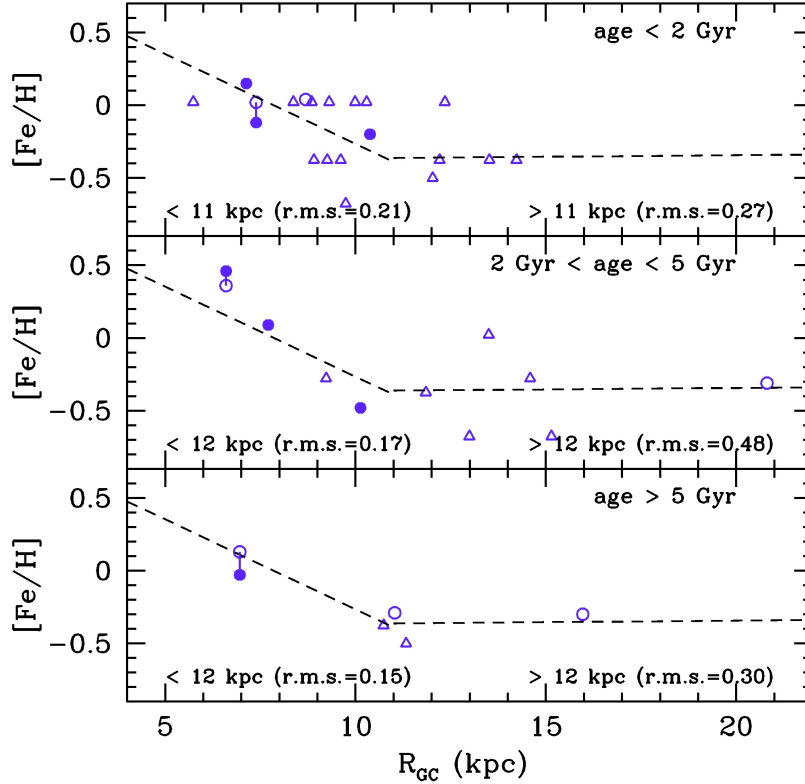


Figure 8.9: The same as Fig. 8.8 panel a, but for different age selections. In the *top panel* clusters younger than 2 Gyr are plotted. In the *middle panel* OCs in the age range 2–5 Gyr and in the *bottom panel* clusters older than 5 Gyr. The r.m.s. with respect to the fit are shown.

age selections as confirmed in general by the r.m.s values displayed in figure (comparable to the one obtained with the whole sample). Only in the age range 2–5 Gyr there are hints of a steeper gradient in the inner disc. However, the clusters at this Galactocentric distance range are still too few (only 3 with HRS analysis) for a statistically significant analysis. The bins corresponding to the outer disc and the old tail of the age distribution (clusters older than 2 Gyr) are populated by a few clusters and more objects are needed for a robust analysis.

In the case of a step distribution, in panel (b) of Fig. 8.8, a gap in the radial metallicity distribution seems visible in the range $7 \lesssim R_{GC} \lesssim 9$ kpc. Even though for these distances we have several OCs that still lack accurate metallicity estimates from HRS, this reminds similar findings outlined in Lépine et al. (2011). They suggested that such a gap coincides with the corotation radius (8.5 kpc) and, from dynamical arguments, different metallicity evolution inside and outside the corotation radius are expected (see Ch. 1 for details). Therefore, we divided our sample with respect to $R_{GC} = 8.5$ kpc and computed the average metallicity values, which compares well with Lépine et al. (2011).

The two interpretations of the metallicity distribution imply different GCE mechanisms, as described in Ch. 1. Our clusters cannot prove or disprove these scenarios yet. However, it is clear that a simple single-slope gradient cannot be the right answer. We still have too few objects at any R_{GC} , we are biased toward ages younger than 3 Gyr, and many metallicities come from photometry. More clusters with $7 \lesssim R_{GC} \lesssim 9$ kpc (the range around the corotation radius at which a gap in the distribution seems visible) and in the outer disc ($R_{GC} > 11$ kpc, where the metallicity gradients flattens) should be studied in detail, and a more precise abundance determination has to be performed.

8.2.2 Galactic chemical evolution model

In order to better understand our results in the context of the chemical evolution of the Galaxy, we compared them with the GCE model described in Romano et al. (2010). Very briefly, it is based on the *two-infall model* case B for the chemical evolution of the Galaxy (see Chiappini et al. 1997, 2001 for details). The inner halo and thick disk of the Milky Way are assumed to form on a relatively short timescale (about 1 Gyr) out of a first infall episode, whereas the thin disk forms inside-out on longer timescales (7 Gyr in the solar vicinity) during a second independent episode of extragalactic gas infall. The Galactic disk is approximated by several independent rings, 2 kpc wide. Radial flows and outflows are not considered here. The adopted SFR is proportional to both the total mass and the gas surface densities. The efficiency of conversion of gas into stars is higher during the halo/thick-disk phase than during the thin-disk phase. Furthermore, it drops to zero every time the gas density drops below a critical density threshold. The stellar lifetimes are taken into account in detail. As for the stellar IMF, the Kroupa et al. (1993) IMF is assumed in the 0.1–100 M_{\odot} mass range. The rate of SNe Ia explosions is calculated as in Matteucci & Greggio (1986). SNe Ia explode in close binary systems when a CO white dwarf has reached a critical mass limit because of accretion of hydrogen-rich matter from a main-sequence or red giant companion. The yields for SNe Ia are taken from Iwamoto et al. (1999), model W7. As for single stars, several sets of stellar yields are analysed by Romano et al. (2010) (see their table 2). Here we show the results of their model 1 (the reference model in the paper), that adopts the metallicity dependent yields of Woosley & Weaver (1995) case B for massive stars.

We chose to use the results of the model for the present-day epoch and for 2, 4, 6, and 8 Gyr ago. We found that the model for 4 Gyr ago, about the epoch at which the Sun

formed, predicts a $[\text{Fe}/\text{H}]$ abundance which is about 0.1 dex larger than the solar value (the model adopts the iron content derived by Grevesse & Sauval 1998). This inconsistency is mainly due to the choice of the stellar yields. As described in Romano et al. (2010), chemical evolution models assuming different yields can predict quite different element abundances even if they assume similar galactic parameters in their recipe. They concluded that, despite several considerable improvements in the field of stellar evolution and nucleosynthesis in recent years, no single combination of stellar yields is found which is able to reproduce at once all the available measurements of chemical abundances and abundance ratios in the MW. Therefore, we decided to apply a shift of 0.1 dex in $[\text{Fe}/\text{H}]$ to reconcile the predictions of the solar iron abundance at the Sun's position and formation epoch.

In Fig. 8.10 the radial metallicity distribution of our OCs and the model predictions for the different epochs are plotted. The typical error of our chemical abundance estimates

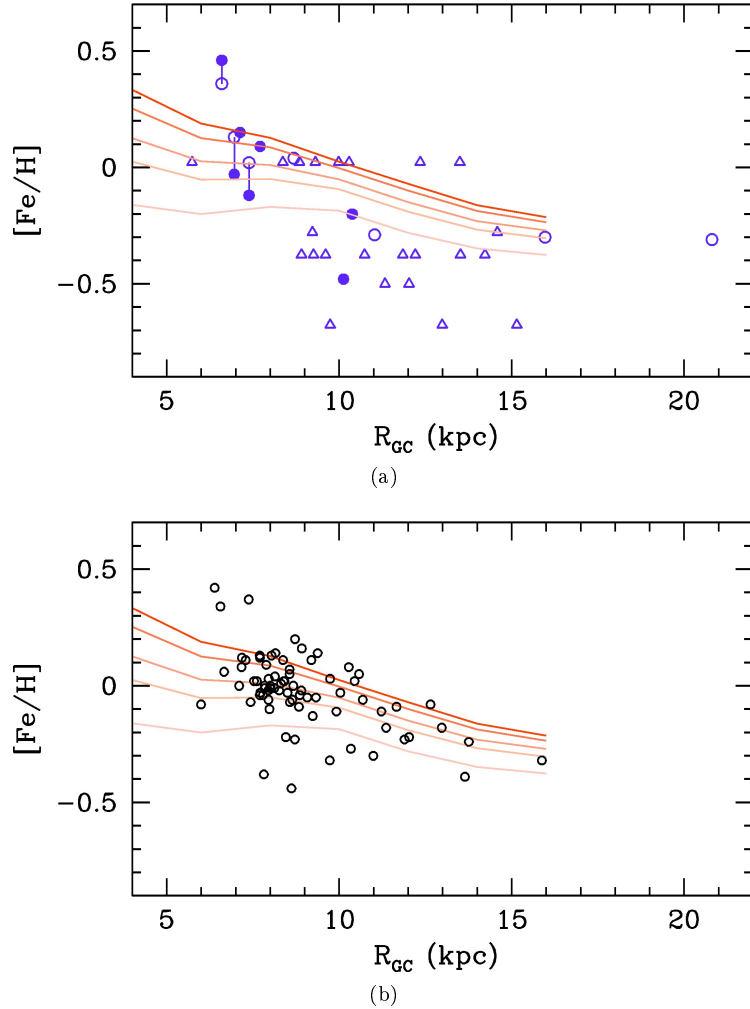


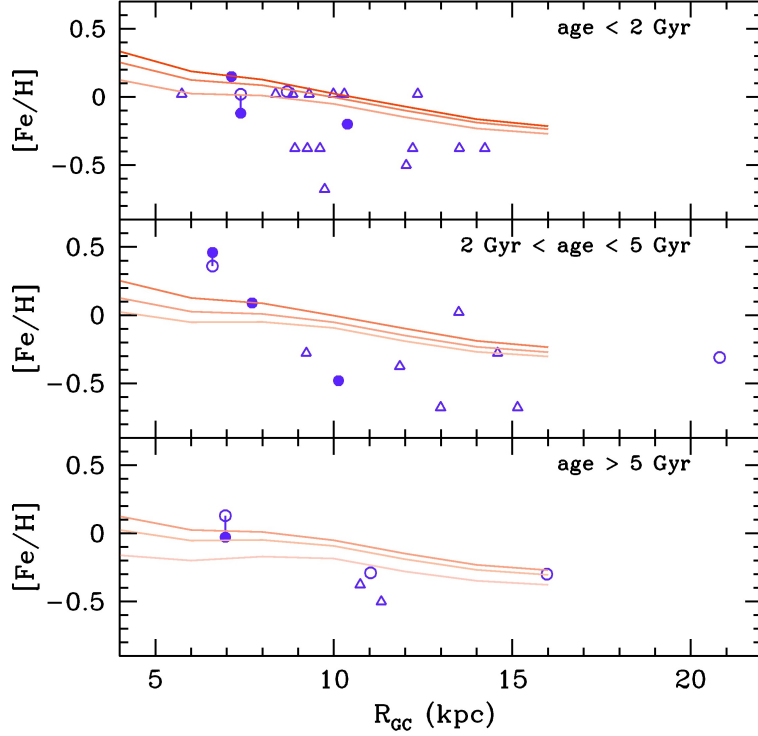
Figure 8.10: Panel (a): radial metallicity distribution of the BOCCE OCs. The typical error of our $[\text{Fe}/\text{H}]$ estimates is of the order of 0.1 dex. Panel (b): the same but for the data described in Heiter et al. (2014). The continuous lines are the predictions of the GCE models for different epochs: present-day (the darkest colour) and 2, 4, 6, and 8 Gyr (the lightest colour) ago.

is of the order of 0.1 dex. In panel (b) of the same figure the metallicity of Heiter et al. (2014) are considered. The model is able to reliably describe the chemical properties of the Galactic disc in the range 4–16 kpc. Outside this range the degree of complexity required to predict the chemical evolution and the poor observational constraints would produce more uncertain results. For example, the origin of the outer disc is still debated and it might be due to a merger events, as proposed e.g. by Yong et al. (2012). In this case, the standard recipe of the GCE models should take into account a different mechanism for gas accretion. This notwithstanding, even focusing within 4 and 16 kpc we were able to interpret most of the R_{GC} space spanned by our clusters. From this comparison the agreement between the model and the data is far from optimal. However, for the inner disc they span the same range of metallicity while for the outer one the models are in general more metal rich than data. Even if we exclude from this comparison the photometric metallicities (which reach the lowest abundances in the sample) only the earlier ages (6 and 8 Gyr ago) of the model are in good agreement with our abundances. By looking at the dataset of Heiter et al. (2014), the agreement is much better. There are only a few OCs for which the model is not able to reproduce their metal content: the ones closer to the Galactic centre, with high metallicity, and the few in the solar neighbourhood, particularly metal poor. Despite that Heiter et al. (2014) concluded that no GCE models is able to satisfactory explain the radial metallicity gradient of their sample, the model of Romano et al. (2010) seems, instead, to describe the general appearance of the gradient. There are, however, some inconsistencies. For example, the inner gradient predicted by the model steepens with time but its slope seems in general too shallow with respect to the observations. In order to investigate better this characteristic within our dataset, we performed the same comparison but for different age ranges.

We divided our sample in clusters younger than 2 Gyr, those in the range 2–5 Gyr, and those older than 5 Gyr. In Fig. 8.11 the same comparison of Fig. 8.10 in the three age bins is reproduced. Our conclusions do not change particularly from the previous ones. Models and data span the same metallicity range and both show a decrease of the metallicity with Galactocentric distance. The best agreement is obtained at the older ages, while for the younger clusters the models produce a higher metallicity with respect to our abundances. Moreover, the models predict slopes of the metallicity gradient which are not confirmed by the observations. Our dataset, however, is still composed by a few objects, in particular in the older age bins, and biased towards less accurate photometric metallicity estimations. For example, we do not have a significant statistic to investigate the slope of the radial metallicity gradient with time and to confirm if it is steeper “now” with respect to earlier epochs.

We investigated the radial gradient of other elements rather than iron. In Fig. 8.12 the case of silicon is shown. We concentrated on this element rather than others because it is in general well reproduced by models and well constrained by observations. For other elements, like e.g. magnesium, there are still significant uncertainties on the mechanism of formation and measurements are less reliable. The agreement of $[\text{Si}/\text{Fe}]$ between data and model is not perfect but in general satisfying if we consider the typical error on the abundance determinations (0.1 dex). Both data and predictions suggest a shallow/flat gradient.

The comparison described throughout this section can be extended by adopting different GCE models. However, it is clear that we need to obtain HRS measures of many more clusters to improve the statistical significance, hence we decided to limit the discussion to the model described so far. It is worth noticing that the model used does not consider stellar radial migration which instead has been suggested to have a significant impact on GCE (see e.g. Roškar et al. 2008). A more homogeneous and consistent comparison would be obtained



(a)

Figure 8.11: Radial metallicity distribution of the BOCCE OCs for different age bins. The typical error of our $[\text{Fe}/\text{H}]$ estimates is of the order of 0.1 dex. The continuous lines are the predictions of the GCE models for different epochs: present-day (the darkest colour) and 2, 4, 6, and 8 Gyr (the lightest colour) ago. *Upper panel*: OCs younger than 2 Gyr. The models shown are those at present-day, 2 Gyr ago, and 4 Gyr ago epochs. *Middle panel*: OCs within 2 and 5 Gyr. The models shown are those at 2, 4, and 6 Gyr ago epochs. *Lower panel*: clusters older than 5 Gyr. The models refers to 4, 6, and 8 Gyr ago epochs.

when either dynamics is included in the model or when precise kinematics and positions will be available for the OCs.

Throughout this thesis I described my major contribution to the BOCCE project and outlined its importance and potentiality to unravel the properties of the disc of our Galaxy and the evolution with time of its chemical properties. I also focused on the weak points of the project which are, at present stage, the need to enlarge the sample of objects studied and to align the progress in the HRS analysis to the level obtained in the photometric domain. The advent of the large spectroscopic survey, such as the Gaia-ESO Survey (see Ch. 3), can greatly improve the value of the BOCCE database. For example, if all the spectroscopic estimates of OCs made within such surveys can be homogeneously integrated in the project, the number of objects with HRS estimates would be greatly enhanced. It is not only a matter of quantity but also of quality. The greatest improvements will be achieved thanks to the Gaia mission. Even if its results will be made available only within the next decade, the position and kinematic properties of the OCs will be known with unprecedented precision

for the first time. Thus, it will be possible to estimate more accurate clusters' parameters and put more stringent constraint on the chemical evolution of the MW disc traced by OCs.

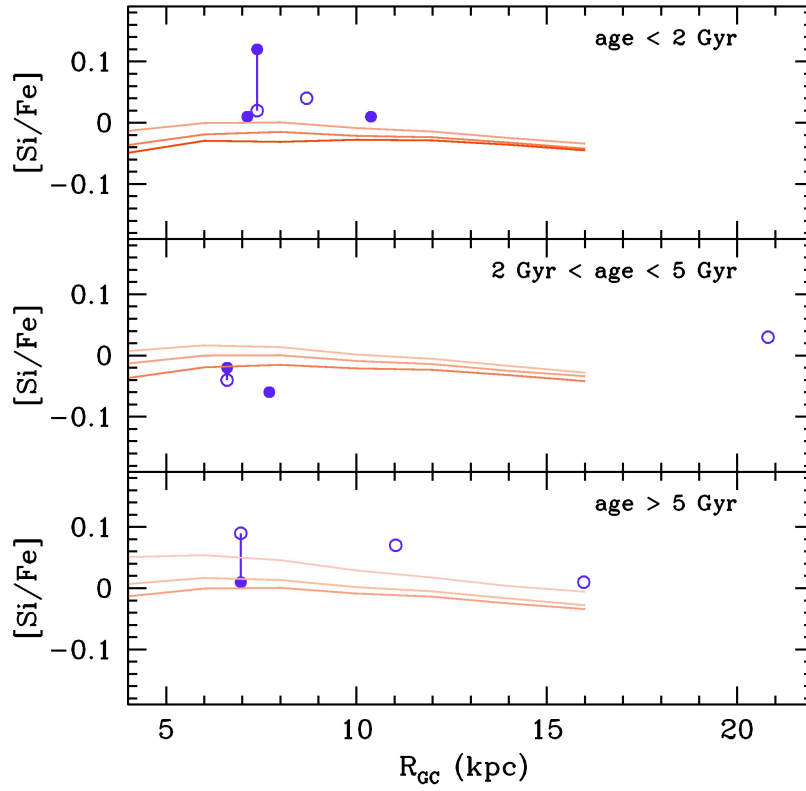


Figure 8.12: The same as Fig. 8.11 but for $[Si/Fe]$. The typical error of our $[Si/Fe]$ estimates is of the order of 0.1 dex.

Chapter 9

Summary and Conclusions

The research work done on open clusters for my thesis embraces two major projects: BOCCE and the Gaia-ESO Survey. The main goal of BOCCE and one of the several ambitious aims of the Gaia-ESO Survey is to define the chemical properties and the evolution of the Galactic disc. This can be done using OCs that are, in fact, among the best tracers of the properties of the disc, as discussed in Ch. 1. The chemical properties of each OC are signatures of the chemical properties of the disc. The position (distance from the Sun and Galactic location) is fundamental to spatially characterise the disc. The age is needed to delineate a time-line, portraying different time-stamps of the chemical and dynamical evolution of the disc.

In short, the BOCCE project aims at a homogeneous study of a large, significant sample of OCs (about 50 objects). We use both photometry and spectroscopy in order to derive accurate cluster's parameters (age, distance, and metallicity are the primary ones). The Gaia-ESO Survey is a public spectroscopic survey designed to complement the Gaia mission with precise spectroscopy of about 10^5 stars belonging to different MW populations. The observation of OCs' stars aims at the chemical and dynamical characterisations of such systems. Even if different in design and goals, the two projects share the goal of an accurate estimate of the OCs' parameters.

Within the BOCCE project I analysed the photometric data for ten OCs, eight of which are already part of three different scientific publications (Donati et al., 2012; Ahumada et al., 2013; Donati et al., 2014a) in which accurate age, distance, approximate metallicity, reddening, differential reddening, and binary fractions are derived using the synthetic CMD technique (see Ch. 4, 5, and 6). Within the Gaia-ESO Survey I participated to the spectral analysis of field and OC stars, focusing my research interests on the latter. With the numerous spectra of the Gaia-ESO Survey it is possible to derive the systemic velocity of the clusters, accurate chemical abundances, and define candidate members. All this information is fundamental, when combined with photometry, for an accurate estimate of age, distance, and reddening (as done e.g. in the case of Trumpler 20: Donati et al. 2014b and Ch. 7). The combination of spectroscopic and photometric analysis for the same objects produces the best estimates presently obtainable; we have to wait for the astrometric results of the Gaia satellite for better performances on the distance and, hence, the age.

OCs have been the subject of many different studies since the early fifties. This notwithstanding, the radial metallicity distribution they define is still under study because no conclusive consensus has been reached. The actual shape of the radial variation is still debated, whether it is a flat distribution with a step-like difference between the inner ($R_{GC} \leq 10 - 12$ kpc) and the outer disc (see e.g. Twarog et al., 1997; Lépine et al., 2011) or there is a negative gradient in the inner disc which flattens in the outer part (see e.g. Friel et al., 2002;

Andreuzzi et al., 2011; Yong et al., 2012). In the last 20 years, all the investigations agree on the following picture: the inner disc is more metal rich than the outer part, there is no evidence of an age-metallicity relation, and there is no significant gradient with height on the Galactic plane. Common requirements invoked in all papers are the need of a homogeneous and accurate analysis, and the usefulness of expanding the HRS observations to a larger number of OCs. In fact, despite the circumstance that OCs are very numerous in the MW (at least about 3000, see Kharchenko et al. 2013), only a fraction of them have been studied in details and only a few have accurate chemical abundance determination obtained through HRS. However, the main problem remains the lack of homogeneity: different authors use different methods and data of disparate qualities, circumstance that seriously jeopardises the accurate estimation of the OCs properties, introducing systematics (see discussion in Ch. 2).

The Gaia-ESO Survey will dramatically increase the number of HRS observations of OCs. The stellar atmosphere parameters, chemical abundances, and RV of about 10^4 stars in ~ 100 OCs will be derived with a homogeneous analysis. With this legacy it will be possible to investigate in details the chemical patterns and the kinematical properties of each cluster and shed more light on their origin and formation. This will consequently improve our comprehension of the properties of the Galactic disc. For example, understanding whether the outer disc's clusters are of extra galactic origin, accreted by merger events (see e.g. Yong et al. 2005 and Carraro & Costa 2007) is important to correctly interpret the metallicity distribution of the disc in the light of GCE models. The Gaia-ESO Survey will allow comparing the chemical pattern of inner and outer clusters (using e.g. iron-peak and α -elements, that trace different environment of star formation) and relating the kinematical properties of the outer disc with dynamical models of the Galaxy, giving important hints on the origin of these systems.

Already after the first six months of observations it was possible to analyse the chemical patterns of three old OCs of the inner disc (see Magrini et al. 2013b and Ch. 7) and to assess their genuine nature. We not only did find homogeneous chemical properties within each cluster, supporting the paradigm that OCs are SSPs, but we were also able to propose that they probably formed in different environments, even if they are located at similar Galactocentric distances (R_{GC} about 6-7 kpc). In particular, NGC 6705 showed abundance ratios similar to those of the inner disc/bulge stars, at variance with the other two clusters considered. If their different formation scenario is confirmed, they probably suffered a different dynamical history which then led them at similar distances from the centre of the Galaxy. It has been suggested that dynamical mechanisms, such as star migration (see Ch. 1 for further details), can significantly change the position of stars (and possibly of star clusters). This requires important revisions of GCE models, in which star motion is not considered.

The large dataset of chemical abundances and RVs is optimal to study the clusters properties, in combination with photometric data of good quality, as done for example in the case of Tr 20 (see Donati et al. 2014b and Ch. 7). The accurate HRS metallicity, the membership from RV analysis, and public photometric catalogues were used to determine the evolutionary status of the cluster with unprecedented accuracy. Moreover, the stellar atmosphere parameters derived with the spectral analysis of the Survey data were used to better constrain the age of the cluster in the theoretical plane of effective temperature and surface gravity and to investigate the key evolutionary phase of red clump. We plan to apply a similar analysis to all the OCs that will be observed during the Gaia-ESO Survey in order to build a homogeneous sample.

Unfortunately, there is not a photometric counterpart of the Survey providing homogeneous photometry for the same OC sample, and the trade-off of using different photo-

metric dataset must be accepted. Large photometric surveys do exist, such as SDSS and IPHAS/UVEX and VPHAS+ in the optical, and 2MASS or VISTA, in the IR. However, a complete overlap of the clusters is not guaranteed and we need to use a non homogeneous photometric dataset for deriving clusters' ages and distances.

In this sense, the BOCCE project has additional value with respect to the Gaia-ESO Survey. It was designed to combine photometric and spectroscopic observations of OCs in a unique framework. It started in the early nineties, aiming at studying a large sample of old OCs (about 50), fulfilling the stringent requirement of homogeneity. Photometry and HRS observations are the main ingredients to derive the clusters parameters and all the data reductions and analyses are made with the same methods. The age, distance, reddening, and approximate metallicity are obtained through the analysis of photometric imaging of OCs in several different optical filters (mainly *BVI* passbands). The sCMD is the technique used to derive them (see Ch. 4 for details). It makes use of a library of stellar evolutionary models to reproduce the main features of the observational CMDs. The set of parameters that gives the best match between synthetic and empirical CMDs are adopted as the clusters' parameters. Three different evolutionary tracks are considered (presently we use the BBC, FRA, and FST tracks), thus minimising model-dependent conclusions and determining more robust clusters' parameters. In fact, each stellar model has different recipes concerning the input physics and consequently predicts different results when used with the same dataset. The sCMD technique is also used to quantify the fraction of unresolved binaries and the DR across the clusters' face. Both shape in slightly different ways the CMD morphology and the impact of their effect can be constrained with the sCMD technique.

The BOCCE sample now comprises 34 OCs with complete photometric analysis and 10 more are underway. I studied eight of these 34 clusters, see Ch. 5 and 6 for details. I estimated age, distance, approximate metallicity, and average reddening by using the sCMD technique. To estimate the binary fractions I used a statistical method, independent of the sCMD technique. For one cluster (NGC 2141) I statistically quantified the DR by comparing the positions of MS stars on the empirical CMD as a function of their spatial position on the FoV. Such analysis was particularly relevant to explain the elongated shape of the RC of the cluster and the significant spread in colour of the MSTO phase, and to constrain with better accuracy age and distance. The relatively large FoV of the observations for Be 81 and NGC 2141 allowed the determination of their structural parameters and total mass by studying their density profiles. Even though this type of analysis is not of primary importance within the BOCCE project, it is interesting to compare the structural properties and the masses of young and old OCs in the context of cluster formation mechanisms and environment and dynamics.

The spectroscopic part of the BOCCE project, which began later (the first publication is Bragaglia et al. 2001 for NGC 6819) is lagging behind the photometric analysis and HRS chemical abundances are presently available only for 11 of these 34 OCs. However, spectroscopic data is already acquired for ten more clusters and should be obtained for three more in a forthcoming observing run. We mainly observe bright and cool stars in the RC phase, deriving metallicity and detailed composition (light elements, α , iron-peak, and heavy elements). Even with the limitations discussed above, using the 34 OCs it is possible to draw a preliminary picture of the disc properties (see Ch. 8). These OCs span Galactocentric distances in the range 5–20 kpc, ages from 0.1 to about 8 Gyr, and have typical thin disc metallicities ($-0.5 \lesssim [\text{Fe}/\text{H}] \lesssim 0.5$ dex). With the present dataset we can not discriminate between a radial metallicity gradient and a step distribution. In the first case a steep negative metallicity gradient of $-0.11 \text{ dex kpc}^{-1}$ is found in the inner disc (within 12 kpc from the Galactic centre) and a flat distribution in the outer part. In the second

case, the average metallicity of the inner disc ($[\text{Fe}/\text{H}] \sim 0.1$ dex) is 0.4 dex higher than the outer one. We do not find any significant relation between age and metallicity of the OCs (in agreement with similar findings in literature) or age and Galactocentric distance. We rather find a considerable spread in ages at each distance bin.

Setting our data in the framework of the GCE models, we compared the results of the radial metallicity gradient with the predictions of model 1 of Romano et al. (2010). The agreement between our data and the models is far from satisfactory. Even if the models are able to reproduce the general decrease in metallicity with R_{GC} , the slope(s) is not correct and there seem to be offsets. This has been found by others, like e.g. Heiter et al. (2014). The differences may be attenuated adopting a different recipe for the stellar yields, which can significantly change the chemical abundances predicted by GCE models (see Romano et al. 2010 for details). Interestingly, the model provides a negative gradient with a slope, for the inner region of the disc, which steepens with time (steeper for younger objects). Unfortunately, we cannot confirm this trend because of the poor statistical power of our sample.

However, further analyses are needed to advance in this field. The number of OCs should be expanded to better sample the age-distance-metallicity parameter space. For example, the very old tail of the OCs analysed so far (older than 2 Gyr) comprises only about half of our sample. This means that the very old age range is poorly sampled compared to the age range 0.1–2 Gyr. However, as described in Ch. 1, the known OCs older than 2 Gyr are very few, naturally limiting our investigations. The Galactocentric distance range around 8.5 kpc deserve a significant sampling in metallicity. In fact, as suggested by Lépine et al. (2011), this is the distance of the corotation radius of the MW determined from dynamical models, which may imply an independent chemical evolution of the disc within and outside this distance. The outer and inner discs deserve as well a finer sampling in R_{GC} to better understand the radial metallicity distribution both at very short and at large distances from the centre. The same is true for the inner disc.

The BOCCE project and the Gaia-ESO Survey benefit from each other. With OCs in common between the two projects, it will be possible to homogenise the clusters' parameters on a single framework. For example, it will be possible to put on a common scale the HRS metallicity estimates of the BOCCE clusters with the HRS estimates of the Gaia-ESO Survey, thus producing a unique, large, homogeneous database of clusters' chemical abundances. The interpretation of the Galactic disc properties would clearly benefit from this. Moreover, this reasoning can be expanded to other ongoing spectroscopic surveys (see Ch. 3 for a brief description of the main ones), considerably improving the HRS information on OCs. However, as demonstrated by dynamical models of the Galaxy (see Ch. 1), the star motions (and possibly the cluster motions) can not be neglected in GCE models. The kinematics of clusters and stars is then important for an accurate understanding of the Galactic disc properties. Dynamical mechanisms, such as radial migration, can significantly alter the current interpretation of the radial metallicity distribution as depicted by OCs. In this context, the Gaia mission, which will provide accurate astrometry for about 1 billion of stars (see description in Ch. 3), is of paramount importance. With measures of distances and proper motions with unprecedented accuracy, Gaia will revolutionise our knowledge of the MW structure and will provide improvements to several astrophysical fields from stellar evolution to cosmology.

Bibliography

- Adams F.C. & Myers P.C. (2001); *Modes of Multiple Star Formation*. ApJ, vol. 553, pp. 744–753. doi:10.1086/320941. astro-ph/0102039.
- Ahumada A.V., Cignoni M., Bragaglia A., et al. (2013); *NGC 2849 and NGC 6134: two more BOCCE open clusters*. MNRAS, vol. 430, pp. 221–233. doi:10.1093/mnras/sts593.
- Ahumada J.A. (2002); *CCD Photometry of the Southern Open Cluster NGC 6134*. In T. Lejeune & J. Fernandes, eds., *Observed HR Diagrams and Stellar Evolution*, vol. 274 of *Astronomical Society of the Pacific Conference Series*, p. 307.
- Ahumada J.A. (2003); *CCD Photometry of the Open Clusters NGC 2658, NGC 2849, and NGC 3247*. Rev. Mexicana Astron. Astrofis., vol. 39, pp. 41–53.
- Ahumada J.A. & Lapasset E. (2007); *New catalogue of blue stragglers in open clusters*. A&A, vol. 463, pp. 789–797. doi:10.1051/0004-6361:20054590.
- Amôres E.B., Lépine J.R.D., & Mishurov Y.N. (2009); *The corotation gap in the Galactic HI distribution*. MNRAS, vol. 400, pp. 1768–1774. doi:10.1111/j.1365-2966.2009.15611.x. 0907.4822.
- Andreuzzi G., Bragaglia A., Tosi M., & Marconi G. (2011); *Old open clusters and the Galactic metallicity gradient: Berkeley 20, Berkeley 66 and Tombaugh 2*. MNRAS, vol. 412, pp. 1265–1282. doi:10.1111/j.1365-2966.2010.17986.x. 1011.2349.
- Anthony-Twarog B.J. & Twarog B.A. (1985); *Faint stellar photometry in clusters. II - NGC 6791 and NGC 6535*. ApJ, vol. 291, pp. 595–610. doi:10.1086/163100.
- Anthony-Twarog B.J., Deliyannis C.P., Twarog B.A., et al. (2010); *Wiy Open Cluster Study. XXXIX. Abundances in NGC 6253 from Hydra Spectroscopy of the Li 6708 Å Region*. AJ, vol. 139, pp. 2034–2051. doi:10.1088/0004-6256/139/5/2034. 1003.2587.
- Arp H. & Cuffey J. (1962); *The star cluster NGC 2158*. ApJ, vol. 136, p. 51. doi:10.1086/147350.
- Asplund M., Grevesse N., Sauval A.J., & Scott P. (2009); *The Chemical Composition of the Sun*. ARA&A, vol. 47, pp. 481–522. doi:10.1146/annurev.astro.46.060407.145222. 0909.0948.
- Balaguer-Núñez L., Jordi C., Galadí-Enríquez D., & Masana E. (2004); *uvby- H_{β} CCD photometry of NGC 1817 and NGC 1807*. A&A, vol. 426, pp. 827–834. doi:10.1051/0004-6361:20041333. astro-ph/0407456.
- Balaguer-Núñez L., Jordi C., & Galadí-Enríquez D. (2005); *uvby $H\beta$ CCD photometry and membership segregation of the open cluster NGC 2548; gaps in the Main Sequence of open clusters*. A&A, vol. 437, pp. 457–466. doi:10.1051/0004-6361:20041792. astro-ph/0504044.
- Balaguer-Núñez L., Tian K.P., & Zhao J.L. (1998); *Determination of proper motions and membership of the open clusters NGC 1817 and NGC 1807*. A&AS, vol. 133, pp. 387–394. doi:10.1051/aas:1998324.

- Balcells M., Benn C.R., Carter D., et al. (2010); *Design drivers for a wide-field multi-object spectrograph for the William Herschel Telescope*. In *Society of Photo-Optical Instrumentation Engineers (SPIE) Conference Series*, vol. 7735 of *Society of Photo-Optical Instrumentation Engineers (SPIE) Conference Series*. doi:10.1117/12.856947. 1008.0600.
- Balser D.S., Rood R.T., Bania T.M., & Anderson L.D. (2011); *H II Region Metallicity Distribution in the Milky Way Disk*. *ApJ*, vol. 738, 27. doi:10.1088/0004-637X/738/1/27. 1106.1660.
- Barrado y Navascués D., Deliyannis C.P., & Stauffer J.R. (2001); *WIYN Open Cluster Study. V. Lithium Depletion and Metallicity in G and K Dwarfs of the Open Cluster M35*. *ApJ*, vol. 549, pp. 452–466. doi:10.1086/319045. astro-ph/0011125.
- Bastian N. (2011); *Cluster Disruption: From Infant Mortality to Long Term Survival*. In *Stellar Clusters & Associations: A RIA Workshop on Gaia*, pp. 85–97. 1107.2140.
- Bastian N. & de Mink S.E. (2009); *The effect of stellar rotation on colour-magnitude diagrams: on the apparent presence of multiple populations in intermediate age stellar clusters*. *MNRAS*, vol. 398, pp. L11–L15. doi:10.1111/j.1745-3933.2009.00696.x. 0906.1590.
- Baumgardt H. & Kroupa P. (2007); *A comprehensive set of simulations studying the influence of gas expulsion on star cluster evolution*. *MNRAS*, vol. 380, pp. 1589–1598. doi:10.1111/j.1365-2966.2007.12209.x. 0707.1944.
- Bertelli G., Bressan A., Chiosi C., et al. (1994); *Theoretical isochrones from models with new radiative opacities*. *A&AS*, vol. 106, pp. 275–302.
- Bessell M.S., Castelli F., & Plez B. (1998); *Model atmospheres broad-band colors, bolometric corrections and temperature calibrations for O - M stars*. *A&A*, vol. 333, pp. 231–250.
- Binney J. & Tremaine S. (2008); *Galactic Dynamics: Second Edition* (Princeton University Press).
- Bohm-Vitense E. (1995); *White Dwarf Companions to Hyades F Stars*. *AJ*, vol. 110, p. 228. doi:10.1086/117511.
- Borissova J., Bonatto C., Kurtev R., et al. (2011); *New Galactic star clusters discovered in the VVV survey*. *A&A*, vol. 532, A131. doi:10.1051/0004-6361/201116662. 1106.3045.
- Bragaglia A. & collaborators (in preparation); *The Gaia-ESO Survey: Target Selection of Open Cluster Stars*. *A&A*.
- Bragaglia A. & Tosi M. (2006); *The Bologna Open Cluster Chemical Evolution Project: Midterm Results from the Photometric Sample*. *AJ*, vol. 131, pp. 1544–1558. doi:10.1086/499537. astro-ph/0511020.
- Bragaglia A., Carretta E., Gratton R.G., et al. (2001); *Metal Abundances of Red Clump Stars in Open Clusters. I. NGC 6819*. *AJ*, vol. 121, pp. 327–336. doi:10.1086/318042. astro-ph/0009321.
- Bragaglia A., Tosi M., Andreuzzi G., & Marconi G. (2006a); *BVI photometry of the very old open cluster Berkeley 17**. *MNRAS*, vol. 368, pp. 1971–1981. doi:10.1111/j.1365-2966.2006.10266.x. astro-ph/0603050.
- Bragaglia A., Tosi M., Carretta E., et al. (2006b); *Photometric and spectroscopic study of the intermediate-age open cluster NGC 3960*. *MNRAS*, vol. 366, pp. 1493–1502. doi:10.1111/j.1365-2966.2005.09929.x. astro-ph/0511832.
- Bragaglia A., Sestito P., Villanova S., et al. (2008); *Old open clusters as key tracers of Galactic chemical evolution. II. Iron and elemental abundances in NGC 2324, NGC 2477 NGC 2660, NGC 3960, and Berkeley 32*. *A&A*, vol. 480, pp. 79–90. doi:10.1051/0004-6361:20077904.

- Bragaglia A., Gratton R.G., Carretta E., et al. (2012); *Searching for multiple stellar populations in the massive, old open cluster Berkeley 39*. A&A, vol. 548, A122. doi:10.1051/0004-6361/201220366. 1211.1142.
- Bragaglia A., Sneden C., Gratton R.G., et al. (submitted Jan. 2014); *Searching for Chemical Signatures of Multiple Stellar Populations in the Old, Massive Open Cluster NGC 6791*. ApJ.
- Bressan A., Fagotto F., Bertelli G., & Chiosi C. (1993); *Evolutionary sequences of stellar models with new radiative opacities. II - $Z = 0.02$* . A&AS, vol. 100, pp. 647–664.
- Bressan A., Marigo P., Girardi L., et al. (2012); *PARSEC: stellar tracks and isochrones with the PAdova and TRieste Stellar Evolution Code*. MNRAS, vol. 427, pp. 127–145. doi:10.1111/j.1365-2966.2012.21948.x. 1208.4498.
- Brown J.A., Wallerstein G., Geisler D., & Oke J.B. (1996); *Chemical abundances in the Outer Disk Clusters Tombaugh 2, Melotte 71, and NGC 2112*. AJ, vol. 112, p. 1551. doi:10.1086/118122.
- Bruntt H., Frandsen S., Kjeldsen H., & Andersen M.I. (1999); *Strömgren photometry of the open clusters NGC 6134 and NGC 3680*. A&AS, vol. 140, pp. 135–143. doi:10.1051/aas:1999412.
- Burkhead M.S., Burgess R.D., & Haisch B.M. (1972); *Photometric observations of the star cluster NGC 2141*. AJ, vol. 77, pp. 661–665. doi:10.1086/111333.
- Cabrera-Cano J. & Alfaro E.J. (1985); *Analysis of relative proper motion - an improved method to assign membership probabilities in open clusters*. A&A, vol. 150, pp. 298–301.
- Cameron L.M. (1985); *Metallicities and Distances of Galactic Clusters as Determined from UBV Data - Part Three - Ages and Abundance Gradients of Open Clusters*. A&A, vol. 147, p. 47.
- Cantat-Gaudin T. & collaborators (in preparation); *The Gaia-ESO Survey: Looking for multiple stellar populations in the massive cluster M 11*. A&A.
- Cantat-Gaudin T., Donati P., Pancino E., et al. (2013); *DOOp, an automated wrapper for DAOSPEC*. ArXiv e-prints. 1312.3676.
- Cardelli J.A., Clayton G.C., & Mathis J.S. (1989); *The relationship between infrared, optical, and ultraviolet extinction*. ApJ, vol. 345, pp. 245–256. doi:10.1086/167900.
- Carpenter J.M. (2000); *2MASS Observations of the Perseus, Orion A, Orion B, and Monoceros R2 Molecular Clouds*. AJ, vol. 120, pp. 3139–3161. doi:10.1086/316845. astro-ph/0009118.
- Carraro G. (2013); *The Milky Way thin disk structure as revealed by stars and young open clusters*. ArXiv e-prints. 1307.0569.
- Carraro G. & Chiosi C. (1994a); *Galactic orbits of the old open clusters NGC 188, NGC 2682, NGC 2420, NGC 752 and NGC 2506*. A&A, vol. 288, pp. 751–758.
- Carraro G. & Chiosi C. (1994b); *The Galactic system of old open clusters: age calibration and age-metallicity relation*. A&A, vol. 287, pp. 761–768.
- Carraro G. & Costa E. (2007); *Photometry of the five marginally studied open clusters Collinder 74, Berkeley 27, Haffner 8, NGC 2509, and VdB-Hagen 4*. A&A, vol. 464, pp. 573–580. doi:10.1051/0004-6361:20066350. astro-ph/0611705.
- Carraro G. & Ortolani S. (1994); *Deep CCD BV photometry of the poorly studied open cluster NGC 4815*. A&AS, vol. 106, pp. 573–579.
- Carraro G., Ng Y.K., & Portinari L. (1998); *On the Galactic disc age-metallicity relation*. MNRAS, vol. 296, pp. 1045–1056. doi:10.1046/j.1365-8711.1998.01460.x. astro-ph/9707185.

- Carraro G., Girardi L., & Chiosi C. (1999); *Is the Galactic disc older than the halo?* MNRAS, vol. 309, pp. 430–442. doi:10.1046/j.1365-8711.1999.02851.x.
- Carraro G., Hassan S.M., Ortolani S., & Vallenari A. (2001); *An optical and near IR study of the old open cluster NGC 2141.* A&A, vol. 372, pp. 879–884. doi:10.1051/0004-6361:20010558. astro-ph/0105027.
- Carraro G., Girardi L., & Marigo P. (2002); *The intermediate-age open cluster NGC 2158.* MNRAS, vol. 332, pp. 705–713. doi:10.1046/j.1365-8711.2002.05326.x. astro-ph/0202018.
- Carraro G., Bresolin F., Villanova S., et al. (2004); *Metal Abundances in Extremely Distant Galactic Old Open Clusters. I. Berkeley 29 and Saurer 1.* AJ, vol. 128, pp. 1676–1683. doi:10.1086/423912. astro-ph/0406679.
- Carraro G., Geisler D., Villanova S., et al. (2007); *Old open clusters in the outer Galactic disk.* A&A, vol. 476, pp. 217–227. doi:10.1051/0004-6361:20078113. 0709.2126.
- Carraro G., Villanova S., Demarque P., et al. (2008); *The old open cluster NGC 2112: updated estimates of fundamental parameters based on a membership analysis.* MNRAS, vol. 386, pp. 1625–1634. doi:10.1111/j.1365-2966.2008.13143.x. 0802.3243.
- Carraro G., Costa E., & Ahumada J.A. (2010); *Photometric Characterization of the Galactic Star Cluster Trumpler 20.* AJ, vol. 140, pp. 954–961. doi:10.1088/0004-6256/140/4/954. 1007.4782.
- Carraro G., Anthony-Twarog B.J., Costa E., et al. (2011); *A UBVI and uvbyCaH β Analysis of the Intermediate-age Open Cluster, NGC 5822.* AJ, vol. 142, 127. doi:10.1088/0004-6256/142/4/127. 1108.0587.
- Carraro G., Perren G., Vázquez R.A., & Moitinho A. (2013); *A couple of recent developments in the structure of the outer disk of the Milky Way.* ArXiv e-prints. 1310.1517.
- Carrera R. & Pancino E. (2011); *Chemical abundance analysis of the open clusters Berkeley 32, NGC 752, Hyades, and Praesepe.* A&A, vol. 535, A30. doi:10.1051/0004-6361/201117473. 1107.2242.
- Carrera R., Gallart C., Pancino E., & Zinn R. (2007); *The Infrared Ca II Triplet as Metallicity Indicator.* AJ, vol. 134, p. 1298. doi:10.1086/520803. 0705.3335.
- Carretta E., Bragaglia A., Gratton R.G., & Tosi M. (2004); *Iron abundances from high-resolution spectroscopy of the open clusters NGC 2506, NGC 6134, and IC 4651.* A&A, vol. 422, pp. 951–962. doi:10.1051/0004-6361:20047142. astro-ph/0404298.
- Carretta E., Bragaglia A., Gratton R.G., & Tosi M. (2005); *High-resolution spectroscopy of the old open cluster Collinder 261: abundances of iron and other elements.* A&A, vol. 441, pp. 131–140. doi:10.1051/0004-6361:20052875. astro-ph/0505606.
- Carretta E., Bragaglia A., & Gratton R.G. (2007); *The chemical abundance of the very metal-rich old open clusters NGC 6253 and NGC 6791.* A&A, vol. 473, pp. 129–141. doi:10.1051/0004-6361:20065213. 0706.2780.
- Carretta E., Bragaglia A., Gratton R.G., et al. (2010); *Properties of stellar generations in globular clusters and relations with global parameters.* A&A, vol. 516, A55. doi:10.1051/0004-6361/200913451. 1003.1723.
- Chabrier G. (2001); *The Galactic Disk Mass Budget. I. Stellar Mass Function and Density.* ApJ, vol. 554, pp. 1274–1281. doi:10.1086/321401. astro-ph/0107018.
- Chen L. & Hou J.L. (2009); *Galactic Open Clusters and the LOCS Project.* In B. Soonthornthum, S. Komonjinda, K.S. Cheng, & K.C. Leung, eds., *The Eighth Pacific Rim Conference on Stellar Astrophysics: A Tribute to Kam-Ching Leung*, vol. 404 of *Astronomical Society of the Pacific Conference Series*, p. 343.

- Chen L., Hou J.L., & Wang J.J. (2003); *On the Galactic Disk Metallicity Distribution from Open Clusters. I. New Catalogs and Abundance Gradient*. AJ, vol. 125, pp. 1397–1406. doi:10.1086/367911. astro-ph/0212542.
- Chiappini C., Matteucci F., & Gratton R. (1997); *The Chemical Evolution of the Galaxy: The Two-Infall Model*. ApJ, vol. 477, p. 765. doi:10.1086/303726. astro-ph/9609199.
- Chiappini C., Matteucci F., & Romano D. (2001); *Abundance Gradients and the Formation of the Milky Way*. ApJ, vol. 554, pp. 1044–1058. doi:10.1086/321427. astro-ph/0102134.
- Cignoni M., Tosi M., Bragaglia A., et al. (2008); *Disentangling the Galaxy at low Galactic latitudes*. MNRAS, vol. 386, pp. 2235–2241. doi:10.1111/j.1365-2966.2008.13194.x. 0803.0674.
- Cignoni M., Beccari G., Bragaglia A., & Tosi M. (2011); *Three new bricks in the wall: Berkeley 23, Berkeley 31 and King 8*. MNRAS, vol. 416, pp. 1077–1091. doi:10.1111/j.1365-2966.2011.19104.x. 1105.4440.
- Cirasuolo M., Afonso J., Bender R., et al. (2012); *MOONS: a multi-object optical and near-infrared spectrograph for the VLT*. In *Society of Photo-Optical Instrumentation Engineers (SPIE) Conference Series*, vol. 8446 of *Society of Photo-Optical Instrumentation Engineers (SPIE) Conference Series*. doi:10.1117/12.925871. 1208.5780.
- Claria J.J. & Mermilliod J.C. (1992); *Membership, binarity and metallicity of red giants in the open cluster NGC 6134*. A&AS, vol. 95, pp. 429–436.
- Cole A.A., Smecker-Hane T.A., Tolstoy E., et al. (2004); *The effects of age on red giant metallicities derived from the near-infrared CaII triplet*. MNRAS, vol. 347, pp. 367–379. doi:10.1111/j.1365-2966.2004.07223.x. astro-ph/0309614.
- Corsaro E., Stello D., Huber D., et al. (2012); *Asteroseismology of the Open Clusters NGC 6791, NGC 6811, and NGC 6819 from 19 Months of Kepler Photometry*. ApJ, vol. 757, 190. doi:10.1088/0004-637X/757/2/190. 1205.4023.
- Daflon S. & Cunha K. (2004); *Galactic Metallicity Gradients Derived from a Sample of OB Stars*. ApJ, vol. 617, pp. 1115–1126. doi:10.1086/425607. astro-ph/0409084.
- D’Antona F., Montalbán J., Kupka F., & Heiter U. (2002); *The Böhm-Vitense Gap: The Role of Turbulent Convection*. ApJ, vol. 564, pp. L93–L96. doi:10.1086/338911.
- de Bruijne J.H.J., Hoogerwerf R., & de Zeeuw P.T. (2000); *Two Böhm-Vitense Gaps in the Main Sequence of the Hyades*. ApJ, vol. 544, pp. L65–L67. doi:10.1086/317296. astro-ph/0011162.
- de Jong R.S., Bellido-Tirado O., Chiappini C., et al. (2012); *4MOST: 4-metre multi-object spectroscopic telescope*. In *Society of Photo-Optical Instrumentation Engineers (SPIE) Conference Series*, vol. 8446 of *Society of Photo-Optical Instrumentation Engineers (SPIE) Conference Series*. doi:10.1117/12.926239. 1206.6885.
- De Silva G.M., Freeman K.C., Asplund M., et al. (2007); *Chemical Homogeneity in Collinder 261 and Implications for Chemical Tagging*. AJ, vol. 133, pp. 1161–1175. doi:10.1086/511182. astro-ph/0611832.
- Dean J.F., Warren P.R., & Cousins A.W.J. (1978); *Reddenings of Cepheids using BVI photometry*. MNRAS, vol. 183, pp. 569–583.
- Dias W.S. & Lépine J.R.D. (2005); *Direct Determination of the Spiral Pattern Rotation Speed of the Galaxy*. ApJ, vol. 629, pp. 825–831. doi:10.1086/431456. astro-ph/0503083.
- Dias W.S., Alessi B.S., Moitinho A., & Lépine J.R.D. (2002); *New catalogue of optically visible open clusters and candidates*. A&A, vol. 389, pp. 871–873. doi:10.1051/0004-6361:20020668. astro-ph/0203351.

- Dominguez I., Chieffi A., Limongi M., & Straniero O. (1999); *Intermediate-Mass Stars: Updated Models*. ApJ, vol. 524, pp. 226–241. doi:10.1086/307787. astro-ph/9906030.
- Donati P., Bragaglia A., Cignoni M., et al. (2012); *The anticentre old open clusters Berkeley 27, Berkeley 34 and Berkeley 36: new additions to the BOCCE project*. MNRAS, vol. 424, pp. 1132–1148. doi:10.1111/j.1365-2966.2012.21289.x. 1205.3684.
- Donati P., Beccari G., Bragaglia A., et al. (2014a); *NGC 1817, NGC 2141 and Berkeley 81: three BOCCE clusters of intermediate age*. MNRAS, vol. 437, pp. 1241–1258. doi:10.1093/mnras/stt1944. 1311.2469.
- Donati P., Cantat Gaudin T., Bragaglia A., et al. (2014b); *The Gaia-ESO Survey: Reevaluation of the parameters of the open cluster Trumpler 20 using photometry and spectroscopy*. A&A, vol. 561, A94. doi:10.1051/0004-6361/201322911. 1312.3925.
- Dotter A., Chaboyer B., Jevremović D., et al. (2008); *The Dartmouth Stellar Evolution Database*. ApJS, vol. 178, pp. 89–101. doi:10.1086/589654. 0804.4473.
- Drew J.E. (2012); *Science from the Next Generation Imaging and Spectroscopic Surveys*. ESO Workshop.
- Drew J.E., Greimel R., Irwin M.J., et al. (2005); *The INT Photometric H α Survey of the Northern Galactic Plane (IPHAS)*. MNRAS, vol. 362, pp. 753–776. doi:10.1111/j.1365-2966.2005.09330.x. astro-ph/0506726.
- Dutra C.M. & Bica E. (2001); *New infrared star clusters and candidates in the Galaxy detected with 2MASS*. A&A, vol. 376, pp. 434–440. doi:10.1051/0004-6361:20010978. astro-ph/0107286.
- Elmegreen B.G. (2011); *Star Formation on Galactic Scales: Empirical Laws*. In C. Charbonnel & T. Montmerle, eds., *EAS Publications Series*, vol. 51 of *EAS Publications Series*, pp. 3–17. doi:10.1051/eas/1151001. 1101.3108.
- Emerson J.P., Sutherland W.J., McPherson A.M., et al. (2004); *The Visible & Infrared Survey Telescope for Astronomy*. The Messenger, vol. 117, pp. 27–32.
- Fagotto F., Bressan A., Bertelli G., & Chiosi C. (1994); *Evolutionary sequences of stellar models with new radiative opacities. IV. $Z=0.004$ and $Z=0.008$* . A&AS, vol. 105, pp. 29–38.
- Fitzgerald M.P. (1970); *The Intrinsic Colours of Stars and Two-Colour Reddening Lines*. A&A, vol. 4, p. 234.
- Freeman K. & Bland-Hawthorn J. (2002); *The New Galaxy: Signatures of Its Formation*. ARA&A, vol. 40, pp. 487–537. doi:10.1146/annurev.astro.40.060401.093840. astro-ph/0208106.
- Friel E.D. (1995); *The Old Open Clusters Of The Milky Way*. ARA&A, vol. 33, pp. 381–414. doi:10.1146/annurev.aa.33.090195.002121.
- Friel E.D. & Janes K.A. (1993); *Metallicities and radial velocities of old open clusters*. A&A, vol. 267, pp. 75–91.
- Friel E.D., Janes K.A., Hong L., et al. (1995); *New results for the oldest open clusters: kinematics and metallicities of the old disk*. In E.J. Alfaro & A.J. Delgado, eds., *The Formation of the Milky Way*, pp. 189–190.
- Friel E.D., Janes K.A., Tavares M., et al. (2002); *Metallicities of Old Open Clusters*. AJ, vol. 124, pp. 2693–2720. doi:10.1086/344161.
- Friel E.D., Jacobson H.R., Barrett E., et al. (2003); *Abundances of Red Giants in the Old Open Cluster Collinder 261*. AJ, vol. 126, pp. 2372–2384. doi:10.1086/378600.

- Friel E.D., Jacobson H.R., & Pilachowski C.A. (2005); *Abundances of Red Giants in Old Open Clusters. II. Berkeley 17*. AJ, vol. 129, pp. 2725–2730. doi:10.1086/430146.
- Friel E.D., Jacobson H.R., & Pilachowski C.A. (2010); *Abundances of Red Giants in Old Open Clusters. V. Be 31, Be 32, Be 39, M 67, NGC 188, and NGC 1193*. AJ, vol. 139, pp. 1942–1967. doi:10.1088/0004-6256/139/5/1942.
- Friel E.D., Donati P., Bragaglia A., et al. (submitted); *The Gaia-ESO Survey: Properties of the intermediate age open cluster NGC 4815*. A&A.
- Frinchaboy P.M. & SDSS-III Collaboration (2010); *The SDSS-III/Apache Point Observatory Galactic Evolution Experiment (SDSS-III/APOGEE)*. In *American Astronomical Society Meeting Abstracts #215*, vol. 42 of *Bulletin of the American Astronomical Society*, p. #470.04.
- Frinchaboy P.M., Majewski S.R., Crane J.D., et al. (2004); *Star Clusters in the Galactic Anticenter Stellar Structure and the Origin of Outer Old Open Clusters*. ApJ, vol. 602, pp. L21–L24. doi:10.1086/382504. astro-ph/0311101.
- Frinchaboy P.M., Thompson B., Jackson K.M., et al. (2013); *The Open Cluster Chemical Analysis and Mapping Survey: Local Galactic Metallicity Gradient with APOGEE Using SDSS DR10*. ApJ, vol. 777, L1. doi:10.1088/2041-8205/777/1/L1. 1308.4195.
- Geisler D., Villanova S., Carraro G., et al. (2012); *The Unique Na:O Abundance Distribution in NGC 6791: The First Open(?) Cluster with Multiple Populations*. ApJ, vol. 756, L40. doi:10.1088/2041-8205/756/2/L40. 1207.3328.
- Genovali K., Lemasle B., Bono G., et al. (2013); *On the metallicity distribution of classical Cepheids in the Galactic inner disk*. A&A, vol. 554, A132. doi:10.1051/0004-6361/201321650. 1305.2742.
- Giallongo E., Ragazzoni R., Grazian A., et al. (2008); *The performance of the blue prime focus large binocular camera at the large binocular telescope*. A&A, vol. 482, pp. 349–357. doi:10.1051/0004-6361:20078402. 0801.1474.
- Gilmore G. & collaborators (in preparation); *The Gaia-ESO Survey*. A&A.
- Gilmore G., Randich S., Asplund M., et al. (2012); *The Gaia-ESO Public Spectroscopic Survey*. The Messenger, vol. 147, pp. 25–31.
- Giorgi E.E., Vázquez R.A., Baume G., et al. (2002); *NGC 2571: An intermediate-age open cluster with a White Dwarf candidate*. A&A, vol. 381, pp. 884–893. doi:10.1051/0004-6361:20011633.
- Girardi L. (1999); *A secondary clump of red giant stars: why and where*. MNRAS, vol. 308, pp. 818–832. doi:10.1046/j.1365-8711.1999.02746.x. astro-ph/9901319.
- Girardi L., Bressan A., Bertelli G., & Chiosi C. (2000a); *Evolutionary tracks and isochrones for low- and intermediate-mass stars: From 0.15 to 7 M_{sun} , and from $Z=0.0004$ to 0.03*. A&AS, vol. 141, pp. 371–383. doi:10.1051/aas:2000126. astro-ph/9910164.
- Girardi L., Mermilliod J.C., & Carraro G. (2000b); *On the peculiar red clump morphology in the open clusters NGC 752 and NGC 7789*. A&A, vol. 354, pp. 892–898. astro-ph/0001068.
- Girardi L., Rubele S., & Kerber L. (2009); *Discovery of two distinct red clumps in NGC 419: a rare snapshot of a cluster at the onset of degeneracy*. MNRAS, vol. 394, pp. L74–L78. doi:10.1111/j.1745-3933.2008.00614.x. 0901.0773.
- Girardi L., Eggenberger P., & Miglio A. (2011); *Can rotation explain the multiple main-sequence turn-offs of Magellanic Cloud star clusters?* MNRAS, vol. 412, pp. L103–L107. doi:10.1111/j.1745-3933.2011.01013.x. 1101.1880.

- Glatt K., Grebel E.K., Sabbi E., et al. (2008); *Age Determination of Six Intermediate-Age Small Magellanic Cloud Star Clusters with HST/ACS*. AJ, vol. 136, 1703. doi:10.1088/0004-6256/136/4/1703. 0807.3744.
- Gonzalez G. & Wallerstein G. (2000); *Elemental Abundances in the Inner Galaxy Open Cluster M11*. PASP, vol. 112, pp. 1081–1088. doi:10.1086/316601.
- Gratton R., Sneden C., & Carretta E. (2004); *Abundance Variations Within Globular Clusters*. ARA&A, vol. 42, pp. 385–440. doi:10.1146/annurev.astro.42.053102.133945.
- Gratton R., Bragaglia A., Carretta E., & Tosi M. (2006); *The Metallicity of the Old Open Cluster NGC 6791*. ApJ, vol. 642, pp. 462–469. doi:10.1086/500729. astro-ph/0601027.
- Gratton R.G. & Contarini G. (1994); *Elemental Abundances in the Old Open Clusters NGC2243 and MELOTTE:66*. A&A, vol. 283, p. 911.
- Grevesse N. & Sauval A.J. (1998); *Standard Solar Composition*. Space Sci. Rev., vol. 85, pp. 161–174. doi:10.1023/A:1005161325181.
- Grevesse N., Asplund M., & Sauval A.J. (2007); *The Solar Chemical Composition*. Space Sci. Rev., vol. 130, pp. 105–114. doi:10.1007/s11214-007-9173-7.
- Gustafsson B., Edvardsson B., Eriksson K., et al. (2008); *A grid of MARCS model atmospheres for late-type stars. I. Methods and general properties*. A&A, vol. 486, pp. 951–970. doi:10.1051/0004-6361:200809724. 0805.0554.
- Gutermuth R.A., Myers P.C., Megeath S.T., et al. (2008); *Spitzer Observations of NGC 1333: A Study of Structure and Evolution in a Nearby Embedded Cluster*. ApJ, vol. 674, pp. 336–356. doi:10.1086/524722. 0710.1860.
- Harris G.L.H. & Harris W.E. (1977); *The Hyades-age cluster NGC 1817*. AJ, vol. 82, pp. 612–619. doi:10.1086/112094.
- Hasegawa T., Malasan H.L., Kawakita H., et al. (2004); *New Photometric Data of Old Open Clusters in the Anti-Galactic Center Region*. PASJ, vol. 56, pp. 295–311.
- Heiter U., Soubiran C., Netopil M., & Paunzen E. (2014); *On the metallicity of open clusters. II. Spectroscopy*. A&A, vol. 561, A93. doi:10.1051/0004-6361/201322559. 1311.2306.
- Henry R.B.C., Kwitter K.B., Jaskot A.E., et al. (2010); *Abundances of Galactic Anticenter Planetary Nebulae and the Oxygen Abundance Gradient in the Galactic Disk*. ApJ, vol. 724, pp. 748–761. doi:10.1088/0004-637X/724/1/748. 1009.1921.
- Hill V. & Pasquini L. (1999); *A Super Lithium Rich giant in the metal-poor open cluster Berkeley 21*. A&A, vol. 348, pp. L21–L24. astro-ph/9907106.
- Hills J.G. (1980); *The effect of mass loss on the dynamical evolution of a stellar system - Analytic approximations*. ApJ, vol. 235, pp. 986–991. doi:10.1086/157703.
- Hou J.L., Prantzos N., & Boissier S. (2000); *Abundance gradients and their evolution in the Milky Way disk*. A&A, vol. 362, pp. 921–936. astro-ph/0007164.
- Hurley J. & Tout C.A. (1998); *The binary second sequence in cluster colour-magnitude diagrams*. MNRAS, vol. 300, pp. 977–980. doi:10.1046/j.1365-8711.1998.01981.x. astro-ph/9807108.
- Iwamoto K., Brachwitz F., Nomoto K., et al. (1999); *Nucleosynthesis in Chandrasekhar Mass Models for Type IA Supernovae and Constraints on Progenitor Systems and Burning-Front Propagation*. ApJS, vol. 125, pp. 439–462. doi:10.1086/313278. astro-ph/0002337.

- Jacobson H.R., Friel E.D., & Pilachowski C.A. (2007); *Na, Al, and O Abundances of Open Clusters NGC 7142, NGC 6939, and IC 4756*. AJ, vol. 134, pp. 1216–1230. doi:10.1086/520927.
- Jacobson H.R., Friel E.D., & Pilachowski C.A. (2008); *Abundances of Red Giants in Old Open Clusters. III. NGC 7142*. AJ, vol. 135, pp. 2341–2349. doi:10.1088/0004-6256/135/6/2341.
- Jacobson H.R., Friel E.D., & Pilachowski C.A. (2009); *Abundances of Red Giants in Old Open Clusters. IV. NGC 1817, NGC 1883, NGC 2141, and NGC 2158*. AJ, vol. 137, pp. 4753–4765. doi:10.1088/0004-6256/137/6/4753.
- Jacobson H.R., Friel E.D., & Pilachowski C.A. (2011a); *A Chemical Abundance Study of Red Giants in Open Clusters NGC 2204 and NGC 2243*. AJ, vol. 141, 58. doi:10.1088/0004-6256/141/2/58.
- Jacobson H.R., Pilachowski C.A., & Friel E.D. (2011b); *A Chemical Abundance Study of 10 Open Clusters Based on WIYN-Hydra Spectroscopy*. AJ, vol. 142, 59. doi:10.1088/0004-6256/142/2/59. 1107.4139.
- Janes K.A. (1979); *Evidence for an abundance gradient in the galactic disk*. ApJS, vol. 39, pp. 135–156. doi:10.1086/190568.
- Janes K.A. & Phelps R.L. (1994); *The galactic system of old star clusters: The development of the galactic disk*. AJ, vol. 108, pp. 1773–1785. doi:10.1086/117192.
- Janes K.A., Tilley C., & Lynga G. (1988); *Properties of the open cluster system*. AJ, vol. 95, pp. 771–784. doi:10.1086/114676.
- Jílková L., Carraro G., Jungwiert B., & Minchev I. (2012); *The origin and orbit of the old, metal-rich, open cluster NGC 6791. Insights from kinematics*. A&A, vol. 541, A64. doi:10.1051/0004-6361/201117347. 1203.0546.
- Johnson H.L. & Knuckles C.F. (1955); *The Hyades and Coma Berenices Star Clusters*. ApJ, vol. 122, p. 209. doi:10.1086/146079.
- Joshi Y.C. (2005); *Interstellar extinction towards open clusters and Galactic structure*. MNRAS, vol. 362, pp. 1259–1266. doi:10.1111/j.1365-2966.2005.09391.x. astro-ph/0507069.
- Kalirai J.S. & Tosi M. (2004); *Interpreting the colour-magnitude diagrams of open star clusters through numerical simulations*. MNRAS, vol. 351, pp. 649–662. doi:10.1111/j.1365-2966.2004.07813.x. astro-ph/0403420.
- Kaluzny J. (1998); *CCD photometry of distant open clusters. IV. Trumpler 5*. A&AS, vol. 133, pp. 25–28. doi:10.1051/aas:1998453.
- Keller S.C., Schmidt B.P., Bessell M.S., et al. (2007); *The SkyMapper Telescope and The Southern Sky Survey*. PASA, vol. 24, pp. 1–12. doi:10.1071/AS07001. astro-ph/0702511.
- Kharchenko N.V., Piskunov A.E., Schilbach E., et al. (2013); *Global survey of star clusters in the Milky Way. II. The catalogue of basic parameters*. A&A, vol. 558, A53. doi:10.1051/0004-6361/201322302. 1308.5822.
- Kim S.C., Kyeong J., & Sung E.C. (2009); *Near-Infrared Photometric Study of the Old Open Cluster Trumpler 5*. Journal of Korean Astronomical Society, vol. 42, pp. 135–144. 0912.4588.
- King I. (1962); *The structure of star clusters. I. an empirical density law*. AJ, vol. 67, p. 471. doi:10.1086/108756.
- King I.R. (1966); *The structure of star clusters. III. Some simple dynamical models*. AJ, vol. 71, p. 64. doi:10.1086/109857.

- Kjeldsen H. & Frandsen S. (1991); *Stellar photometric stability. II - Ages and distances for 13 open clusters with time series observations*. A&AS, vol. 87, pp. 119–152.
- Koch A., Odenkirchen M., Grebel E.K., & Caldwell J.A.R. (2004); *A calibration map for Wide Field Imager photometry*. Astronomische Nachrichten, vol. 325, pp. 299–306. doi:10.1002/asna.200310176. astro-ph/0310301.
- Kormendy J., Drory N., Bender R., & Cornell M.E. (2010); *Bulgeless Giant Galaxies Challenge Our Picture of Galaxy Formation by Hierarchical Clustering*. ApJ, vol. 723, pp. 54–80. doi:10.1088/0004-637X/723/1/54. 1009.3015.
- Kovtyukh V.V., Soubiran C., & Belik S.I. (2004); *A new Böhm-Vitense gap in the temperature range 5560 to 5610 K in the main sequence hm-Vitense gap in the main sequence*. A&A, vol. 427, pp. 933–936. doi:10.1051/0004-6361:20041449. astro-ph/0409753.
- Kroupa P. (2002); *The Initial Mass Function and Its Variation (Review)*. In E.K. Grebel & W. Brandner, eds., *Modes of Star Formation and the Origin of Field Populations*, vol. 285 of *Astronomical Society of the Pacific Conference Series*, p. 86. astro-ph/0102155.
- Kroupa P., Tout C.A., & Gilmore G. (1993); *The distribution of low-mass stars in the Galactic disc*. MNRAS, vol. 262, pp. 545–587.
- Kurucz R. (1993); *Opacities for Stellar Atmospheres: [+0.5a],[+0.0a],[-0.5a] +.4 alpha*. Opacities for Stellar Atmospheres: [+0.5a],[+0.0a],[-0.5a] +.4 alpha. Kurucz CD-ROM No. 9. Cambridge, Mass.: Smithsonian Astrophysical Observatory, 1993., vol. 9.
- Kyeong J.M., Byun Y.I., Sung E.C., & Chun M.S. (2004); *UBVIJHK Photometric Study of the Open Cluster NGC 2849*. AJ, vol. 128, pp. 2331–2338. doi:10.1086/424939.
- Lada C.J. & Lada E.A. (2003); *Embedded Clusters in Molecular Clouds*. ARA&A, vol. 41, pp. 57–115. doi:10.1146/annurev.astro.41.011802.094844. astro-ph/0301540.
- Landolt A.U. (1992); *UBVRI photometric standard stars in the magnitude range 11.5-16.0 around the celestial equator*. AJ, vol. 104, pp. 340–371. doi:10.1086/116242.
- Lasker B.M., Lattanzi M.G., McLean B.J., et al. (2008); *The Second-Generation Guide Star Catalog: Description and Properties*. AJ, vol. 136, pp. 735–766. doi:10.1088/0004-6256/136/2/735. 0807.2522.
- Leavitt H.S. & Pickering E.C. (1912); *Periods of 25 Variable Stars in the Small Magellanic Cloud*. Harvard College Observatory Circular, vol. 173, pp. 1–3.
- Lépine J.R.D., Acharova I.A., & Mishurov Y.N. (2003); *Corotation, Stellar Wandering, and Fine Structure of the Galactic Abundance Pattern*. ApJ, vol. 589, pp. 210–216. doi:10.1086/374596.
- Lépine J.R.D., Cruz P., Scarano S. Jr., et al. (2011); *Overlapping abundance gradients and azimuthal gradients related to the spiral structure of the Galaxy*. MNRAS, vol. 417, pp. 698–708. doi:10.1111/j.1365-2966.2011.19314.x. 1106.3137.
- Li Z., Mao C., Chen L., & Zhang Q. (2012); *Combined Effects of Binaries and Stellar Rotation on the Color-Magnitude Diagrams of Intermediate-age Star Clusters*. ApJ, vol. 761, L22. doi:10.1088/2041-8205/761/2/L22. 1302.0099.
- Lindoff U. (1972); *An investigation of four southern open clusters*. A&AS, vol. 7, p. 231.
- Luck R.E. & Lambert D.L. (2011); *The Distribution of the Elements in the Galactic Disk. III. A Reconsideration of Cepheids from $l = 30^\circ$ to 250°* . AJ, vol. 142, 136. doi:10.1088/0004-6256/142/4/136. 1108.1947.
- Lynga G. & Palous J. (1987); *The local kinematics of open star clusters*. A&A, vol. 188, pp. 35–38.

- Maderak R.M., Deliyannis C.P., King J.R., & Cummings J.D. (2013); *WIYN Open Cluster Study. LVII. Oxygen Abundances of Solar-type Dwarfs in the Hyades and NGC 752*. AJ, vol. 146, 143. doi:10.1088/0004-6256/146/6/143.
- Maeder A. (1974); *Stellar evolution near the main sequence: on some systematic differences between cluster sequences and model calculations*. A&A, vol. 32, pp. 177–190.
- Magrini L., Sestito P., Randich S., & Galli D. (2009); *The evolution of the Galactic metallicity gradient from high-resolution spectroscopy of open clusters*. A&A, vol. 494, pp. 95–108. doi:10.1051/0004-6361/200810634. 0812.0854.
- Magrini L., Randich S., Zoccali M., et al. (2010); *Open clusters towards the Galactic centre: chemistry and dynamics. A VLT spectroscopic study of NGC 6192, NGC 6404, NGC 6583*. A&A, vol. 523, A11. doi:10.1051/0004-6361/201015395.
- Magrini L., Randich S., Friel E., et al. (2013a); *FAMA: An automatic code for stellar parameter and abundance determination*. A&A, vol. 558, A38. doi:10.1051/0004-6361/201321844. 1307.2367.
- Magrini L., Randich S., Romano D., et al. (2013b); *The Gaia-ESO Survey: Abundance ratios in the inner-disk open clusters Trumpler 20, NGC 4815, NGC 6705*. ArXiv e-prints. 1312.6472.
- Malkin Z. (2013); *Statistical analysis of the determinations of the Sun's Galactocentric distance*. In R. de Grijs, ed., *IAU Symposium*, vol. 289 of *IAU Symposium*, pp. 406–409. doi:10.1017/S1743921312021825. 1306.5519.
- Marigo P., Girardi L., Bressan A., et al. (2008); *Evolution of asymptotic giant branch stars. II. Optical to far-infrared isochrones with improved TP-AGB models*. A&A, vol. 482, pp. 883–905. doi:10.1051/0004-6361/20078467. 0711.4922.
- Matteucci F. & Greggio L. (1986); *Relative roles of type I and II supernovae in the chemical enrichment of the interstellar gas*. A&A, vol. 154, pp. 279–287.
- McMahon R. (2012); *Science from the Next Generation Imaging and Spectroscopic Surveys*. ESO Workshop.
- Mermilliod J.C. & Mayor M. (1989); *Red giants in open clusters. I - Binarity and stellar evolution in five Hyades-generation clusters: NGC 2447, 2539, 2632, 6633, and 6940*. A&A, vol. 219, pp. 125–141.
- Mermilliod J.C. & Mayor M. (1990); *Red giants in open clusters. III - Binarity and stellar evolution in five intermediate-age clusters: NGC 2360, 2423, 5822, 6811, and IC 4756*. A&A, vol. 237, pp. 61–72.
- Mermilliod J.C., Claria J.J., Andersen J., & Mayor M. (1997); *Red giants in open clusters. VII. Melotte 71*. A&A, vol. 324, pp. 91–96.
- Mermilliod J.C., Latham D.W., Glushkova E.V., et al. (2003); *Red giants in open clusters. X. NGC 1817*. A&A, vol. 399, pp. 105–112. doi:10.1051/0004-6361:20021777.
- Mermilliod J.C., Andersen J., Latham D.W., & Mayor M. (2007); *Red giants in open clusters. XIII. Orbital elements of 156 spectroscopic binaries*. A&A, vol. 473, pp. 829–845. doi:10.1051/0004-6361:20078007.
- Mermilliod J.C., Mayor M., & Udry S. (2008); *Red giants in open clusters. XIV. Mean radial velocities for 1309 stars and 166 open clusters*. A&A, vol. 485, pp. 303–314. doi:10.1051/0004-6361:200809664.
- Miglio A., Brogaard K., Stello D., et al. (2012); *Asteroseismology of old open clusters with Kepler: direct estimate of the integrated red giant branch mass-loss in NGC 6791 and 6819*. MNRAS, vol. 419, pp. 2077–2088. doi:10.1111/j.1365-2966.2011.19859.x. 1109.4376.

- Milone A.P., Bedin L.R., Piotto G., & Anderson J. (2009); *Multiple stellar populations in Magellanic Cloud clusters. I. An ordinary feature for intermediate age globulars in the LMC?* A&A, vol. 497, pp. 755–771. doi:10.1051/0004-6361/200810870. 0810.2558.
- Milone A.P., Piotto G., Bedin L.R., et al. (2012); *The ACS survey of Galactic globular clusters. XII. Photometric binaries along the main sequence.* A&A, vol. 540, A16. doi:10.1051/0004-6361/201016384. 1111.0552.
- Minniti D. (1995); *Abundances and velocities for open and globular cluster giants: The data.* A&AS, vol. 113, p. 299.
- Mitschang A.W., De Silva G., Zucker D.B., et al. (2013); *Quantitative chemical tagging, stellar ages and the chemo-dynamical evolution of the Galactic disc.* ArXiv e-prints. 1312.1759.
- Mollá M., Ferrini F., & Diaz A.I. (1997); *Evolution of Spiral Galaxies. VII. Time Evolution of the Radial Distributions of Abundances.* ApJ, vol. 475, p. 519. doi:10.1086/303550.
- Montalto M., Santos N.C., Villanova S., et al. (2012); *Abundance analysis of four members of the metal-rich open cluster NGC 6253.* MNRAS, vol. 423, pp. 3039–3048. doi:10.1111/j.1365-2966.2012.21040.x.
- Moustakas J., Kennicutt R.C. Jr., Tremonti C.A., et al. (2010); *Optical Spectroscopy and Nebular Oxygen Abundances of the Spitzer/SINGS Galaxies.* ApJS, vol. 190, 233. doi:10.1088/0067-0049/190/2/233. 1007.4547.
- Mucciarelli A., Pancino E., Lovisi L., et al. (2013); *GALA: An Automatic Tool for the Abundance Analysis of Stellar Spectra.* ApJ, vol. 766, 78. doi:10.1088/0004-637X/766/2/78. 1302.3618.
- Ortolani S., Bica E., Barbuy B., & Zoccali M. (2005); *The old open clusters Berkeley 36, Berkeley 73 and Biurakan 13 (Berkeley 34).* A&A, vol. 439, pp. 1135–1135. doi:10.1051/0004-6361:20041458e.
- Panagia N. & Tosi M. (1981); *Galactic metal abundance gradient in young stellar population.* A&A, vol. 96, pp. 306–309.
- Pancino E., Carrera R., Rossetti E., & Gallart C. (2010); *Chemical abundance analysis of the open clusters Cr 110, NGC 2099 (M 37), NGC 2420, NGC 7789, and M 67 (NGC 2682).* A&A, vol. 511, A56. doi:10.1051/0004-6361/200912965. 0910.0723.
- Parisi M.C., Clariá J.J., Piatti A.E., & Geisler D. (2005); *Washington photometry of open cluster giants: two moderately metal-poor anticentre clusters.* MNRAS, vol. 363, pp. 1247–1256. doi:10.1111/j.1365-2966.2005.09520.x.
- Pasquini L., Avila G., Blecha A., et al. (2002); *Installation and commissioning of FLAMES, the VLT Multifibre Facility.* The Messenger, vol. 110, pp. 1–9.
- Pedicelli S., Bono G., Lemasle B., et al. (2009); *On the metallicity gradient of the Galactic disk.* A&A, vol. 504, pp. 81–86. doi:10.1051/0004-6361/200912504. 0906.3140.
- Perryman M.A.C., de Boer K.S., Gilmore G., et al. (2001); *GAIA: Composition, formation and evolution of the Galaxy.* A&A, vol. 369, pp. 339–363. doi:10.1051/0004-6361:20010085. astro-ph/0101235.
- Pietrinferni A., Cassisi S., Salaris M., & Castelli F. (2004); *A Large Stellar Evolution Database for Population Synthesis Studies. I. Scaled Solar Models and Isochrones.* ApJ, vol. 612, pp. 168–190. doi:10.1086/422498. astro-ph/0405193.
- Platais I., Melo C., Fulbright J.P., et al. (2008); *Trumpler 20 - an old and rich open cluster.* MNRAS, vol. 391, pp. 1482–1488. doi:10.1111/j.1365-2966.2008.14011.x. 0809.4458.

- Platais I., Melo C., Quinn S.N., et al. (2012); *The Effects of Differential Reddening and Stellar Rotation on the Appearance of Multiple Populations in Star Clusters: The Case of Trumpler 20*. *ApJ*, vol. 751, L8. doi:10.1088/2041-8205/751/1/L8. 1203.1053.
- Portegies Zwart S.F., McMillan S.L.W., & Gieles M. (2010); *Young Massive Star Clusters*. *ARA&A*, vol. 48, pp. 431–493. doi:10.1146/annurev-astro-081309-130834. 1002.1961.
- Portinari L. & Chiosi C. (1999); *On star formation and chemical evolution in the Galactic disc*. *A&A*, vol. 350, pp. 827–839. astro-ph/9908326.
- Prisinzano L., Carraro G., Piotto G., et al. (2001); *Luminosity and mass function of galactic open clusters I. NGC 4815*. *A&A*, vol. 369, pp. 851–861. doi:10.1051/0004-6361:20010202. astro-ph/0101371.
- Purgathofer A. (1961); *Dreifarbentphotometrie der offenen Sternhaufen NGC 1502, 1807 und 1817. Mit 9 Textabbildungen*. *ZAp*, vol. 52, p. 186.
- Purgathofer A. (1964); *Dreifarbentphotometrie in offenen Sternhaufen sowie in zwei Sternfeldern im Cyg*. *Annalen der K.K. Sternwarte Wien*, vol. 26, pp. 37–73.
- Randich S. & Gilmore G. (2013); *The Gaia-ESO Public Spectroscopic Survey*. *The Messenger*.
- Recio-Blanco A. & collaborators (in preparation); *The Gaia-ESO Survey: The analysis of high-resolution GIRAFFE spectra of FGK-type stars*. *A&A*.
- Reddy A.B.S., Giridhar S., & Lambert D.L. (2012); *The chemical abundances of open clusters: NGC 752, NGC 1817, NGC 2360 and NGC 2506*. In *Astronomical Society of India Conference Series*, vol. 4 of *Astronomical Society of India Conference Series*, pp. 197–199.
- Robin A.C., Reyl e C., Derri ere S., & Picaud S. (2003); *A synthetic view on structure and evolution of the Milky Way*. *A&A*, vol. 409, pp. 523–540. doi:10.1051/0004-6361:20031117.
- Romano D., Karakas A.I., Tosi M., & Matteucci F. (2010); *Quantifying the uncertainties of chemical evolution studies. II. Stellar yields*. *A&A*, vol. 522, A32. doi:10.1051/0004-6361/201014483. 1006.5863.
- Rood R.T., Quireza C., Bania T.M., et al. (2007); *The Abundance Gradient in Galactic H II Regions*. In A. Vallenari, R. Tantal o, L. Portinari, & A. Moretti, eds., *From Stars to Galaxies: Building the Pieces to Build Up the Universe*, vol. 374 of *Astronomical Society of the Pacific Conference Series*, p. 169.
- Rosvick J.M. (1995); *Photometry of the intermediate-age open cluster NGC 2141*. *MNRAS*, vol. 277, pp. 1379–1384.
- Ro skar R., Debattista V.P., Quinn T.R., et al. (2008); *Riding the Spiral Waves: Implications of Stellar Migration for the Properties of Galactic Disks*. *ApJ*, vol. 684, pp. L79–L82. doi:10.1086/592231. 0808.0206.
- Ro skar R., Debattista V.P., Quinn T.R., & Wadsley J. (2012); *Radial migration in disc galaxies - I. Transient spiral structure and dynamics*. *MNRAS*, vol. 426, pp. 2089–2106. doi:10.1111/j.1365-2966.2012.21860.x. 1110.4413.
- Sacco G. & collaborators (in preparation); *The Gaia-ESO Survey: processing of the FLAMES-UVES spectra*. *A&A*.
- Sagar R. & Griffiths W.K. (1998); *BVI CCD photometry of the distant open star clusters Berkeley 81, Berkeley 99, NGC 6603 and NGC 7044*. *MNRAS*, vol. 299, pp. 1–23. doi:10.1046/j.1365-8711.1998.01551.x.
- Salaris M. & Cassisi S. (2005); *Evolution of Stars and Stellar Populations* (John Wiley & Sons).

- Salaris M., Weiss A., & Percival S.M. (2004); *The age of the oldest Open Clusters*. A&A, vol. 414, pp. 163–174. doi:10.1051/0004-6361:20031578. astro-ph/0310363.
- Salpeter E.E. (1955); *The Luminosity Function and Stellar Evolution*. ApJ, vol. 121, p. 161. doi:10.1086/145971.
- Santos N.C., Lovis C., Pace G., et al. (2009); *Metallicities for 13 nearby open clusters from high-resolution spectroscopy of dwarf and giant stars. Stellar metallicity, stellar mass, and giant planets*. A&A, vol. 493, pp. 309–316. doi:10.1051/0004-6361:200811093. 0811.2392.
- Schlegel D.J., Finkbeiner D.P., & Davis M. (1998); *Maps of Dust Infrared Emission for Use in Estimation of Reddening and Cosmic Microwave Background Radiation Foregrounds*. ApJ, vol. 500, p. 525. doi:10.1086/305772. astro-ph/9710327.
- Schönrich R. & Binney J. (2009); *Chemical evolution with radial mixing*. MNRAS, vol. 396, pp. 203–222. doi:10.1111/j.1365-2966.2009.14750.x. 0809.3006.
- Seleznev A.F., Carraro G., Costa E., & Loktin A.V. (2010); *Homogeneous photometry and star counts in the field of 9 Galactic star clusters*. New A, vol. 15, pp. 61–75. doi:10.1016/j.newast.2009.05.011. 0905.3017.
- Sellwood J.A. & Binney J.J. (2002); *Radial mixing in galactic discs*. MNRAS, vol. 336, pp. 785–796. doi:10.1046/j.1365-8711.2002.05806.x. astro-ph/0203510.
- Sestito P., Bragaglia A., Randich S., et al. (2006); *Old open clusters as key tracers of Galactic chemical evolution. I. Fe abundances in NGC 2660, NGC 3960, and Berkeley 32*. A&A, vol. 458, pp. 121–134. doi:10.1051/0004-6361:20065175. astro-ph/0607438.
- Sestito P., Randich S., & Bragaglia A. (2007); *Element abundances in the metal-rich open cluster NGC 6253*. A&A, vol. 465, pp. 185–196. doi:10.1051/0004-6361:20066643. astro-ph/0701182.
- Sestito P., Bragaglia A., Randich S., et al. (2008); *Open clusters as key tracers of Galactic chemical evolution. III. Element abundances in Berkeley 20, Berkeley 29, Collinder 261 and Melotte 66*. A&A, vol. 488, pp. 943–958. doi:10.1051/0004-6361:200809650. 0807.2313.
- Shaver P.A., McGee R.X., Newton L.M., et al. (1983); *The galactic abundance gradient*. MNRAS, vol. 204, pp. 53–112.
- Sigurdsson S. & Phinney E.S. (1995); *Dynamics and Interactions of Binaries and Neutron Stars in Globular Clusters*. ApJS, vol. 99, p. 609. doi:10.1086/192199. astro-ph/9412078.
- Skrutskie M.F., Cutri R.M., Stiening R., et al. (2006); *The Two Micron All Sky Survey (2MASS)*. AJ, vol. 131, pp. 1163–1183. doi:10.1086/498708.
- Smiljanic R. & collaborators (in preparation); *The Gaia-ESO Survey: The analysis of high-resolution UVES spectra of FGK-type stars*. A&A.
- Snedden C., Bean J., Ivans I., et al. (2012); *MOOG: LTE line analysis and spectrum synthesis*. Astrophysics Source Code Library, 1202.009.
- Snedden C.A. (1973); *Carbon and Nitrogen Abundances in Metal-Poor Stars*. Ph.D. thesis, THE UNIVERSITY OF TEXAS AT AUSTIN.
- Soderblom D.R., Hillenbrand L.A., Jeffries R.D., et al. (2013); *Ages of young stars*. ArXiv e-prints. 1311.7024.
- Stanghellini L. & Haywood M. (2010); *The Galactic Structure and Chemical Evolution Traced by the Population of Planetary Nebulae*. ApJ, vol. 714, pp. 1096–1107. doi:10.1088/0004-637X/714/2/1096. 1003.0759.

- Stetson P.B. (1987); *DAOPHOT - A computer program for crowded-field stellar photometry*. PASP, vol. 99, pp. 191–222. doi:10.1086/131977.
- Stetson P.B. (1994); *The center of the core-cusp globular cluster M15: CFHT and HST Observations, ALLFRAME reductions*. PASP, vol. 106, pp. 250–280. doi:10.1086/133378.
- Stetson P.B. & Pancino E. (2008); *DAOSPEC: An Automatic Code for Measuring Equivalent Widths in High-Resolution Stellar Spectra*. PASP, vol. 120, pp. 1332–1354. doi:10.1086/596126. 0811.2932.
- Subramaniam A. & Bhatt B.C. (2007); *Photometric study of distant open clusters in the second quadrant: NGC 7245, King 9, King 13 and IC 166*. MNRAS, vol. 377, pp. 829–834. doi:10.1111/j.1365-2966.2007.11648.x. astro-ph/0703075.
- Taylor B.J. (2006); *The Benchmark Cluster Reddening Project. I. Reddening Values for the Hyades, Coma, and Praesepe*. AJ, vol. 132, pp. 2453–2468. doi:10.1086/508610.
- Tosi M. (1988); *Models of galactic chemical evolution - The problem of uniqueness*. A&A, vol. 197, pp. 33–46.
- Tosi M. (1996); *Comparison of Chemical Evolution Models for the Galactic Disk*. In C. Leitherer, U. Fritze-von-Alvensleben, & J. Huchra, eds., *From Stars to Galaxies: the Impact of Stellar Physics on Galaxy Evolution*, vol. 98 of *Astronomical Society of the Pacific Conference Series*, p. 299. astro-ph/9512096.
- Tosi M., Greggio L., Marconi G., & Focardi P. (1991); *Star formation in dwarf irregular galaxies - Sextans B*. AJ, vol. 102, pp. 951–974. doi:10.1086/115925.
- Tosi M., Bragaglia A., & Cignoni M. (2007); *The old open clusters Berkeley 32 and King 11*. MNRAS, vol. 378, pp. 730–740. doi:10.1111/j.1365-2966.2007.11827.x. 0704.0550.
- Twarog B.A., Ashman K.M., & Anthony-Twarog B.J. (1997); *Some Revised Observational Constraints on the Formation and Evolution of the Galactic Disk*. AJ, vol. 114, p. 2556. doi:10.1086/118667. astro-ph/9709122.
- Vallée J.P. (2005); *The Spiral Arms and Interarm Separation of the Milky Way: An Updated Statistical Study*. AJ, vol. 130, pp. 569–575. doi:10.1086/431744.
- van den Bergh S. (1958); *Old Galactic Clusters. With 1 figure in the text*. ZAp, vol. 46, p. 176.
- VandenBerg D.A., Bergbusch P.A., & Dowler P.D. (2006); *The Victoria-Regina Stellar Models: Evolutionary Tracks and Isochrones for a Wide Range in Mass and Metallicity that Allow for Empirically Constrained Amounts of Convective Core Overshooting*. ApJS, vol. 162, pp. 375–387. doi:10.1086/498451. astro-ph/0510784.
- Ventura P., Zeppieri A., Mazzitelli I., & D'Antona F. (1998); *Full spectrum of turbulence convective mixing: I. theoretical main sequences and turn-off for $0.6 \leq M \leq 15 M_{\odot}$* . A&A, vol. 334, pp. 953–968.
- Villanova S., Carraro G., Bresolin F., & Patat F. (2005); *Metal Abundances in Extremely Distant Galactic Old Open Clusters. II. Berkeley 22 and Berkeley 66*. AJ, vol. 130, pp. 652–658. doi:10.1086/430958. astro-ph/0504282.
- Villanova S., Randich S., Geisler D., et al. (2010); *The metallicity of the open cluster Tombaugh 2*. A&A, vol. 509, A102. doi:10.1051/0004-6361/200913258. 0911.3044.
- von Hippel T. & Sarajedini A. (1998); *WIYN Open Cluster Study. I. Deep Photometry of NGC 188*. AJ, vol. 116, pp. 1789–1800. doi:10.1086/300561. astro-ph/9806100.

- Warren S.R. & Cole A.A. (2009); *Metallicities and radial velocities of five open clusters including a new candidate member of the Monoceros stream*. MNRAS, vol. 393, pp. 272–296. doi:10.1111/j.1365-2966.2008.14268.x. 0811.2925.
- Woosley S.E. & Weaver T.A. (1995); *The Evolution and Explosion of Massive Stars. II. Explosive Hydrodynamics and Nucleosynthesis*. ApJS, vol. 101, p. 181. doi:10.1086/192237.
- Wu Z.Y., Zhou X., Ma J., & Du C.H. (2009); *The orbits of open clusters in the Galaxy*. MNRAS, vol. 399, pp. 2146–2164. doi:10.1111/j.1365-2966.2009.15416.x. 0909.3737.
- Yang W., Meng X., Bi S., et al. (2011); *The Contributions of Interactive Binary Stars to Double Main-sequence Turnoffs and Dual Red Clump of Intermediate-age Star Clusters*. ApJ, vol. 731, L37. doi:10.1088/2041-8205/731/2/L37. 1103.3128.
- Yong D., Carney B.W., & Teixeira de Almeida M.L. (2005); *Elemental Abundance Ratios in Stars of the Outer Galactic Disk. I. Open Clusters*. AJ, vol. 130, pp. 597–625. doi:10.1086/430934. astro-ph/0504193.
- Yong D., Carney B.W., & Friel E.D. (2012); *Elemental Abundance Ratios in Stars of the Outer Galactic Disk. IV. A New Sample of Open Clusters*. AJ, vol. 144, 95. doi:10.1088/0004-6256/144/4/95. 1206.6931.
- York D.G., Adelman J., Anderson J.E. Jr., et al. (2000); *The Sloan Digital Sky Survey: Technical Summary*. AJ, vol. 120, pp. 1579–1587. doi:10.1086/301513. astro-ph/0006396.
- Zucker D.B., De Silva G., Freeman K.C., et al. (2013); *GALAH Takes Flight*. In *American Astronomical Society Meeting Abstracts*, vol. 221 of *American Astronomical Society Meeting Abstracts*, p. #234.06.